HAL
open science

Nonlinear active control of turbulent separated flows : Theory and experiments

Maxime Feingesicht

To cite this version:

Maxime Feingesicht. Nonlinear active control of turbulent separated flows : Theory and experiments. Other. Ecole Centrale de Lille, 2017. English. NNT : 2017ECLI0024 . tel-01801155

HAL Id: tel-01801155

https://theses.hal.science/tel-01801155v1

Submitted on 28 May 2018

HAL is a multi-disciplinary open access archive for the deposit and dissemination of scientific research documents, whether they are published or not. The documents may come from teaching and research institutions in France or abroad, or from public or private research centers.

L'archive ouverte pluridisciplinaire **HAL**, est destinée au dépôt et à la diffusion de documents scientifiques de niveau recherche, publiés ou non, émanant des établissements d'enseignement et de recherche français ou étrangers, des laboratoires publics ou privés.

N° d'ordre : 344

CENTRALE LILLE

THESE

Présentée en vue
d'obtenir le grade de

DOCTEUR

En

Spécialité : Sciences et technologies de l'information et de la communicaiton

Par

Maxime Feingesicht

DOCTORAT DELIVRE PAR CENTRALE LILLE

Titre de la thèse :
Contrôle non linéaire actif d'écoulements turbulents décollés : Théorie et expérimentations.

Soutenue le 11 décembre 2017 devant le jury d'examen :

Président	**Bernard Brogliato, Directeur de recherche INRIA, BIPOP**
Rapporteur	**Louis Cattafesta, Professeur, Florida State University**
Rapporteur	**Bernd Noack, Directeur de recherche CNRS, LIMSI**
Rapporteur	**Sophie Tarbouriech, Directrice de recherche CNRS, LAAS**
Membre	**Bernard Brogliato, Directeur de recherche INRIA, BIPOP**
Membre	**Quentin Gallas, Ingénieur de recherche ONERA, DAAP**
Invité	**Laurent Keirsbulck, Maître de conférences, UVHC**
Directeur de thèse	**Jean-Pierre Richard, Professeur, Centrale Lille**
Co-encadrant	**Andrey Polyakov, Chargé de recherche INRIA, INRIA**
Co-encadrant	**Franck Kerhevé, Maître de conférences, Université de Poitiers**

Thèse préparée dans le Laboratoire CRIStAL UMR 9189

Ecole Doctorale SPI 072 (Lille I, Lille III, Artois, ULCO, UVHC, Centrale Lille)

CENTRALE LILLE

THESE

Présentée en vue
d'obtenir le grade de

DOCTEUR

En

Spécialité : Sciences et technologies de l'information et de la communicaiton

Par

Maxime Feingesicht

DOCTORAT DELIVRE PAR CENTRALE LILLE

Titre de la thèse :
Contrôle non linéaire actif d'écoulements turbulents décollés : Théorie et expérimentations.

Soutenue le 11 décembre 2017 devant le jury d'examen :

Président	**Bernard Brogliato, Directeur de recherche INRIA, BIPOP**
Rapporteur	**Louis Cattafesta, Professeur, Florida State University**
Rapporteur	**Bernd Noack, Directeur de recherche CNRS, LIMSI**
Rapporteur	**Sophie Tarbouriech, Directrice de recherche CNRS, LAAS**
Membre	**Bernard Brogliato, Directeur de recherche INRIA, BIPOP**
Membre	**Quentin Gallas, Ingénieur de recherche ONERA, DAAP**
Invité	**Laurent Keirsbulck, Maître de conférences, UVHC**
Directeur de thèse	**Jean-Pierre Richard, Professeur, Centrale Lille**
Co-encadrant	**Andrey Polyakov, Chargé de recherche INRIA, INRIA**
Co-encadrant	**Franck Kerhevé, Maître de conférences, Université de Poitiers**

Thèse préparée dans le Laboratoire CRIStAL UMR 9189

Ecole Doctorale SPI 072 (Lille I, Lille III, Artois, ULCO, UVHC, Centrale Lille)

CENTRALE LILLE

THESIS

Defended in order

to become

DOCTOR

In

Field: Sciences et technologies de l'information et de la communicaiton

By

Maxime Feingesicht

Ph. D. DELIVERED BY CENTRALE LILLE

Title of the thesis:
Nonlinear active control of turbulent separated flows: Theory and experiments.

Defended the 11th of December 2017 with the jury composition:

President	**Bernard Brogliato, INRIA Senior Researcher, BIPOP**
Reporter	**Louis Cattafesta, Professor, Florida State University Bernd**
Reporter	**Noack, CNRS Senior Researcher, LIMSI**
Reporter	**Sophie Tarbouriech, CNRS Senior Researcher, LAAS**
Member	**Bernard Brogliato, INRIA Senior Researcher, BIPOP**
Member	**Quentin Gallas, ONERA Research Engineer, DAAP Laurent**
Guest	**Keirsbulck, Associate Professor, UVHC**
Thesis supervisor	**Jean-Pierre Richard, Professor, Centrale Lille**
Co-monitor	**Andrey Polyakov, INRIA Junior Researcher, INRIA**
Co-monitor	**Franck Kerhevé, Associate Professor, Université de Poitiers**

Thesis prepared in the Laboratory CRIStAL UMR 9189

Ecole Doctorale SPI 072 (Lille I, Lille III, Artois, ULCO, UVHC, Centrale Lille)

Centrale Lille n'entend donner aucune approbation ni improbation aux opinions émises dans les thèses : ces opinions devront être considérées comme propres à leurs auteurs.

Centrale Lille neither endorse nor censure authors' opinions expressed in the thesis: these opinions must be considered to be those of their authors.

Mots clés : contrôle des écoulements, contrôle par modes glissants, contrôle non linéaire, systèmes bilinéaires, systèmes à retard

Keywords: flow control, sliding mode control, nonlinear control, bilinear systems, time-delay systems

This thesis has been prepared at the following research units:

CRIStAL UMR 9189
Université Lille 1
Bâtiment M3 extension
Avenue Carl Gauss
59655 Villeneuve d'Ascq Cedex
France

☎ (33)(0)3 28 77 85 41
Site `https://www.cristal.univ-lille.fr/`

Centrale Lille
Cité Scientifique
59651 Villeneuve d'Ascq Cedex
France

☎ (33)(0)3 20 33 53 53
Site `https://www.ec-lille.fr/`

INRIA Lille - Nord Europe
Parc scientifique de la Haute-Borne 40, avenue Halley - Bât A - Park Plaza 59650 Villeneuve d'Ascq - France

☎ (33)(0)3 59 57 78 00
Site `https://www.inria.fr/centre/lille`

À ma famille

Thanks

This thesis was financed by Centrale Lille and the Région Hauts-de-France in the framework of the CNRS Research Federation on Ground Transports and Mobility, in articulation with the ELSAT2020 project supported by the European Community, the French Ministry of Higher Education and Research, the Hauts-de-France Regional Council. The research was conducted in the Non-A Team of INRIA Nord Europe and the CRIStAL laboratory.

I would first like to thank Pr. Louis Cattafesta, Dr. Bernd Noack and Dr. Sophie Tarbouriech for reviewing my thesis. I would also like to thank Dr. Bernard Brogliato, Dr. Quentin Gallas and Dr. Laurent Keirsbulck for accepting to be members of my thesis jury.

I extend the warmest thanks to my thesis advisor Jean-Pierre Richard and to my co-advisors Andrey Polyakov and Franck Kerhervé. Their constant support and help where key to the results obtained during my Ph. D. and made me grow both from a scientific and a personal standpoint. All this would have not been possible without them and for this I will be forever grateful for all the time they devoted to me.

I thank all the members from ONERA who helped me with the design of the model and control, the gathering of the data, the experimental testing and for making their experimental setup available for me, most notably Julien Dandoins, Quentin Gallas, Bruno Mialon, Christophe Verbeke and Vianney Nowinski.

In a similar fashion, I thank the members of the LAMIH who helped me with the experimental testing of the control and for making their experimental setup available for me, most notably Laurent Keirsbulck, Camila Chovet, Marc Lippert and Baptiste Plumejeau.

I would also like to thank all the members (current or former) from the LML for the data they provided me, amongst others Cédric Raibaudo, Jean-Marc Foucaut and Michel Stanislas.

I thank INRIA Nord Europe for allowing me to use one of their offices to work during the 3 years of my Ph. D., supporting me during trips for summer schools and conferences. I particularly thank Corinne Jamroz for her invaluable administrative help.

I warmly thank all the members from the Non-A Team and the CRIStAL laboratory and the Ph. D. and postdocs for their good mood and all the good times we had together : Rosane, Denis, Wilfrid, Alban, Gang, Lotfi, Laurentiu, Christophe, Roudy, Yacine, Stanislav, Mert, Lucien, Désirée, Zohra, Jijju, Paco, Hafiz, Tatiana, Qi, Yue, Tona, Haik, Matteo, Héctor, Manuel, Gabriele, Nadhynee, Konstantin.

Finally, I thank my family for their unfailing support during all these years.

Table of contents

Thanks **xv**

Table of contents **xvii**

List of Figures **xix**

List of Tables **xxiii**

Nomenclature **xxv**

Introduction **1**

1 State of the art **5**
1.1 Generalities on flow control 5
1.2 Special case of separated flows 7
1.3 Active flow control 14
1.4 Modeling strategies 20
1.5 Control strategies 31

2 Experimental configurations **37**
2.1 Test case I : Massively separated turbulent boundary layer . . . 38
2.2 Test case II : Separated flow over a plain flap 45
2.3 Test case III : Flow over an Ahmed body 51

3 Identification algorithm **61**
3.1 Derivation of SISO models from PDE models 62
3.2 Input delays identification 63
3.3 Bilinear delay-difference model 66
3.4 Identification of state delays 69
3.5 Results of identification and comparison 71
3.6 Conclusions 76

4 Model-based control **79**
4.1 Control aims 79
4.2 Open-loop optimal control 81
4.3 Setpoint tracking control 88
4.4 Experimental results 95

Conclusion **107**

Bibliography **111**

A Sketch of the proof of Theorem 1 **127**

B NOMAD **129**

C Identification results **133**
C.1 Models for the test case II 133
C.2 Models for the test case III 136

D Publications **137**
D.1 Paper presented in the European Control Conference ECC16 - Aalborg, Denmark - June 2016 137
D.2 Paper published in the International Journal of Robust and Nonlinear Control 144

Extended abstract **165**

List of Figures

1.1 Objective of flow reattachment in the ideal case 8
1.2 Examples of configurations on which flow control can be applied 8
1.3 Examples of canonical configurations on which flow control can be applied 9
1.4 Boundary layer developing over a flat plate with zero-pressure gradient (the figure is taken from [114]) 11
1.5 Typical regions of a turbulent boundary layer (adapted from [62]) 11
1.6 Flow separation and adverse pressure gradient (Taken from [49]). Zone A presents the initial boundary layer, zone B the transition towards flow separaiton and zone C the separated flow 13
1.7 Flow separation and adverse pressure gradient (Taken from [114]). 15
1.8 Examples of perturbations on a system 19
1.9 Common flowchart for control choice in Flow Control (Taken from [19]) 21
1.10 Mesh points for the finite difference method (Taken from [102]) 26

2.1 Schematics of the experimental set-up. Enlarged picture : ramp model. Zoom : region of the flap with locations of the hot-film sensors and active air blowers (Only the hot-film 1 is used in this thesis for identification) 39
2.2 Photography of the ramp model. The flow is coming from the left 39
2.3 Uncontrolled and controlled streamlines 40
2.4 Voltage output of one hot-film : maximum, minimum and averaged signals 43
2.5 Sets of data gathered in the LML 44
2.6 Schematic of placement of the wing inside the wind tunnel . . 46
2.7 Schematic of the wing 46
2.8 Schematic of the flap with sensors placement 47
2.9 Photo of the passive vortex generators placed before the flap . 48
2.10 Sets of data gathered in the ONERA 49
2.10 Sets of data gathered in the ONERA 50

2.11 Frequency response of the actuation device. V_j is the mean velocity of the jet, V_{j0} is the mean velocity of the jet in steady blowing and DC is the duty cycle. 52
2.12 Schematic of the Ahmed body 54
2.13 Natural flow characteristics in the symmetry plane ($z = 0$) . . . 55
2.14 Time-histories response of the pressures and forces measurements due to a steady blowing step actuation ($Re_h = 9{\times}10^4$, $C_\mu = 1.355\%$). 56
2.15 Example of simultaneous measurement of the Q-switch signal of the laser cavity B and the unsteady pressures (p_1 and p_2) and forces (F_D and F_L) during a PIV acquisition. + subscript denotes the h/U_∞ normalisation. 57
2.16 Sets of data gathered in the LAMIH 58
2.16 Sets of data gathered in the LAMIH 59

3.1 Identification of the input state-dependent delay for data set N°2 64
3.2 Fitting of the input state-dependent delays 65
3.3 Identified model with state-dependent input delay, zoom on data set N°3 73
3.4 Averaged identified model with state-dependent input delay, zoom on data set N°3 74

4.1 Open-loop optimal control for the TC II with $\alpha = 0.78$. Flow conditions : $U = 34.5$m/s, $q = 25$g/s, AoA = 24° 96
4.2 Open-loop optimal control for the TC II with $\alpha = 0.62$. Flow conditions : $U = 34.5$m/s, $q = 25$g/s, AoA = 24° 97
4.3 Sliding Mode control for the TC II with $y^* = 0.25$V. Flow conditions : $U = 34.5$m/s, $q = 25$g/s, AoA = 24° 99
4.4 Sliding Mode control for the TC II with $y^* = 0.4$V. Flow conditions : $U = 34.5$m/s, $q = 25$g/s, AoA = 24° 99
4.5 Sliding Mode control for the TC II with $y^* = 0.25$V. Flow conditions : $U = 14.5$m/s, $q = 25$g/s, AoA = 24° 100
4.6 Sliding Mode control for the TC II with $y^* = 0.25$V. Flow conditions : $U = 34.5$m/s, $q = 25$g/s, AoA = 10° 100
4.7 Sliding Mode control for the TC II with $y^* = 0.25$V. Flow conditions : $U = 34.5$m/s, $q = 25$g/s, AoA = Time varying 101
4.8 Sliding Mode control for the TC II with $y^* = 0.25$V. Flow conditions : $U = 34.5$m/s, $q = 25$g/s, AoA = Time varying 102
4.9 Sliding Mode control for the TC II with $y^* = 0.25$V. Flow conditions : $U = 34.5$m/s, $q = 25$g/s, AoA = Time varying, vortex generators placed before the flap 102

4.10 Sliding Mode control for the TC II with $y^* = 0.25$V. Flow conditions : $U = 34.5$m/s, $q = 15$g/s, AoA = 24° 103
4.11 Sliding Mode control for the TC II with $y^* = 0.4$V. Flow conditions : $U = 34.5$m/s, $q = 15$g/s, AoA = 24° 103
4.12 Time evolution of (top) drag, (middle) DC* and (bottom) control command u obtained using slide mode control. Test Case III. . 104
4.13 Command law found by the SMC algorithm during a given test sequence for which the pressure measured upstream show significant variations. Test case III. 105
4.14 Command law found by the SMC algorithm during a given test sequence for which the pressure measured upstream show quasi sinusoidal variations. Test case III. 105

B.1 Example of different mesh configurations with $n = 2$ 131
B.2 Flowchart of the NOMAD algorithm 131

C.1 Identified model for test case II, zoom on data set N°2 135
C.2 Identified model for test case II, zoom on data set N°9 135

D.1 Présentation de l'expérience du LML 166
D.2 Présentation de l'expérience de l'ONERA 167
D.3 Schéma du corps d'Ahmed du LAMIH. 167

List of Tables

2.1 Operating conditions and range of control parameters for the test case I 41
2.2 Position of the hot-film sensors 47
2.3 Range of control parameters & operating conditions for model identification : Test case II 49
2.4 PIV cases and associated parameters. 57
2.5 Range of control parameters & operating conditions for model identification : test case III 57

3.1 Values of the delays and identified coefficients (all values have No Unit) for the complete model 72
3.2 Comparison of L_2 norm values, FIT coefficients and correlation for state-dependent and fixed input delay models for the complete model 72
3.3 Values of the delays and identified coefficients (all values have No Unit) for the averaged model 74
3.4 Comparison of L_2 norm values, FIT coefficients and correlation for state-dependent and fixed input delay models for the averaged model 75

4.1 Value of the cost function J for several DC 97

C.1 Delays and coefficients of the model of the test case II with $N_1 = 10$, $N_2 = 10$ and $N_3 = 3$ 134
C.2 Values of the criteria of the model of the test case II with $N_1 = 10$, $N_2 = 10$ and $N_3 = 3$ 134
C.3 Delays and coefficients of the model of the test case II with $N_1 = 2$, $N_2 = 2$ and $N_3 = 1$ 134
C.4 Values of the criteria of the model of the test case II with $N_1 = 2$, $N_2 = 2$ and $N_3 = 1$ 136
C.5 Delays and coefficients of the model of the test case III with $N_1 = 2$, $N_2 = 2$ and $N_3 = 1$ 136

C.6 Values of the criteria of the model of the test case III with $N_1 = 2$, $N_2 = 2$ and $N_3 = 1$ 136

Nomenclature

Acronyms

PDE	Partial Differential Equation
POD	Proper Orthogonal Decomposition
SISO	Single-Input Single-Output
TC	Test Case
APG	Adverse Pressure Gradient
PIV	Particle Image Velocimetry
VG	Vortex Generator
NSE	Navier-Stokes Equations
SMC	Sliding Mode Control
ARX	Auto-Regressive eXogeneous
ARMAX	Auto-Regressive Moving Average eXogeneous
NARMAX	Nonlinear Auto-Regressive Moving Average eXogeneous
PID	Proportional Integral Derivative
LML	Laboratoire de Mécanique de Lille
ONERA	Office National d'Études et de Recherches Aérospatiales
LAMIH	Laboratoire d'Automatique, de Mécanique et d'Informatique industrielles et Humaines

Symbols

$\mathbb{R}$	set of real numbers
$\mathbb{R}_+$	set of real non-negative numbers : $\mathbb{R}_+ = \{x \in \mathbb{R} \mid x \geq 0\}$
e^x	Exponential function
e	Euler's number : $e = e^1$
$O(h)$	"Big O" notation : $f(t) \to O(h)$ as $t \to +\infty \Leftrightarrow \exists M > 0, t_0 > 0 : \lvert f(t)\rvert \geq Mh, \forall t \geq t_0$
$\mathbf{C}_\Omega$	space of continuous functions
$\mathbb{1}$	unit constant function : $\mathbb{1}(s) = 1$, $\forall s \in \Omega$; $\mathbb{1} \in \mathbf{C}_\Omega$
$\mathbf{L}^2_\Omega$	space of quadratically integrable functions : $\lVert z\rVert_{\mathbf{L}^2_\Omega} = \sqrt{\int_\Omega z^2(s)ds}$
$\mathbf{L}^\infty_\Omega$	space of locally measurable essentially bounded functions : $\lVert z\rVert_{L^\infty} = \operatorname*{ess\,sup}_{s\in\Omega} \lvert z(s)\rvert$
U_∞	freestream velocity
Re	Reynolds number
St	Strouhal number
C_μ	momentum coefficient
f_+	reduced frequency
DC	duty cycle

Introduction

The current developments in transportation industry are impacted by the desire to reach higher speed for smaller travel times and the need to reduce the energy consumption for sustainable development. Both scientific and industrial communities are looking for lower costs of transportation and drastic reduction of the CO_2 emitted every year.

One of the causes of these energy losses relates to aerodynamic issues such as drag or flow separation over the vehicle. Historically, separation was handled by passive flow control. Passive control is done by modifying the geometry of the vehicle by changing its shape or by adding small devices ("passive actuators") fixed on the surface at appropriate places. Theses devices can be static or retractable. While passive control does not require energy to power the devices, they can lead to significant increase of the total drag and can not generally adapt to the natural dynamics of the flow. Amongst the most common passive control techniques are vortex generators. These devices take the form of inclined or helical airfoils of small dimensions fixed normal to the surface upstream or in the region where the separation occurs.

Passive flow control suffers from the issue of not being adaptable to a change in the experimental conditions and hence lack robustness. Modification of the actuators in regard to changes in the flow dynamics, known as Active Flow Control (AFC), requires first some flexibility of these devices. Their action can be computed independently of the result obtained (open-loop control), but such a solution also lacks robustness. The only issue for an actual adaptation to the perturbed environmental conditions is known in control theory as "closed-loop control". In addition to the flexibility of the active devices, one needs some feedback from the flow itself which means, experimentally, real-time

measurements. These two conditions (flexibility and real-time measurements) are necessary in order to apply active control techniques allowing to maintain the flow in a given state satisfying the desired objective (drag, noise, or again vibration reduction for example), despite perturbations or change in inflow conditions.

AFC is divided in two main categories. The first one is model-free control. Among others, recent developments in model-free techniques led to controllers based on machine learning techniques and showed promising results. However, machine learning requires numerous experiments before being efficient and the reliability and convergence of the algorithms are not well proven. The second category is model-based control. Model-based robust control of separated flows remains of particular interest and can be implemented on real systems without too much complexity if the model is chosen to be sufficiently simple. But it requires to have a model of the flow, may it be from physical equations or from identification. The first approach would be to use partial differential equations, namely the Navier-Stockes Equations (NSE), but this implies complicated (or even impossible) online calculations and the way to design controllers/observers remains open.

The alternative proposed in this work is to use "grey-box" identification techniques so to derive a simpler model that can be useful for control purpose. The model suggested is a bilinear, delayed difference equation which is able to catch non-linear mechanisms. Such a model will be shown to be quite realistic in an identification perspective. It is much simpler than NSE, however remains nonlinear and behaves in an infinite dimensional space.

This PhD work benefited from the platform CONTRAERO (`http://contraero.univ-lille1.fr`) developed by the Nord-Pas-de-Calais regional consortium. The control strategy developed by implemented and tested for the three different flow configurations conducted respectively in :

— the wind tunnel of LML (high Reynolds number large boundary layer wind-tunnel). In this setup, the flow develops along a slightly inclined flat plate to recover a zero pressure streamwise gradient followed by a inclined flap along which the boundary layer occurs separation and reattaches further downstream to the floor of the wind-tunnel.

— the L2 wind tunnel of ONERA. The flow develops on a test model placed in the center of the wind tunnel between two vertical plates. The test model consists of a flat plate and a plain flap based on a NACA 4412 airfoil shape. The angle of the flap can be adjusted between 2°and 37°.
— the wind tunnel of LAMIH, equipped with an Ahmed body (classically used as a geometric simplification of a car). The model is mounted over a raised floor with a sharp leading-edge to control the boundary layer thickness.

A unique control hardware setup, based on an Arduino Mega microcontroller (`https://store.arduino.cc/arduino-mega-2560-rev3`), was designed for the the overall tests. In addition, the same type of model (bilinear with delays) was used to model the different plants. The derived model was found sufficiently simple and accurate to model the flow state in the overall configurations examined.

In all three situations, we used the same kind of simplified model (bilinear with delays) which was sufficiently well adapted to the measured data. This makes us consider that such reduced models cas be seen as an original contribution of this work.

The present manuscript is organized as follows : an overview of the state of the art and the current problems that flow control tries to solve is given in Chapter 1. Chapter 2 describes the experimental setups and data used in this thesis. Chapter 3 presents and justifies the Signe-Input Single-Output (SISO) bilinear delayed models introduced in this thesis and describes our identification algorithm. Open-loop and feedback controllers based on the identified models to answer the problems mentioned in the Chapter 1 are presented in Chapter 4. Finally, conclusions on the obtained results and the perspectives for futures works are presented.

Chapter 1

State of the art

1.1 Generalities on flow control

A large portion of nowadays CO_2 emissions from transportation are due to aerodynamic forces interacting with the vehicle and causing drag, lift or download, lateral forces, moments in roll or again pitch and yaw impacting maneuverability and fuel consumption. These forces arise from two-sources : form (or pressure) drag and viscous friction. The form drag comes from a difference in static pressure around the vehicle induced by the shape itself forcing the flow to exchange pressure for velocity in order to maintain total pressure. On the other side, the friction drag is due in part to friction of the fluid on the surface of the vehicle and in part to the way the friction alters the main flow downstream or back of the vehicle. Its explanation comes about from understanding the action of boundary layers over an object as it will be detailed further.

In the case of a modern airplane for example, friction drag amounts to about 60% of the total drag, while the remainder being mostly shape, induced and trim drag [68]. For high-speed trains such as TGV, the total drag is divided between 60% of friction drag and 40% of shape drag (mainly roof equipment) [113]. Again, at 50 km/h, the total drag represents 50% of the energy losses of a car and these losses can reach 80% at 130km/h [19]. Viscous drag reduction is therefore of high interest for environmental concerns as well as costs of the transportation industry. As mentioned in [127], reducing the world consumption

of commercial jet by 1% will result in more than 1 million dollars a day of costs reduction, without accounting for the environmental benefits that are much more difficult to estimate. A broad variety of methods has been introduced in the past in a attempt to reduce friction or form drags thanks to materials quality improvements (weight, roughness etc...) or shape designs [144]. Most of them are however not efficient enough mainly because limited by technical constraints (dimensions required for passengers, security, technical feasibility of the solution, cost of the manufacturing/implementation).

A well-recognized solution to this problem is flow control. Flow control is a field of constantly growing interest, both in the academic and industrial communities. This discipline is an interface between Fluid Mechanics and Control Theory. Flow control aims at altering the natural flow state into a more desired one by either modifying the geometry of the obstacle (known as passive control [1]), or by adding energy/momemtum into the flow (known as active control). Impact of flow control in transportation industry is consequently major and can lead to a significant cut in energy losses and costs, or again in noise disturbances. A simplified view of the objective of flow control is shown in Figure 1.1. The image on the left presents a case of uncontrolled turbulent flows, where the energy losses are high. The image on the right shows the result of an ideal, yet unattainable, control which perfectly reattaches the flow. The right image is the goal towards which control for flow reattachment is aiming.

Extensive research in flow control have been conducted since a century and the pioneering work of Stalker [135, 134]. The task remains particularly difficult due to the highly dimensional nature of flows which are known to be governed by the Navier-Stokes (NS) equations. These equations represent a high-fidelity model of the flow and form a system of non-linear partial differential equations difficult to handle. In addition, the existence of a global solution is still an open problem. As a first consequence, most of the most promising strategies developed at laboratory level were not extended to real-world aeronautical applications. One can however cite the example of Andino, Whalen et al

1. Note that while the term "passive control" is regularly used, the term "manipulation" should be more appropriate since, as discussed further in the document, it does not really offer any control on the flow.

[**andino_flow_nodate**, 146] who tested flow separation control using sweeping jets on a full-scale Boeing 757 tail. The last example is one among multiple others illustrating the large potential for applications of flow control. Typical examples of engineering problems concerned here are illustrated in Figure 1.2.

Due to the complexity of finding a formal mathematical solution for the Navier-Stokes equations, numerical simulations and experiments are used to investigate fluids. Solving numerically the NS equations is feasible but time consuming. While experimental works are unyielding and subject to different kind of errors (measurements, repeatability etc...) these remain essential for scientists. Nowadays, the continuously increasing computation capabilities motivate the coupling of numerical and experimental approaches. Data-assimilation or data-driven techniques have gain large interest in the last years for examples. There is no doubt that the discipline of flow control will largely benefit from these in the near future. For industrial needs however, control strategies coupling formal control theory and a reduced-order model of the flow state are still preferred. Many control algorithm exist that can be applied to flow control problems depending on the needs of robustness and optimality of the control with little knowledge of the flow (see Section 1.5.2). Another consequence of the complexity of the Navier-Stokes equations is the heuristic geometry simplication. The engineering systems illustrated in Figure 1.2 are tackled by focusing on canonical configurations such as depicted in Figure 1.3. These simplified configurations allow the underlying mechanisms and their effect on drag, noise emission, heat transfer or mixing for example to be examined and understood in details.

1.2 Special case of separated flows

The main focus of this thesis concerns flow reattachment. This section is therefore intended to give the main elements of the flow physics behind such phenomena.

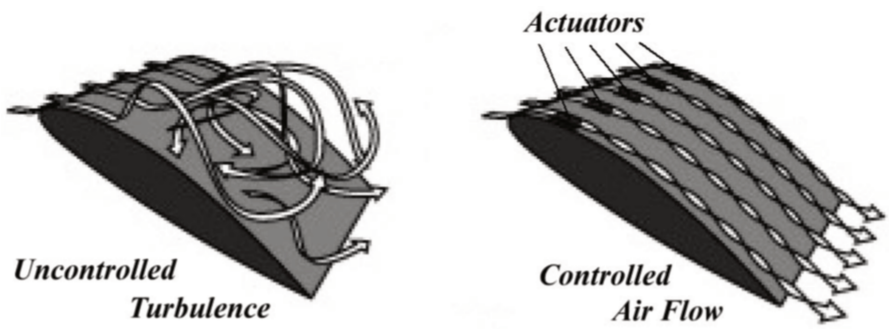

Figure 1.1 – Objective of flow reattachment in the ideal case

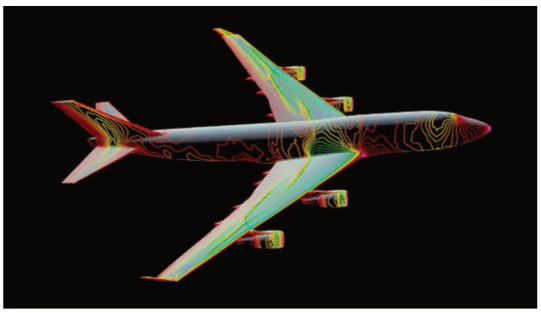

(a) Plane (Credit : NASA, taken from `http://howthingsfly.si.edu/aerodynamics`)

(b) Car (photo by Robert G. Bulmahn)

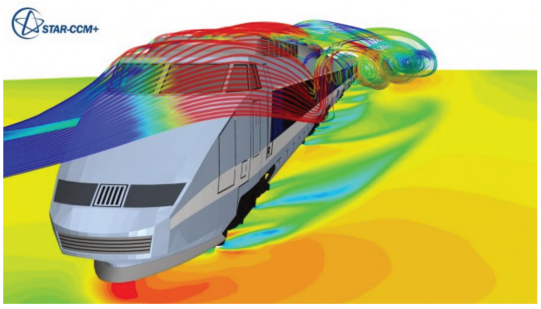

(c) Train (taken from `http://mdx2.plm.automation.siemens.com/cfdImage`

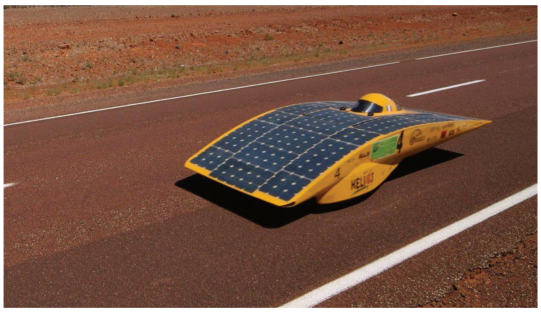

(d) Solar car (courtesy of Association Hélios, taken from `http://www.helioscar.fr/fr/cars`)

Figure 1.2 – Examples of configurations on which flow control can be applied

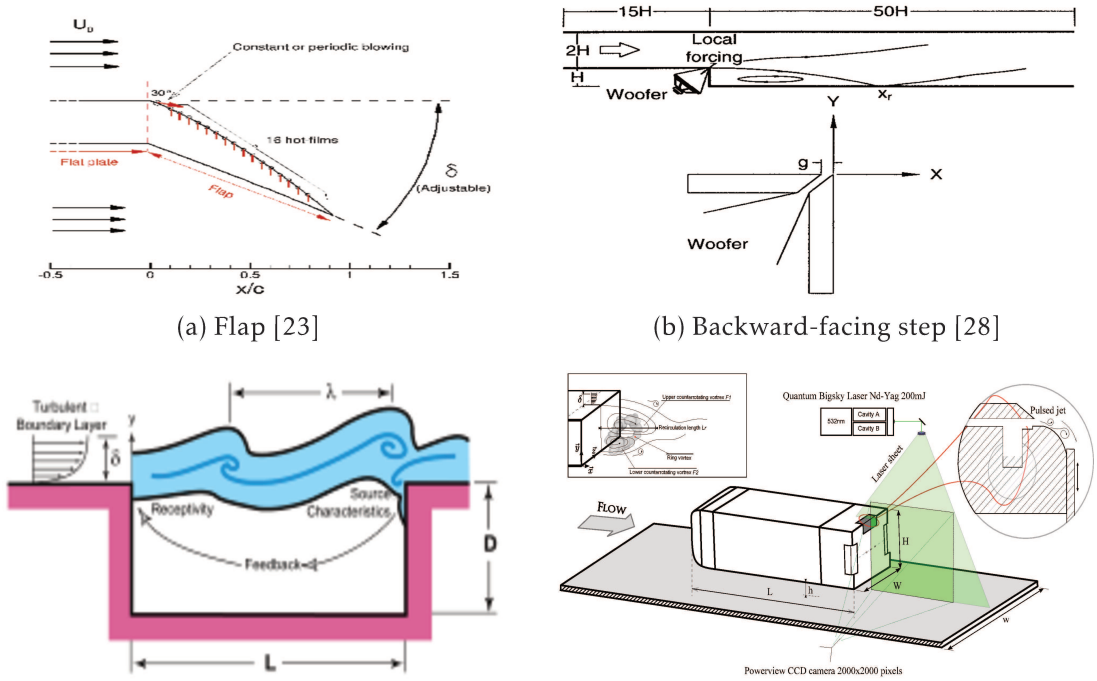

(a) Flap [23]

(b) Backward-facing step [28]

(c) Cavity [21]

(d) Ahmed body [83]

Figure 1.3 – Examples of canonical configurations on which flow control can be applied

1.2.1 Boundary layers : main elements

Every object in a moving flow (or equivalently a moving object in a stationary flow) is subjected to the development of a thin layer of fluid close to the surface where viscous forces are predominant over inertial forces. The no-slip condition on the surface imposes a velocity-gradient between the surface and the freestream. This region of the flow was initially postulated by Prandtl in 1904 [112] and is referred as "boundary layer". The thickness of this region, δ, defined as the distance from the surface where the mean streamwise velocity is 99% of the freestream velocity U_∞, depends mainly on the local Reynolds number, Re_δ. The later characterizes the ratio between the inertial and viscous forces and is defined as : Re = $\frac{\rho U_\infty L}{\mu}$ where ρ is the density of the fluid in kg/m^3, μ the dynamic viscosity of the fluid in kg/(m.s) and L the streamwise characteristic length in m.

For a flow developing on a flat plate, due to viscous diffusion, the boundary layer increases in height. Three regions can be identified : a laminar boundary layer, a transition region and a turbulent boundary layer. All the three regimes are illustrated in Figure 1.4 and are, for example, described by White [147]. Near the leading edge of the plate, the boundary layer is laminar. The flow is mostly two-dimensional and the boundary layer thickness increases slowly with the stream-wise direction in $x^{\frac{1}{2}}$ [62]. When the thickness is high enough, the boundary layer becomes less stable and more receptive to external perturbations (acoustic for example). Tollmien-Schlichting (T-S) waves develop and can be amplified. These T-S waves become rapidly three-dimensional. Turbulent spots appear and propagate in the flow, until the boundary layer becomes totally turbulent [147]. The turbulent boundary layer increases more rapidly in height (in $x^{\frac{4}{5}}$).

Two main regions can be identified in a turbulent boundary layer and illustrated in Figure 1.5 :

1. an inner near wall region. A height of 0.1δ is usually accepted to characterize this region [63, 61]. In this region, the mean streamwise velocity U^+ depends on the fluid characteristics (the viscosity μ and the density ρ)

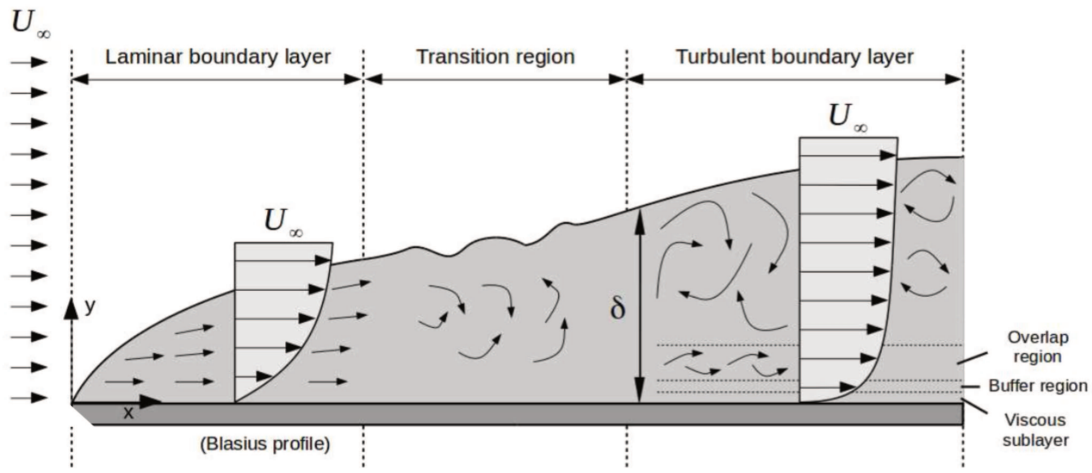

Figure 1.4 – Boundary layer developing over a flat plate with zero-pressure gradient (the figure is taken from [114])

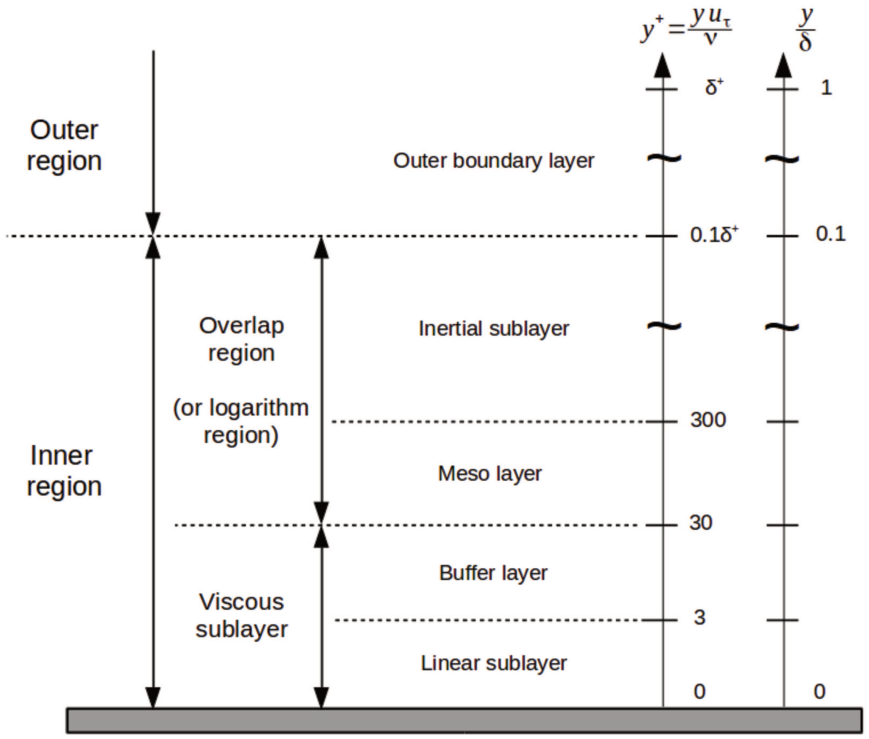

Figure 1.5 – Typical regions of a turbulent boundary layer (adapted from [62])

and the wall shear stress τ_w :

$$U^+ = f(y^+) \text{ with } U^+ = \frac{U}{u_\tau}, y^+ = \frac{\rho y u_\tau}{\mu} \text{ and } u_\tau = \sqrt{\frac{\tau_w}{\rho}}\Big|_{y=0} \tag{1.1}$$

The inner region can be divided in subregions. (1) Near to the wall, the turbulent shear stress $\rho\langle u'v'\rangle$ is negligible compared to the viscous term $\mu\frac{\mathrm{d}U}{\mathrm{d}y}$. This zone is called "viscous sublayer" or "linear sublayer", for $0 \leq y^+ \leq 3-5$, and the velocity profile is $U^+ = y^+$. (2) Above the linear sublayer, for $5 \leq y^+ \leq 30$, these two terms are comparable. This zone is called the "buffer layer". (3) Above the buffer zone, $\rho\langle u'v'\rangle$ becomes predominant. By integration of the Reynolds average equations, a log-law can be found :

$$U^+ = (1/\kappa)\ln(y^+) + C \tag{1.2}$$

with κ and C constants. For zero-pressure gradient boundary layers, the most common values used for these constants are $\kappa = 0.41$ and $C = 5.0$ [35, 61].

2. an outer region, for $y \geq 0.1\delta$, corresponding to a description of the velocity profile using the defect-law :

$$\frac{U - U_\infty}{u_\tau} = f\left(\frac{y}{\delta}\right) \tag{1.3}$$

where U_∞ is the freestream velocity. Coles [29] for example suggested a "wake law", as a complement of the log-law, mostly accepted now in the community.

In addition to the boundary layer thickness δ, other quantities are defined for the characterization of the turbulent boundary layer :

1. the displacement thickness δ^* :

$$\delta^* = \int_0^\delta \left(1 - \frac{U(y)}{U_\infty}\right)\mathrm{d}y \tag{1.4}$$

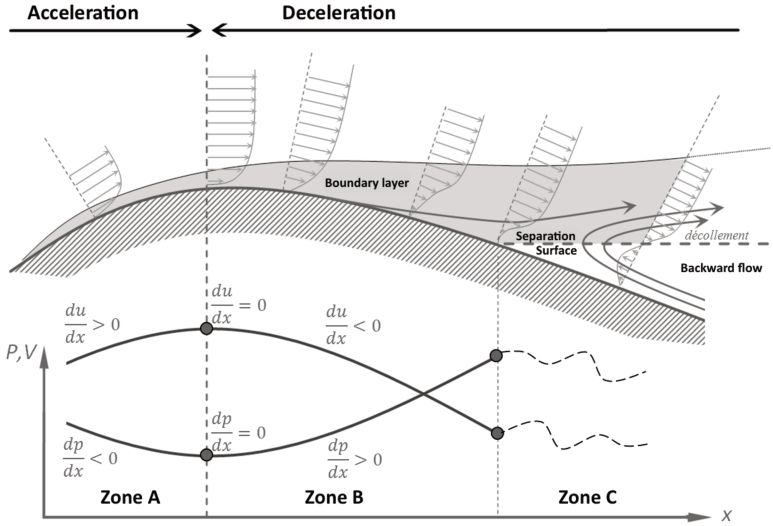

Figure 1.6 – Flow separation and adverse pressure gradient (Taken from [49]). Zone A presents the initial boundary layer, zone B the transition towards flow separaiton and zone C the separated flow

2. the momentum thickness θ :

$$\theta = \int_0^{\delta} \frac{U(y)}{U_\infty}\left(1 - \frac{U(y)}{U_\infty}\right)\mathrm{d}y \tag{1.5}$$

3. the shape factor H :

$$H = \frac{\delta^*}{\theta} \tag{1.6}$$

Extensive details on boundary layer flows can be found in [138, 125, 111].

1.2.2 Flow separation

Most of the flows, and more precisely flows for industrial applications (ground vehicles, aircraft...), are submitted to pressure gradients, particularly adverse pressure gradients (APG). APG flows are expressed by an increase of the pressure in the streamwise direction ($\frac{\mathrm{d}P}{\mathrm{d}x} > 0$) and the decrease of the velocity. A sketch of the boundary layer evolution under APG due to a smoothly curved surface is suggested in Figure 1.6. The velocity decreases across the boundary layer. Far from the wall, the flow is driven by the freestream flow and maintains

high momentum. But near to the wall, due to viscosity, the fluid is already slower and more sensitive to the pressure gradient. Eventually, the velocity goes to zero and the flow separates. Separated flow can also be generated by a sudden change of the wall geometry (backward-facing step, bluff body with a sharp edge, diffuser...). Separation is imposed and the separation point is fixed at this sharp edge [8, 35]. The existence of separated flows for these configurations is unavoidable, but its strength and length are dependent of the upstream-flow characteristics.

Boundary layer separation is an unsteady phenomena. For example, the beginning (the separation point x_S) and the end (the reattachment point x_R) of the separation bubble fluctuates along the wall.

Taking an airfoil as an example for flow separation, it is known that transverse instabilities can increase with the airfoil edges or defects on curvature, which accelerates the separation ([60]). Second, as sketched in Figure 1.7, the separation point can move due to the shear layer flapping and the nearby Kelvin-Helmholtz oscillations.

For airfoils, it is suggested that the dynamics of the flows can be split into three configurations depending on the attack angle α in [97]. When no separation is present, only shedding of structures downstream of the trailing edge is present and corresponds to a Strouhal number $\mathrm{St} = fc\sin(\alpha)/U_\infty = 0.18$ ([38]), with c the airfoil chord. For low angles of attack, a small separation bubble is present on the airfoil. Kelvin-Helmholtz instabilities develops at the separation point. Flapping mode linked to the separation bubble dynamics is also characterized by a Strouhal number $\mathrm{St} = fL_{sep}/U_\infty \approx 0.2$. Finally, for high angles of attack, the boundary layer is massively separated and no separation bubble can be identified. But Kelvin- Helmholtz instabilities at the separation point and wake frequencies due to the shedding are still present on and downstream the airfoil.

1.3 Active flow control

Historically, separation was handled by passive flow control [73, 55, 145]. Passive control is done by modifying the geometry of the vehicle by changing its shape or by adding small devices ("passive actuators") on the surface at

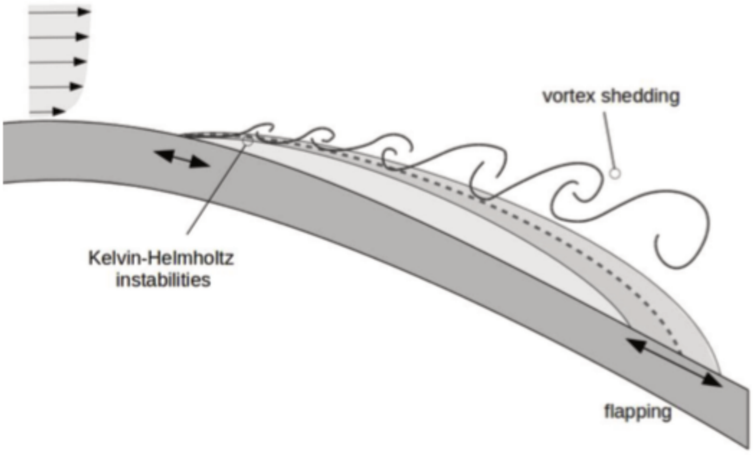

Figure 1.7 – Flow separation and adverse pressure gradient (Taken from [114]).

appropriate places. Theses devices can be static or retractable [91]. While they have no energy cost, they can lead to significant increase of the total drag and can not generally adapt to the natural dynamics of the flow. Passive control has been very extensively studied in the literature. Amongst the most common passive control techniques are vortex generators [150, 152, 141, 54, 90, 67]. The flow is perturbed close to the surface by small inclined or helical airfoils fixed normal to the surface upstream from the separation. In [50], a special coating which is described as a dense cluster of hair was applied to the surface of a solid in order to reduce the drag. Optimization of the design of the shape with respect to certain criteria has also been studied in the litterature as in [76, 119, 118, 98, 99, 72].

Passive flow control suffers from the issue of not being adaptable to a change in the experimental conditions and hence lack robustness. Modification of the actuators in regard to changes in the flow dynamics, known as Active Flow Control (AFC), requires first some flexibility of these devices, and secondly some feedback from the flow itself which means, experimentally, real-time measurements. These two conditions are necessary in order to apply active control techniques allowing to maintain the flow in a given state satisfying the desired objective (drag, noise, or again vibration reduction for example), despite perturbations or change in inflow conditions.

1.3.1 Actuators

Active flow control, at the opposite of passive control, uses actuators to apply some actions on the flow. Such actuators require some energy (electrical, pneumatic and/or other) and must be controlled in some way. The problem of active flow control is then to find the control algorithm that drives the actuators such that their action on the flow leads to maintain the later in a desired state [126].

The actuation is often done using fluid (air or water) jets. These jets can be of two kinds [130] :

1. *Non-zero net mass flow jets* : these jets can either be blowing or be turned off. One simple example is the one of a valve connected to a tank of compressed air. The valve can be open or closed, allowing the air to flow or not [131, 132, 130].
2. *Zero net mass flow jets* : these jets have a zero net mass flow as they alternatively blow out and suck in air. The periodic suction and ejection can, for example, be induced by a vibrating diaphragm of a piezoelectric device [89, 66, 131, 132, 130].

Other types of actuators include electromechanical devices, voice-coil drivers, powered resonance tubes [117], fluidic oscillating jets [116], or again plasma actuators [33]. Extensive reviews about actuators can be found in [21] and [**cattafesta_review_nodate**]. It is to be noted that plasma actuators seem very promising currently as they have the advantages of being non-intrusive, having a highly modular nature and having some way of manipulating the boundary layer [139, 32].

1.3.2 Sensors

As mentioned previously, active flow control requires real-time information on the flow state to be available. Experimentally, the amount of information is sparse and limited to data coming from sensors either integrated into the walls or directly distributed into the flow. The later can be intrusive or non-intrusive if optical metrology is used for example. Due to the limited amount of information

available, which are in addition generally contaminated by noise, flow models are necessary as described later in Section 1.4.

Extensive reviews of the different kind of sensors used in literature can be found in [21] and [103]. Wall-pressure sensors [89] and hot-film sensors [128, 52, 114] are generally preferred. The later is used to obtain a measure of the friction along the wall.

Several types of wall-pressure sensors exist. Amongst others we can mention piezoresistive pressure transducers [136]. Their small size, linearity from input pressure to output voltage and flat response over a large band of frequencies make them easy to implement and a good method for pressure measurement.

An alternative to wall-pressure sensor is hot-film sensor. Such sensors are sensitive to the wall-shear stress. The measurement of wall shear stress using an electrically heated element set into the surface is a well established technique that relies upon the similarity between the velocity profile adjacent to the wall and the temperature profile of the thermal boundary layer that is generated by the element. Since flush-mounted, these sensors are almost non-intrusive (they still add heat to the flow) and offer a simple and cost-effective technique to provide reliable qualitative information on the state of the boundary layer. The main issue with hot-films is that their calibration is difficult and needs to be repeated very often as their rest voltage tends to drift away with temperature changes and prolonged usage.

A new kind of very promising hybrid sensors using hot-film and hot-wire technologies are developed in [64, 65]. These sensor are extremely small as they are developed using the MEMS (Microelectromechanical systems) technology, have high efficiency and sensitivity, can be easily implemented and integrated due to their limited size.

1.3.3 Control objectives and performances : robustness *vs* optimality

As mentioned in the introduction, the current work aims at providing a control methodology to be applied for different experimental configurations in the context of flow separation control or again drag reduction. In terms of

performances, we want the control to maintain a given objective for a minimum of energy expenditure of the actuators. The main performances targeted are thus twofold :

1. *Setpoint tracking* : track a setpoint (i.e. prescribed state of the flow system) defined by the user, which can be either a constant value or a time varying signal. The tracking should be as fast as possible so to reduce the periods of time out of the setpoint.
2. *Energy minimization* : minimize the energy consumption, by considering the trade-off between the cost of the control and the energy saved by the controlled flow.

The first index relies with robust control while the second relies with optimal control.

Robustness is defined as keeping the desired behavior of the system even in the presence of perturbations [153]. These perturbations may be due, for example, to :

— model uncertainties
— unknown inputs
— some technical failure (i.e. sensors or actuators malfunction)
— changes of the incoming flow

A schematic of how perturbations impact the system can be found in 1.8a.

The definition of robustness is given in [14] :

Definition 1. *Consider the following nonlinear model :*

$$\dot{x}(t) = f(x(t)) + g(x(t), u(t)) + d(t) \tag{1.7}$$

$$x(0) = x_0 \tag{1.8}$$

where x is the state, u is the control, d some perturbation, f and g are appropriate operators. Note $x_{unperturbed}(t)$ the trajectory of the unperturbed system with a control $u_{unperturbed}$. The controller u is said to be robust if the trajectories of the perturbed system coincide with $x_{unperturbed}$ when both have the same initial condition x_0.

In our case, the robustness problem can be explained using the following

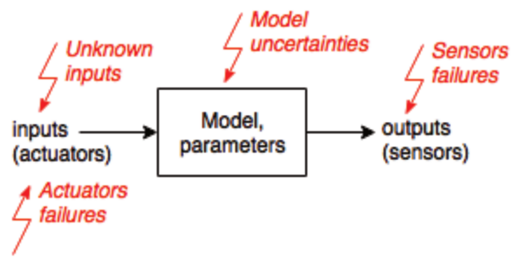

(a) Exemple of possible perturbations on a system

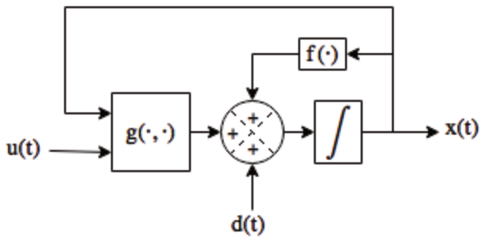

(b) External perturbation block diagram

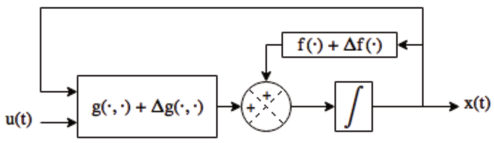

(c) Model uncertainties block diagram

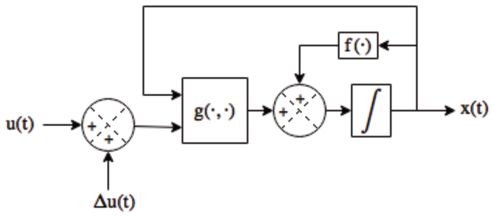

(d) Actuator failure block diagram

FIGURE 1.8 – Examples of perturbations on a system

nonlinear model :

$$\dot{x}(t) = f(x(t)) + g(x(t), u(t)) + d(t) \tag{1.9}$$

where x is the state, u is the control, d some perturbation, f and g are appropriate operators. An example of a robust control would be to steer $\|x(t)\|$ to 0 (or to $O(\alpha)$) as long as $\|d(t)\| \leq \alpha$ with α depending on the system and the control limited in the certain way. The perturbation d can come from different sources as seen before :

1. External perturbation, then $d(t)$ is some unknown signal. See Figure 1.8b
2. Parameters of the model not being exactly known. Suppose that f and g are replaced by $f + \Delta f$ and $g + \Delta g$ where Δf and Δg are unknown. We can then write $d(t) = \Delta f(x(t)) + \Delta g(x(t), u(t))$. See Figure 1.8c
3. Some actuator failure resulting in $u(t)$ being replaced by $u(t) + \Delta u(t)$ and therefore $d(t) = g(x(t), u(t)) - g(x(t), u(t) + \Delta u(t))$. See Figure 1.8d

Optimal control can be used with the objective of, for example, energy mi-

nimization. The controller will be designed in order to minimize some cost function that can be, amongst many, energy consumption, time to reach the objective or any other kind of function to minimize. Optimality and robustness present a trade-off between other, meaning that a control cannot be optimal and robust at the same time.

Feasibility of the control is also to be taken into account. All physical quantities are bounded, therefore the value of the control is also bounded and depends on the considered system. If the control is a voltage then, for example, it may be bounded between 0 and U_{max}. Derivative of the control may also be bounded because of actuators limitations or to ensure a longer life time for the components.

There exist several other performance indexes of control systems like precision, speed, energetic effectiveness, simplicity of realization, etc.

1.4 Modeling strategies

The flowchart presented in Figure 1.9 (taken from [19]) gives a view of the hierarchisation of control strategies in terms of plant modeling. Depending on the knowledge of the flow, models can be chosen from Navier-Stokes equation (nonlinear PDE) to input-output models identified from data. This section will present some of the most commonly used modeling techniques in flow control.

Note that the control developed in this thesis, which is a nonlinear control based on a bilinear model, does not fit in this flowchart, highlighting its novelty in Flow Control.

1.4.1 High-fidelity models

These models are often called white-box models as everything in the model is known and represents physical quantities.

1.4.1.1 Navier-Stokes equations

The dynamics of a fluid are ruled by the Navier Stokes equation :

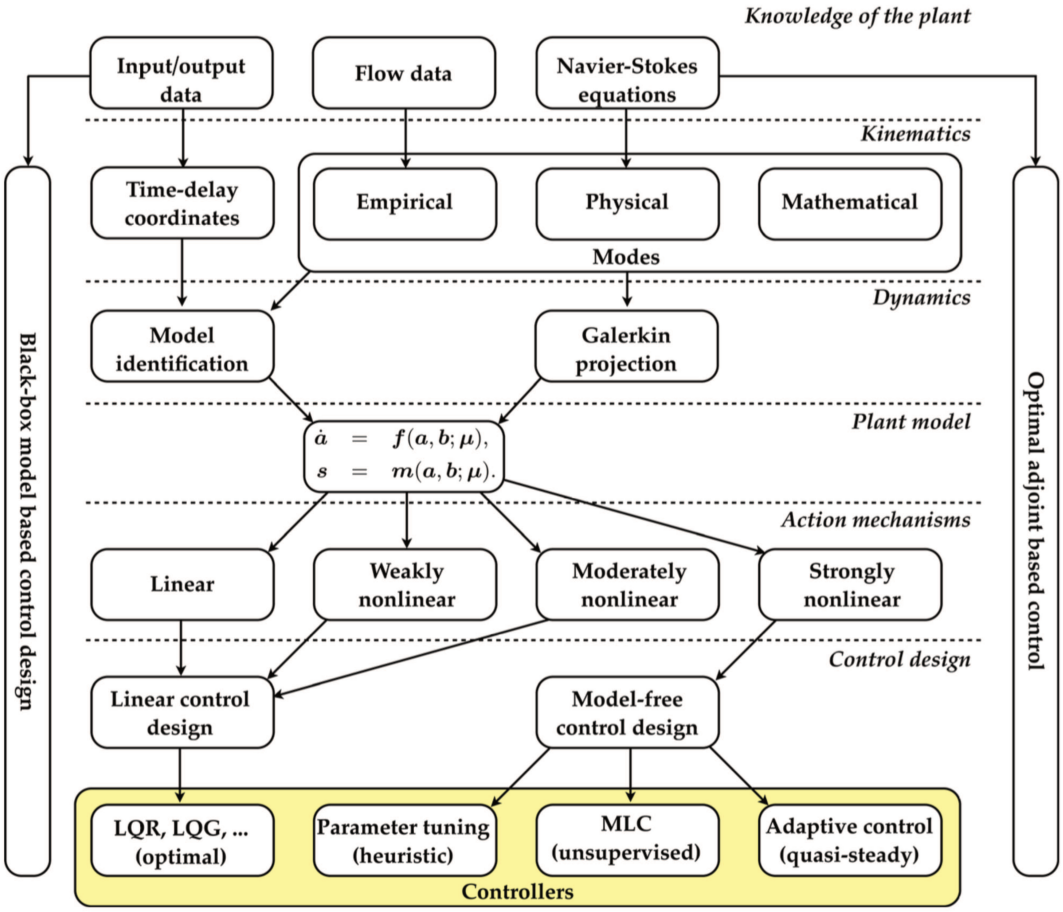

Figure 1.9 – Common flowchart for control choice in Flow Control (Taken from [19])

$$\frac{\partial \rho \vec{U}}{\partial t} + \nabla \cdot \left(\rho \vec{U} \otimes \vec{U}\right) = -\nabla p + \nabla \cdot \bar{\bar{\tau}} + \rho \vec{g} \tag{1.10}$$

where ρ is the density of the fluid, p is the pressure, $\vec{U}$ is a vector containing flow speeds, $\bar{\bar{\tau}}$ is the stress tensor and $\vec{g}$ is the vector containing the gravity action.

This equation is a Partial Differential Equation (PDE). It is known for being extremely complex to prove if solutions always exist and how to find these solutions. Extensive litterature exist on the study of the Navier Stokes equation, for example [137] and [31].

This equation is often accompanied by a continuity equation coming from mass conservation properties :

$$\frac{\partial \rho}{\partial t} + \nabla \cdot \left(\rho \vec{V}\right) = 0 \tag{1.11}$$

As this equation is, most of the time, too complex to use it for the design of a controller that can be implemented in real time without an extremely high computational cost, it is most of the time approximated in order to reduce the order and complexity of the system.

1.4.1.2 Partial Differential equations

In order to simplify the study of flows, many other PDEs were developed for more specific cases. For example, we can cite the Burgers equation (see Equation (1.12), [20]) used to study the combined effects of nonlinear advection and diffusion and as a simple yet inaccurate way to approach turbulence and the Korteweg–de Vries equation (see Equation (1.13), [86]) that is used to describe the evolution of long one-dimensional waves called solitons.

$$\frac{\partial v}{\partial t} + v\frac{\partial v}{\partial x} = \nu \frac{\partial^2 v}{\partial x^2} \tag{1.12}$$

$$\frac{\partial v}{\partial t} + \frac{\partial^3 v}{\partial x^3} + 6v\frac{\partial v}{\partial x} = 0 \tag{1.13}$$

with v the flow speed.

1.4.2 Reduced-order models

1.4.2.1 Petrov-Galerkin method

Several methods exist for the approximation of PDEs. One of the most common ones is the Galerkin method. Galerkin method uses weak formulations of PDEs. As an example, consider the simple 3D Poisson equation :

$$-\Delta u = f \text{ in } \Omega \tag{1.14}$$

$$u = 0 \text{ on } \partial\Omega \tag{1.15}$$

where $\Omega \subset \mathbb{R}^3$ and $u \in \mathcal{U}$ with $\mathcal{U}$ some function space.

Let us denote by $\langle \cdot, \cdot \rangle$ some scalar product in $\mathcal{U}$ such that $\langle u, v \rangle = \int_\Omega uv \mathrm{d}V$. We take the scalar product of equation (1.14) with some function $v \in \mathcal{U}$:

$$\langle -\Delta u, v \rangle = \langle f, v \rangle \tag{1.16}$$

Using Green's identity, we get :

$$\int_\Omega \nabla u \cdot \nabla v \mathrm{d}V = \int_\Omega f v \mathrm{d}V \tag{1.17}$$

Equation (1.17) is called the weak formulation of the Poisson equation (1.14). It can be written using a bilinear form a on $\mathcal{U} \times \mathcal{U}$ and a linear form l on $\mathcal{U}$ with :

$$a(u, v) = \int_\Omega \nabla u \cdot \nabla v \mathrm{d}V \tag{1.18}$$

$$l(v) = \int_\Omega f v \mathrm{d}V \tag{1.19}$$

Then, the Lax-Milgram theorem [104] gives the unicity of the solution u to the equation $a(u, v) = l(v)$.

As the space $\mathcal{U}$ is of infinite dimension, it is not useful for calculations. We then want to find the solution in a finite dimensional space noted $\mathcal{U}_h$ and

contained in $\mathcal{U}$. We then have the following approximation :

$$\text{find } u_h \in \mathcal{U}_h \text{ such that } a(u_h, v_h) = l(v_h), \forall v_h \in \mathcal{U}_h$$

We note $N = dim(\mathcal{U}_h)$ and take a basis $(\phi_i)_{i=1,\dots,N}$ of $\mathcal{U}_h$. We can therefore write :

$$u_h(x) = \sum_{i=1}^{N} U_i \phi_i(x)$$

Considering that any $v_h \in \mathcal{U}_h$ can be expressed in the basis (ϕ), we take for v_h each ϕ_i and rewrite the problem as :

$$\text{find } (U_1, \dots, U_N) \text{ such that } \sum_{i=1}^{N} a(\phi_i, \phi_j) U_i = l(\phi_i),\ j = 1, \dots, N$$

This is a linear system of equations $AU = L$ with :

$$U = (U_1, \dots, U_N)^T \tag{1.20}$$

$$A_{ij} = (a(\phi_i, \phi_j)) \tag{1.21}$$

$$L_j = (l(\phi_j)) \tag{1.22}$$

As the function ϕ_i define a basis, they are orthogonal and their scalar product are null, so A will be sparse. Anymore, the finite element method gives the best estimation in the sense of the two following facts :

— *Galerkin orthogonality* [121, 140] : As we have :

$$a(u, v_h) = l(v_h),\ \forall v \in \mathcal{U}_h$$

$$a(u_h, v_h) = l(v_h),\ \forall v \in \mathcal{U}_h$$

by substracting we deduce that :

$$a(u - u_h, v_h) = 0,\ \forall v \in \mathcal{U}_h$$

— *Céa's lemma* [22] : The Galerkin solution u_h to u is the near-best fit to u in

the norm $\|\cdot\|_{H^1(\Omega)}$:

$$\|u-u_h\|_{H^1(\Omega)} \leq \frac{c_1}{c_0} \min_{v_h \in V_h} \|u-v_h\|_{H^1(\Omega)} \leq \frac{c_0}{c_1} C(u) h^s$$

where c_0 and c_1 are constants, $C(u)$ is a positive constant depending on the smoothness of u, h is the mesh size and s is a positive real number depending on the smoothness of u. If we take the energy norm $\|v\|_E = \|v\|_a = \sqrt{a(v,v)}$, the Galerkin solution u_h is the best fit to u.

One of the most famous methods using the Galerkin projections is called the Finite Element Method [121, 140] where the finite dimensional space $\mathcal{U}_h$ is chosen to be a space of piecewise polynomial functions and the space Ω is discretized using a mesh. The mesh is often chosen to be made of triangular or rectangular elements, even if other polygons are possible, The finer the mesh, the closer (in some sense) the result of the FEM will be to the solution of the PDE, meaning that typically the mesh will be designed to be finer around interest points where the state is supposed to be varying the most.

1.4.2.2 Finite Differences Method

Another commonly used method is Finite Differences [96]. It relies on space discretisation on a grid and approximating derivatives, often by first or second order approximations. Let us consider again the Poisson equations (1.14) and (1.15) but this time in 2 dimensions on a square, i.e. $\Omega = [0,L]\times[0,L] \subset \mathbb{R}^2$. We discretise over a uniform grid with h the space discretisation step, such that h divides L, see Figure 1.10 :

$$x_i = ih \tag{1.23}$$

$$y_i = jh \tag{1.24}$$

with $i = 0,1,\ldots,N$, $j = 0,1,\ldots,N$ and $N = \frac{L}{h}$. We can then use the indexes i and j instead of the positions x_i and y_j. i and j will also be used as indexes for matrices that contain that contain the values of the various variables at each discretisation point. We will then write $u(i,j,t)$ and $f(i,j,t)$ instead of $u(x_i,y_j,t)$ and $f(x_i,y_j,t)$.

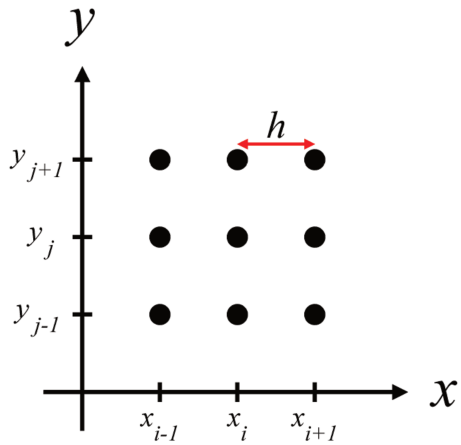

FIGURE 1.10 – Mesh points for the finite difference method (Taken from [102])

In this 2D plane, the Poisson equation (1.14) becomes :

$$\frac{\partial^2 u(i,j,t)}{\partial x^2} + \frac{\partial^2 u(i,j,t)}{\partial y^2} = f(i,j,t) \tag{1.25}$$

We then approximate the space derivatives using finite differences. For example, the three-point approximation for the second derivative is given by :

$$\frac{\partial^2 u(i,j,t)}{\partial x^2} = \frac{u(i-1,j,t) - 2u(i,j,t) + u(i+1,j,t)}{h^2} \tag{1.26}$$

Using this approximation in (1.25), we get :

$$4u(i,j,t) - u(i-1,j,t) - u(i+1,j,t) - u(i,j-1,t) - u(i,j+1,t) = h^2 f(i,j,t) \tag{1.27}$$

We create a vector :

$$U(t) = [u(1,1,t) \quad u(1,2,t) \quad \dots \quad u(1,N-1,t) \quad u(2,1,t) \quad \dots \quad u(N-1,N-1,t)]^T \tag{1.28}$$

The values of $u(0,j,t)$, $u(N,j,t)$, $u(i,0,t)$ and $u(i,N,t)$ for $i,j = 0,\dots,N$ are given by the boundary conditions of the equation.

It is then easy to see that :

$$AU(t) = b(t) \tag{1.29}$$

$$A = \begin{bmatrix} D & -I & 0_{N-1} & 0_{N-1} & 0_{N-1} & \cdots & 0_{N-1} \\ -I & D & -I & 0_{N-1} & 0_{N-1} & \cdots & 0_{N-1} \\ 0_{N-1} & -I & D & -I & 0_{N-1} & \cdots & 0_{N-1} \\ \vdots & & \ddots & \ddots & \ddots & & \vdots \\ 0_{N-1} & & \cdots & -I & D & -I & 0_{N-1} \\ 0_{N-1} & & \cdots & 0_{N-1} & -I & D & -I \\ 0_{N-1} & & \cdots & 0_{N-1} & 0_{N-1} & -I & D \end{bmatrix} \tag{1.30}$$

$$D = \begin{bmatrix} 4 & -1 & 0 & 0 & 0 & \cdots & 0 \\ -1 & 4 & -1 & 0 & 0 & \cdots & 0 \\ 0 & -1 & 4 & -1 & 0 & \cdots & 0 \\ \vdots & & \ddots & \ddots & \ddots & & \vdots \\ 0 & & \cdots & -1 & 4 & -1 & 0 \\ 0 & & \cdots & 0 & -1 & 4 & -1 \\ 0 & & \cdots & 0 & 0 & -1 & 4 \end{bmatrix} \tag{1.31}$$

$$b = h^2 \begin{bmatrix} f(1,1,t) \\ f(1,2,t) \\ \vdots \\ f(N-1,N-1,t) \end{bmatrix} + BC \tag{1.32}$$

where 0_{N-1} is the $N-1$ by $N-1$ square matrix containing only zeros, I is the identity matrix of size $N-1$ by $N-1$. D is of size $N-1$ by $N-1$ and A contains $N-1$ times the matrix D on its diagonal. BC is a vector containing the boundary conditions information.

Once these matrices have been obtained, it is necessary to solve the system $Au = b$ at each instant of time which is easy as A is invertible.

1.4.2.3 Special case of Proper Orthogonal Decomposition (POD-Galerkin)

The Proper Orthogonal Decomposition, namely POD, was initially popularized in fluid mechanics by Lumley [95] for the detection of spatial coherent patterns, or "coherent structures" in turbulent flows. The POD takes foundation in the Karhunen-Loeve theory which is also closely related to Principal

Component Analysis (PCA [149]) or again Singular Value Decomposition [69]). These theorems offer a representation of stochastic process as an infinite linear combination of orthogonal functions.

POD has been used extensively in fluid mechanics not only to investigate a large range of flows, among which cylinder wake flows [15] or again boundary layer flows [9, 85] to cite just a few examples, but also to build reduced-order dynamical systems thanks to Galerkin projection of the Navier-Stokes equations onto the POD basis. For a given flow velocity field $\vec{U}(x,t)$, the POD expansion may read as,

$$\vec{U}(x,t) = \sum_{k=1}^{+\infty} \vec{\Phi}_k(x) a_k(t) \tag{1.33}$$

where $\Phi_k(x)$ are the spatial modes and $a_k(t)$ the temporal coefficient.

The classical scalar product $\langle \cdot, \cdot \rangle$ and norm $\|\cdot\|$ in $\mathbf{L}^2_\Omega$, the space of quadratically integrable functions on Ω are defined as :

$$\langle f(x), g(x) \rangle_{\mathbf{L}^2_\Omega} = \int_\Omega f(x) g(x) \mathrm{d}x \tag{1.34}$$

$$\|f(x)\|_{\mathbf{L}^2_\Omega} = \sqrt{\int_\Omega f^2(x) \mathrm{d}x} \tag{1.35}$$

Note that $\vec{U} \in \Omega \times \mathbb{R}^+$, $\vec{\Phi}_k \in \Omega$ and $a_k \in \mathbb{R}^+$.

Following the Loeve's theorem, Lumley defined "coherent structures" as the spatial patterns which has the largest mean square projection on the velocity field. Mathematically, this is equivalent to finding Φ such as,

$$\max_{\Phi \in \mathbf{L}^2_\Omega} \frac{\overline{\langle \vec{U}(t,\cdot), \vec{\Phi} \rangle^2}}{\|\vec{\Phi}\|^2} \tag{1.36}$$

where $\bar{\cdot}$ is a time averaging operator : $\overline{f(t)} = \lim_{T \to +\infty} \frac{1}{T} \int_0^T f(t) \mathrm{d}t$. Finding the POD basis satisfying this condition is known to be equivalent to solve the Fredholm

integral equation given by,

$$\int_{\Omega} \overline{U(x,t)U(x',t)}\Phi_k(x')dx' = \lambda_k \Phi_k(x)$$

The spatial modes $\Phi_k(x)$ are consequently defined as the eigenfunctions of the two-point correlation tensor $\overline{U(x,t)U(x',t)}$ while λ_k are its eigenvalues which also represent the energy transported by the spatial modes. They can be made orthogonal such that,

$$\int_{\Omega} \Phi_i(x)\Phi_j(x)dx = \delta_{ij}$$

Finally, to satisfy the expansion given in Equation (1.33), the temporal coefficient may be read as,

$$a_k(t) = (U, \Phi_k) = \int_{\Omega} U(x,t)\Phi_k(x)dx$$

Combining POD to educe a reduce-order representation of the flow field by retaining a limited number of modes in the expansion of Equation (1.33) with Garlerkin projection technique has been used by a large number of authors to derive reduced-order dynamical systems (ROM) in particular for flow control. An exhaustive review of reduced-order modeling has been given by [105].

The reader can refer to [43] for more details about POD.

1.4.3 Input-output model identification

1.4.3.1 Auto-regressive methods

Based on measured data, many model identification techniques exist. The first step for model identification is choosing a model. The most commonly used ones [92] are linear models in discrete time called ARX (3.30) (Auto-Regressive eXogeneous) and ARMAX (1.38) (Auto-Regressive Moving Average eXogeneous) and consider SISO (Single Input Single Output) models. These models are more focused at control design and do not attempt to have an exact reconstruction of the data but rather to approximate them closely enough so that the control will work efficiently.

$$y(k) + a_1 y(k-1) + \cdots + a_{n_a} y(k-n_a) = b_1 u(k-n_k) + \cdots + b_{n_b} u(k-n_k-n_{n_b}+1) + e(k) \tag{1.37}$$

$$\begin{aligned} y(k) + a_1 y(k-1) + \cdots + a_{n_a} y(k-n_a) = {} & b_1 u(k-n_k) + \cdots + b_{n_b} u(k-n_k-n_{n_b}+1) \\ & + c_1 e(k-1) + \cdots + c_{n_c} e(k-n_c) \end{aligned} \tag{1.38}$$

where k is the current time step, n_k is a time delay for the output to be affected by the input, n_a, n_b and n_c are the number of coefficients a_i, b_j and c_l to find.

The difference between the two models is that the ARMAX applies some kind of moving average to the noise e and therefore takes into account previous values.

Once the model has been chosen, it is necessary to use experimental data in order to estimate the coefficients of the model. If the model is linear in the coefficients, such as ARX and ARMAX, it is possible to use the well known Least-Square Method [92].

The quality of the identification highly depends on the number of the data. The more data are available, the closer the model will be to the system to identify.

Numerous other identification methods and model types exist, such as, amongst other, statistical modeling [3], fuzzy modeling [27], nonlinear ARMAX (NARMAX) [26].

1.4.3.2 Bilinear models

One the most simple type of nonlinear models are bilinear ones. These models can be seen as a special case of NARMAX models. Bilinear models are extensively used in the literature as simple approximations of the nonlinear models of complex systems. In [100] a class of simple bilinear models is presented as a modeling tool for biological and physical systems and the controllability of such kind of systems is proven, [48] models a distillation column as a bilinear system and presents the identification algorithm for the coefficients of the model, [148] derives a system of bilinear equations to model the microbial cellgrowth and product formation of various waste treatment and fermentation systems and uses this system of equations for observer design and online control as biological

sensors for this type of application are not accurate enough, [151] uses a bilinear model to design a controller that is applied to a headbox control of a paper machine.

Due to this interest in bilinear models, several identification techniques have been developed. In [123] a technique for the identification of multi-input multi-output bilinear systems with white noise inputs is developed based on deterministic-stochastic methods and applied to the identification of a heat exchanger. In [51], a similar identification method is developed and applied to a distillation column.

It will be shown in Section 3.1 that a bilinear model can be derived from approximation and discretization of the Burgers equation.

1.5 Control strategies

1.5.1 Model-based control methods

Model-based control, as opposed to model-free control, uses some kind of model of the system for control design. The model may be obtained in various ways, for example from some physical considerations and parameter identification. As common in control theory, there exist open-loop and closed-loop model-based controls. A review of many model-based control methods can be found in [18].

Open-loop model-based control is simply finding the best input signal giving the desired result by analyzing of the model.

Closed-loop model-based control consists in finding a control law that depends on output measurements of the system, giving it the ability to track desired setpoints efficiently.

1.5.1.1 Open-loop control

Model-based open loop control uses a model of the plant in order to design an open-loop control that is generally used to obtain some kind of optimality.

In [124], an open loop control is designed in order to minimize an H_∞ norm.

In [53], the control is designed to minimize the trade-off between the control energy cost and the energy savings of drag reduction.

Open loop control has the advantage of being easy to implement and does not require any sensing on the system. This comes at the disadvantage of not being robust to perturbations that occur in most physical systems as well as not having the possibility of doing setpoint tracking.

1.5.1.2 Linear closed-loop control

The other form of model-based control is using a closed loop. This means that the controller uses measurements on the system to adapt to its evolution and change the control accordingly. An extensive study of linear closed-loop control can be found in [70] and [122].

One of the simplest closed loop control method is state feedback [80]. Consider a linear state-space system :

$$\dot{x}(t) = Ax(t) + Bu(t) \tag{1.39}$$

Choosing $u = Kx$ such that the eigenvalues of $A - BK$ are in the left half of the complex plane ensures asymptotic stability of the system (1.39).

Numerous other closed loop model-based control exist and can be chosen based on the model properties or on desired control objectives such as robustness to perturbations, noise rejection, optimality of some criteria, finite/fixed time convergence.

As closed loop control requires measurements on the plant, it can be more difficult to implement, mostly if sensors are unreliable or their installation requires some modification of the plant.

1.5.2 Model-based nonlinear control methods

Many model-based nonlinear control methods exist but they are usually not generic methods and are developed for a small set of models and applications. We will first expose the Sliding Mode Control method which is amongst the most generic methods and then quickly mention a few other existing methods.

1.5.2.1 Sliding Mode Control

As we will mostly focus on air blower jets actuated as relays, Sliding Mode Control [143] is well adapted for the considered experimental setup. The basic idea of Sliding Mode Control is to choose a surface in the state space of the system on which the system is behaving in a desired way (stability, speed of convergence, asymptotic/finite-time convergence).

Consider a simple system :

$$\dot{x}(t) = f(x(t), t) + g(x(t), t)u(t) \tag{1.40}$$

where $x(t) \in \mathbb{R}^n$, $u(t) \in \{0, 1\}$ and the functions $f : \mathbb{R}^n \times \mathbb{R} \to \mathbb{R}^n$ and $g : \mathbb{R}^n \times \mathbb{R} \to \mathbb{R}^n$ are assumed to be continuous and sufficiently smooth so that the solution $x(t)$ exists and is unique.

We chose an hypersurface, called the sliding surface, defined by

$$\{x \in \mathbb{R}^n : \sigma(x) = 0\} \tag{1.41}$$

We design the control as follows :

$$u(t) = \begin{cases} 1 & \text{if} \quad \sigma(x) < 0, \\ 0 & \text{if} \quad \sigma(x) > 0, \end{cases} \tag{1.42}$$

Simply put, it means that if we are "over" the surface we set the control at 1 in order to rise to the surface and if we are "under" the surface, we set the control to 0.

The surface 1.41 is to be designed in order to get the desired type of convergence and stability.

Once the surface has been chosen, the stability and convergence analysis is a 3-step proof :

1. Check that the system reaches the surface from any initial condition that is deemed acceptable for the system.

2. Check that, once the system reaches the sliding surface, it stays on it. This

is done by checking that :

$$\dot{\sigma}(x)\sigma(x) < 0 \tag{1.43}$$

3. Check that the behavior of the system on the surface, i.e. once $\sigma(x) = 0$, is as desired

Note that usually (see [143]) the step 3 is announced as the first one. However, in practice the design the sliding surface may be motivated by some control restrictions. The proof, that sliding motion on this surface will imply some required behavior of the system, can be made on the last stage (see Chapter 4).

One the major advantages of the Sliding Mode Control technique is its robustness to perturbations. This is studied and proved in [143, 142]. It is also designed explicitly for relay control systems, which fits the air jets that we use for control of the flow.

1.5.2.2 Other techniques

Apart from Sliding Mode Control, many nonlinear control techniques have been developed. Each method has its own interest and application. We can cite, amongst others, feedback linearization [82], adaptive control [6], backstepping control [94, 81], , Small Gain Theorem [78] and homogeneity based control [93, 120]. Others techniques and reviews can be found in [133, 77].

An extensive review about nonlinear control methods can be found in [87].

1.5.3 Model-free control

As indicated by its name, model-free control is a control method that does not require knowledge of the model. Usually, it is based on experimental tests, numerous data and trial and error methods. As for model-based control, the control can be open or closed loop.

One of the most common closed loop model-free control is the PID [7]. Consider a SISO (Single Input Single Output) system, for which the value of the control is noted u and the vale of the output (measurement) of the system is noted y. The PID control aims at tracking the value of the setpoint y^*, thus

reducing the tracking error $e = y^* - y$ as close to 0 as possible. The control is given by :

$$u(t) = K_p e(t) + K_i \int_0^t e(t)dt + K_d \frac{\mathrm{d}e(t)}{\mathrm{d}t} \tag{1.44}$$

In the model-free case, coefficients K_p, K_i, K_d can be found by trial and error on the system until the desired behavior is reached. This method is easy to apply but can be very time consuming and doesn't ensure any result.

Another form of "model-free" control is suggested in [57] where the use ultra-local models of the form $y^{(\nu)} = F + \alpha u$ and estimate F online in order to obtain the control u to use at each instant of time.

It is also possible to design control based on numerous data without knowing a priori the equation giving the value of the control. This is achieved, for example, by using Genetic Programming. In this case, an evolutionnary algorithm creates the control law by picking and mixing functions from a predetermined list of admissible functions following the evolutionnary rules of, amongst others, the Genetic Algorithm. Such model-free flow control algorithm is described in [96, 16, 101, 56, 44] and has been succesfully applied to flow control in [45, 41].

A review of other model-free control methods can be found in [19]. All of them need long time experimentation for tuning of control. Another challenging issue is robustness of model-free control. Up to now there is no clear way to prove that small variations of system parameters will not imply large degradation of the control quality.

Chapter 2

Experimental configurations

As stated in the introduction of the manuscript, the present work aims to demonstrate the potential of sliding mode control for aerodynamic purposes such as flow reattachment or again drag reduction. Three test cases were considered during this work : (TC.I) a massively separated turbulent boundary layer over a two-dimensional ramp, (TC.II) a separated flow over a two-dimensional flap, and (TC.III) the flow over an Ahmed body. For the two first test cases, the control objective is to maintain the flow reattached despite upstream perturbations or changes in a given range of the operating conditions. For the third case, the control objective is to reduce and maintain the drag at a fixed level despite perturbations in the operating conditions. From the engineering point of view, the control hardware is similar for the three test cases as well as the modus operandi for plant modelling. Only the plant –which includes the flow itself, the actuation set-up and the sensors– to be controlled is different.

The present chapter describes the experimental set-up used for each of the test cases. This includes details on the flow geometry, the sensing, the actuation, the acquisition and control hardwares and finally the modus operandi.

2.1 Test case I : Massively separated turbulent boundary layer

2.1.1 Flow configuration

The first test case considered is that of a massively separated turbulent boundary layer. The Reynolds number, based on the momentum thickness, where the flow separates is 20600. This flow was examined in details in [35, 114] in the large boundary layer wind-tunnel at Laboratoire de Mécanique de Lille (France) for control purposes. As schematically depicted in Figure D.1a and illustrated in Figure D.1b, the boundary layer flow first develops along a 15 m long flat horizontal plate (corresponding to the floor of the wind-tunnel) before reaching a smooth convergent where it occurs acceleration. The flow continues to develop downstream along a slightly inclined flat plate to recover a zero pressure streamwise gradient. This is followed by a inclined flap along which the boundary layer occurs separation and reattaches further downstream to the floor of the wind-tunnel. The height of the ramp at the leading edge of the flap is $H_s = 175$ mm, while the boundary layer thickness just before separation is $\delta = 190$ mm. Velocity streamlines for the time-averaged flow, obtained by PIV measurements conducted in [114] are reported in Figure 2.3. In the present configuration, the location where the flow separates from the wall is located at the edge between the inclined flat plate and the flap. Just downstream of the edge, a shear layer forms and a recirculation region appears along the flap due to flow separation. The border between positive and negative streamwise mean velocity is represented as the blue line in Figure 2.3. Below this blue line, the flow is, in average, reversed compared to the flow above the line. Complete characterisation of the baseline flow can be found in [35, 115].

2.1.2 Actuation setup

An ensemble of 22 round co-rotated air jets of 0.03δ in diameter aligned in the spanwise direction parallel to the flap edge and located $\sim 1.5\delta$ upstream the separation is used for actuation. The jets are driven by fast-switching two-stated

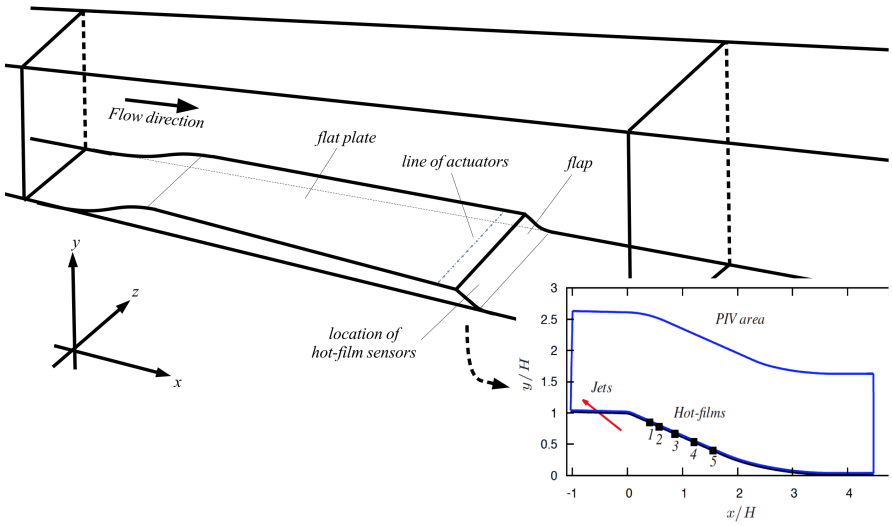

FIGURE 2.1 – Schematics of the experimental set-up. Enlarged picture : ramp model. Zoom : region of the flap with locations of the hot-film sensors and active air blowers (Only the hot-film 1 is used in this thesis for identification)

FIGURE 2.2 – Photography of the ramp model. The flow is coming from the left

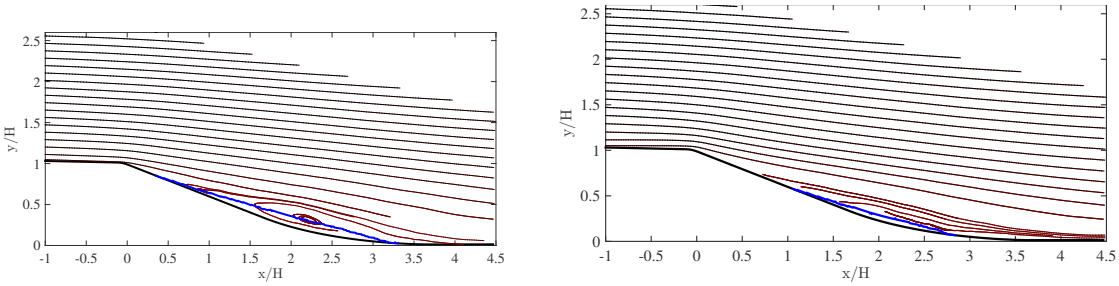

(a) Streamlines for the natural flow without control

(b) Streamlines for the flow under continuous actuation

FIGURE 2.3 – The blue line represents the border between the reversed flow (negative streamwise velocity, region of the flow below the line) and the freestream (positive streamwise velocity, region of the flow above the line). In the controlled case Figure 2.3b the recirculation region is shown to be drastically reduced and the flow almost fully reattached to the wall.

solenoid valve (Festo® MHE2). Complete details of the actuators and their modelling can be found in [128, 115] and [17] respectively. The valves are alimented by pressurised dried air. For a given air pressure level, the actuators can be driven in both frequency (f) and duty-cycle (DC), the two control parameters. An example of the time-averaged response of the flow to continuous blowing of the actuators is given in Figure 2.3b. Compared to the baseline flow, the region of reversed flow is drastically reduced and the flow is found to be almost fully attached to the bottom wall. The reader can refer to [36, 114] for an exhaustive parametric study of the flow response to various control parameters. In practice, sequences of pulsed actuation with different duty-cycle and frequencies were examined and repeated over a sufficient long time such that the flow experiences repetitive reattachments (actuation ON) and separation (actuation OFF) sequences. The motivation for this is to obtain a phase-averaged view of the flow response.

2.1.3 Sensors & Flow survey

For real-time survey of the flow state, hot-film sensors (Senflex® SF9902) located along the flap are used and its voltage output $E(t)$ is offset such as $E(t) - E_0$ (with E_0 the average film voltage for the baseline flow). An increase the hot-film output is representative of flow reattachment along the wall. Overall

	Operating cond.			Control param.				Sensor
Case	U_∞ (m/s)	Other	v^*	f (Hz)	f^+	DC (%)	C_μ (%)	
I	10		5	[0-8]	[0-0.14]	[50-100]	[4.1 – 8.2]	Hot-film

Table 2.1 – Operating conditions and range of control parameters for the test case I

details of the arrangement can be found in [115]. For the present purpose, only the most upstream hot-film sensor is used. This sensor is located $0.5H_s$ downstream of the ramp's leading edge and midway of the wind-tunnel in the spanwise direction. This sensor was found to offer the largest signal-to-noise ratio and to be the most sensitive to flow changes due to actuation [115].

2.1.4 Open-loop tests

The system response, in terms of hot-film output with offset $E(t) - E_0$ is first explored thanks to successive open-loop periodic forcing with varying frequency f and duty-cycle DC as mentioned previously. The range of control parameters and operating conditions considered are detailed in Table 2.1. In the later, the excitation frequency f is given also as the normalized frequency $f^+ = f * H/U_\infty$ corresponding to a Strouhal number. The momentum coefficient is defined following [4] as,

$$C_\mu = \frac{\rho_j S_j V_j^2}{(1/2)\rho_0 S U_\infty^2}$$

where ρ_j is the air density of the jets, U_j is the mean jet velocity, S_j is the jet cross section, ρ_0 is the reference air density for the main flow, U_0 the reference freestream velocity at the jet position and S_0 the reference area. Here, we will choose $S_0 = \lambda\delta$ with λ the distance between two jets and δ the boundary layer thickness.

Average responses of the hot-film output for the different forcing considered further in the manuscript for the plant modeling are shown in Figure 2.5a to 2.5e. In the caption of the plots are given the frequency and DC used for the input signal (4Hz, 50%DC means a frequency of 4Hz and a duty cycle of 50%, constant means that the input is constant and equal to 1). As observed in

[115, 128], when continuous actuation is used (DC=100%), the hot-film output exhibits an averaged response which is well described by a first-order law (See Figure 2.4). When pulsed actuation is used, the response of the hot-film output is still dominated by a first-order response but oscillations are clearly visible and whose amplitude depends on the control parameters. These oscillations have been well described by [115] as the signature of the vortices periodically generated by the actuators and interacting with the shear-layer while traveling downstream. When the actuators are activated, contra-rotating vortices are generated [115]. Due to the distance between the actuators and the hot-film sensor, a time-delay is necessary before the hot-film can sense changes in the flow dynamics. This time delay is manifest in Figure 2.5a for all the different control parameters examined and is similar indicating that it only depends on the convection velocity of the traveling vortices. Note that time-delays inherent to the actuator itself have been well characterized by [17, 114, 128] and were found negligible compared to that intrinsic to the flow response to actuation. The main effect of the actuators is to force the flow to reattach to the wall, leading to an increase in the hot-film output. This increase is manifest when examining the results of Figure 2.5. Above this transient, the flow reaches a stationary state while the actuation is maintained. Once the control is turned off, a short time-delay is again necessary before the hot-film sensor can sense flow changes indicating a return to the natural separated state.

Note that since the hot-film sensor is highly sensitive to perturbations, and since the flow in the separated regions is highly unsteady and depends on the boundary layer state just before separation, the instantaneous response of the hot-film output may significantly differ from the its averaged response. This is well manifest in Figure 2.4 where instantaneous response of the hot-film output due to repeated sequence of continuous forcing are reported. This result gives an indication of how much the hot-film sensor is sensitive and has been used further to bound the averaged sensor's response.

This first test case was considered in the present work only to validate the modeling strategy presented in Chapter 3.

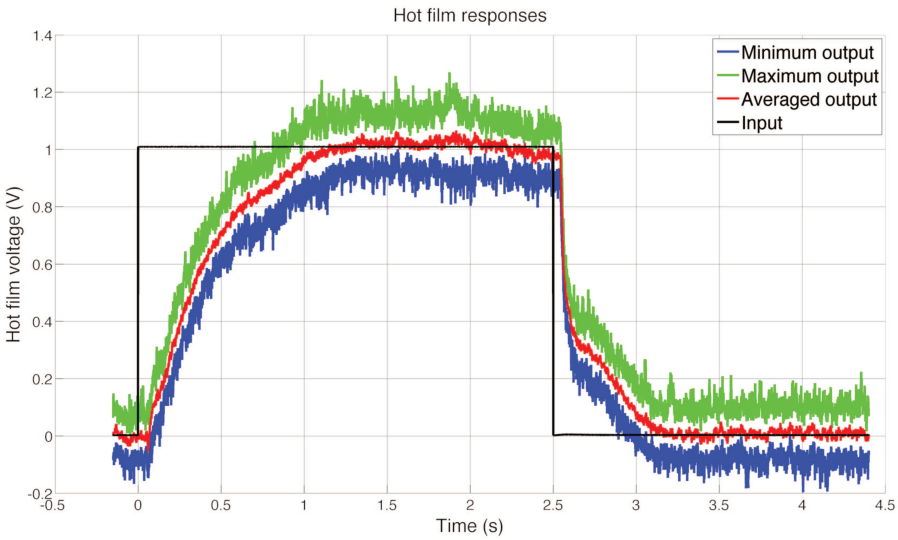

FIGURE 2.4 – Voltage output of one hot-film : maximum, minimum and averaged signals

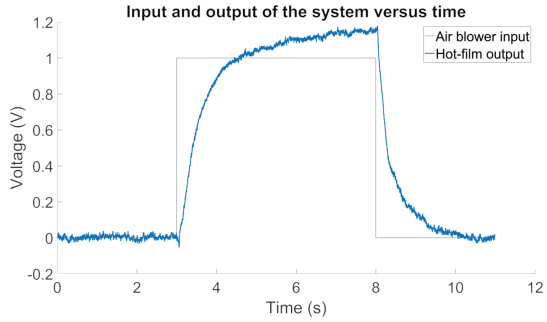

(a) Set of data N°1 used for identification : constant

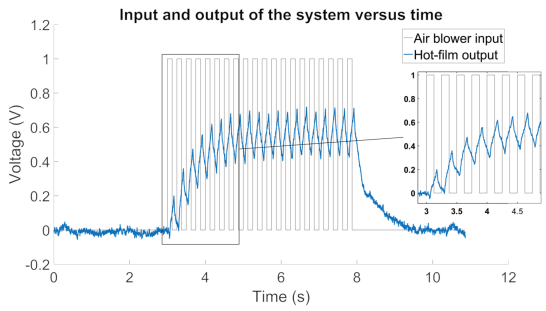

(b) Set of data N°2 used for identification : 4Hz ($f^+ = 0.07$), 50%DC

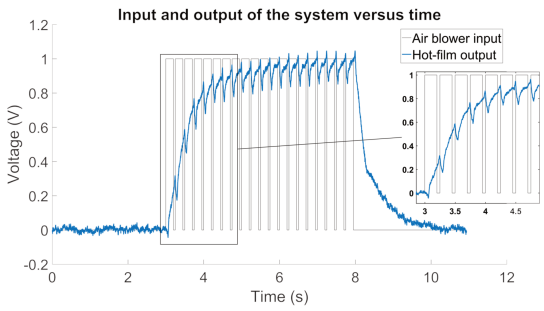

(c) Set of data N°3 used for identification : 4Hz ($f^+ = 0.07$), 80%DC

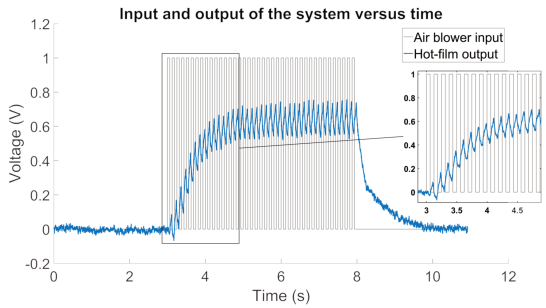

(d) Set of data N°4 used for identification : 8Hz ($f^+ = 0.14$), 50%DC

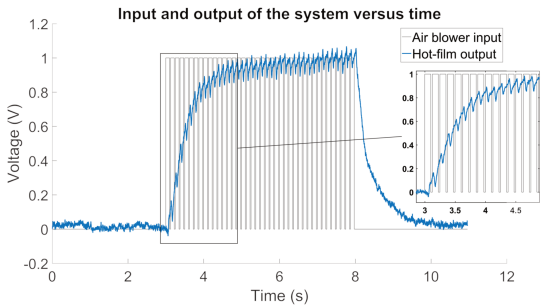

(e) Set of data N°5 used for identification : 8Hz ($f^+ = 0.14$), 80%DC

FIGURE 2.5 – Sets of data gathered in the LML

2.2 Test case II : Separated flow over a plain flap

2.2.1 Flow configuration

The second test case considered is that of a separated flow over a plain flap with variable angles of attack considered. This configuration was extensively examined by Chabert and co-authors [25, 24] for the development of closed-loop linear control strategies. Experiments have been conducted in the L1 wind tunnel located at ONERA Lille research center. The test model is presented in Figure D.2a and consists of an 867-mm-long flat plate and a plain flap (chord length c = 220mm) based on a NACA 4412 airfoil shape with a width of 800mm. This leads to an aspect ratio of 0.275. The model is installed between two thin flat plates in the center of the test circular section of 2.40m diameter as illustrated in Figure D.2b. The deflection angle of the flap can be varied from 2° to 37°. The wind-tunnel tests were performed at average free-stream velocities ranging from 14 m/s to 50 m/s. In this range, the external turbulence level is about 1.3%.

2.2.2 Actuation setup

Seven blowing slits are integrated into the leading edge of the flap and along its whole span. Each of them are driven by fast-switching two-stated solenoid valves (Festo® MHE2), same as that used for test case I. The slits are 0.25-mm-wide and 90-mm-long and share a common pipe of compressed air alimented by a constant feeding pressure up to 7 bar. The slits are separated from each other by 7 mm (0.9% of the span) and cover 80% of the total span. The jets blow with a fixed angle of 30° with respect to the local flap tangent. Full details of the actuation arrangement can be found in [25].

2.2.3 Sensors & Flow survey

For flow survey, hot-film sensors (Senflex® SF9902) are installed along the chord of the flap (see Figure 2.8 for the schematic of the wing with the sensors and 2.2 for a table with their positions) and are equiped with a Dantec® acquisition system coupled with a Keysight® E1413 A/D converter. The hot-film

Figure 2.6 – Schematic of placement of the wing inside the wind tunnel

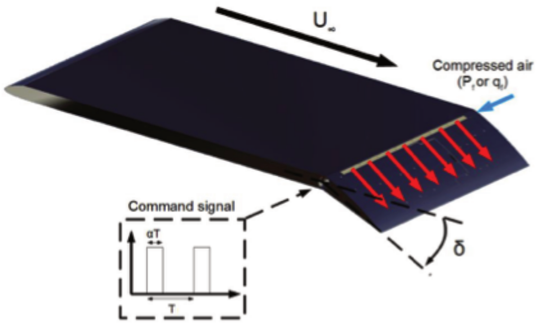

Figure 2.7 – Schematic of the wing

voltage signals are simultaneously acquired by an Arduino Mega ® (see a picture of an Arduino Mega and its implementation with the wiring in the test case II in Figures 2.8a and 2.8b) card at low sampling frequency (100 Hz). The same card is used to compile the control command driving the actuators, making the control experimental set-up very compact and operational for real-time application. A Keysight® E1433 digitizer was also used for high frequency sampling of the signals for post-processing of the data. Similarly to test case I, the hot-film output with offset constitutes the signal of interest to represent the flow state.

For this second test case, the control objective is to maintain the flow attached along the flap despite changes in the angle of attack up to the stall angle and despite changes in the incoming flow. Unsteady perturbations of the incoming flow were arbitrarily introduced thanks either to time varying angle of attack of the flap or to the presence of an array of aligned passive vortex generators located just upstream the edge of the flap such as illustrated in figure 2.9 and as discussed further in the manuscript.

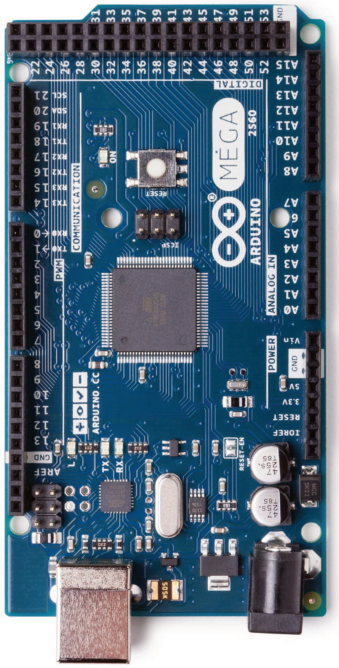

(a) Photo of an Arduino Mega

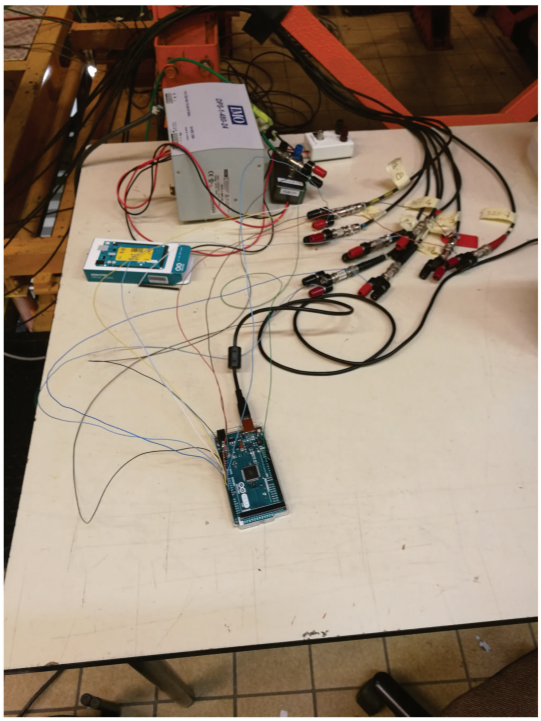

(b) Photo of the Arduino used in the test case II with the wiring

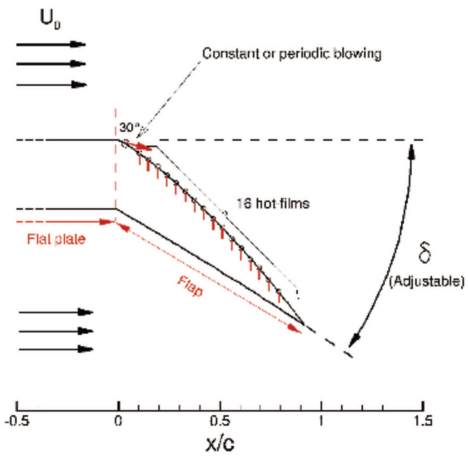

FIGURE 2.8 – Schematic of the flap with sensors placement

	x/c (-)	Δ_{slot} (mm)
X_{01}	0,102	15
X_{02}	0,148	25
X_{03}	0,193	35
X_{04}	0,239	45
X_{05}	0,284	55
X_{06}	0,330	65
X_{07}	0,375	75
X_{08}	0,420	85
X_{09}	0,466	95
X_{10}	0,511	105
X_{11}	0,557	115
X_{12}	0,602	125
X_{13}	0,648	135
X_{14}	0,693	145
X_{15}	0,739	155
X_{16}	0,784	165

Table 2.2 – Position of the hot-film sensors

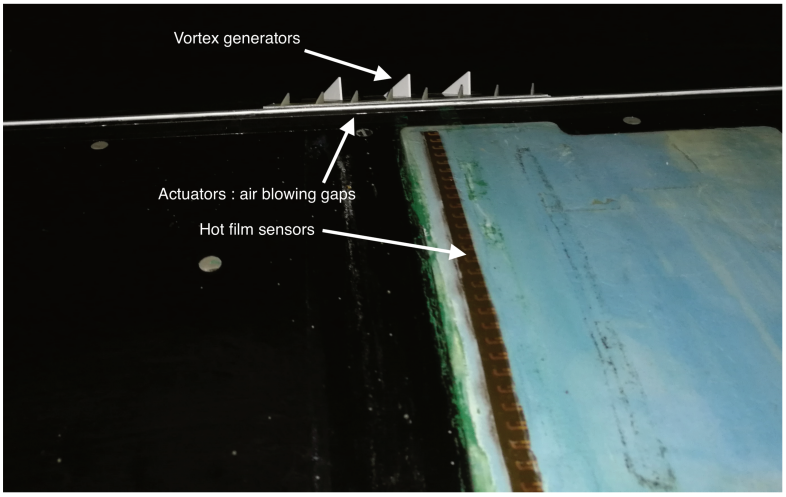

Figure 2.9 – Photo of the passive vortex generators placed before the flap

2.2.4 Open-loop tests

The same modus operandi than that used for test case I is considered. Only one hot-film will be used for identification : the closest one to the blowers on Figure 2.8, with its position given by the line X_{01} in Table 2.2. Open-loop forcing for different control parameters (DC and f) was effected and the averaged response of the hot-film output was computed. The range of the control parameters and operating conditions are reported in Table 2.3. The frequency of the open-loop inputs was limited to 30Hz as it was experimentally determined that after 30Hz the obtained data are too similar to the ones of a continuous actuation case. A total of 11 datasets were collected and will be used for the model identification as discussed in Chapter 3. The overall results are shown in Figures 2.10a to 2.10e. Similarly to test case I, an overall first-order response of the hot-film output is observed with again oscillations during the transient and stationary states. The physical explanations given for test case I remains here valid. For the calculation of C_μ, we will here choose S_0 as the surface of the flap and for the normalized frequency $f^+ = f * c/U_\infty$.

	Operating cond.			Control param.				Sensor
Case	U_∞ (m/s)	Other	v^*	f (Hz)	f^+	DC (%)	C_μ (%)	
II	34.5	AoA=24°		[0-30]	[0-0.191]	[50-100]	[1.31-2.63]	Hot-film

Table 2.3 – Range of control parameters & operating conditions for model identification : Test case II

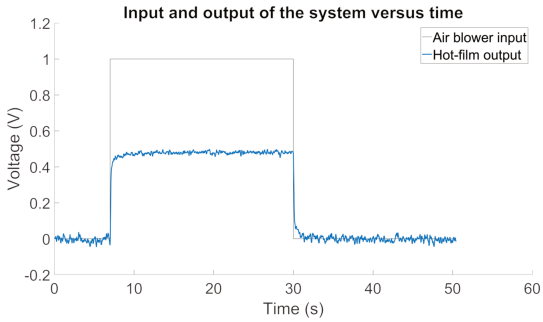

(a) Set of data N°1 used for identification : constant

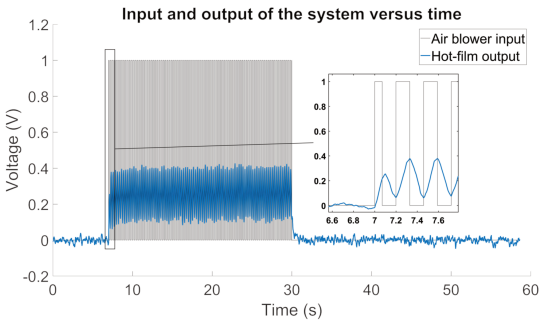

(b) Set of data N°2 used for identification : 4Hz ($f^+ = 0.026$), 50%DC

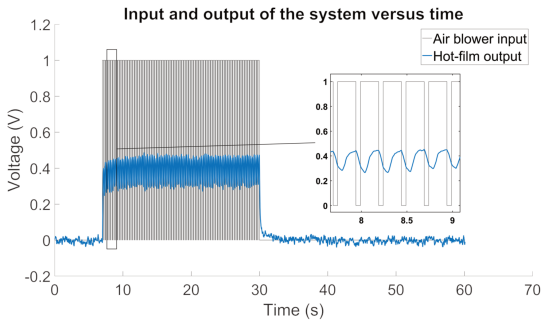

(c) Set of data N°3 used for identification : 4Hz ($f^+ = 0.026$), 80%DC

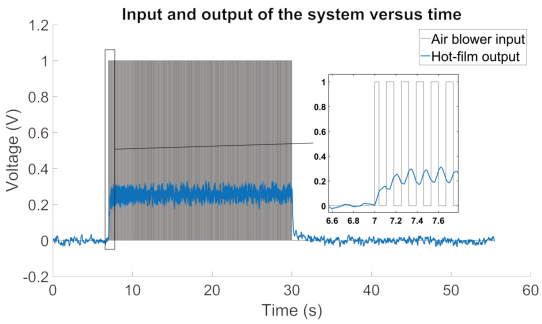

(d) Set of data N°4 used for identification : 8Hz ($f^+ = 0.051$), 50%DC

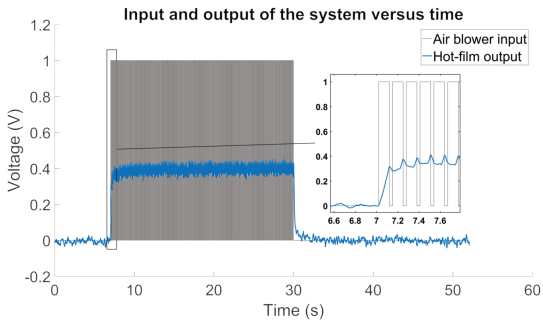

(e) Set of data N°5 used for identification : 8Hz ($f^+ = 0.051$), 80%DC

FIGURE 2.10 – Sets of data gathered in the ONERA

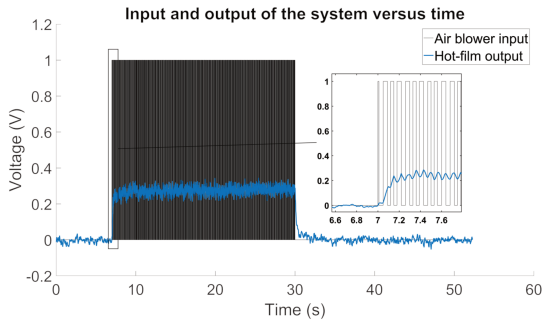

(f) Set of data N°6 used for identification : 16Hz ($f^+ = 0.102$), 50%DC

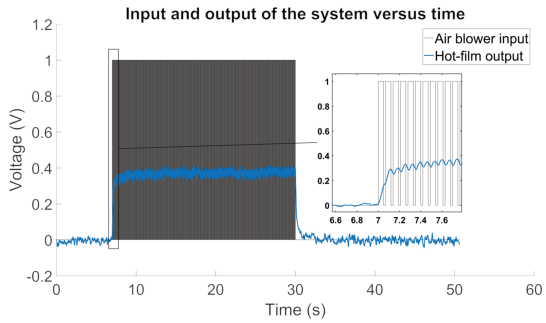

(g) Set of data N°7 used for identification : 16Hz ($f^+ = 0.102$), 80%DC

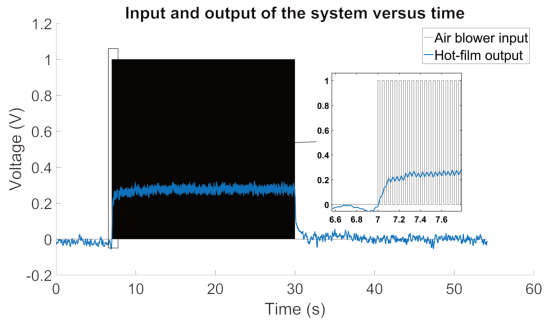

(h) Set of data N°8 used for identification : 25Hz ($f^+ = 0.159$), 50%DC

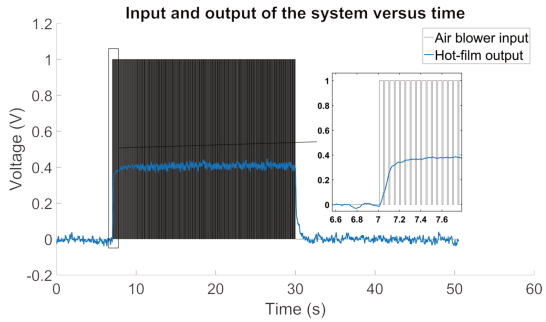

(i) Set of data N°9 used for identification : 25Hz ($f^+ = 0.159$), 80%DC

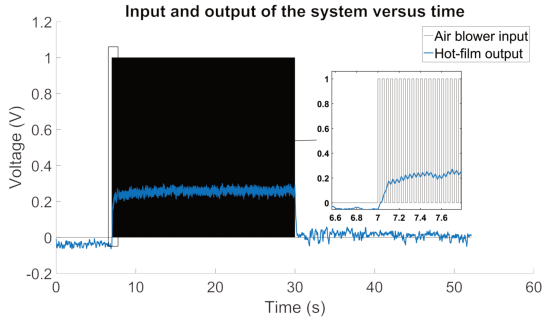

(j) Set of data N°10 used for identification : 30Hz ($f^+ = 0.191$), 50%DC

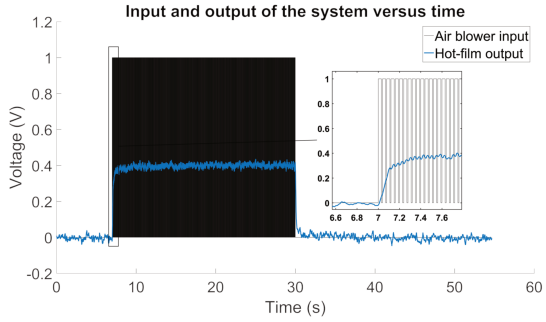

(k) Set of data N°11 used for identification : 30Hz ($f^+ = 0.191$), 80%DC

FIGURE 2.10 – Sets of data gathered in the ONERA

2.3 Test case III : Flow over an Ahmed body

2.3.1 Flow configuration

The third and last test case considered is that of the flow over an Ahmed body. This configuration is classically used as a geometric simplification for a typical car. Experiments were conducted in the closed-loop wind tunnel of LAMIH (Valenciennes). The test section is 2 m wide, 2 m high and 10 m long. The lateral walls are made in perspex in order to allow optimal measurements. The maximum free-stream velocity is about 60m/s with a turbulence intensity of approximately 0.6%. The blunt-edged bluff body is a simplified car model similar to the square back Ahmed body [2]. It has the following dimensions : height h = 0.135 m, width w = 170 m and length l = 0.370 m. Its front edges are rounded with a radius r = 0.05 m. The model is mounted over a raised floor with a sharp leading-edge to control the boundary layer thickness. The model is installed with a ground clearance of g = 0.035 m. The support on which the model is mounted is connected to the drag balance detailed in the following paragraph. The blockage ratio is 0.57%. A cartesian coordinate system with x, y and z representing streamwise, transverse (normal to ground) and spanwise directions, respectively is used, with origin located on the raised floor at the streamwise position of the rear surface. All the results presented in this thesis are obtained with a constant free-stream velocity U_∞= 10m/s. The Reynolds number based on the height of the model is Re_h=9×10^4.

2.3.2 Actuation set-up

For control purposes, the model is equipped with an actuator slit at the trailing edge, as illustrated in Figure 2.12. The slit width is h_{slit}=0.1mm and the actuation length is w_a=150mm. The pressurized air, which is supplied by a compressed air reservoir, can be blown tangentially to the free-stream velocity through the slit. The pulsed blowing is driven by a Festo® MHE2 solenoid valve similar to that used in the previous test cases. In addition, a rounded surface adjacent to the slit exit is installed with an additional plate in order to blow the jet in a predefined direction. Figure 2.12 shows a close-up view of

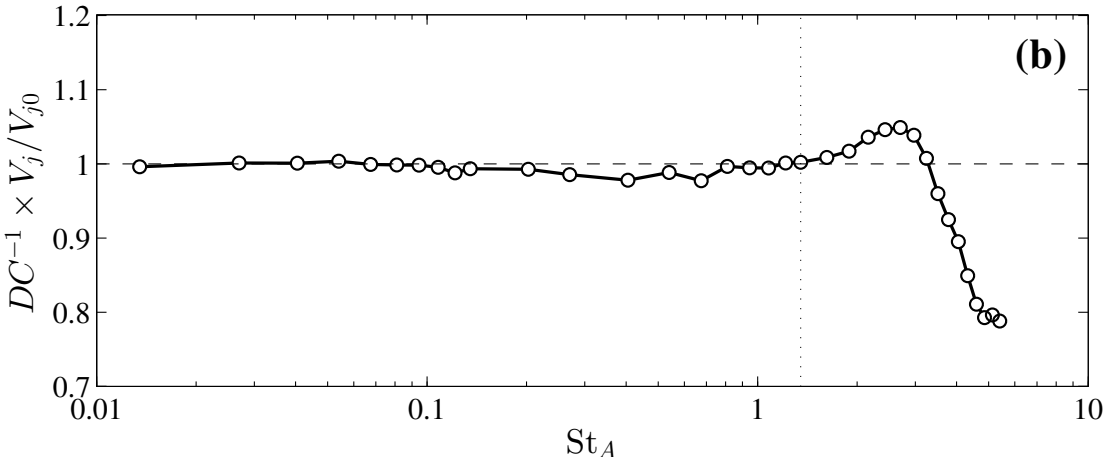

FIGURE 2.11 – Frequency response of the actuation device. V_j is the mean velocity of the jet, V_{j0} is the mean velocity of the jet in steady blowing and DC is the duty cycle.

the Coanda surface at the exit zone. The frequency response of the actuation device, reported in Figure 2.11, indicates that the jet exit velocity is constant (for a given air pressure) for forcing frequencies below 100 Hz, which corresponds to a Strouhal number, based on the body height $St_A = f_a.h/U_\infty$, equal to 1.35). Above this critical value, the jet exit velocity first shows a slight increase before decreasing drastically as the actuation frequency is increased. The maximum forcing frequency actuation considered for the present work is therefore 100 Hz. As discussed further, this frequency is beyond the range of forcing frequencies of interest for drag reduction.

2.3.3 Sensors & Flow survey

In contrast to the previous test cases, the objective of the control is here to reduce the drag of the body and to maintain a given drag reduction despite changes in the inflow conditions over a given range. Drag force real-time measurements were thus performed thanks to a 6-components DELTA ATI aerodynamic balance model built in the raised floor. The balance has a sensing range of 0 to 165 N with a resolution of 0.03 N and a high signal-to-noise ratio. The maximum error associated with repeatability and hysteresis was found to be approximately

0.5 %. The drag measured by the balanced is consequently considered as the only information available to model the overall plant.

In addition, in order to investigate the topology of the uncontrolled and controlled flows, a standard two-component Tsi particle image velocimetry (Piv) system is used. The flow is seeded with oil particles by using a jet atomizer upstream of the stagnation chamber allowing homogenous dispersion of the particles throughout the test section. The system consists of a double-pulse laser system generating the light sheet and two cameras (2000×2000 pixels charge-coupled-device Powerview with a 50 mm optical lens) recording the light scattered by the tracer particles. The frequency-doubled laser (Q-switched Nd :Yag operating at 532 nm; dual-head BigSky) emits laser pulses with a maximum energy of 200 mJ. A multipass algorithm with a final interrogation window size of 16×16 pixels^2 and 50 % overlapping is applied. The resulting Piv domain is about 3.7h×1.8h on the x-y plane passing through the middle plan of the Ahmed body as it shown in Figure 2.12. For every test cases (reported in Table 2.4), 2000 double-frame pictures are recorded to assure the velocity fields statistics convergence. The Piv time-uncorrelated snapshots are recorded with a repetition rate of a 7Hz. In order to maintain the causality between the dynamical aspect (instantaneous flow fields) and the global behavior (drag, lift and surface-pressures time-histories) of the bluff body, unsteady pressure need to be recorded simultaneously with the Piv measurements. To achieve the synchronization, the Q-switch signal of the laser cavity B was recorded simultaneously with the pressure transducer and the forces signals using a 32-channel A/D converter Dewesoft data acquisition system, at a sampling frequency of 20kHz, and a cutoff filtered at 6kHz is used for the Q-switch and another of 1kHz with a cutoff filtered at300Hz.

The mean cross-stream velocity field in the symmetry plane of the Ahmed body (z/h=0) for the natural flow is reported in Figure 2.13a as colormap with streamlines superimposed. This figure provides a view of the average fluid motion over the Ahmed body. Just behind the back of the body, a recirculation area is manifest. Its core is located at about $x/h = 0.25$ and $y/h = 0.4$. This region entrains the flow from the ground clearance to surround it and towards the

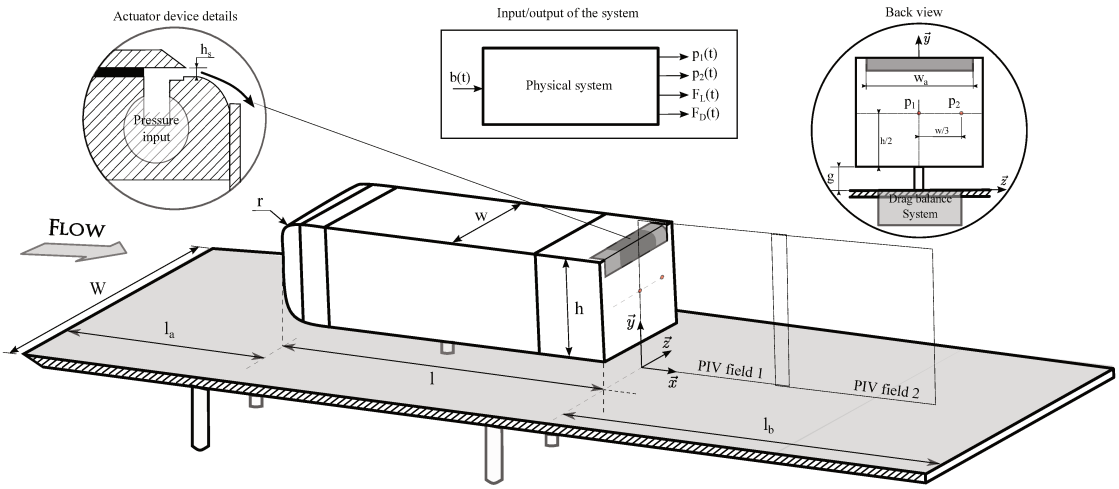

Figure 2.12 – Schematic of the Ahmed body

top edge of the body. This "suction" effect is such that a second recirculation area forms further downstream along the wall at roughly $x/h = 1$. An isoline of forward flow probability of 50% is also shown in Figure 2.13a. The length of the main recirculation area is estimated to $L_r = 1.15h$. Figure 2.13b shows a typical instantaneous vector velocity fields (colored by the norm of the velocity vector) for the uncontrolled configuration. In order to highlight the unsteady flow [71] is used herein. The presence of coherent Kelvin-Helmholtz roll-up in the vicinity of the upper edge, with a typical length scale, $\lambda_K H \simeq 0.5h$, is manifest as observed by other authors [13]. In addition, while not reported here, the different velocity snapshots reveal a flapping motion of the wake associated with the shedding of the vortices from the top edge of the body.

2.3.4 Open-loop tests

The same modus operandi than that used for TC.I and TC.II is considered. Open-loop forcing for different control parameters (DC and f) was effected and the averaged response of the aerodynamic forces (particularly drag force) is computed. The range of control parameters and operating conditions considered for open-loop forcing are given in Table 2.5. Note that the air pressure for the actuation is maintained fixed to $P_a = 6bars$. The momentum coefficient is defined

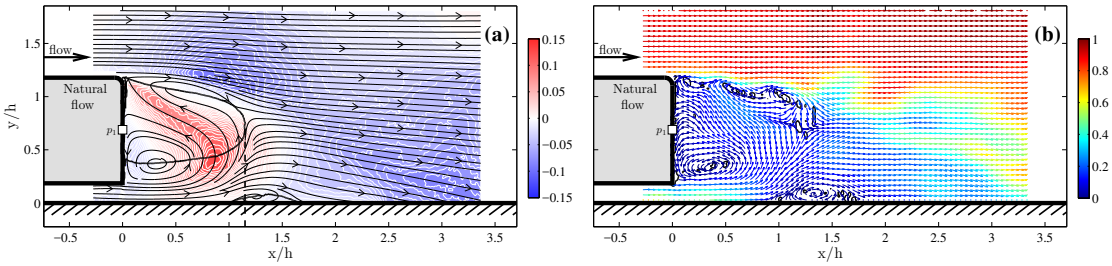

(a) (b)

Figure 2.13 – Natural flow characteristics in the symmetry plane ($z = 0$), (a) Time-averaged cross-stream velocity ($\bar{v}^+$) with the associate streamlines and the iso-line of the forward flow probability of 50%. The recirculating flow length L_r is also displayed by the vertical dashed line. (b) Instantaneous flow field #265 captured by the Piv. The velocity field is indicated by dimensionless norm colored arrows. The Γ_2 criterion is displayed by black iso-lines revealing the unforced shear-layer vortex street formation and the position of the classical main wake structures.

following [4] as,

$$C_\mu = \frac{S_j V_j^2}{(1/2) S U_\infty^2} = DC \times C_{\mu 0}$$

where S and S_j are respectively the slit and the Ahmed cross-sectional area and V_j the mean jet exit velocity. $C_{\mu 0}$ refers to the steady blowing momentum coefficient. The normalized frequency $f^+ = f * h/U_\infty$.

The same Arduino system than that described for TC.II is implemented with the instantaneous drag from the balance as the main input. The pressure sensors and the other aerodynamical forces are not considered in this thesis.

Overall, 13 datasets were considered for identification of the plant's model (detailed in Chapter 3). As justified further in Chapter 4, the model that will be identified is supposed to have positive solutions, therefore as the output of the drag balance is negative, the opposite value is considered. The drag responses to different forcing are presented in Figure 2.16a to 2.16e. In the caption of the plots are given the frequency and DC used for the input signal. As it can be seen in the figures, when the actuators are activated, the drag decreases (represented by an increase on the plots, remember that the plots of the drag responses show

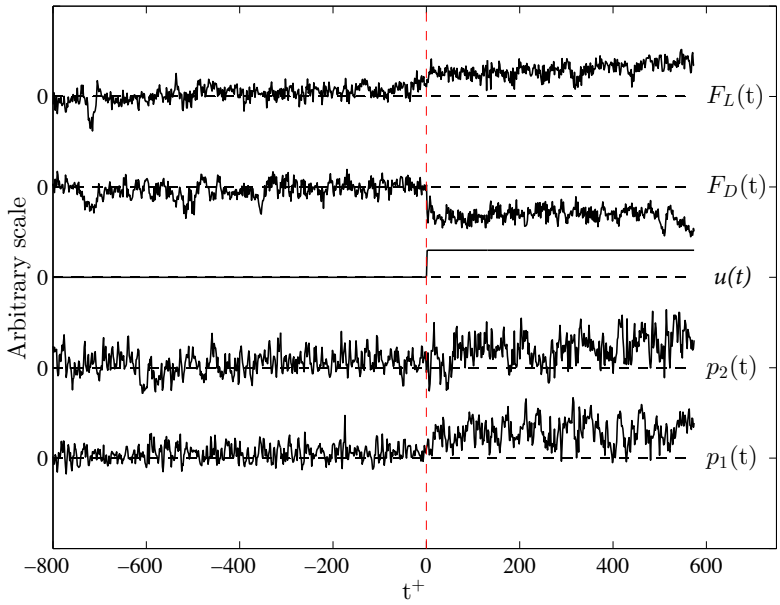

FIGURE 2.14 – Time-histories response of the pressures and forces measurements due to a steady blowing step actuation ($Re_h = 9 \times 10^4$, $C_\mu = 1.355\%$).

the opposite value of what is measured on the drag balance). Similarly to test cases I and II, the drag response is dominated by a first-order response with visible oscillations when a pulsed actuation is used. Also noticeable is the noise in the signals which is much more important in this test case than in the previous ones. In addition, the voltage output of the drag balance does not reach the same steady value each time the actuators are deactivated after an actuation sequence. This is particularly manifest in Figure 2.16a.

The main effect of the actuators is to increase the pressure at the back of the Ahmed body, inducing a reduction in the drag. Contrary to the previous test cases, as the drag balance measures the drag on the whole Ahmed body, there is close to no time-delay between a change in the actuation and a change in the output of the balance. This is showed in Figure 2.14 for a constant actuation where F_L is the lift, F_D is the drag, u is the control signal, p_1 and p_2 are unsteady pressures measured at the back of the Ahmed body.

This third test case will be considered for robust closed-loop tracking control.

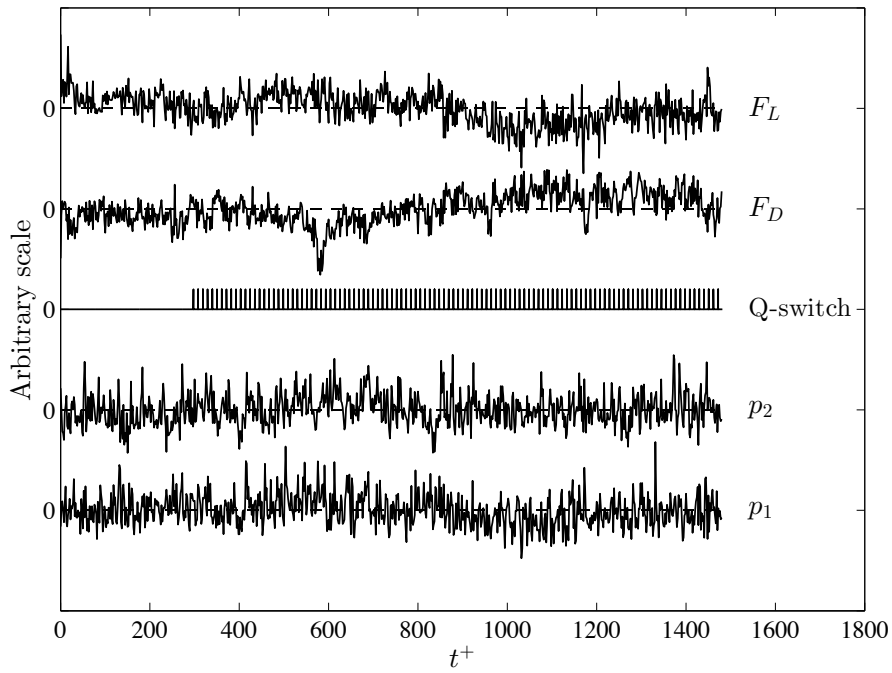

FIGURE 2.15 – Example of simultaneous measurement of the Q-switch signal of the laser cavity B and the unsteady pressures (p_1 and p_2) and forces (F_D and F_L) during a PIV acquisition. + subscript denotes the h/U_∞ normalisation.

Cases	C_μ(%)	f_a(Hz)	St_A	L_r/h
Natural flow (ref)		-	-	1.15
Steady blowing	1.355	0	0	0.87
Forcing frequency	0.678	5	0.0675	0.83
		10	0.1350	0.85
		30	0.4050	0.84

Table 2.4 – PIV cases and associated parameters.

	Operating cond.			**Control param.**				**Sensor**
Case	U_∞ (m/s)	Other	v^*	f (Hz)	f^+	DC (%)	C_μ (%)	
III	10			[0-100]	[0-1.35]	[50-100]	[0.678-1.355]	Force balance

Table 2.5 – Range of control parameters & operating conditions for model identification : test case III

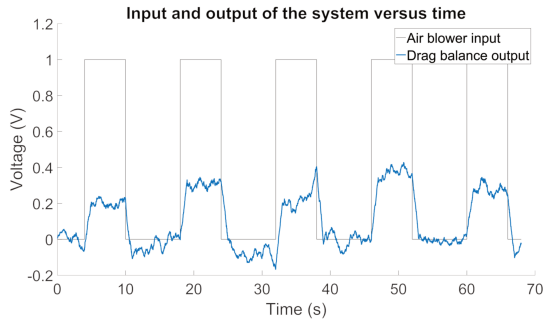

(a) Set of data N°1 used for identification : constant

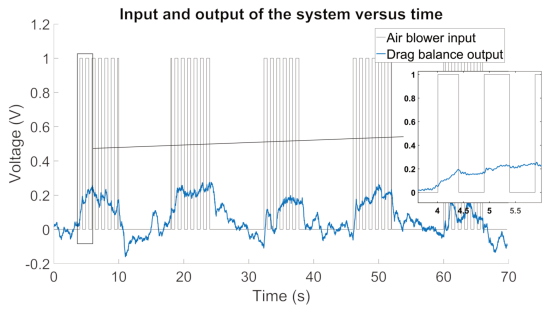

(b) Set of data N°2 used for identification : 1Hz ($f^+ = 0.0135$), 50%DC

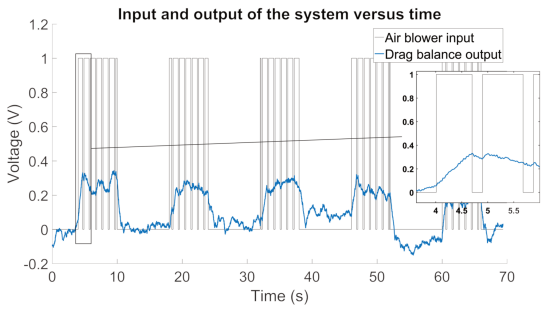

(c) Set of data N°3 used for identification : 1Hz ($f^+ = 0.0135$), 80%DC

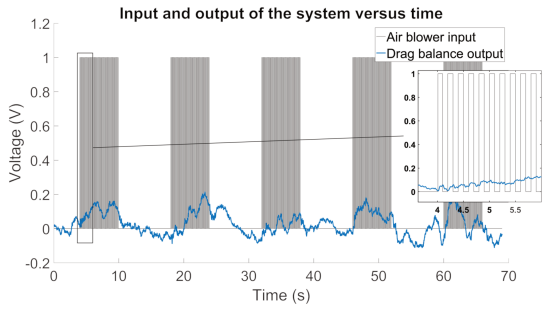

(d) Set of data N°4 used used for identification : 5Hz ($f^+ = 0.0675$), 50%DC

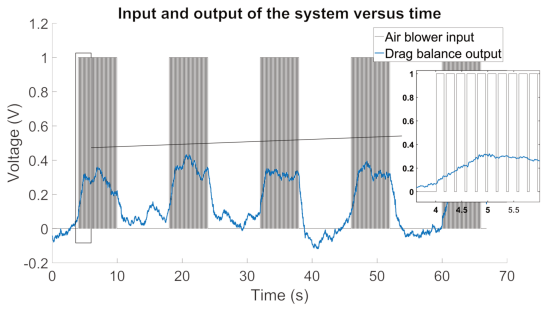

(e) Set of data N°5 used for identification : 5Hz ($f^+ = 0.0675$), 80%DC

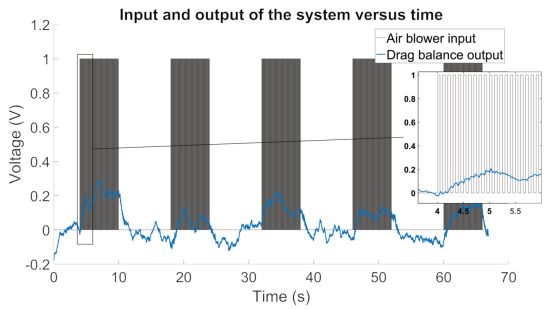

(f) Set of data N°6 used for identification : 10Hz ($f^+ = 0.135$), 50%DC

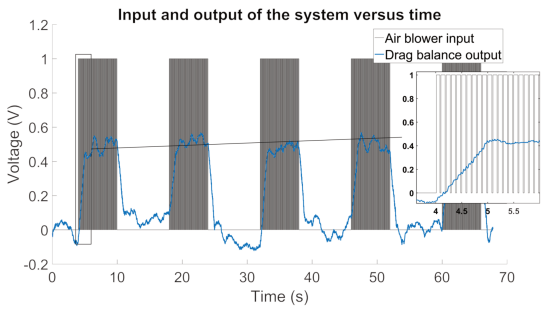

(g) Set of data N°7 used for identification : 10Hz ($f^+ = 0.135$), 80%DC

FIGURE 2.16 – Sets of data gathered in the LAMIH

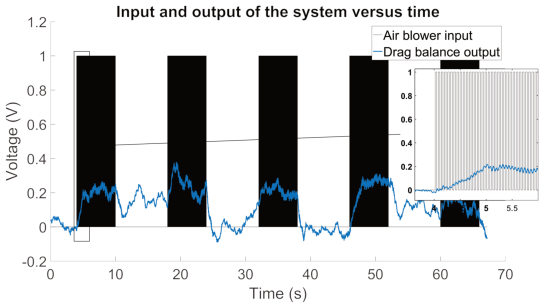

(h) Set of data N°8 used for identification : 20Hz ($f^+ = 0.27$), 50%DC

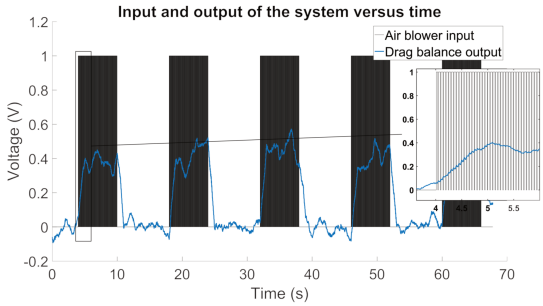

(i) Set of data N°9 used for identification : 20Hz ($f^+ = 0.27$), 80%DC

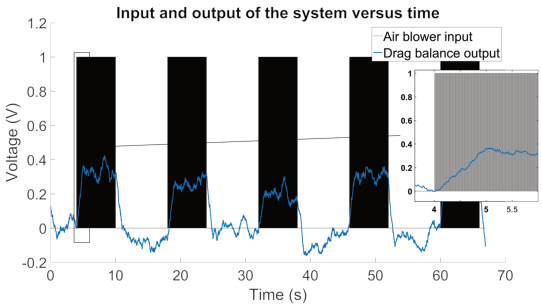

(j) Set of data N°10 used for identification : 50Hz ($f^+ = 0.675$), 50%DC

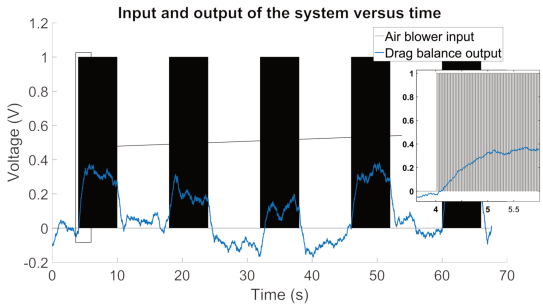

(k) Set of data N°11 used for identification : 50Hz ($f^+ = 0.675$), 80%DC

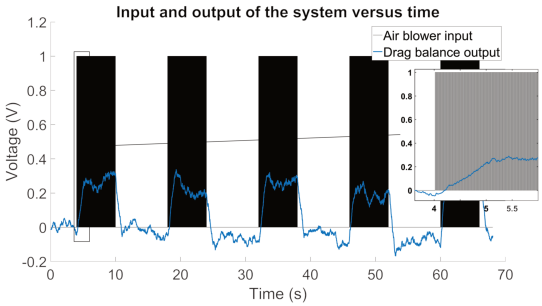

(l) Set of data N°12 used for identification : 100Hz ($f^+ = 1.35$), 50%DC

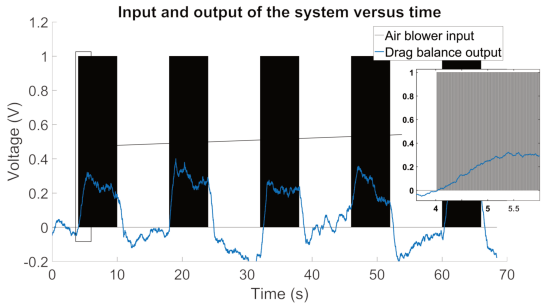

(m) Set of data N°13 used for identification : 100Hz ($f^+ = 1.35$), 80%DC

FIGURE 2.16 – Sets of data gathered in the LAMIH

Chapter 3

Identification algorithm

Following the classical hierarchisation of modeling strategies detailed in Chapter 1, black-box model is considered in the present work. This chapter presents the identification method developed and applied to the different flow control systems as detailed further. A single-input single-output (SISO) model is used in order to describe the flow state behavior. The input data consists of the control command signals driving the actuators while the output is the signal from the sensor used to survey the flow state.

In the first section, SISO bilinear delayed models are derived from approximations of the Burgers equation. In the second section, the method for the identification of the delays is detailed and the models are extended to state-dependent input delays. The third section presents the method for identification of the coefficients of the models and averaged models are introduced. The fourth section presents the technique and the criteria for the optimization of the delays. In the fifth section, results of identification for the test case I are shown. Finally, a conclusion is presented in the last and sixth section.

In the following, the term "plant" will be used to describe the physical system while "model" will be used for its mathematical description needed to be found.

3.1 Derivation of SISO models from PDE models

We will here show that the models considered in Subsection 3.3.1 that we will use for identification and control design can be derived from simple approximations of physical equations and more specifically the Burgers equation, named after Johannes Martinus Burgers who studied this equation in [20].

Let us consider the Burgers equation (3.1), which is a simplified 1D version of the Navier-Stokes equation :

$$\frac{\partial v}{\partial t}(x,t) + v(x,t)\frac{\partial u}{\partial x}(x,t) - \nu\frac{\partial^2 v}{\partial x^2}(x,t) = 0 \tag{3.1}$$

with $\nu > 0$ the viscosity and $t > 0$ and $0 < x < 1$.

It is known that Burgers equation (3.1) admits travelling waves solutions of the form [42] :

$$v(x,t) = F(x - ct) \tag{3.2}$$

where c is the velocity of the wave and is given by $c = v(0,0)$.

Therefore, the value of v at any point of the interval $[0,1]$ and at any time can be computed from the value of v at $x = 0$ with a delay.

Now, we discretize Equation (3.1) with a 3 points scheme using central finite differences for first and second order space derivatives with a step $\Delta x = \frac{1}{2}$:

$$\dot{v}\left(\tfrac{1}{2},t\right) + 2v\left(\tfrac{1}{2},t\right)(v(1,t) - v(0,t)) - 4\nu\left(v(1,t) - 2v(\tfrac{1}{2},t) + v(0,t)\right) = 0 \tag{3.3}$$

We note

$$y(t) = v(1,t) \tag{3.4}$$

as the output (or measure) of the system and

$$u(t) = v(0,t) \tag{3.5}$$

as the input to the system.

Rewriting Equation (3.3), we get :

$$\dot{v}\left(\tfrac{1}{2},t\right) + 2v\left(\tfrac{1}{2},t\right)(y(t) - u(t)) - 4\nu\left(y(t) - 2v(\tfrac{1}{2},t) + u(t)\right) = 0 \tag{3.6}$$

Using Equation (3.2), we can write :

$$v\left(\tfrac{1}{2},t\right) = F\left(\tfrac{1}{2} - ct\right) = v\left(1,\left(t + \tfrac{1}{2c}\right)\right) = v\left(1,(t+h)\right) = y(t+h) \tag{3.7}$$

$$v\left(\tfrac{1}{2},t\right) = F\left(\tfrac{1}{2} - ct\right) = v\left(0,\left(t - \tfrac{1}{2c}\right)\right) = v\left(0,(t-h)\right) = u(t-h) \tag{3.8}$$

with $h = \frac{1}{2c}$.

We finally get :

$$\dot{y}(t+h) = -2u(t-h)y(t) + 2y(t+h)u(t) + 4\nu\Big(y(t) - 2y(t+h) + u(t)\Big) \tag{3.9}$$

Changing the time scale leads to :

$$\dot{y}(t) = -2u(t-2h)y(t-h) + 2y(t)u(t-h) + 4\nu\Big(y(t-h) - 2y(t) + u(t-h)\Big) \tag{3.10}$$

Note that in Equation (3.10), we can interchange $y(t+h)$ and $u(t-h)$.

This method can be generalized to more discretization points in order to get more accurate but more complicated models.

3.2 Input delays identification

The Equation (3.10) obtained in Section 3.1 is a bilinear delayed SISO system. A simple explanation of why the model contains input delays is as follows : if the actuator is placed before the sensors in the physical system, the flow will take some time to travel the distance between them, thus implying a delay which depends on the speed of the flow. Considering that the sensors are quick enough to react to a change in the flow, the input delay can be directly estimated from the output of the hot-film.

Figure 3.1 shows the output signal of the sensor as well as the input signal to the actuator from a set of data gathered in the test case I presented in Section 2.1. The delays considered are that describing the time intervals between the different rising/falling edges of the input command and the rising/falling edges of the sensor's response such as highlighted by the red/green dots in Figure 3.1. While not reported here, the values of these delays are found to depend on the choice

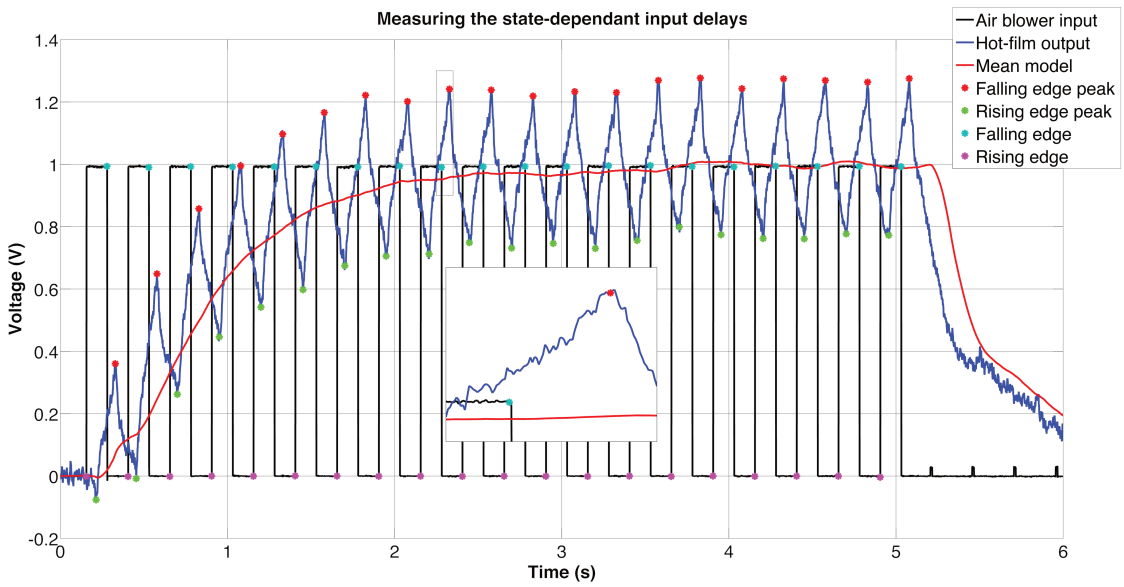

FIGURE 3.1 – Identification of the input state-dependent delay for data set N°2

of the control parameters. This justifies to include time-varying delays in the input command u in model Equation (3.10). Analyzing the value of these delays shows that the delay is not constant and is changing depending on the output of the sensor. Therefore, this a motivation to modify Equation (3.10) to include time varying delays in the input u.

We then need to obtain the function giving the state-dependent input delay, which will be noted $\tilde{h}(y_k)$. In order to take in account the prehistory of the state-function of the time-delayed system in a simple way, the function giving the delay will be evaluated using the mean value (averaged value) of this state-function, which corresponds to measure the value on an averaged, smoother model, as described in (3.11).

$$\widetilde{y_k} = \frac{1}{W} \sum_{s=1}^{W-1} y_{k-s} \tag{3.11}$$

where W is the averaging window and y_k is the output of the system at sample k.

As, once the time delay has expired, the system has a fast response to a change in the input, our method will not be influenced by the phase of the system and

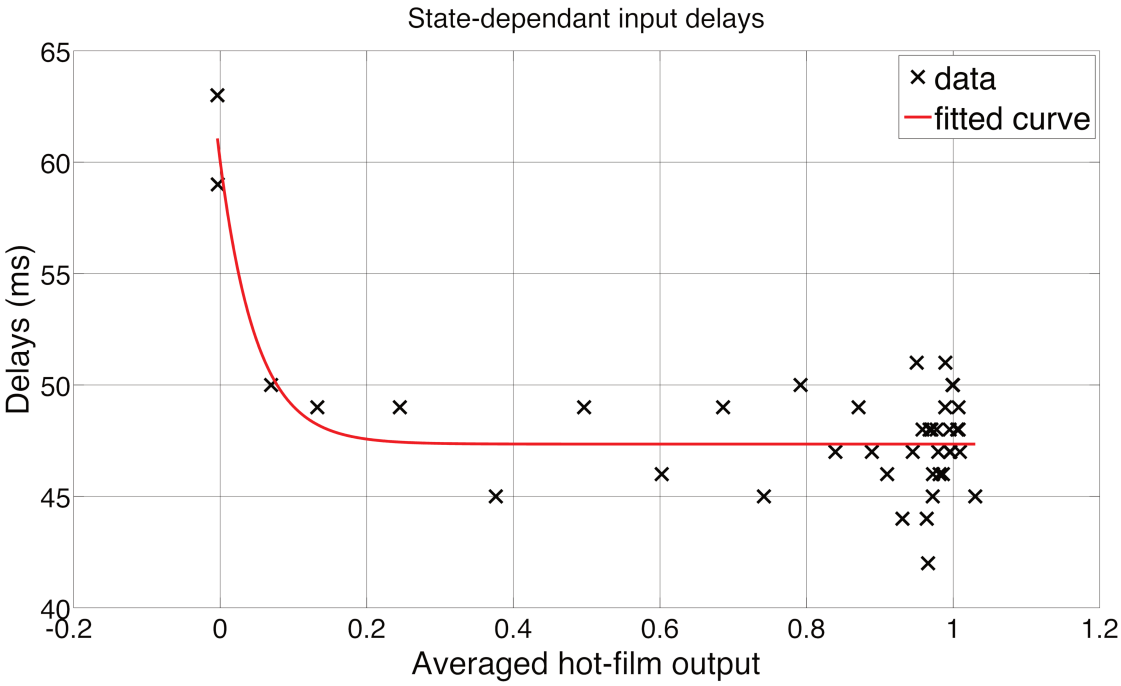

FIGURE 3.2 – Fitting of the input state-dependent delays

will give sufficiently good estimation of the input delays.

Applying this to the available data sets, each having a different input signal, and plotting the measured delays versus the sensor's output, we obtain Figure 3.2. The fitting is done using Matlab's "fit" function.

The fitted function is given by ((3.12)).

$$\widetilde{h}(\widetilde{y_k}) = 47.35 + 12.69\,\mathrm{e}^{-20.18\widetilde{y_k}} \tag{3.12}$$

where $\widetilde{y_k}$ is the averaged system output as defined in Equation (3.11) and $\widetilde{h}(\widetilde{y_k})$ is the state dependent input delay that will be used in the identified model in the next section.

A linear statistical analysis on the values of the state-dependent input delay for the fitting presented in Figure 3.2 gives the following values :

— Mean = 47.83
— Standard deviation = 2.70
— Correlation coefficient with the model input $\mathrm{Cor}(\widetilde{h}, u)$ = -0.07
— Correlation coefficient with the model output $\mathrm{Cor}(\widetilde{h}, y)$ = -0.30

with

$$\mathrm{Cor}(\widetilde{h}, u) = \frac{\mathrm{Cov}(\widetilde{h}, u)}{\sigma_{\tilde{h}}\sigma_u} \tag{3.13}$$

$$\mathrm{Cor}(\widetilde{h}, y) = \frac{\mathrm{Cov}(\widetilde{h}, y)}{\sigma_{\tilde{h}}\sigma_y} \tag{3.14}$$

where $\mathrm{Cov}(X, Y)$ is the covariance between X and Y, σ_X is the standard deviation of X. The value of $\widetilde{h}$ is computed at each instant k using the formula given in Equation (3.12).

3.3 Bilinear delay-difference model

3.3.1 Identification of parameters

Being motivated by the results of the Section 3.1 and mostly Equation (3.10), bilinear models of the plant are considered. A discrete form is also preferred as the model to be identified is based on experimental data which are discrete by definition. The first model uses constant input delay based on the PDE approximation presented in Section 3.1 and generalizing the number of terms using summations. The second one uses state dependent input delays based on the delay analysis from Section 3.2. These two models are given by :

$$y_{k+1} = \sum_{i=1}^{N_1}\left(a_i y_{k-\tau_i}\right) + \sum_{l=1}^{N_3}\left(b_l + \sum_{j=1}^{N_2}\left(c_{jl} y_{k-\bar{\tau}_j}\right)\right) u_{k-h_l} \quad , \quad 0 \le k \le N-1 \tag{3.15}$$

$$y_{k+1} = \sum_{i=1}^{N_1}\left(a_i y_{k-\tau_i}\right) + \sum_{l=1}^{N_3}\left(b_l + \sum_{j=1}^{N_2}\left(c_{jl} y_{k-\bar{\tau}_j}\right)\right) u_{k-\widetilde{h}_l(\widetilde{y}_k)} \quad , \quad 0 \le k \le N-1 \tag{3.16}$$

$$y_m = 0, m < 0 \tag{3.17}$$

where k is the time step, N the number of measures taken (or total number of time steps), considering that $y_j = 0$ for $j < 0$; τ_i , $\bar{\tau}_j$ and h_l are delays ; N_1, N_2 and N_3 are respectively the number of delays τ, $\bar{\tau}$ and input delays (h or $\widetilde{h}$) ;

$\widetilde{h}_l(\widetilde{y_k}) = \text{round}(f_l\widetilde{h}(\widetilde{y_k}))$ are the state dependent input delays of the second model with f_l some multiplicative factors used to derive several state-dependent input delays from the delay identification (such as Equation (3.12)); a_i, b_l and c_{jl} are the coefficients to identify.

The bilinear models are simple enough for easy control design while still capturing nonlinear dynamics of the Navier-Stokes (or Burgers) equation, namely terms of the form $u(x,t)\frac{\partial u(x,t)}{\partial x}$. In addition, the model is chosen to include time delays in order to have an infinite dimension similarly to a partial differential equation. Linear first order models derived for the flow control system of LML can be found in [115], where it is demonstrated that this type of model capture the mean tendency but not the oscillations around it. Definitely, we do not intend to represent exactly the plant, as we focus more on simple control design that is sufficiently robust to overcome the inaccuracies of our identified model.

The variables N_1, N_2 and N_3 are to be chosen by the user in a compromise between complexity of the model and precision. It will also impact the time required for the optimization used in the identification process. Furthermore, augmenting the size of the model makes control design more complicated.

The identification has been done using a least-square method [92] if the delays are selected.

Rewriting the discrete-time models in order to use a least-square method leads to (3.18).

$$\begin{cases} M(\tau,\bar{\tau},h) = \begin{bmatrix} y_{0-\tau_1} & \cdots & y_{0-\tau_{N_1}} & u_{0-h_1} & \cdots & u_{0-h_{N_3}} & y_{0-\bar{\tau}_1}u_{0-h_1} & y_{0-\bar{\tau}_2}u_{0-h_1} & \cdots & y_{0-\bar{\tau}_{N_2}}u_{0-h_{N_3}} \\ \vdots & \vdots & \vdots & \vdots & \vdots & \vdots & \vdots & \vdots & \vdots & \vdots \\ y_{(N-1)-\tau_1} & \cdots & y_{(N-1)-\tau_{N_1}} & u_{(N-1)-h_1} & \cdots & u_{(N-1)-h_{N_3}} & y_{(N-1)-\bar{\tau}_1}u_{(N-1)-h_1} & y_{(N-1)-\bar{\tau}_2}u_{(N-1)-h_1} & \cdots & y_{(N-1)-\bar{\tau}_{N_2}}u_{(N-1)-h_{N_3}} \end{bmatrix} \\ A = \begin{bmatrix} a_1 & \dots & a_{N_1} & b_1 & \dots & b_{N_3} & c_{11} & c_{21} & \dots & c_{N_2N_3} \end{bmatrix}^T \\ x = \begin{bmatrix} y_1 & \dots & y_N \end{bmatrix}^T \\ \|MA - x\| \to \min\limits_A \\ size(x) = [N,1] \quad ; \quad size(A) = [N_1 + N_3 + N_2 * N_3, 1] \quad ; \quad size(M) = [N, N_1 + N_3 + N_2 * N_3] \end{cases} \tag{3.18}$$

To obtain the values of the coefficients contained in the matrix A, we use the Moore-Penrose pseudo-inverse on the matrix M. Noting M^+ the Moore-Penrose

pseudo-inverse of M, we obtain (3.19).

$$A(\tau, \bar{\tau}, h) = M^{+}x \tag{3.19}$$

where $\tau = (\tau_1, \ldots, \tau_{N_1})$, $\bar{\tau} = (\bar{\tau}_1, \ldots, \bar{\tau}_{N_2})$ and $h = (h_1, \ldots, h_{N_3})$

While the identification will be done using discrete time models as the data are gathered in a discrete time manner, the control will be designed using continuous time models. In the continuous time domain, these systems are described by (3.20) and (3.21), where T is the sampling period and the function $\widetilde{y}(t)$ is defined by (3.22).

$$\dot{y}(t) = \frac{1}{T}\left(-y(t) + \sum_{i=1}^{N_1}(a_i y(t-\tau_i T)) + \sum_{l=1}^{N_3}\left(b_l + \sum_{j=1}^{N_2}\left(c_{jl} y\left(t-\widetilde{\tau}_j T\right)\right)\right) u(t-h_l T)\right) \tag{3.20}$$

$$\dot{y}(t) = \frac{1}{T}\left(-y(t) + \sum_{i=1}^{N_1}(a_i y(t-\tau_i T)) + \sum_{l=1}^{N_3}\left(b_l + \sum_{j=1}^{N_2}\left(c_{jl} y\left(t-\widetilde{\tau}_j T\right)\right)\right) u\left(t-\widetilde{h}_l(\widetilde{y}(t))T\right)\right) \tag{3.21}$$

$$\widetilde{y}(t) = \frac{1}{WT}\int_0^{WT} y(t-s)ds \tag{3.22}$$

where W is the moving average window size. As before, using a moving average allows to take into account the prehistory of the signal y as well as smoothing the state-dependent input delay function

3.3.2 Averaged model

Based on the idea used to develop $\widetilde{y}$ for the state dependent delay identification, we can develop an averaged model using equations (3.23) and (3.24). This model will ease the development of control on the system by separating the part with slow dynamics (averaged part, low frequency components of the flow, exhibits the tendency of the signal) from the one with fast dynamics (difference between non-averaged and averaged part, high frequency components of the flow, exhibits the oscillations around the tendency of the signal).

$$y_k^{avg} = \frac{1}{W}\sum_{i=0}^{W-1} y_{k-i} \tag{3.23}$$

$$u_k^{avg} = \frac{1}{W}\sum_{i=0}^{W-1} u_{k-i} \tag{3.24}$$

The averaged models are given by (3.25) and (3.26).

$$y_{k+1}^{avg} = \sum_{i=1}^{N_1}\left(a_i^{avg} y_{k-\tau_i^{avg}}^{avg}\right) + \sum_{l=1}^{N_3}\left(b_l^{avg} + \sum_{j=1}^{N_2}\left(c_{jl}^{avg} y_{k-\bar{\tau}_j^{avg}}^{avg}\right)\right) u_{k-h_l^{avg}}^{avg} \tag{3.25}$$

$$y_{k+1}^{avg} = \sum_{i=1}^{N_1}\left(a_i^{avg} y_{k-\tau_i^{avg}}^{avg}\right) + \sum_{l=1}^{N_3}\left(b_l^{avg} + \sum_{j=1}^{N_2}\left(c_{jl}^{avg} y_{k-\bar{\tau}_j^{avg}}^{avg}\right)\right) u_{k-\widetilde{h}_l^{avg}(y_k^{avg})}^{avg} \tag{3.26}$$

3.4 Identification of state delays

The quality of the identification will be estimated using the three following indicators : the L_2 error norm $\varepsilon(\tau,\bar{\tau},h,A)$ given by (3.27), the fit coefficient as defined in [37] $\mathrm{FIT}(\tau,\bar{\tau},h,A)$ given by (3.28) for the first system and the correlation coefficient between the data and the identified model $\rho(\tau,\bar{\tau},h,A)$ given by (3.29) for the first system.

$$\varepsilon(\tau,\bar{\tau},h,A) = \|x - x^{simu}(\tau,\bar{\tau},h,A)\| \tag{3.27}$$

$$\mathrm{FIT}(\tau,\bar{\tau},h,A) = 1 - \sqrt{\frac{\sum_{k=1}^{N}(y_k - y_k^{\mathrm{simu}})^2}{\sum_{k=1}^{N}(y_k - \bar{y}_k)^2}} \tag{3.28}$$

$$\rho(\tau,\bar{\tau},h,A) = \frac{\mathrm{cov}(x, x^{simu})}{\sigma_x \sigma_{x^{simu}}} \tag{3.29}$$

where $x = [y_0, y_1, \ldots, y_N]^T$ is the vector of data and $x^{sim}(\tau,\bar{\tau},h,A)$ is the vector obtained by simulating the system using the identified coefficients, y_k is the measured system output (data) at sample k, y_k^{simu} is the simulated system output

at sample k using the coefficients $A = A(\tau, \bar{\tau}, h)$ identified by formula (3.19) and $\bar{y}_k$ is the average of the measured system output (therefore constant signal). cov(X,Y) is the covariance matrix between the vectors X and Y and σ_X is the standard deviation of the vector X.

Note that, for the system with fixed input delays, we will denote these indicators ε_1, FIT_1 and ρ_1 and for the system with state-dependent input delays we will denote them ε_2, FIT_2 and ρ_2.

As the fixed delays τ, $\bar{\tau}$ and h and the multiplicative factor f, are still to be determined, we can run an optimization algorithm that minimizes ε in order to find these delays, i.e.

$$\varepsilon \rightarrow \min_{\tau, \bar{\tau}, h}$$

The chosen algorithms for optimization are Genetic Algorithm (GA, see [40]) and NOMAD (Nonlinear Optimization with the MADS Algorithm, see Chapter B of the Appendix for more details), which is based on the Mesh Adaptative Direct Search (MADS) algorithm. It is capable of blackbox optimization for nonlinear objective functions, with linear and nonlinear equalities and inequalities constraints on continuous, integer or binary variables. NOMAD and the MADS algorithm are very well documented in [12, 88, 11, 10]. NOMAD is implementend in the Opti Toolbox for Matlab, see [34].

NOMAD has the advantage of being faster than GA to complete the optimization, usually finishing in 20% less function evaluations but parallel computing is not yet supported in Matlab. Therefore, for quick optimization (depending on the number of parameters and data) we use NOMAD and for long optimization we will use GA in parallel computing on a cluster (14 to 16 workers in parallel).

The overall algorithm that is used is described as follows :

1. Start
2. Use NOMAD to find the optimal set of delays by minimizing one of the three criteria : ε, FIT or ρ.
3. Calculate the coefficients of the matrix A with the set of delays determined by NOMAD
4. Test the coefficients by simulating the model
5. End

3.5 Results of identification and comparison

This section will present the results of the identification on the test case (TC) I. The results for test cases II and III are presented in the Chapter C of the Appendix.

3.5.1 Non-averaged model identification results for the TC I

To obtain identified coefficients that best fit the data of the TC I, and by extension the sets generated for different pulsed inputs, we will apply the identification process to the concatenation of all of the data sets.

The identification is done using only 4 data sets, the fifth one being used for testing purposes. The fifth data set that is excluded from the identification is chosen to be the one with an input signal of frequency 8Hz and DC 80%.

For the 4 concatenated data sets, the least-square errors are $\varepsilon_1 = 10.1529$ for the model with constant input delay and $\varepsilon_2 = 9.7349$ for the model with state-dependent input delay.

The values of the delays values and the identified coefficients can be found in the Table 3.1 for $N_1 = 5$, $N_2 = 10$ and $N_3 = 1$. Is is noticeable that the L_2 norm of the state-dependent input delay model is smaller that the one with fixed delay as it can be seen in the Table 3.2, where the f stands for the frequency of the pulses and DC for the duty cycle in case of pulsed input signals.

In Table 3.2 it is noticeable that the correlation coefficient between data and model output is very high, typically around 99.7%, meaning that our model capture well enough the dynamics of the data.

The simulation of the identified model with state-dependent input delay leads to Figure 3.3 for the data set N°3. As it can be seen in Table 3.2, the models with constant input delay is very close to the model with state-dependent input delay so the model with constant input delay is not plotted here, as the plots of both models would be extremely similar. The plot in Figure 3.3 exhibits some non-physical behavior that are due to the small number of coefficients of the model and the fact that we are not trying to exactly reproduce the data.

	Fixed delay	State-dependent delay
τ_i	$\begin{bmatrix} 1 & 48 & 352 & 371 & 496 \end{bmatrix}$	$\begin{bmatrix} 1 & 44 & 123 & 479 & 496 \end{bmatrix}$
$\bar{\tau}_i$	$\begin{bmatrix} 1 & 66 & 242 & 249 & 260 & \dots \\ \dots & 276 & 300 & 409 & 475 & 491 \end{bmatrix}$	$\begin{bmatrix} 1 & 73 & 242 & 264 & 299 & \dots \\ \dots & 335 & 414 & 477 & 494 & 500 \end{bmatrix}$
h_l	49	$f = 1$
a_i	$\begin{bmatrix} 0.9744 & 0.0171 & -0.0028 \\ \dots & 0.0040 & 0.0009 \end{bmatrix}$	$\begin{bmatrix} 0.9759 & 0.0141 & 0.0025 \\ \dots & -0.0042 & 0.0055 \end{bmatrix}$
b_l	0.0063	0.0080
c_{jl}	$\begin{bmatrix} -0.0116 & 0.0070 & 0.0483 & 0.0253 \\ \dots & -0.0455 & -0.0243 & -0.0038 \\ \dots & -0.0014 & -0.0074 & 0.0138 \end{bmatrix}$	$\begin{bmatrix} -0.0228 & 0.0138 & 0.0621 & -0.0286 \\ \dots & -0.0186 & -0.0121 & -0.0035 \\ \dots & -0.0056 & 0.0189 & -0.0049 \end{bmatrix}$

Table 3.1 – Values of the delays and identified coefficients (all values have No Unit) for the complete model

Set of data	Fixed delay			State-dependent delay		
	ε	FIT	ρ	ε	FIT	ρ
Data set N°1 (constant)	4.78	90.43%	0.9981	4.69	90.61%	0.9984
Data set N°2 ($f = 4Hz$, $DC = 50\%$)	6.24	87.62%	0.9964	5.70	88.70%	0.9958
Data set N°3 ($f = 4Hz$, $DC = 80\%$)	3.00	94.03%	0.9984	3.07	93.90%	0.9985
Data set N°4 ($f = 8Hz$, $DC = 50\%$)	5.63	88.76%	0.9961	5.10	89.82%	0.9965
Concatenated data sets	10.13	89.91%	0.9950	9.48	90.55%	0.9955
Data set not used in identification (set N°5, $f = 8Hz$, $DC = 80\%$)	3.77	92.53%	0.9972	4.01	92.04%	0.9969

Table 3.2 – Comparison of L_2 norm values, FIT coefficients and correlation for state-dependent and fixed input delay models for the complete model

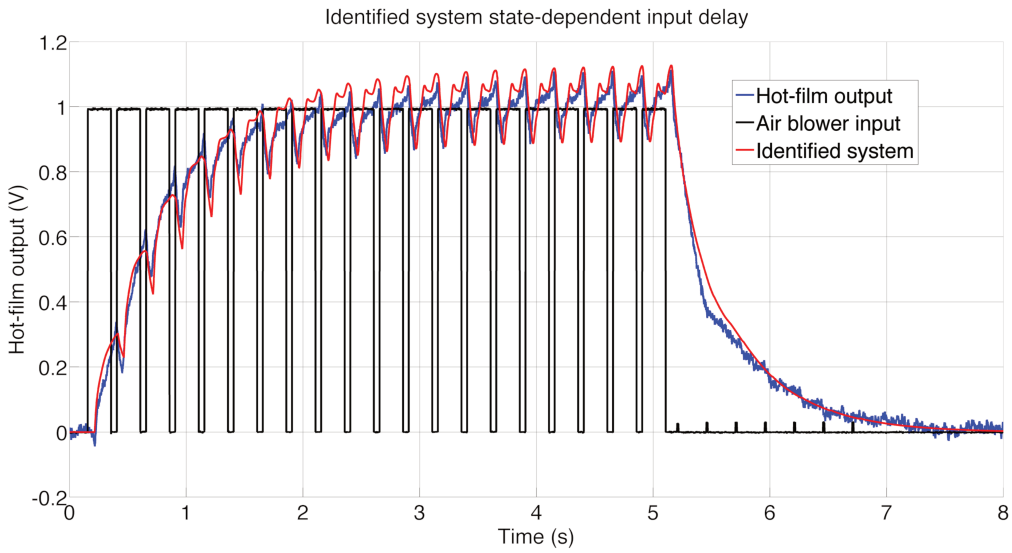

FIGURE 3.3 – Identified model with state-dependent input delay, zoom on data set N°3

3.5.2 Averaged model identification results for the TC I

For $N_1 = 2$, $N_2 = 2$ and $N_3 = 2$, the delays and identified coefficients for the averaged model are presented in the Table 3.3. As it can be seen in the Table 3.4, applying the same analysis as before for the compelete model, it is noticeable that the L_2 norm of the state-dependent input delay model is smaller that the one with fixed delay as for the complete model.

As it can be seen in Table 3.2, the models with constant input delay is very close to the model with state-dependent input delay so the model with constant input delay is not plotted here, as the plots of both models would be extremely similar. Figure 3.4 presents the simulation results of the identified averaged model for data set N°2.

	Fixed delay	State-dependent delay
τ_i^{avg}	$\begin{bmatrix} 1 \\ 269 \end{bmatrix}$	$\begin{bmatrix} 6 \\ 384 \end{bmatrix}$
$\bar{\tau}_i^{avg}$	$\begin{bmatrix} 1 \\ 307 \end{bmatrix}$	$\begin{bmatrix} 6 \\ 454 \end{bmatrix}$
h_l^{avg}	$\begin{bmatrix} 49 \\ 417 \end{bmatrix}$	$f^{avg} = \begin{bmatrix} 1.5513 \\ 106.7560 \end{bmatrix}$
a_i^{avg}	$\begin{bmatrix} 1.0027 \\ -0.0027 \end{bmatrix}$	$\begin{bmatrix} 1.0117 \\ -0.0121 \end{bmatrix}$
b_l^{avg}	$\begin{bmatrix} 0.0009 \\ 0.0030 \end{bmatrix}$	$\begin{bmatrix} 0.0096 \\ 0.0000 \end{bmatrix}$
c_{jl}^{avg}	$\begin{bmatrix} -0.0008 \\ 0.0045 \\ -0.0085 \\ 0.0010 \end{bmatrix}$	$\begin{bmatrix} -0.0179 \\ 0.0088 \\ -0.0490 \\ 0.0208 \end{bmatrix}$

Table 3.3 – Values of the delays and identified coefficients (all values have No Unit) for the averaged model

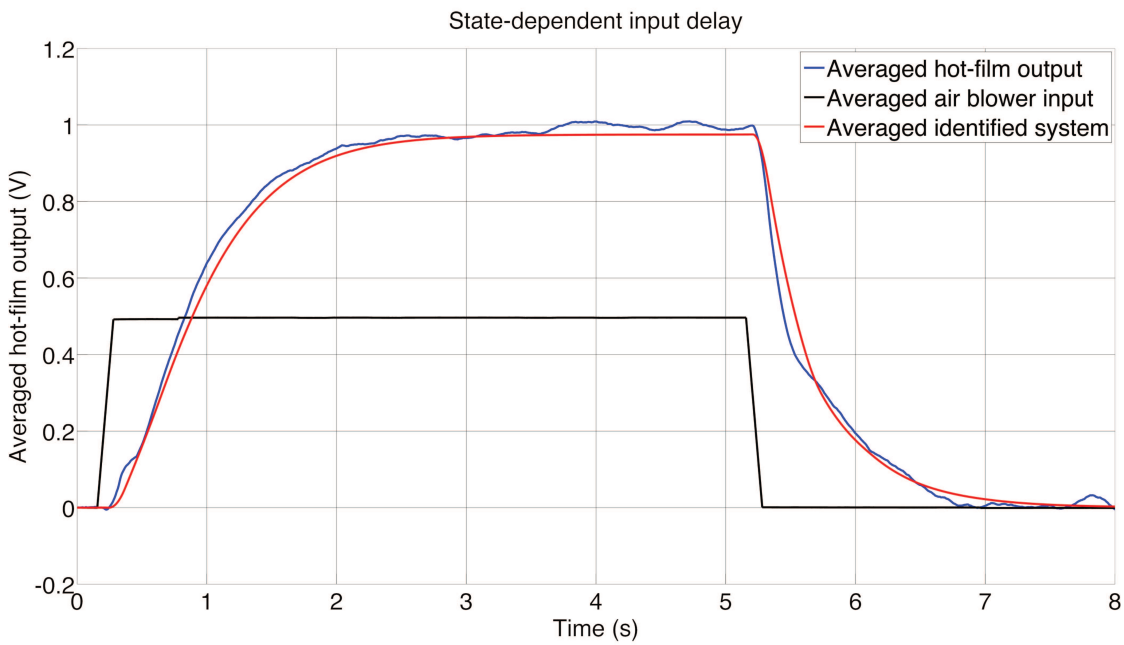

Figure 3.4 – Averaged identified model with state-dependent input delay, zoom on data set N°3

Set of data	Fixed delay			State-dependent delay		
	ε	FIT	ρ	ε	FIT	ρ
Data set N°1 (constant)	2.57	94.84%	0.9991	2.32	95.34%	0.9992
Data set N°2 ($f = 4Hz$, $DC = 50\%$)	6.82	86.21%	0.9979	2.72	94.49%	0.9987
Data set N°3 ($f = 4Hz$, $DC = 80\%$)	3.19	93.63%	0.9994	1.62	96.77%	0.9995
Data set N°4 ($f = 8Hz$, $DC = 50\%$)	5.76	88.38%	0.9976	2.90	94.14%	0.9987
Data set not used in identification N°1 (constant)	4.05	92.07%	0.9978	2.83	94.45%	0.9985
Data set not used in identification N°2 ($f = 8Hz$, $DC = 80\%$)	3.40	93.25%	0.9990	2.45	95.12%	0.9991
Concatenated data sets	10.23	89.72%	0.9969	4.87	95.10%	0.9988

Table 3.4 – Comparison of L_2 norm values, FIT coefficients and correlation for state-dependent and fixed input delay models for the averaged model

3.5.3 Comparison with an ARX model

Let us compare this method to an ARX model (3.30).

$$y_{k+1} = \sum_{i=0}^{N_1^{ARX}-1} (a_i y_{k-i}) + \sum_{l=0}^{N_3^{ARX}-1} b_l u_{k-h-l} \quad , \quad 0 \leq k \leq N-1 \tag{3.30}$$

where h is the time needed for the input to affect the output.

A fixed delay τ_y could be added to every instance of y in the right hand side of 3.30 : y_{k-i} becoming $y_{k-i-\tau_y}$ but the best value would be $\tau_y = 0$ as the current value of y has a high impact on the computation of the next value. The same remark can be done for u.

We identify both models on the 4 data sets used in Section 3.5.1. The bilinear model is the one presented in Tables 3.1 and 3.2 with $N_1 = 5$, $N_2 = 10$, and $N_3 = 1$. In order to have the some number of delays in both models, we will chose $N_1^{ARX} = 15$ and $N_3^{ARX} = 1$. As the optimization for the bilinear model gives $h = 49$, we will take the same value in the ARX model. The ARX model has FIT = 81.71% and $\varepsilon = 17.21$. We recall that the bilinear model has FIT = 89.91% and $\varepsilon = 10.13$. Therefore, the bilinear model gives better identification results than the ARX model for the same number of coefficients. The better identification will result in a control requiring less energy to ensure robustness is the case of robust control or to an optimization of the cost function closer to the physical optimum in the case of optimal control.

This comparison, as well as the considerations from Section 3.1, justify the use of our model instead of linear or ARX models for the identification of a SISO model and the control of flows.

3.6 Conclusions

A new bilinear SISO model of flow control system is introduced. Its structure is motivated by discretization of physical models (Burgers equation). The model contains state and input delays. Two models have been developed : the first one has constant input delays while the second has state-dependent input delays.

The scheme for parameter identification is developed. High precision and

low complexity of the bilinear model is demonstrated for different experimental setups. In particular, the bilinear SISO model for the test case II (see, Section C.1 of the Appendix) having only 43 parameters shows the precision FIT= 80%, while models in the literature of flow identificaiton often have more one hundread coefficients [75] or even several thousands [37] to reach identical FIT values.

The comparison between the two bilinear models has been conducted, showing that the model with state-dependent input delays is more accurate but that the difference in accuracy of both models is small. The models have also been compared to a simple ARMAX model, which is commonly used in the literature for flow identification, showing that the bilinear models developed here have significantly better accuracy for the same number of coefficients.

Simulation the models show some inaccuracies mainly around peaks but these are caused partly by noise in the data signal, the fact that we wish to fit several type of input-output and the simplicity of our model as we do need seek exact fitting but good tendency estimation, which is what we get here.

As the constant and state-dependent input delays models are extremely close, we will only consider constant input delays for modeling of the test cases II and III. This will ease the design of controllers while having a very neglectable impact on the precision of the identification.

Chapter 4

Model-based control

This chapter presents the control algorithms that were designed on the models obtained in Chapter 3. The first section describes the control objectives and constraints related to flow control problem and the available experimental setups. In the second section, an open-loop optimal control algorithm is designed and simple equations for its derivation are provided. In the third part, a robust feedback control algorithm is presented using the Sliding Mode Control methodology. Sufficient conditions are obtained to allow the simple design and the robustness of the algorithm to be proven. Finally, experimental applications of the obtained results are discussed in the fourth section.

4.1 Control aims

The main definitions for optimal and tracking controls are first recalled here in the next paragraphs.

4.1.1 Optimal Control

Let's suppose that the optimal case for the flow control problem considered is to maximize the value of the output of the plant y for a minimum amount of

actuation energy cost. The cost functional for such problem may be written as,

$$J(y,u) = \lim_{T\to+\infty} \frac{1}{T}\int_0^T \Big(\alpha y(s) - (1-\alpha)u^2(s)\Big)ds \tag{4.1}$$

with $0 \le \alpha \le 1$, where α can be understood as a percentage of how much weight we put on the maximization of y, the remaining percentage $1-\alpha$ quantifying the weight of the energy cost of the control. Maximizing J leads to maximizing the average of y while taking into account the energy cost of the control $= \lim_{T\to+\infty} \frac{1}{T}\int_0^T u^2(s)ds$. The optimization problem is therefore :

$$\text{Design a control law } u \text{ such that } J(y,u) \to \max. \tag{4.2}$$

The trade-off between the turbulence reduction and the energy consumed by the actuation is provided by the choice of the parameter α. In addition, note that in the case of a switching input u, as it is the case in the present work since on-off relay actuators are used, the control command u can take only values 0 or 1. Therefore, one can write $u^2(t) = u(t)$ and the cost functional can be rewritten as,

$$J(y,u) = \lim_{T\to+\infty} \frac{1}{T}\int_0^T (\alpha y(s) - (1-\alpha)u(s))\,ds \tag{4.3}$$

4.1.2 Setpoint Tracking Control

The second control problem to be studied here is stabilization of the output y at the desired setpoint y^*. The relay nature of actuators motivates us to apply sliding mode principles in order to design a robust feedback law, which guarantees $y(t) \to y^*$ as $\quad t \to \infty$.

4.2 Open-loop optimal control

4.2.1 Model Description and Basic Assumptions

Let us consider the functional differential equation

$$\dot{y}(t) = A(y_\tau(t)) + \sum_{i=1}^{N_3} (b_i + B_i(y_\tau(t-h_i)))u(t-h_i), \tag{4.4}$$

where $y_\tau(t) \in \mathbf{C}^1_{[-\tau,0]}$ is the state of the system, $(y_\tau(t))(s) = y(t+s)$ for $s \in [-\tau, 0]$, $A : \mathbf{C}^1_{[-\tau,0]} \subset \mathbf{L}^2_{[-\tau,0]} \to \mathbb{R}$ and $B_i : \mathbf{C}^1_{[-\tau,0]} \subset \mathbf{L}^2_{[-\tau,0]} \to \mathbb{R}$ are linear continuous functionals, $b_i \in \mathbb{R}_+$ are positive constants, $u(t) \in \{0,1\}$ is the relay control input, $h_i \in \mathbb{R}_+$ are input delays. For any $u \in \mathbf{L}^\infty_{\mathbb{R}_+}$ the considered system has a unique Caratheodory solution [74].

We assume that *the system* (4.4) *with* $y(s) = 0$ *for all* $s \le 0$ *has bounded positive solution for any input signal* $u \in \boldsymbol{L}^\infty_{\mathbb{R}_+} : u(t) \in \{0,1\}$. We also assume that *the class of admissible control inputs is restricted to* ω*-periodic functions* $u(t) = u(t+\omega)$, $\forall t > 0$.

4.2.2 Elements of Averaging Analysis

Let us introduce some additional notations.

— $\mathbf{L}^2_\Omega$ is the Hilbert space of quadratically integrable functions $\Omega \subseteq \mathbb{R} \to \mathbb{R}$ with the norm $\|\cdot\|_{\mathbf{L}^2}$ induced by the inner product $\xi \cdot \eta = \int_\Omega \xi(s)\eta(s)ds$.

— If $\tau > 0$, $\xi \in \mathbf{L}^\infty_{\mathbb{R}}$ and $t \in \mathbb{R}$ then

$$\xi_\tau(t) \in \mathbf{L}^\infty_{[-\tau,0]} : (\xi_\tau(t))(\sigma) = \xi(t+\sigma) \text{ for } \sigma \in [-\tau, 0],$$

$$\bar{\xi}_\tau(t) \in \mathbf{L}^\infty_{[-\tau,0]} : (\bar{\xi}_\tau(t))(\sigma) = \xi(t-\sigma) \text{ for } \sigma \in [-\tau, 0],$$

— For $\xi, \nu \in \mathbf{L}^\infty_\Omega$ with $\mathbb{R}_+ \subset \Omega$ let us define the operation

$$\langle \xi, \nu \rangle := \lim_{T \to +\infty} \frac{1}{T} \int_0^T \xi(\tau)\nu(\tau)d\tau,$$

which, in particular, defines the scalar product in the space $\mathbf{L}^\infty_{\mathbb{R}_+}$.

— For $\xi, \nu \in \mathbf{L}^{\infty}_{\mathbb{R}}$ let us define $\langle \xi_\tau, \nu \rangle \in \mathbf{L}^{\infty}_{[-\tau,0]}$ as

$$\langle \xi_\tau, \nu \rangle(\sigma) := \lim_{T\to+\infty} \tfrac{1}{T}\int_0^T \xi(s+\sigma)\nu(s)ds \text{ for } \sigma \in [-\tau, 0].$$

Lemma 1. *If $\xi, \nu \in \boldsymbol{L}^{\infty}_{\mathbb{R}}$ and $\tau \in \mathbb{R}_+$ then $\langle \xi_\tau, \nu \rangle = \langle \xi, \bar{\nu}_\tau \rangle$.*

Proof. The change of integration variable $\theta = s + \sigma$ gives

$$\langle \xi_\tau, \nu \rangle(\sigma) = \lim_{T\to+\infty} \int_0^T \frac{\xi(s+\sigma)\nu(s)}{T} ds = \lim_{T\to+\infty} \int_0^{T+\sigma} \frac{\xi(\theta)\nu(\theta-\sigma)}{T} d\theta = \langle \xi, \bar{\nu}_\tau \rangle(\sigma)$$

for $\sigma \in [-\tau, 0]$. ■

This proposition immediately implies the following

Corollary 1. *If $\xi \in \boldsymbol{L}^{\infty}_{\mathbb{R}}$ and $\tau \in \mathbb{R}_+$ then $\langle \xi_\tau, \mathbb{1} \rangle \in \boldsymbol{C}_{[-\tau,0]}$ is the constant function : $\langle \xi_\tau, \mathbb{1} \rangle(\sigma) = \langle \xi, \mathbb{1} \rangle$ for all $\sigma \in [-\tau, 0]$, where $\mathbb{1} \in \boldsymbol{C}_{\mathbb{R}}$ is the unit constant function (i.e. $\mathbb{1}(s) = 1$ for all $s \in \mathbb{R}$).*

Lemma 2. *If $\Phi : \boldsymbol{L}^2_{[-\tau,0]} \to \mathbb{R}_+$ is a linear continuous functional then $\langle \Phi(\xi_\tau), \nu \rangle = \Phi(\langle \xi_\tau, \nu \rangle)$ for any $\xi, \nu \in \boldsymbol{L}^{\infty}_{\mathbb{R}}$.*

Proof. Since Φ is the linear continuous functional $\mathbf{L}^2_{[-\tau,0]} \to \mathbb{R}_+$ then by Riesz Theorem [39] it can be presented as

$$\Phi(\eta) = \mu \cdot \eta = \int_{-\tau}^0 \mu(s)\eta(s)ds, \quad \eta \in \mathbf{L}^2_{[-\tau,0]}$$

with some $\mu \in \mathbf{L}^2_{[-\tau,0]}$. Hence,

$$\frac{1}{T}\int_0^T \Phi(\xi_\tau(s))\nu(s)ds = \frac{1}{T}\int_0^T \int_{-\tau}^0 \mu(\sigma)\xi(s+\sigma)d\sigma\,\nu(s)ds = \int_{-\tau}^0 \mu(\sigma)\frac{1}{T}\int_0^T \xi(s+\sigma)\nu(s)dsd\sigma.$$

Taking the limit for both sides we complete the proof. ■

Corollary 2. *If $\Phi : \boldsymbol{L}^2_{[-\tau,0]} \to \mathbb{R}_+$ is a linear continuous functional then*

$$\lim_{T\to+\infty} \frac{1}{T}\int_0^T \Phi(\xi_\tau(s))ds = \langle \xi, \mathbb{1} \rangle \Phi(\mathbb{1}),$$

for any $\xi \in \boldsymbol{L}^{\infty}_{\mathbb{R}}$*, where* $\mathbb{1} \in \boldsymbol{C}_{\mathbb{R}_+}$ *is the unit constant function.*

Lemma 3. *If* $A : \boldsymbol{C}^1_{[-\tau,0]} \subset \boldsymbol{L}^2_{[-\tau,0]} \to \mathbb{R}$ *and* $B : \boldsymbol{C}^1_{[-\tau,0]} \subset \boldsymbol{L}^2_{[-\tau,0]} \to \mathbb{R}$ *are linear continuous functionals and the system* (4.4) *has bounded solution for any* $u \in \boldsymbol{L}^{\infty}_{\mathbb{R}}$ *then*

$$\sum_{i=1}^{N_2} b_i \langle u, \mathbb{1}\rangle + \langle y, B_i(\bar{u}_\tau)\rangle + \langle y, \mathbb{1}\rangle A(\mathbb{1}) = 0,$$

where $\mathbb{1}$ *is the unit constant function,* y *is a solution to* (4.4) *with* $u \in \boldsymbol{L}^{\infty}_{\mathbb{R}}$ *and* $\bar{u}_\tau(t) \in \boldsymbol{L}^{\infty}_{[-\tau,0]} : (\bar{u}_\tau(t))(\sigma) = u(t-\sigma)$ *for* $\sigma \in [-\tau, 0]$.

Proof. From the equation (4.4) we have

$$\begin{aligned}\int_0^T \frac{\dot{y}(s)}{T} ds &= \int_0^T \frac{A(y_\tau(s))}{T} + \sum_{i=1}^{N_2} \frac{b_i + B_i(y_\tau(s-h_i))u(s-h_i)}{T} ds \\ &= A\left(\int_0^T \frac{y_\tau(s)}{T} ds\right) + \sum_{i=1}^{N_2} \frac{1}{T} \int_{-h_i}^{T-h_i} b_i u(s) + B_i\left(y_\tau(s)\right) u(s) ds.\end{aligned}$$

Since the function y is bounded then $\lim_{T\to+\infty} \frac{1}{T}\int_0^T \dot{y}(s)ds = \lim_{T\to+\infty} \frac{1}{T}(y(T) - y(0)) = 0$ and using Corollary 1 and Lemma 2 we derive $\lim_{T\to+\infty} \frac{1}{T}\int_0^T A\left(y_\tau(s)\right) ds = \langle y, \mathbb{1}\rangle A(\mathbb{1})$. Since

$$\lim_{T\to+\infty} \frac{1}{T} \int_{-h_i}^{T-h_i} B_i\left(y_\tau(s)\right) u(s) ds = \langle B_i(y_\tau), u\rangle$$

then

$$0 = \langle y, \mathbb{1}\rangle A(\mathbb{1}) + \langle u, \mathbb{1}\rangle \sum_{i=1}^{N_2} b_i + \langle B_i(y_\tau), u\rangle.$$

Finally, Lemmas 1 and 2 imply $\langle B_i(y_\tau), u\rangle = B_i(\langle y_\tau, u\rangle) = B_i(\langle y, \bar{u}_\tau\rangle) = \langle y, B_i(\bar{u}_\tau)\rangle$. ■

4.2.3 Periodic Forcing

In the periodic case, the optimization problem $J(y,u) \to \max$ subject to (4.4) considered over infinite interval of time can be reduced to the optimal control

over finite time interval. Indeed, if for any ω-periodic input $u \in \mathbf{L}^{\infty}_{\mathbb{R}_+}$ the system (4.4) has a unique stable ω-periodic solution y^{ω} then

$$J(y^{\omega}, u) = \frac{1}{\omega}\int_0^{\omega} \alpha y^{\omega}(s) - (1-\alpha)u(s)ds. \tag{4.5}$$

To solve this optimization problem we need a proper algorithm of finding of periodic solutions to the system (4.4) with a given periodic control input u. Existence of periodic solution to a particular system (4.4) as well as algorithm for its finding is provided by the next theorem.

Theorem 1 ([110]). *If $0 = h_0 < h_1 < ... < h_m$ and*

— *a function $f : \mathbb{R}_+ \times \mathbb{R}^{n(m+1)} \to \mathbb{R}$ is measurable and ω-periodic : $f(t,\boldsymbol{x}) = f(t+\omega,\boldsymbol{x})$, $t \in \mathbb{R}_+$, $\boldsymbol{x} \in \mathbb{R}^{n(m+1)}$, and satisfies Lipschitz condition :*

$$|f(t,\boldsymbol{x}) - f(t,\boldsymbol{y})| \le \sum_{i=0}^{n-1}\sum_{j=0}^{m} l_{ij}|x_{ij} - y_{ij}|,\ \boldsymbol{x},\boldsymbol{y} \in \mathbb{R}^{n(m+1)},$$

where $l_{ij} \ge 0$ are constants, $\boldsymbol{x} = (x_{00}, x_{01}, ..., x_{ij}, ...) \in \mathbb{R}^{n(m+1)}$ and $\boldsymbol{y} = (y_{00}, y_{01}, ..., y_{ij}, ...) \in \mathbb{R}^{n(m+1)}$,

— *a liner functional $\mathcal{A} : \boldsymbol{C}^n_{[-h_m,0]} \to \mathbb{R}$ is defined as*

$$\mathcal{A}x_{h_m}(t) = \sum_{i=0}^{m}\sum_{j=0}^{n} a_{ij}x^{(j)}(t-h_i), \quad a_{ij} \in \mathbb{R},$$

$$x_{h_m}(t) = x(t+s) \text{ for } s \in [-h_m, 0],$$

— *the frequency $\theta = \frac{2\pi}{\omega}$ satisfies the non-resonance conditions : $L(\mathrm{i}k\theta) \neq 0$ for $k = 0, \pm1, \pm2, ...$ where $p = 0, 1, ..., n-1$ and $L(\lambda) = \sum_{i=0}^{m}\sum_{j=0}^{n} a_{ij}\lambda^j e^{-h_i\lambda}$ is the characteristic quasi-polynomial of the operator $\mathcal{A}$,*

— *the inequality $q = \sum_{p=0}^{n-1} l_p\sigma_p < 1$ holds for $l_p = l_{p0} + l_{p1} + ... + l_{pm}$ and $\sigma_p = \max_{r\in\mathbb{R}}\left|\frac{(\mathrm{i}r\theta)^p}{L(\mathrm{i}r\theta)}\right|$, where i is the imaginary unit,*

then the equation $\mathcal{A}x_{h_m}(t) = f(t, x(t), x(t-h_1), ..., x^{(n-1)}(t-h_m))$ has a unique ω-periodic solution $x_\omega \in \boldsymbol{C}_{[0,\omega]}$,
which satisfies the estimate $\|x^{(i)}_\omega\|_{\boldsymbol{L}^2_{[0,\omega]}} \le \frac{\sigma_i}{1-q}\|f(t,\boldsymbol{0})\|_{\boldsymbol{L}^2_{[0,\omega]}}$, $i = 0, 1, ..., n-1$ and can be found by means of iterations

$$\mathcal{A}x^{[k+1]}_{h_m}(t) = f(t, \boldsymbol{x}^{[k]}(t)), k = 0, 1, 2, ..., \tag{4.6}$$

where $x^{[0]}$ *is an arbitrary* ω*-periodic function and* $\mathbf{x}^{[k]}(t) = (x^{[k]}(t), x^{[k]}(t-h_1), \ldots, x^{[k]}(t-h_m), \ldots) \in \mathbb{R}^{n(m+1)}$ *and the following estimate*

$$\left\| \frac{d^i x^{[k]}}{dt^i} - \frac{d^i x_\omega}{dt^i} \right\|_{\boldsymbol{L}^2_{[0,\omega]}} \leq \frac{q^k}{1-q} \sigma_i \sum_{p=0}^{n-1} l_p \left\| \frac{d^p x^{[0]}}{dt^p} - \frac{d^p x_\omega}{dt^p} \right\|_{\boldsymbol{L}^2_{[0,\omega]}} \tag{4.7}$$

holds for $i = 0, 1, 2, \ldots, n-1$.

To the best of our knowledge, the proof of Theorem 1 for $\mathbf{L}^2$ spaces has never been presented in English literature. Its proof given originally in [110] is sketched in Appendix A.

The formula (4.6) provides simple recursive procedure for numerical finding of periodic solution with precision controlled by the formula (4.7). Combination of this algorithm with some infinite dimensional optimization procedure [79] allows us to find numerically an optimal input signal u for a fixed period ω. The corresponding algorithms are usually computationally hard. That is why, for practice, it is also important to provide a simple suboptimal algorithm. One has the following proposition :

Proposition 1. *If for any* ω*-periodic input signal* $u \in \boldsymbol{L}^\infty_{\mathbb{R}}$ *the poitive system* (4.4) *has a unique globally asymptotically stable periodic solution and* $A(\mathbb{1}) + \omega^{-1} \int_0^\omega \sum_{i=1}^{N_2} B_i(\bar{u}_\tau(s))ds < 0$, *then,*

$$J(y,u) \geq \tilde{J}(u) = \frac{1}{\omega} \left(\alpha - 1 - \frac{\alpha \sum_{i=1}^{N_2} b_i}{A(\mathbb{1}) + \omega^{-1} \int_0^\omega \sum_{i=1}^{N_2} B_i(\bar{u}_\tau(s))ds} \right) \int_0^\omega u(s)ds$$

Proof of Proposition 1. In the periodic case, we derive $\langle u, \mathbb{1} \rangle = \frac{1}{\omega} \int_0^\omega u(s)ds$, $\langle y, \mathbb{1} \rangle = \frac{1}{\omega} \int_0^\omega y^\omega(s)ds$ and $\langle y, B_i(\bar{u}_\tau) \rangle = \frac{1}{\omega} \int_0^\omega B_i(\bar{u}_\tau(s)) y^\omega(s)ds$, where y^ω is ω-periodic solution that corresponds to ω-periodic control input u. On the one hand, the functional B_i is linear and continuous, so it is bounded and there exists a constant M such that $M - B_i(\bar{u}_\tau(s)) \geq 0$ for all $s \in [0, \omega]$. On the other hand, for any $\xi, \eta \in \mathbf{L}^\infty_{[0,\omega]}$ we

have $\xi \cdot \eta \leq \|\xi\|_{\mathbf{L}^2_{[0,\omega]}} \|\eta\|_{\mathbf{L}^2_{[0,\omega]}}$ and $\|\xi\|_{\mathbf{L}^2_{[0,\omega]}} \leq \frac{1}{\sqrt{\omega}} \|\xi\|_{\mathbf{L}^1_{[0,\omega]}}$. Hence, taking into account positivity of the system (4.4) we derive

$$\begin{aligned}
\frac{1}{\omega}\int_0^\omega -B_i(\bar{u}_\tau(s))y^\omega(s)ds &= -\frac{M}{\omega}\int_0^\omega y^\omega(s)ds + \frac{1}{\omega}\int_0^\omega (M - B_i(\bar{u}_\tau(s)))y^\omega(s)ds \\
&\leq -\frac{M}{\omega}\int_0^\omega y^\omega(s)ds + \left(\frac{1}{\omega}\int_0^\omega M - B_i(\bar{u}_\tau(s))ds\right)\left(\frac{1}{\omega}\int_0^\omega y^\omega(s)ds\right) \\
&= \left(-\frac{1}{\omega}\int_0^\omega B_i(\bar{u}_\tau(s))ds\right)\left(\frac{1}{\omega}\int_0^\omega y^\omega(s)ds\right)
\end{aligned}$$

Taking into account Lemma 3 we derive

$$\langle u, \mathbb{1}\rangle \sum_{i=1}^{N_2} b_i = -A(\mathbb{1})\langle y, \mathbb{1}\rangle - \sum_{i=1}^{N_2} \langle y, B_i(\bar{u}_\tau)\rangle \leq -\left(A(\mathbb{1}) + \frac{1}{\omega}\int_0^\omega \sum_{i=1}^{N_2} B_i(\bar{u}_\tau(s))ds\right)\langle y, \mathbb{1}\rangle.$$

which completes the proof. ■

Therefore, if conditions of Proposition 1 holds then the sub-optimal control can be found by means of maximization of the functional $\tilde{J}(u)$.

If periodic control inputs are restricted to

$$u_{\omega,t'}(t) = \begin{cases} 1 & \text{for} \quad t \in [k\omega, k\omega + t'), \\ 0 & \text{for} \quad t \in [k\omega + t', (k+1)\omega), \end{cases} \tag{4.8}$$

then, in the view of Proposition 1, a quasi optimal solution to (D.5) can be found from the finite dimensional optimization problem : $\tilde{J}(u_{\omega,t'}) \to \max$. Such class of input signals is motivated by natural practical demands to minimize the number of switchings.

Using the fact that $\bar{u}$ is ω-periodic such that $\frac{1}{\omega}\int_0^\omega \bar{u}(s)ds = \frac{t'}{\omega}$ and Riesz Theorem

[39], we can write for some $\mu_i \in \mathbf{L}^2_{[-\tau,0]}$:

$$\begin{aligned}\frac{1}{\omega}\int_0^{\omega}\sum_{i=1}^{N_2} B_i(\bar{u}_\tau(s))ds &= \frac{1}{\omega}\int_0^{\omega}\sum_{i=1}^{N_2}\int_{-\tau}^{0}\mu_i(\sigma)\bar{u}_\tau(s+\sigma)d\sigma ds \\ &= \sum_{i=1}^{N_2}\int_{-\tau}^{0}\mu_i(\sigma)\left(\frac{1}{\omega}\int_0^{\omega}\bar{u}_\tau(s+\sigma)ds\right)d\sigma \\ &= \sum_{i=1}^{N_2}\int_{-\tau}^{0}\mu_i(\sigma)\left(\frac{t'}{\omega}\right)d\sigma = \frac{t'}{\omega}\sum_{i=1}^{N_2} B_i(\mathbb{1})\end{aligned}$$

In this case, the condition $A(\mathbb{1}) + \omega^{-1}\int_0^{\omega}\sum_{i=1}^{N_2} B_i(\bar{u}_\tau(s))ds < 0$ of Proposition 1 simplifies to $A(\mathbb{1}) + \frac{t'}{\omega}\sum_{i=1}^{N_2} B_i(\mathbb{1}) < 0$, and $\tilde{J}(u)$ to :

$$\tilde{J}(u) = \left(\alpha - 1 - \frac{\alpha\sum_{i=1}^{N_2} b_i}{A(\mathbb{1}) + \frac{t'}{\omega}\sum_{i=1}^{N_2} B_i(\mathbb{1})}\right)\frac{t'}{\omega} \tag{4.9}$$

This optimization problem can be solved analytically for $\tilde{J}$. For any fixed value ω_0 of ω, the value of t' noted by t'_0 is given by :

$$t'_0 = \begin{cases} 0 & \text{if } \alpha = 0 \\ \omega & \text{if } \alpha = 1 \\ \omega\ \mathrm{sat}_{[0,1]}\left(\frac{-A(\mathbb{1})}{\sum_{i=1}^{N_2} B_i(\mathbb{1})} - \frac{\sqrt{\frac{\alpha}{(\alpha-1)}A(\mathbb{1})\left(\sum_{i=1}^{N_2} b_i\right)}}{\sum_{i=1}^{N_2} B_i(\mathbb{1})}\right) & \text{if } 0 < \alpha < 1 \end{cases} \tag{4.10}$$

where $\mathrm{sat}_{[0,1]}$ is the saturation function on the interval $[0,1]$ such that $\mathrm{sat}_{[0,1]}(x) = x$ for $0 \le x \le 1$, $\mathrm{sat}_{[0,1]}(x) = 1$ for $x > 1$ and $\mathrm{sat}_{[0,1]}(x) = 0$ for $x < 0$

4.3 Setpoint tracking control

4.3.1 Plant Model and Basic Assumptions

For the design of a tracking control we use the simplest model obtained during the identification procedure (4 parameters and 3 delays), namely

$$\dot{y}(t) = a_1 y(t-h) - a_2 y(t-\tau) + (b - cy(t-h) + cy(t-\bar{\tau}))u(t-h), \tag{4.11}$$

$$y(s) = 0, \quad u(s) = 0 \quad \text{for} \quad s \le 0, \tag{4.12}$$

where $a_1 > 0, a_2 > 0, b > 0, c > 0, \bar{\tau} > 0, h > 0, \tau > 0$ are constant parameters, $y(t) \in \mathbb{R}$ - output and $u \in \mathbf{L}^\infty_{\mathbb{R}} : u(t) \in \{0,1\}, t \ge 0$ is the input. Note that for any $u \in L^\infty_{\mathbb{R}_+}$ the considered system has a unique Caratheodory solution [74] at least locally.

We deal with a model of physical system. To exclude non-feasible dynamics we assume that *the system* (D.8), (D.9) *has bounded positive solution for any input signal* $u \in \boldsymbol{L}^\infty_{\mathbb{R}_+} : u(t) \in \{0,1\}$. The sufficient condition of positivity and boundedness of solutions to the system (D.8) is given by the next proposition.

Proposition 2. *If* $c < a_1, (a_1 + c)\tau < a_2\tau < \frac{1}{e}$ *and* $\tau \le h \le \bar{\tau}$ *then the system* (D.8), (D.9) *is positive and its solution is globally bounded for any input signal* $u \in \boldsymbol{L}^\infty$: $u(t) \in \{0,1\}$ *as follows*

$$0 \le y(t) < y_{\max} := \frac{b}{a_2 - a_1} \text{ for all } t \ge 0.$$

In order to prove Proposition 2, we first need Lemmas 4 and 5.

Lemma 4. *If* $a > 0, \tau > 0$ *and* $a\tau < \frac{1}{e}$ *then the system* $\dot{z}(t) = -az(t-\tau) + f(t)$, $z(s) = 0$ *for* $s \le 0$ *is positive for any non-negative* $f \in \boldsymbol{L}^\infty_{\mathbb{R}}$, *i.e.* $z(t) \ge 0$ *if* $f(t) \ge 0$ *for all* $t \ge 0$.

Proof of Lemma 4. See Lemma 4 of [47] or Corollary 15.9 from [1]. ■

Lemma 5. *Let the system* $\dot{z}(t) = -az(t-\tau) + b$ *with* $z(s) = 0$ *for* $s \le 0$ *be positive and* $a > 0, b > 0$, $0 \le a\tau < \ln(2)$. *Then it has a unique solution defined on* $\mathbb{R}_+$ *such that* $0 < z(t) < \frac{b}{a}$ *and* $\dot{z}(t) > 0$ *for all* $t > 0$.

Proof of Lemma 5. For existence and uniqueness of solution of time-delay systems see [58]. Let us suppose a contrary, i.e. there exists $t^* > 0$ such that $z(t^*) = \frac{b}{a}$, but $z(t) < \frac{b}{a}$ for all $t > t^*$. This immediately implies that $\dot{z}(t) > 0$ and $z(t) > 0$ for all $t \in (0, t^*]$.

Let us denote $p(t) = z(t) - a\int_{t-\tau}^{t} z(s)ds$. Hence, we have

$$\dot{p}(t) = -az(t) + b = -ap(t) + b - a^2 \int_{t-\tau}^{t} z(s)ds$$

and

$$\begin{aligned}
z(t) &= \frac{b(1-e^{-at})}{a} + a\int_{t-\tau}^{t} z(s)ds - a^2\int_{0}^{t} e^{-a(t-\sigma)}\int_{\sigma-\tau}^{\sigma} z(s)dsd\sigma \\
&= \frac{b(1-e^{-at})}{a} + a\int_{t-\tau}^{t} z(s)ds - a\int_{0}^{t} e^{-a(t-\sigma)}\int_{t-\tau}^{t} z(\sigma-t+s)dsd\sigma \\
&= \frac{b(1-e^{-at})}{a} + a\int_{t-\tau}^{t}\left(z(s) - a\int_{0}^{t} e^{-a(t-\sigma)}z(\sigma-t+s)d\sigma\right)ds \\
&= \frac{b(1-e^{-at})}{a} + a\int_{t-\tau}^{t}\left(z(s) - a\int_{-t}^{0} e^{a\sigma}z(s+\sigma)d\sigma\right)ds \\
&= \frac{b(1-e^{-at})}{a} + a\int_{t-\tau}^{t}\left(z(s) - ae^{-as}\int_{s-t}^{s} e^{a\sigma}z(\sigma)d\sigma\right)ds \\
&= \frac{b}{a}(1-e^{-at}) + a\int_{t-\tau}^{t} e^{-as}f(s,t)ds,
\end{aligned}$$

where $f(s,t) = e^{as}z(s) - a\int_{s-t}^{s} e^{a\sigma}z(\sigma)d\sigma$. Since for $s \in [t-\tau, t]$ and $0 < t \le t^*$ we have

$$\frac{\partial f}{\partial s} = e^{as}\dot{z}(s) + ae^{as}z(s) - ae^{as}z(s) + ae^{a(s-t)}z(s-t) \ge 0$$

then $z(t) \le \frac{b(1-e^{-at})}{a} + af(t,t)\int_{t-\tau}^{t}\frac{ds}{e^{as}} = \frac{b(1-e^{-at})}{a} + f(t,t)\frac{e^{a\tau}-1}{e^{at}}$ or, equivalently, $z(t) \le$

$\frac{b(1-e^{-at})}{a(2-e^{a\tau})} - \frac{a(e^{a\tau}-1)}{2-e^{a\tau}} \int_0^t e^{-a(t-\sigma)} z(\sigma) d\sigma$. Hence, $z(t) \leq w(t)$, where $w(t)$ satisfies the integral equation $w(t) = \frac{b(1-e^{-at})}{a(2-e^{a\tau})} - \frac{a(e^{a\tau}-1)}{2-e^{a\tau}} \int_0^t e^{-a(t-\sigma)} w(\sigma) d\sigma, w(0) = 0$ or, equivalently,

$$\dot{w}(t) = -a\left(1 + \frac{e^{a\tau}-1}{2-e^{a\tau}}\right) w(t) + \frac{b}{2-e^{a\tau}} = \frac{-aw(t)+b}{2-e^{a\tau}}.$$

Therefore, we derive that $z(t) \leq \frac{b}{a}\left(1 - e^{-\frac{a}{2-e^{a\tau}}t}\right) < \frac{b}{a}$ for all $t > 0$. This contradicts our supposition. ■

Using Lemmas 4 and 5, we can now prove 2 :

Proof of Proposition 2. I. Let us consider the system $\dot{y}(t) = -a_2 y(t-\tau) + f(t)$, $y(s) = 0, s \leq 0$, where f is a locally integrable function. If $f(t) \geq 0$ and $a_2\tau \leq e^{-1}$ then the delay-dependent positivity conditions hold (see, Lemma 1) and $y(t) \geq 0$, for all $t \geq 0$. On the one hand, if $a_1 \geq c$ and $y(s) \geq 0$ for $s \leq t$ then $f(t) = a_1 y(t-h) + (b - cy(t-h) + cy(t-\bar{\tau}))u(t-h) \geq 0$. Therefore, using the method of steps (i.e. considering sequentially the intervals $[0,h], [h,2h]$...) we prove positivity of the system (D.8), (D.9).

II. Now let us prove boundedness of solutions. Suppose the contrary : there exists an input signal $u(t)$ and an instant of time $t^* > 0 : y(t^*) = y_{\max}$ and $y(s) < y_{\max}$ for $s < t^*$.

In this case, since $b - cy(t-h) + cy(t-\bar{\tau}) \geq b - cy(t-h) = (a_2 - a_1)y_{\max} - cy(t-h) > 0$ for all $t \in [0, t^*]$ then $y(s) \leq y_{\mathbb{1}}(s)$ for all $s \leq t^*$, where $y_{\mathbb{1}}$ is the solution to the positive system $\dot{y}_{\mathbb{1}}(t) = (a_1 - c)y_{\mathbb{1}}(t-h) - a_2 y_{\mathbb{1}}(t-\tau) + cy_{\mathbb{1}}(t-\bar{\tau}) + b$. Let us prove boundedness of solutions of the latter system for this purpose let us study the auxiliary system

$$\dot{z}(t) = -(a_2 - a_1)z(t-\tau) + b, \quad z(s) = 0 \text{ for } s \leq 0.$$

For $\Delta(t) = z(t) - y_{\mathbb{1}}(t)$ we derive $\dot{\Delta}(t) = -a_2\Delta(t-\tau) + a_1 z(t-\tau) - (a_1 - c)y_{\mathbb{1}}(t-h) - cy_{\mathbb{1}}(t-\bar{\tau})$. According to Lemma 5 the function z satisfies the inequalities $0 < z(t) < b/(a_2 - a_1) = y_{\max}$ and $\dot{z}(t) > 0$ for all $t > 0$. Hence, $z(t-\tau) \geq z(t-h) \geq z(t-\bar{\tau})$ and

$$\dot{\Delta}(t) = -a_2\Delta(t-\tau) + (a_1 - c)\Delta(t-h) + c\Delta(t-\bar{\tau}) + \eta(t),$$

where $\eta(t) = a_1 z(t-\tau) - (a_1 - c)z(t-h) - cz(t-\bar{\tau}) \geq 0$ and $\Delta(s) = 0$ for $s \leq 0$. Since the latter system is positive (see, the first part of this proof) then $\Delta(t) \geq 0$ and $y_{\mathbb{1}}(t) \leq z(t) < y_{\max}$ for all $t \geq 0$. This contradicts our supposition. ■

4.3.2 Sliding Mode Control for Time Delay Bilinear System

The conventional sliding mode control methodology [143], [46], [129] is developed for delay-free systems. We emphasize again that, in our case, the choice of Sliding Mode control was motivated by the fact that the actuator is working as a relay. In order to design the sliding mode control we need to compensate input delay using, for example, the prediction technique (see, e.g. [106], [5], [59], [107]). Developed originally for linear plants this idea can also be applied for bilinear systems under consideration.

A simple example of a predictor is given here :

Suppose that we study the positive system $\dot{x}(t) = ax(t) + bu(t-h)$ with $a < 0$, $b > 0$ and $u(t) \in \{0,1\}$. The maximum value of $x(t)$ is $x_{max} = -\frac{b}{a}$, with $0 < x(t) < x_{max}$. Consider the following prediction variable : $\sigma(t) = ax(t) + b\int_{t-h}^{t} u(s)ds$. Its derivative is : $\dot{\sigma}(t) = ax(t) + bu(t)$. Note that the control input u is not delayed with respect to the sliding variable σ, so the conventional sliding mode design scheme can be utilized (see, [143]). Take $u(t) = \text{sign}(\sigma(t) - \sigma^*) = \begin{cases} 1 & if \quad \sigma(t) - \sigma^* < 0 \\ 0 & if \quad \sigma(t) - \sigma^* > 0 \end{cases}$, where $\sigma^* = ax^* + b$ and $x^* \in (0, x_{max})$ is the desired value to track. If $\sigma(t) > \sigma^*$ then $\dot{\sigma}(t) = ax(t) < 0$ and, if $\sigma(t) < \sigma^*$ then $\dot{\sigma}(t) = ax(t) + b > ax_{max} + b > 0$. Therefore, $\frac{d}{dt}(\sigma(t) - \sigma^*)(\sigma(t) - \sigma^*) < 0$ and, according to [143], sliding mode arises on the surface $\sigma(t) - \sigma^* = 0$ in a finite time, i.e. $\sigma(t) = \sigma^*$ for $t > t^*$.

Assuming $\bar{\tau} > h$ we introduce the following sliding variable for our model :

$$\sigma(t) = y(t) - a_2 \int_{t-\tau}^{t} y(s)ds + c \int_{t-\bar{\tau}+h}^{t} y(s)ds + \int_{t-h}^{t} a_1 y(s) + (b - cy(s) + cy(s-\bar{\tau}+h))u(s)ds. \quad (4.13)$$

Obviously, the variable σ satisfies the equation

$$\dot{\sigma}(t) = (a_1 - a_2 + c(1-u(t)))y(t) + c(u(t)-1)y(t-\bar{\tau}+h) + bu(t)$$

Proposition 3. *If conditions of Proposition 2 hold and*

$$Q(j\omega) \neq 0 \quad \text{for} \quad \omega \neq 0, \tag{4.14}$$

where $Q(s) = s + a_2 e^{-s\tau} - (a_2 - c)e^{-sh} - ce^{-s\bar{\tau}}, s \in \mathbb{C}$ *and* $j = \sqrt{-1}$, *then the control law*

$$u(t) = \begin{cases} 1 & \text{if} \quad \sigma(t) < \sigma^*, \\ 0 & \text{if} \quad \sigma(t) > \sigma^*, \end{cases} \tag{4.15}$$

with $\sigma^* = y^*(1 + a_2(h - \tau) + c(\bar{\tau} - h))$ *and* $y^* \in \left(0, \frac{b}{a_2 - a_1}\right)$ *guarantees* $y(t) \to y^*$ *as* $t \to +\infty$.

The proof of this proposition is given below, where it is shown that the control (D.11) guarantees finite-time convergence of the sliding variable $\sigma(t)$ to σ^*, so $\sigma(t) = \sigma^*$ for all $t \geq T$. It is worth stressing that when sliding mode arises the system motion is governed by the infinite dimensional dynamic system

$$\sigma^* = y(t) + a_2 \int_{t-h}^{t-\tau} y(s)ds + c \int_{t-\bar{\tau}}^{t-h} y(s)ds.$$

This means that our sliding surface $\sigma = \sigma^*$ is "inifine dimensional". Using condition (4.14) it is proven that the output $y(t)$ tends to y^* asymptotically as $t \to \infty$.

Remark 1. Since

$$Re(Q(j\omega)) = a_2 \cos(\tau\omega) - (a_2 - c)\cos(h\omega) - c\cos(\bar{\tau}\omega)$$

$$Im(Q(j\omega)) = \omega - a_2 \sin(\tau\omega) + (a_2 - c)\sin(h\omega) + c\sin(\bar{\tau}\omega)$$

then to check the condition (4.14) *it is sufficient to consider* $\omega \in (0, 2(a_2 + c)]$.

Proof of Proposition 3. First of all, let us note that $0 < y(t) < \frac{b}{a_2 - a_1}$ for all $t > 0$ due to Proposition 2.

I. Since the system (D.8) is positive, then $y(t) \geq 0$ for all $t \geq 0$. Moreover, if $u(t) = 0$ and $y(t) > 0$ then $\dot{\sigma}(t) < 0$, but if $u(t) = 1$ and $y(t) < \frac{b}{a_2 - a_1}$ then $\dot{\sigma}(t) > 0$. Therefore, while $0 < y(t) < \frac{b}{a_2 - a_1}$ we have $(\sigma(t) - \sigma^*)\frac{d}{dt}(\sigma(t) - \sigma^*) < 0$. Obviously, $\sigma(0) = 0$. To guarantee existence of sliding mode we just need to show that the

state $\sigma(t) = \sigma^* > 0$ is reachable in a finite time $t = t^* > 0$. Let us suppose contrary : $\sigma(t) < \sigma^*$ for all $t > 0$. This means that $u(t) = 1$ for all $t > 0$ and

$$\dot{y}(t) = (a_1 - c)y(t-h) - a_2 y(t-\tau) + cy(t-\bar{\tau}) + b.$$

Using the last identity let us rewrite the formula (4.13) as

$$\sigma(t) = y(t) - a_2 \int_{t-\tau}^{t} y(s)ds + c \int\limits_{t-\bar{\tau}+h}^{t} y(s)ds + \int\limits_{t-h}^{t} \dot{y}(s+h) + a_2 y(s+h-\tau)ds$$

$$\sigma(t) = y(t+h) + a_2 \int_{t}^{t+h-\tau} y(s)ds + c \int\limits_{t-\bar{\tau}+h}^{t} y(s)ds.$$

Let us show that there exists $t^* > 0$ such that $y(t) > y^*$ for all $t > t^*$. Since $\dot{y}(t) > -a_2 y(t-\tau) + b$ for all $t > 0$ then, obviously, there exists $t_1 > 0$ such that $y(t) > \frac{b}{a_2}$ for all $t > t_1$. In this case, we derive $\dot{y}(t) > -a_2 y(t-\tau) + b\left(1 + \frac{a_1}{a_2}\right)$ for all $t > t_1 + \bar{\tau}$ and there exists $t_2 > t_1 + \bar{\tau}$ such that $y(t) > \frac{b}{a_2}\left(1 + \frac{a_1}{a_2}\right)$ for all $t > t_2$, and so on. Therefore, for $t > t_i$ we derive

$$y(t) > \frac{b}{a_2}\left(1 + \frac{a_1}{a_2} + \ldots + \left(\frac{a_1}{a_2}\right)^{i-1}\right) = \frac{b\left(1 - \left(\frac{a_1}{a_2}\right)^i\right)}{a_2 - a_1}$$

and for some i^* we have $y(t_{i^*}) > y^* \in \left(0, \frac{b}{a_2 - a_1}\right)$.

Therefore, for $t > t^* + \bar{\tau}$, $\sigma(t) > y^*(1 + a_2(h - \bar{\tau}) + c(\bar{\tau} - h)) = \sigma^*$ and the sliding mode existence condition [143] holds and $\sigma(t) = \sigma^*$, $\forall t > t^*$.

II. Using the equivalent control method [143] we derive $u_{eq}(t) = \frac{(a_2 - a_1 - c)y(t) + cy(t-\bar{\tau}+h)}{b - cy(t) + cy(t-\bar{\tau}+h)}$ and

$$\sigma^* = y(t) - a_2 \int\limits_{t-\tau}^{t} y(s)ds + c \int\limits_{t-\bar{\tau}+h}^{t} y(s)ds + \int\limits_{t-h}^{t} a_2 y(s) - cy(s) + cy(s - \bar{\tau} + h)ds =$$

$$y(t) + a_2 \int\limits_{t-h}^{t-\tau} y(s)ds + c \int\limits_{t-\bar{\tau}}^{t-h} y(s)ds$$

for all $t > t^*$. Introducing the variable $\Delta(t) = y(t) - y^*$ we obtain the equation

$$\Delta(t) + a_2 \int_{t-h}^{t-\tau} \Delta(s)ds + c \int_{t-\bar{\tau}}^{t-h} \Delta(s)ds = 0. \tag{4.16}$$

It has the characteristic equation $\frac{1}{s}Q(s) = 0$, $s \in \mathbb{C}$. We have already proven that all solutions of the closed-loop system are bounded (see, Proposition 2) and the sliding mode exists for all $t > t^*$, so the equation (4.16) does not have unbounded dynamics. The condition $Q(j\omega) \neq 0$ for all $\omega \neq 0$ implies that this equation does not have non-constant periodic solutions. So, the only stable solution is $\Delta(t) \equiv C$, where $C \in \mathbb{R}$ is some constant. Since $1 + a_2(h - \tau) + c(\bar{\tau} - h) > 0$ then from the equation for $\Delta(t)$ we immediately derive $C = 0$ and $y(t) \to y^*$ as $t \to \infty$. ■

Corollary 3 (Robustness)**.** *Let the model D.8 contain an additive perturbation :*

$$\dot{y}(t) = a_1 y(t) - a_2 y(t-\tau) + (b - cy(t-h) + cu(t-\bar{\tau}))u(t-h) + d(t) \tag{4.17}$$

where $d(t)$ is a bounded signal $\|d(t)\| < \bar{d}$ such that 4.17 remains a positive system. Then under conditions of Proposition 3 for sufficiently small $\bar{d} < \frac{b}{1+\frac{a_2-a_1}{a_2-a_1-c}}$ and for $y^* \in \left(\frac{\bar{d}}{a_2-a_1-c}, \frac{b-\bar{d}}{a_2-a_1}\right)$ one has $y(t) \to y^* + O(h\bar{d})$ as $t \to \infty$.

Sketch of the proof of Corollary 3. The derivative of the sliding variable (4.13) for the system (4.17) is :

$$\dot{\sigma}(t) = (a_1 - a_2 + c(1 - u(t)))y(t) + c(u(t) - 1)y(t - \bar{\tau} + h) + bu(t) + d(t) \tag{4.18}$$

We study two cases :

- If $\sigma(t) > \sigma^*$ then $u(t) = 0$ and

$$\dot{\sigma}(t) = (a_1 - a_2 + c)y(t) - cy(t - \bar{\tau} + h) + d(t) < (a_1 - a_2 + c)y(t) - cy(t - \bar{\tau} + h) + \bar{d} \tag{4.19}$$

  As $c > 0$ and $y(t) > 0, \forall t > 0$, $-cy(t - \bar{\tau} + h) < 0$ and :

$$(a_1 - a_2 + c)y(t) - cy(t - \bar{\tau} + h) + \bar{d} < (a_1 - a_2 + c)y(t) + \bar{d} \tag{4.20}$$

Therefore, to have $\dot{\sigma}(t) < 0$ it is sufficient that :

$$(a_1 - a_2 + c)y(t) + \bar{d} < 0 \Leftrightarrow y(t) > \frac{\bar{d}}{a_2 - a_1 - c} \tag{4.21}$$

- If $\sigma(t) < \sigma^*$ then $u(t) = 1$ and

$$\dot{\sigma}(t) = (a_1 - a_2)y(t) + b + d(t) > (a_1 - a_2)y(t) + b - \bar{d} \tag{4.22}$$

Therefore, to have $\dot{\sigma}(t) > 0$, it is sufficient that :

$$(a_1 - a_2)y(t) + b - \bar{d} > 0 \Leftrightarrow y(t) < \frac{b - \bar{d}}{a_2 - a_1} \tag{4.23}$$

Therefore, to guarantee $\dot{\sigma}(t)(\sigma(t) - \sigma^*) < 0$, it is sufficient to have :

$$\frac{\bar{d}}{a_2 - a_1 - c} < y(t) < \frac{b - \bar{d}}{a_2 - a_1} \tag{4.24}$$

The set $\left[\frac{\bar{d}}{a_2-a_1-c}, \frac{b-\bar{d}}{a_2-a_1}\right]$ is non-empty, if :

$$\frac{\bar{d}}{a_2 - a_1 - c} < \frac{b - \bar{d}}{a_2 - a_1} \Leftrightarrow \bar{d} < \frac{b}{\frac{a_2-a_1}{a_2-a_1-c} + 1} \tag{4.25}$$

Finally, if $\bar{d}$ is bounded as $\bar{d} < \frac{b}{\frac{a_2-a_1}{a_2-a_1-c}+1}$, the sliding mode appears on the surface $\sigma = 0$. This implies that $y \to y^* + O(h\bar{d})$ as $t \to \infty$ (see e.g. [107] for more details).

■

4.4 Experimental results

4.4.1 Open-loop optimal control

The open-loop optimal control has been applied to the test case II. The identification has been done on the data presented in Section 2.2 using a bilinear model with constant input delays. The results of the identification are given

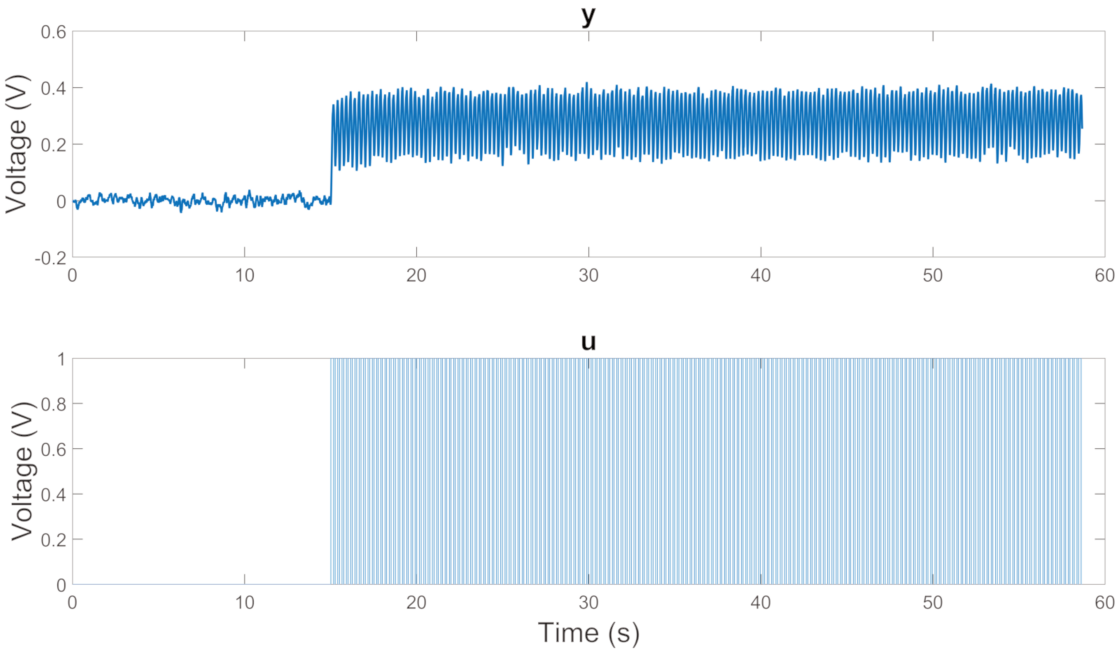

FIGURE 4.1 – Open-loop optimal control for the TC II with $\alpha = 0.78$. Flow conditions : $U = 34.5$m/s, $q = 25$g/s, AoA = 24°

in Section C.1 of the Appendix. The conditions of Proposition 3 are fulfilled by the model as $A(\mathbb{1}) = \sum_{i=1}^{N_1} a_i = -4.4021$ and $\sum_{i=1}^{N_2} B(\mathbb{1}) = \sum_{i=1}^{N_2} \sum_{j=1}^{N_3} c_{ji} = -5934$, therefore $\forall t', \omega, A(\mathbb{1}) + \frac{t'}{\omega} \sum_{i=1}^{N_2} B(\mathbb{1}) < 0$.

Using this model, we design an optimal open-loop control using Equations (D.6) and (D.7). Choosing, for example, $\omega = 0.25$s and $\alpha = 0.78$ leads to $t' = 0.154$s which corresponds to a square wave with frequency 4Hz and DC 62%, while choosing $\alpha = 0.62$ leads to $t' = 0.04544$s which corresponds to a square wave with frequency 4Hz and DC 18%. Therefore the choice of alpha requires care and precision. The results are presented in Figure 4.1 and Figure 4.2 correspond to $\alpha = 0.78$ and $\alpha = 0.62$ respectively. The flow conditions are identical for both plots and are the "nominal conditions" : $U = 34.5$m/s, $q = 25$g/s, AoA = 24°.

A table containing the values of the cost function J is presented in Table 4.1 for several DC with a frequency of 4Hz and for $\alpha = 0.62$ and $\alpha = 0.78$. It can be seen that the case with DC=18% is the best one for $\alpha = 0.62$ as it has the highest value for J but the case with DC=63% is not optimal for $\alpha = 0.78$ when

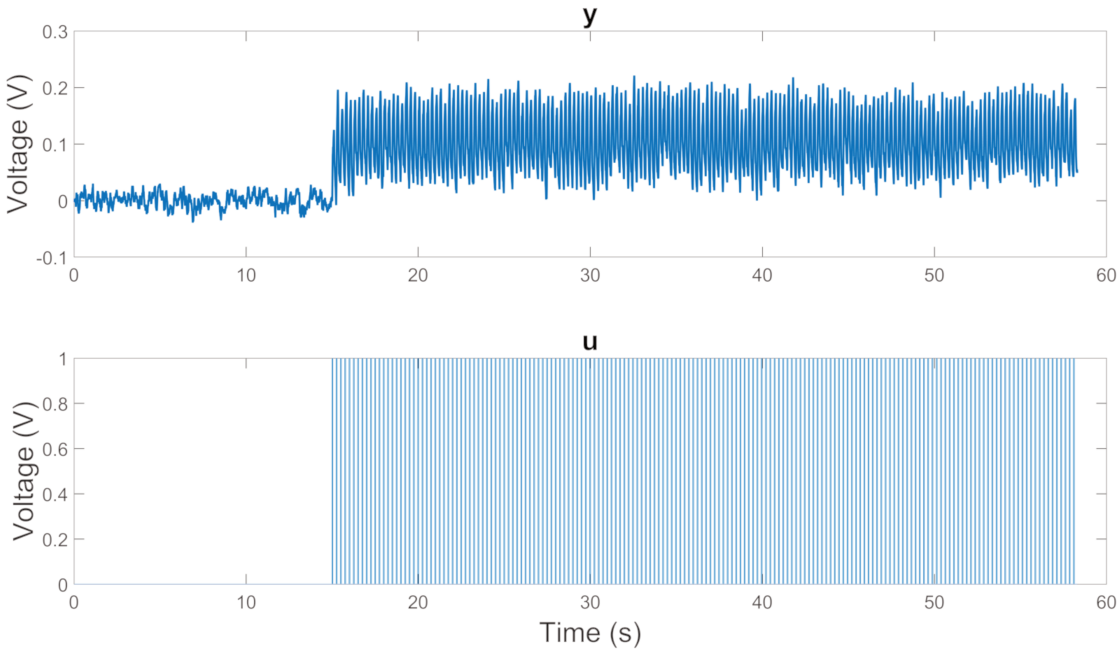

FIGURE 4.2 – Open-loop optimal control for the TC II with $\alpha = 0.62$. Flow conditions : $U = 34.5$m/s, $q = 25$g/s, AoA = 24°

comparing the values of the cost function J in the Table 4.1 and searching for the highest one. Therefore, the suboptimal algorithm developed here may not be working for every experimental case due to its suboptimal nature.

4.4.2 Robust setpoint tracking control

The robust setpoint tracking control has been applied to the TC II (Section 2.2) and III (Section 2.3). The identified models for the plants associated to these

	$\alpha = 0.62$	$\alpha = 0.78$
DC18%	$J = -0.0104$	$J = 0.0378$
DC63%	$J = -0.0627$	$J = 0.0822$
DC50%	$J = -0.0314$	$J = 0.0890$
DC80%	$J = -0.0584$	$J = 0.1328$

Table 4.1 – Value of the cost function J for several DC

two cases are described in the Sections C.1.2 and C.2.1 of the Appendix.

4.4.2.1 Tests conducted on TC II

Results of of closed-loop control using SMC in TC II are presented here. In the caption of each figure are mentioned the setpoint y^* as well as the flow conditions (U, q and AoA). Note that $y_{max} = 0.42$ for this model.

Figure 4.3 and 4.4 present the results for $y^* = 0.25$ and $y^* = 0.4$ in the "nominal" conditions. The next figures are used to prove the experimental robustness of the control. Figure 4.5 shows the results of the control with a flow speed taken down from 34.5m/s to 14.5m/s which corresponds to a reduction of almost 60% of the flow speed while the other conditions do not change. Figure 4.6 corresponds to an angle of attack (AoA) of the flap of 10° instead of 24°. Numerous other tests were conducted in the case of static flow conditions but the plots are not presented here for clarity and to avoid redundancy. In these plots both y and u are in volts and AoA is in degrees. In Figure 4.4 it can be seen the the control is almost always at 1, which can be explained by the fact that the setpoint is at 0.4 and the maximum reachable value by the system is 0.42 with a constant control equal to 1.

These plots show that the SMC is able to maintain the output y at the prescribed setpoint while being robust to perturbations in the flow conditions. The controller's robustness is shown by changing by 60% the freestream velocity or the angle of attack and observing that the output y is still maintained at the setpoint.

The robustness to unsteady perturbation was also tested by having a time varying angle of attack. This is presented in Figure 4.7 with an angle varying between 19° and 29°. It can be seen that, while the angle of attack is varying in time, the output y is almost not deviating from the fixed setpoint of 0.25 or oscillating around it. In Figure 4.8, the angle of attack is varying between 0° and 37°. It can be seen that the output y may deviate from the setpoint but, looking at the control u at the same times, we can see that the control is constant and equal to 1, therefore the actuators do not have enough power to counter this kind of perturbation (very low angle and vortex generators). It can also be seen that,

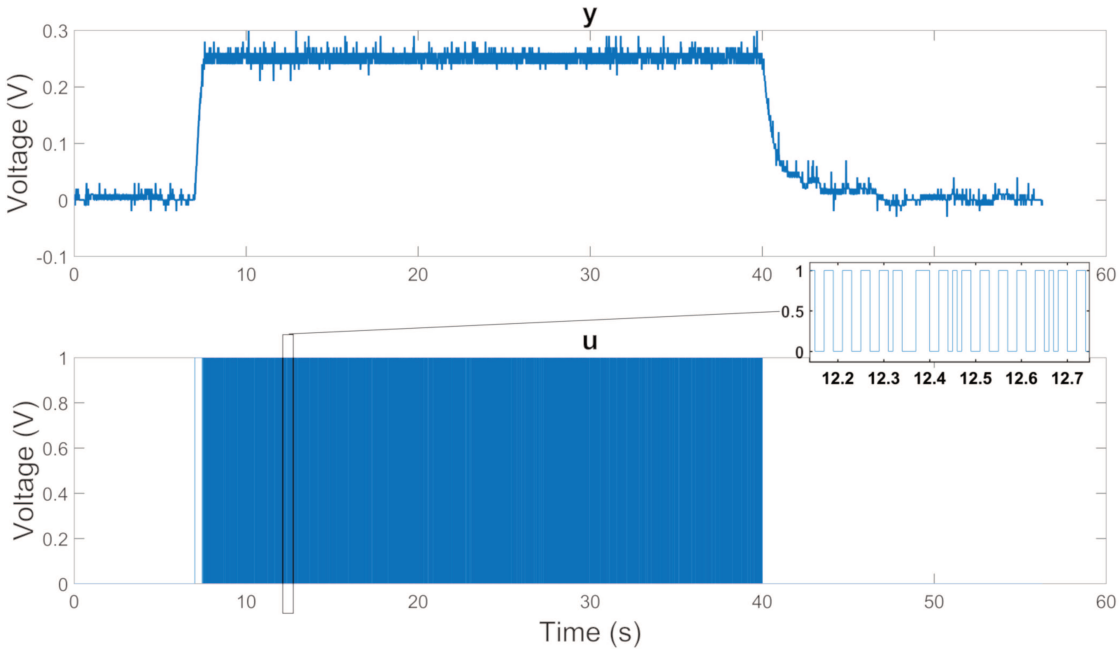

FIGURE 4.3 – Sliding Mode control for the TC II with $y^* = 0.25$V. Flow conditions : $U = 34.5$m/s, $q = 25$g/s, AoA = 24°

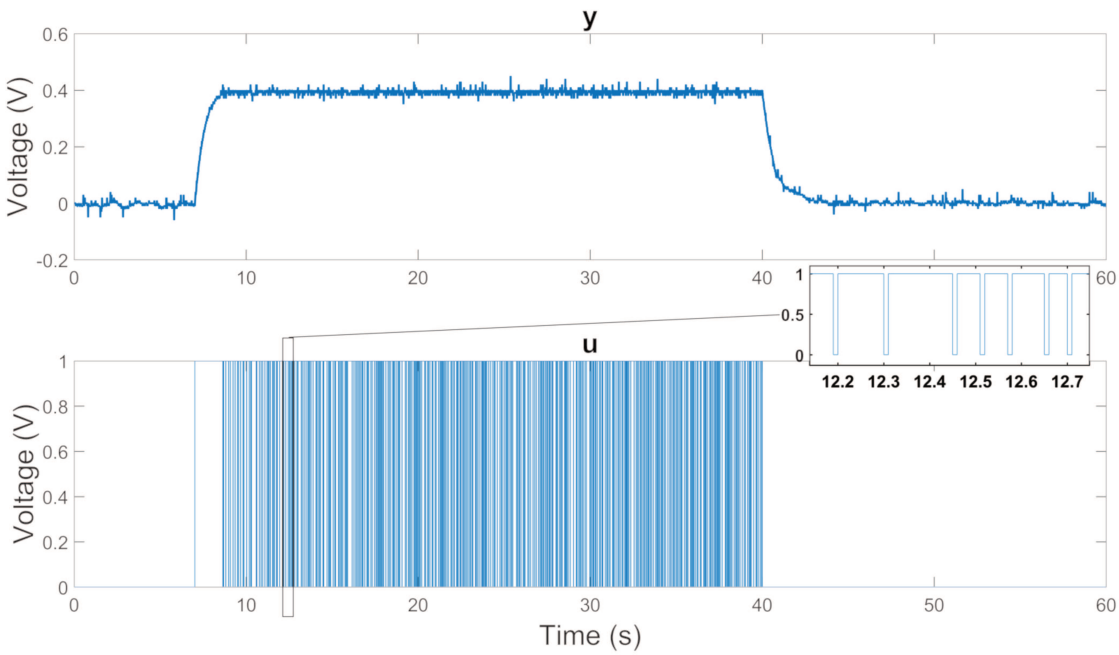

FIGURE 4.4 – Sliding Mode control for the TC II with $y^* = 0.4$V. Flow conditions : $U = 34.5$m/s, $q = 25$g/s, AoA = 24°

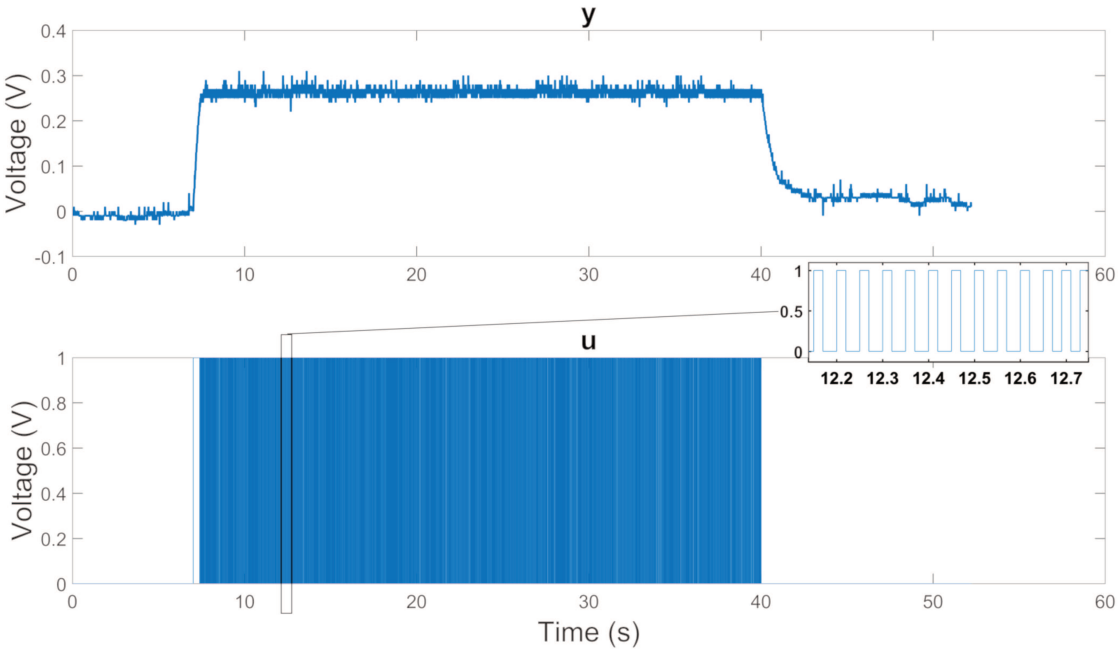

FIGURE 4.5 – Sliding Mode control for the TC II with $y^* = 0.25$V. Flow conditions : $U = 14.5$m/s, $q = 25$g/s, AoA = 24°

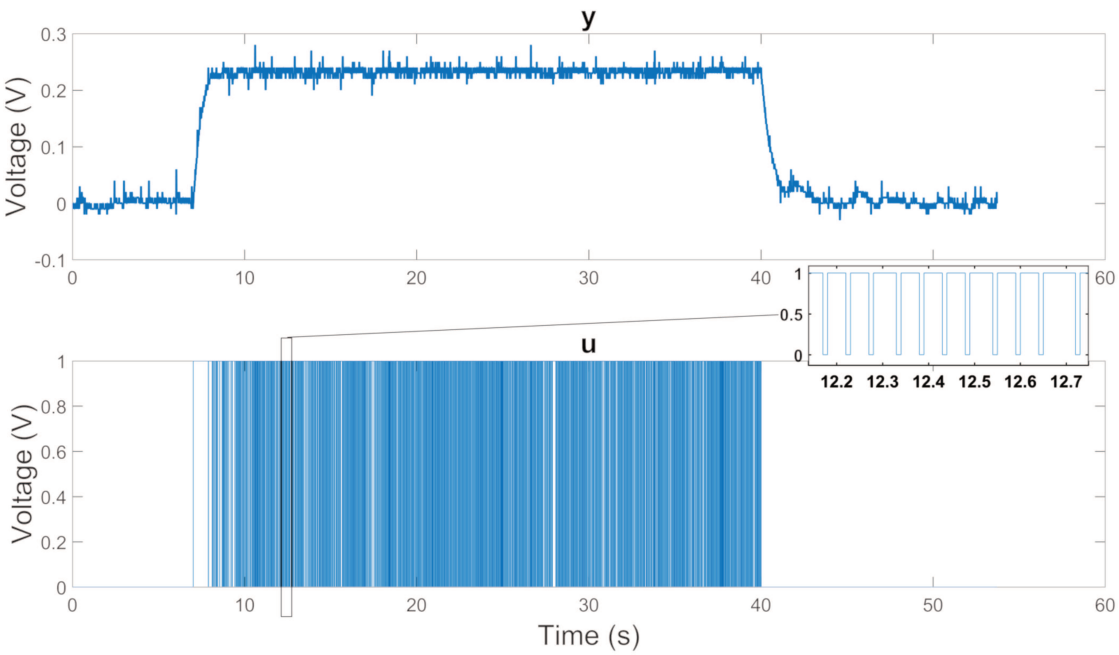

FIGURE 4.6 – Sliding Mode control for the TC II with $y^* = 0.25$V. Flow conditions : $U = 34.5$m/s, $q = 25$g/s, AoA = 10°

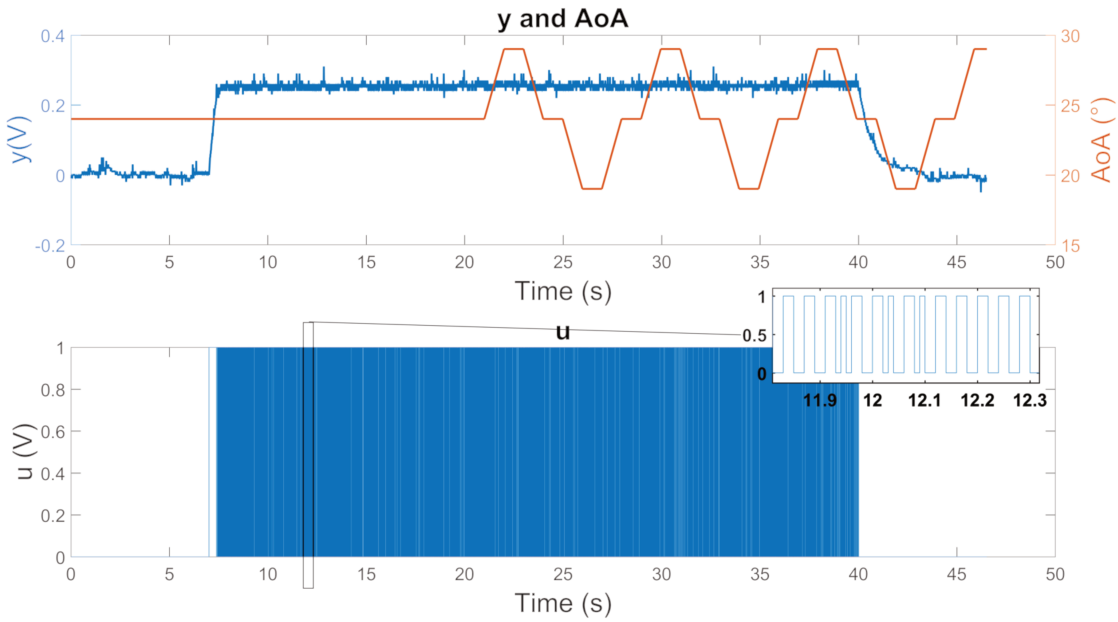

FIGURE 4.7 – Sliding Mode control for the TC II with $y^* = 0.25$V. Flow conditions : $U = 34.5$m/s, $q = 25$g/s, AoA = Time varying

as soon the angle goes above a threshold, the control goes back to the sliding and the output u reaches the setpoint again.

Figure 4.9 shows the results of the control with a time varying angle of attack and vortex generators (VG) placed before the flap. These VGs act here as additional perturbation just upstream the separation line. It can be noticed that there are notable oscillations in the uncontrolled part of the flow (see, for example, the spike around 48s) but that while the SMC is active the influence of the VGs cannot be noticed in the signal y.

Finally, we study the result of the SMC when the mass flow of the actuators is reduced. Figure 4.10 shows the result when $q = 15g/s$ and $y^* = 0.25$. It can be seen that the controller is able to compensate this perturbation as the value of the output reaches the setpoint. In Figure 4.11, we take $y^* = 0.4$ and the controller is not able to reach the setpoint anymore. Looking more closely at the control signal, it can be seen that it is constant and equal to 1, meaning that the actuator does not have a sufficiently strong action on the flow to obtain the required friction gain.

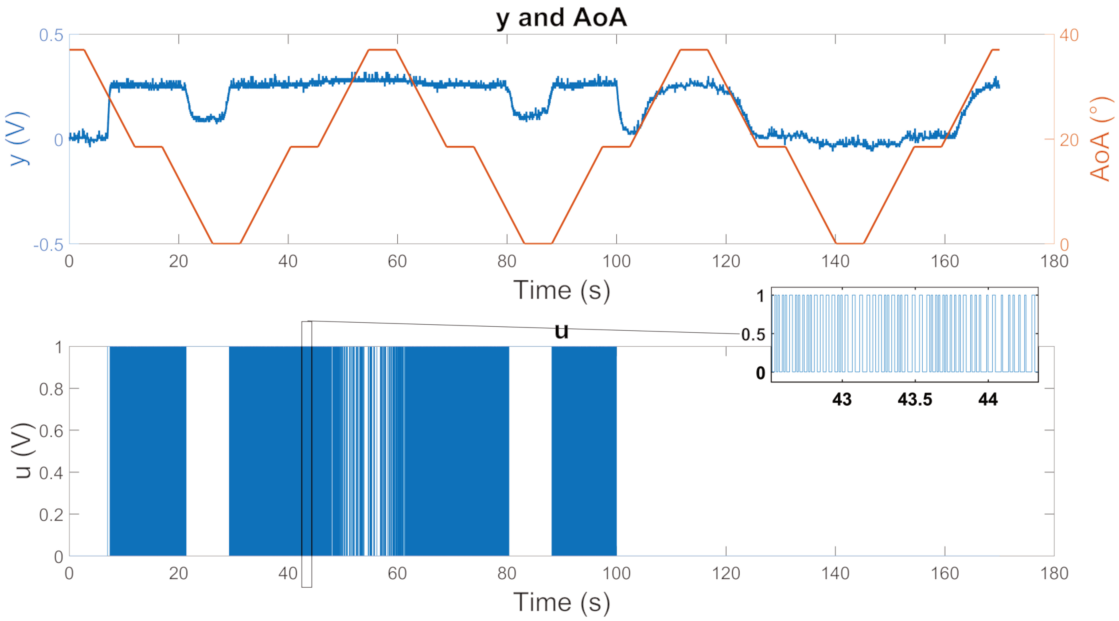

FIGURE 4.8 – Sliding Mode control for the TC II with $y^* = 0.25$V. Flow conditions : $U = 34.5$m/s, $q = 25$g/s, AoA = Time varying

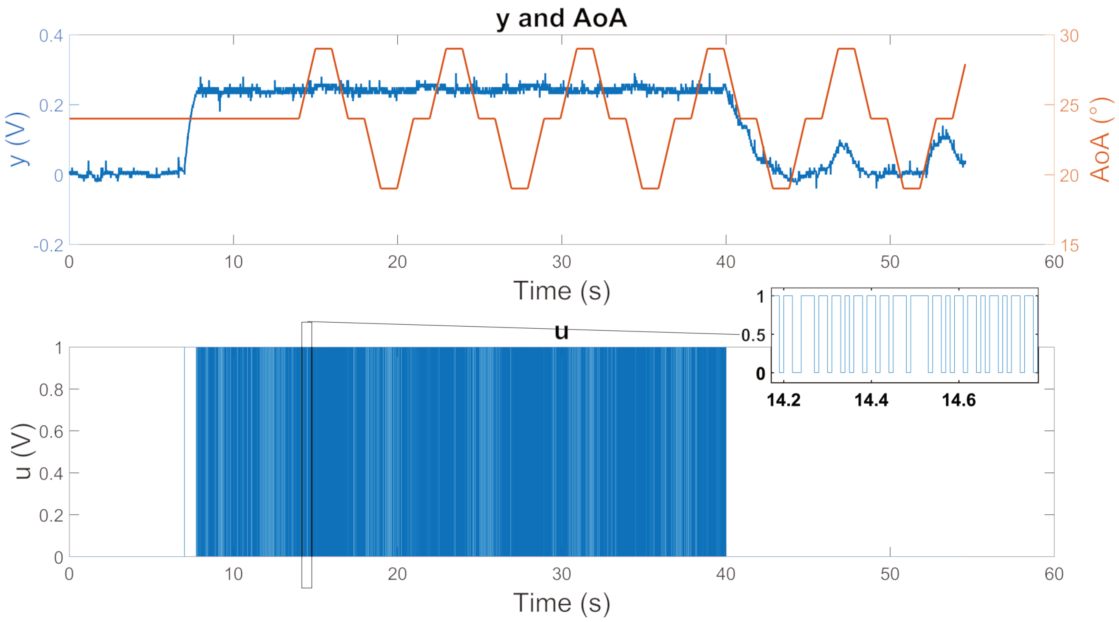

FIGURE 4.9 – Sliding Mode control for the TC II with $y^* = 0.25$V. Flow conditions : $U = 34.5$m/s, $q = 25$g/s, AoA = Time varying, vortex generators placed before the flap

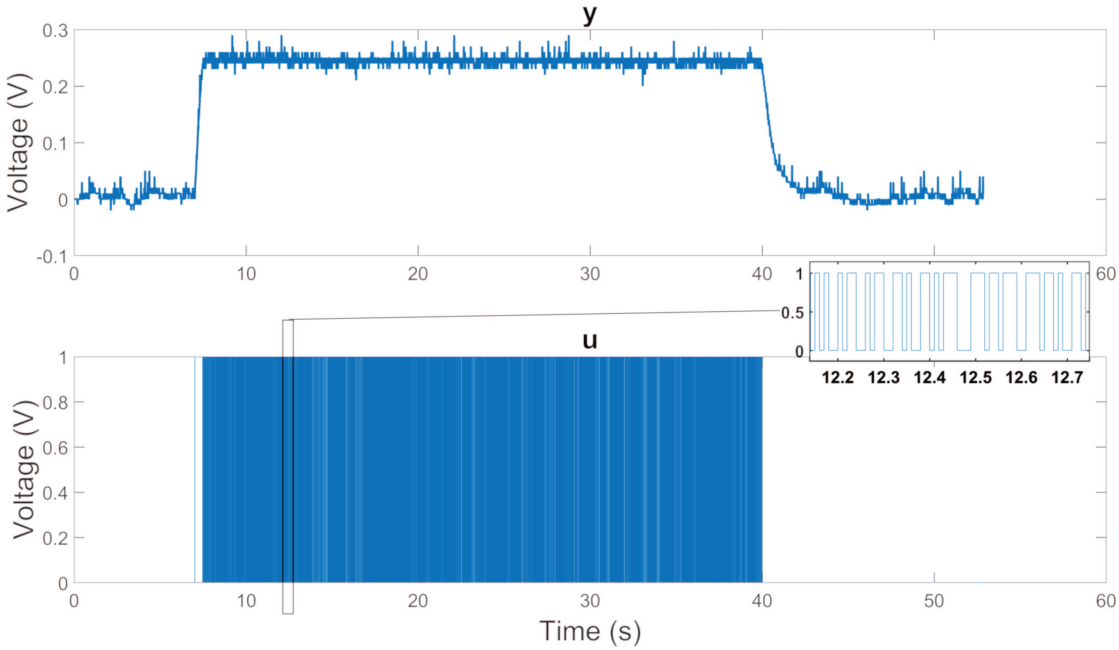

FIGURE 4.10 – Sliding Mode control for the TC II with $y^* = 0.25$V. Flow conditions : $U = 34.5$m/s, $q = 15$g/s, AoA = 24°

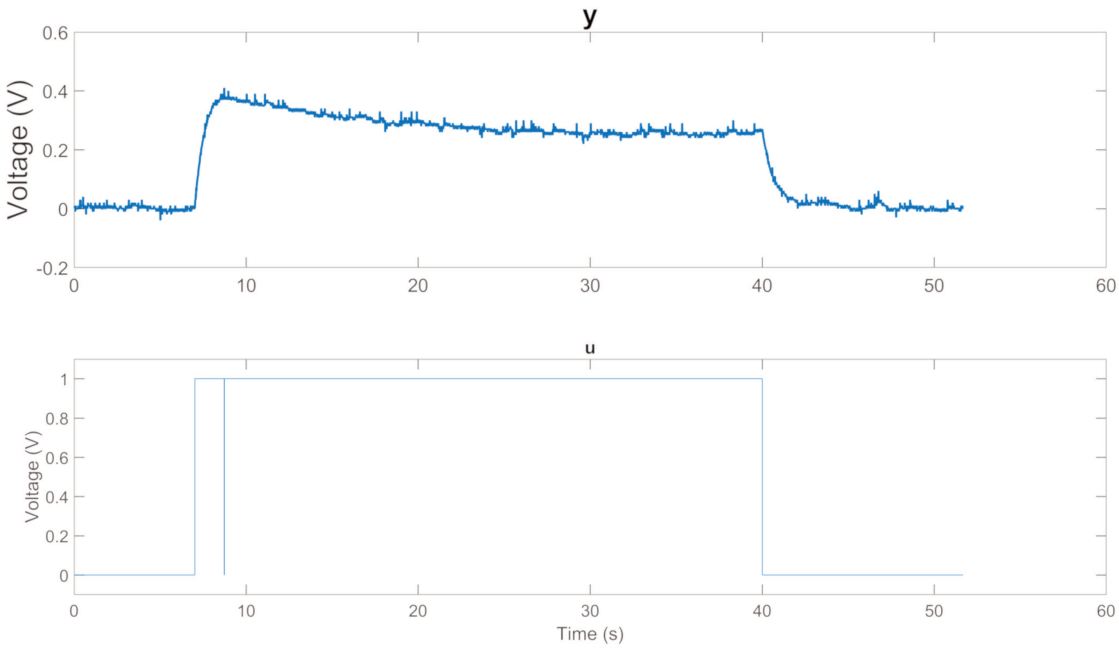

FIGURE 4.11 – Sliding Mode control for the TC II with $y^* = 0.4$V. Flow conditions : $U = 34.5$m/s, $q = 15$g/s, AoA = 24°

4.4.2.2 Tests conducted on TC III

Results of closed-loop control using SMC on TC III are presented in Figure 4.12. In this figure, $DC^* = \frac{1}{T_f}\int_{t-T_f}^{t} b(t)\mathrm{d}t$ is the blowing fraction of the time on the window T_f and corresponds to an extension of the notion of duty cycle to a non-periodic signal. Here, we chose $T_s = 0.3$s. Figure 4.12 presents the results of the application of the Sliding Mode control on the Ahmed body. The reaching and sliding phases are indicated on the figure and separated by vertical dotted lines. The red curve shows the average tendency of the drag F_D. It can be seen that the value of the drag converges to the setpoint s^*.

Figures 4.13 and 4.14 show the result of the control with strong and quasi sinusoidal perturbations in the flow. The perturbation in the p_0 plots represents changes in the upstream pressure and therefore the upstream flow speed. The control u and the blowing fraction DC^* are both found constant and equal to 1 for some period of time, which shows that the actuators are not powerful enough to counter these kinds of perturbation. However, as soon as the perturbation goes below an acceptable threshold, the Sliding Mode occurs again. This proves that, while the control is robust, in the case where the amplitude of the perturbations is too high, the controller will try to compensate the perturbation by keeping the value of the control to 1.

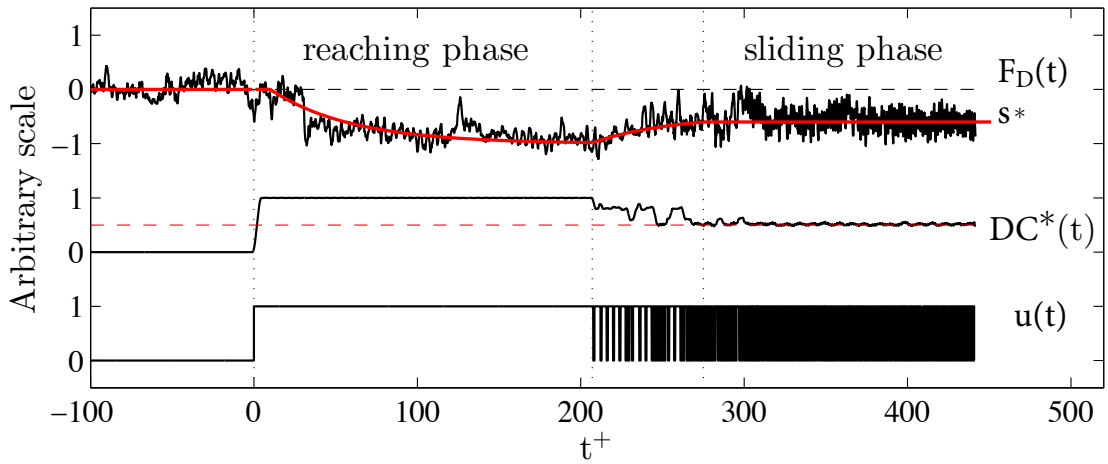

Figure 4.12 – Time evolution of (top) drag, (middle) DC^* and (bottom) control command u obtained using slide mode control. Test Case III.

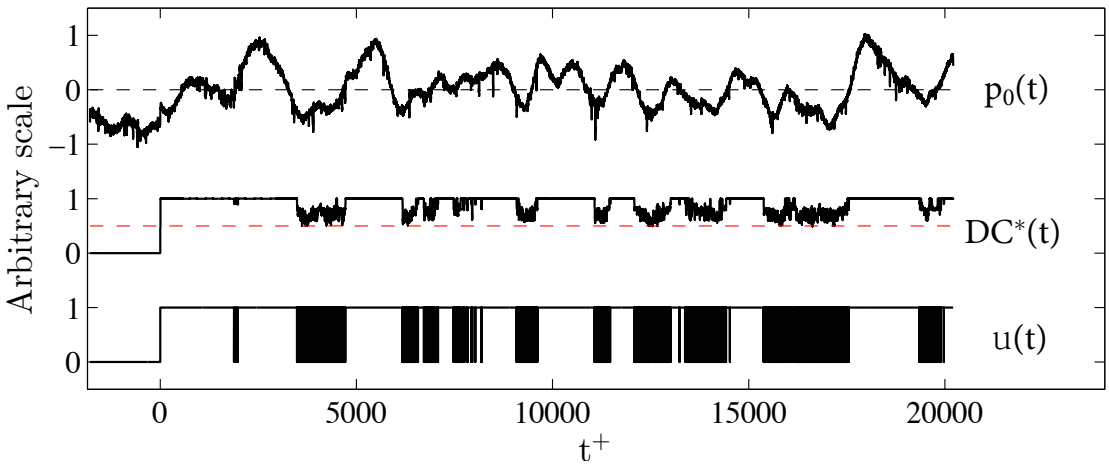

Figure 4.13 – Command law found by the SMC algorithm during a given test sequence for which the pressure measured upstream show significant variations. Test case III.

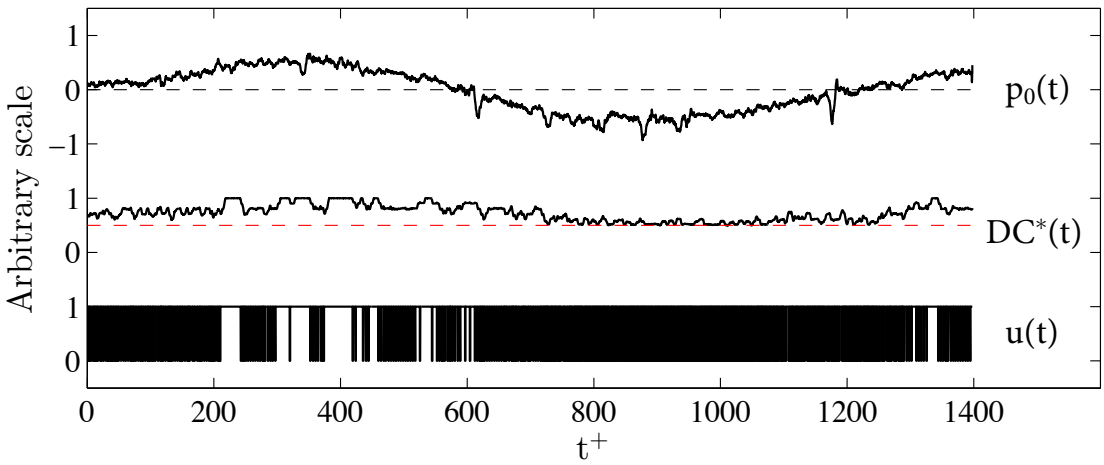

Figure 4.14 – Command law found by the SMC algorithm during a given test sequence for which the pressure measured upstream show quasi sinusoidal variations. Test case III.

Conclusion

This thesis has developed models and active control algorithms for separated flows. The modeling is based on considerations from Fluid Mechanics and Control Theory. The obtained model is used for the design of an optimal open-loop control and a robust feedback control. Of course, in our minds, the most interesting contribution is through the second one, i.e. closed-loop control, which exhibits robustness properties that, to our best knowledge, where not obtained until now, despite the need for it which was depicted in our bibliographic review (Chapter 1).

The models used in this thesis are single-input, single-output (SISO). Their structure is motivated by discretization of the well-known Burgers equation, which is a simplified Navier-Stokes equation. They are bilinear and contain state and input delays, which represents in a simple way the nonlinearities as well as the travel time of information in the flow.

During this research, we had access to three experimental setups belonging to the global platform CONTRAERO (`http://contraero.univ-lille1.fr`), developped by a regional consortium :

— the wind tunnel of LML (high Reynolds number large boundary layer wind-tunnel). In this setup, the flow develops along a slightly inclined flat plate to recover a zero pressure streamwise gradient followed by a inclined flap along which the boundary layer occurs separation and reattaches further downstream to the floor of the wind-tunnel.

— the L2 wind tunnel of ONERA. The flow develops on a test model placed in the center of the wind tunnel between two vertical plates. The test model consists of a flat plate and a plain flap based on a NACA 4412 airfoil shape. The angle of the flap can be adjusted between 2°and 37°.

— the wind tunnel of LAMIH, equipped with an Ahmed body (classically used as a geometric simplification of a car). The model is mounted over a raised floor with a sharp leading-edge to control the boundary layer thickness.

We collected the corresponding data sets either on data acquisition systems (such as PXIe-8102 RT `http://sine.ni.com/nips/cds/view/p/lang/fr/nid/207521` and PXIe-6358 `http://www.ni.com/fr-fr/support/model.pxie-6358.html` from National Instruments) or on an Arduino (`https://www.arduino.cc/`) board which was also used for the control implementation.

Based on analysis of experimental data, two types of such models have been presented. The first one (corresponding to the approximation of Burgers equation) contains constant input delays while the second one has state-dependent input delays. The second is a modification of the first one based on the observation that the experimental data contain such kind of delays.

In our identification process, the delay estimation comes first, and the delay values are then used in the parameter estimation. The delays are obtained through an optimization algorithm. This optimization problem being a mixed integer nonlinear nonconvex problem, specific algorithms have to be employed. The chosen algorithms are NOMAD and Genetic Algorithm as they fulfill the constraints for this optimization and are easily accessible, using Matlab® for example.

The two models are identified and compared using experimental data obtained from the work of [114] on a massively separated turbulent boundary layer. The comparison shows that the model with state-dependent input delays has a better fit to the data but the difference between the two models is generally too small to justify the choice of this model over the one with constant input delay for the design of controllers. The models are also compared to classical ARMAX models and are shown to fit the data more accurately while using the same number of coefficients, or equivalently to use less coefficients for a similar fitting to the data.

Based on the identified models, two controllers are developed. As the actuators considered in this thesis are working as relays (which was the case in the 3 setups), the controls are binary (0 or 1). The first one is an optimal open-loop

control that takes into account the tradeoff between the energy cost of the control and the reattachment of the flow and gives the DC of a square wave depending on the parameters of the model and the frequency of the square wave. It was shown that despite the perturbations in experimental flows and the errors in the modeling, this control does not find the optimal open-loop control signal. The second control is a robust tracking control. This control is based on the Sliding Mode methodology, which involves relay controls and is well-known for its robustness. The conditions for the convergence of the output of the system to the setpoint using this control are obtained and a short proof of perturbation rejection is given. This control has been applied to the two other experimental setups, in the ONERA on a wing-like profile and in the LAMIH on an Ahmed body. It has shown to correctly steer the output to the setpoint, to be computationally cheap (Arduino), to have fast response to a change in the flow and great robustness over a wide range of various experimental conditions (speed, shape of the obstacle, mass flow of the actuators).

Perspectives for future works first include the extension of the feedback control to the case of multiple inputs multiple outputs (MIMO) models. This would, for example, be applicable to the Ahmed body in order to control both the drag, drift and lift using multiple actuators placed in several non-parallel axis. The control could also consider other types of input such as the actuator supply pressure. Another perspective is the use of partial differential equations (PDE) and some newly developed observers and controllers (see [84] for an observer applied to parabolic PDEs, or [109, 108] for finite-time control of evolution equations such as Burgers equation) for PDE in order to get information about the flow and control it without having to use models that are too simplified and fail to reproduce some characteristics of the flow (i.e. turbulence, vortices, solitons). Other robustness formulations than additive perturbation can be considered to cover a wider range of possible perturbation signals. A frequency analysis of the control signals should be done in order to identify if the controller focuses on natural frequencies of the flow (such as Kelvin-Helmholtz, vortex shedding). Finally, an extensive study of both SMC and MLC would allow to compare their efficiency and adaptability as well as the time required for the controller design and their computational cost.

Bibliography

[1] Ravi P. Agarwal et al. *Nonoscillation Theory of Functional Differential Equations with Applications*. en. New York, NY : Springer New York, 2012. isbn : 978-1-4614-3454-2 978-1-4614-3455-9.

[2] S. R. Ahmed, G. Ramm et G. Faltin. *Some Salient Features Of The Time-Averaged Ground Vehicle Wake*. English. SAE Technical Paper 840300. Warrendale, PA : SAE Technical Paper, fév. 1984. doi : 10.4271/840300. url : http://papers.sae.org/840300/.

[3] H. Akaike. « A new look at the statistical model identification ». In : *IEEE Transactions on Automatic Control* 19.6 (déc. 1974), p. 716–723. issn : 0018-9286. doi : 10.1109/TAC.1974.1100705.

[4] Michael Amitay et al. « Aerodynamic Flow Control over an Unconventional Airfoil Using Synthetic Jet Actuators ». In : *AIAA Journal* 39.3 (2001), p. 361–370. issn : 0001-1452. doi : 10.2514/2.1323. url : https://doi.org/10.2514/2.1323.

[5] Z. Artstein. « Linear systems with delayed controls : A reduction ». In : *IEEE Transactions on Automatic Control* 27.4 (août 1982), p. 869–879. issn : 0018-9286. doi : 10.1109/TAC.1982.1103023.

[6] Karl J. Åström et Björn Wittenmark. *Adaptive Control : Second Edition*. en. Google-Books-ID : 4CLCAgAAQBAJ. Courier Corporation, avr. 2013. isbn : 978-0-486-31914-8.

[7] Karl Johan Åström et Tore Hägglund. *PID controllers : theory, design, and tuning*. T. 2. Isa Research Triangle Park, NC, 1995.

[8] Carolyn D Aubertine et John K Eaton. « Turbulence development in a non-equilibrium turbulent boundary layer with mild adverse pressure gradient ». In : *Journal of Fluid Mechanics* 532 (2005), p. 345–364. issn : 1469-7645.

[9] Nadine Aubry et al. « The dynamics of coherent structures in the wall region of a turbulent boundary layer ». In : *Journal of Fluid Mechanics* 192 (juil. 1988), p. 115–173. issn : 1469-7645, 0022-1120. doi : 10.1017/S0022112088001818. url : https://www.cambridge.org/core/journals/journal-of-fluid-mechanics/article/the-dynamics-of-coherent-structures-in-the-wall-region-of-a-turbulent-boundary-layer/717E2487A5A758FF9321242328FB8FAC.

[10] C. Audet et J. Dennis. « Mesh Adaptive Direct Search Algorithms for Constrained Optimization ». In : *SIAM Journal on Optimization* 17.1 (jan. 2006), p. 188–217. issn : 1052-6234. doi : 10.1137/040603371.

[11] Charles Audet, Vincent Béchard et Sébastien Le Digabel. « Nonsmooth optimization through Mesh Adaptive Direct Search and Variable Neighborhood Search ». en. In : *Journal of Global Optimization* 41.2 (oct. 2007), p. 299–318. issn : 0925-5001, 1573-2916. doi : 10.1007/s10898-007-9234-1.

[12] Charles Audet, J. E. Dennis Jr et Sébastien Le Digabel. « Globalization strategies for Mesh Adaptive Direct Search ». en. In : *Computational Optimization and Applications* 46.2 (juin 2009), p. 193–215. issn : 0926-6003, 1573-2894. doi : 10.1007/s10589-009-9266-1.

[13] Diogo Barros et al. « Bluff body drag manipulation using pulsed jets and Coanda effect ». In : *Journal of Fluid Mechanics* 805 (oct. 2016), p. 422–459. issn : 0022-1120, 1469-7645. doi : 10.1017/jfm.2016.508.

[14] Michael Basin, Jesus Rodriguez-Gonzalez et Leonid Fridman. « Optimal and robust control for linear state-delay systems ». In : *Journal of the Franklin Institute* 344.6 (sept. 2007), p. 830–845. issn : 0016-0032. doi : 10.1016/j.jfranklin.2006.10.002. url : http://www.sciencedirect.com/science/article/pii/S0016003206001426.

[15] M. Bergmann et L. Cordier. « Optimal control of the cylinder wake in the laminar regime by trust-region methods and POD reduced-order models ». In : *Journal of Computational Physics* 227.16 (août 2008), p. 7813–7840. issn : 0021-9991. doi : 10.1016/j.jcp.2008.04.034. url : http://www.sciencedirect.com/science/article/pii/S0021999108002659.

[16] Christopher M Bishop. *Pattern recognition and machine learning*. springer, 2006. isbn : 0-387-31073-8.

[17] Caroline Braud et Arthur Dyment. « Model of an impulsive subsonic jet actuator for flow control applications ». In : *Physics of Fluids* 24.4 (avr. 2012), p. 047102. issn : 1070-6631. doi : 10.1063/1.3701377. url : http://aip.scitation.org/doi/abs/10.1063/1.3701377.

[18] Coleman Brosilow et Babu Joseph. *Techniques of Model-based Control*. en. Google-Books-ID : R05I3cqzPWYC. Prentice Hall Professional, 2002. isbn : 978-0-13-028078-7.

[19] Steven L. Brunton et Bernd R. Noack. « Closed-Loop Turbulence Control : Progress and Challenges ». In : *Applied Mechanics Reviews* 67.5 (août 2015), p. 050801–050801. issn : 0003-6900. doi : 10.1115/1.4031175. url : http://dx.doi.org/10.1115/1.4031175.

[20] J. M. Burgers. « A Mathematical Model Illustrating the Theory of Turbulence ». In : *Advances in Applied Mechanics*. Sous la dir. de Richard Von Mises et Theodore Von Kármán. T. 1. Elsevier, jan. 1948, p. 171–199. doi : 10.1016/S0065-2156(08)70100-5. url : http://www.sciencedirect.com/science/article/pii/S0065215608701005.

[21] Louis N. Cattafesta III et al. « Active control of flow-induced cavity oscillations ». In : *Progress in Aerospace Sciences* 44.7–8 (oct. 2008), p. 479–502. issn : 0376-0421. doi : 10.1016/j.paerosci.2008.07.002. url : //www.sciencedirect.com/science/article/pii/S0376042108000584.

[22] Jean Cea. « Approximation variationnelle des problèmes aux limites ». In : *Annales de l'institut Fourier* 14.2 (1964), p. 345–444. issn : 0373-0956. doi : 10.5802/aif.181. url : http://aif.cedram.org/item?id=AIF_1964__14_2_345_0.

[23] Timothee Chabert. *Contrôle expérimental en boucle fermée du décollement sur un volet*. Paris 6, jan. 2014. url : http://www.theses.fr/2014PA066011.

[24] Timothée Chabert, Julien Dandois et Éric Garnier. « Experimental closed-loop control of flow separation over a plain flap using slope seeking ». In : *Experiments in Fluids* 55.8 (2014), p. 1–19.

[25] Timothée Chabert et al. « Experimental detection of flow separation over a plain flap by wall shear stress analysis with and without steady blowing ». In : *Comptes Rendus Mécanique* 342.6 (2014), p. 389–402.

[26] S. Chen et S. A. Billings. « Representations of non-linear systems : the NARMAX model ». In : *International Journal of Control* 49.3 (mar. 1989), p. 1013–1032. issn : 0020-7179. doi : 10.1080/00207178908559683.

[27] Stephen L. Chiu. « Fuzzy Model Identification Based on Cluster Estimation ». In : *Journal of Intelligent & Fuzzy Systems* 2.3 (jan. 1994), p. 267–278. issn : 1064-1246. doi : 10.3233/IFS-1994-2306. url : http://content.iospress.com/articles/journal-of-intelligent-and-fuzzy-systems/ifs2-3-06.

[28] K. B. Chun et H. J. Sung. « Control of turbulent separated flow over a backward-facing step by local forcing ». en. In : *Experiments in Fluids* 21.6 (nov. 1996), p. 417–426. issn : 0723-4864, 1432-1114. doi : 10.1007/BF00189044.

[29] Donald Coles. « The law of the wake in the turbulent boundary layer ». In : *Journal of Fluid Mechanics* 1.2 (juil. 1956), p. 191–226. issn : 1469-7645, 0022-1120. doi : 10.1017/S0022112056000135. url : https://www.cambridge.org/core/journals/journal-of-fluid-mechanics/article/the-law-of-the-wake-in-the-turbulent-boundary-layer/909F95C7270EDC37F2E750C04FCD75BD.

[30] Andrew Conn, Katya Scheinberg et Luis N. Vicente. *Introduction to derivative-free optimization, MPS-SIAM series on Optimization*. Jan. 2009. isbn : 0-89871-668-3 978-0-89871-668-9. doi : 10.1137/1.9780898718768.

[31] Peter Constantin et Ciprian Foias. *Navier-stokes equations*. University of Chicago Press, 1988. isbn : 0-226-11549-6.

[32] Thomas Corke et Martiqua Post. « Overview of Plasma Flow Control : Concepts, Optimization, and Applications ». In : *43rd AIAA Aerospace Sciences Meeting and Exhibit*. American Institute of Aeronautics et Astronautics. doi : 10.2514/6.2005-563. url : https://arc.aiaa.org/doi/abs/10.2514/6.2005-563.

[33] Thomas C. Corke, C. Lon Enloe et Stephen P. Wilkinson. « Dielectric Barrier Discharge Plasma Actuators for Flow Control ». In : *Annual Review of Fluid Mechanics* 42.1 (2010), p. 505–529. doi : 10.1146/annurev-fluid-121108-145550. url : https://doi.org/10.1146/annurev-fluid-121108-145550.

[34] Jonathan Currie et David I. Wilson. « OPTI : Lowering the Barrier Between Open Source Optimizers and the Industrial MATLAB User ». In : *Foundations of Computer-Aided Process Operations*. Sous la dir. de Nick Sahinidis et Jose Pinto. Savannah, Georgia, USA, jan. 2012.

[35] C. Cuvier et al. « Characterisation of a high Reynolds number boundary layer subject to pressure gradient and separation ». In : *Journal of Turbulence* 15.8 (août 2014), p. 473–515. doi : 10.1080/14685248.2014.914217. url : http://dx.doi.org/10.1080/14685248.2014.914217.

[36] Christophe Cuvier. *Contrôle actif du décollement d'une couche limite turbulente en gradient de pression adverse*. Ecole centrale de Lille, sept. 2012. url : http://www.theses.fr/2012ECLI0015.

[37] J Dandois, E Garnier et P-Y Pamart. « NARX modelling of unsteady separation control ». In : *Experiments in fluids* 54.2 (2013), p. 1–17.

[38] A. Darabi et I. Wygnanski. « Active management of naturally separated flow over a solid surface. Part 1. The forced reattachment process ». In : *Journal of Fluid Mechanics* 510 (juil. 2004), p. 105–129. issn : 1469-7645, 0022-1120. doi : 10.1017/S0022112004009231.

[39] E. Brian Davies. *Linear Operators and their Spectra*. en. Google-Books-ID : 6AjuCoaL34AC. Cambridge CB2 2RU, UK : Cambridge University Press, avr. 2007. isbn : 978-1-139-46433-8.

[40] L. (ed) Davis. *Handbook of genetic algorithms*. 1991. url : http://papers.cumincad.org/cgi-bin/works/Show?eaca.

[41] Antoine Debien et al. « Closed-loop separation control over a sharp edge ramp using genetic programming ». en. In : *Experiments in Fluids* 57.3 (mar. 2016), p. 40. issn : 0723-4864, 1432-1114. doi : 10.1007/s00348-016-2126-8. url : http://link.springer.com/article/10.1007/s00348-016-2126-8.

[42] Lokenath Debnath. *Nonlinear Partial Differential Equations for Scientists and Engineers*. en. Google-Books-ID : Ir4yXgBesAsC. Springer Science & Business Media, oct. 2011. isbn : 978-0-8176-8265-1.

[43] J. Delville et al. « Examination of large-scale structures in a turbulent plane mixing layer. Part 1. Proper orthogonal decomposition ». In : *Journal of Fluid Mechanics* 391 (juil. 1999), p. 91–122. issn : 1469-7645, 0022-1120. doi : 10.1017/S0022112099005200.

[44] Richard O. Duda, Peter E. Hart et David G. Stork. *Pattern Classification*. en. Google-Books-ID : Br33IRC3PkQC. John Wiley & Sons, nov. 2012. isbn : 978-1-118-58600-6.

[45] Thomas Duriez, Steven Brunton et Bernd R. Noack. *Machine Learning Control – Taming Nonlinear Dynamics and Turbulence*. en. Google-Books-ID : CxNuDQAAQBAJ. Springer, nov. 2016. isbn : 978-3-319-40624-4.

[46] C. Edwards et S. Spurgeon. *Sliding Mode Control : Theory And Applications*. en. Google-Books-ID : uH2RJhIPsiYC. London EC4A 3DE, UK : CRC Press, août 1998. isbn : 978-0-7484-0601-2.

[47] Denis Efimov et al. « Delay-Dependent Positivity : Application to Interval Observers ». en. In : juil. 2015. url : https://hal.inria.fr/hal-01140336/document.

[48] M. España et I. D. Landau. « Reduced order bilinear models for distillation columns ». In : *Automatica* 14.4 (juil. 1978), p. 345–355. issn : 0005-1098. doi : 10.1016/0005-1098(78)90034-1. url : http://www.sciencedirect.com/science/article/pii/0005109878900341.

[49] Fawzi Fadla. « Caractérisation expérimentale de la dynamique du décollement de couche limite induit par un gradient de pression adverse et un effet de courbure ». fr. Thèse de doct. Université de Valenciennes et du Hainaut-Cambresis, sept. 2014. URL : https://tel.archives-ouvertes.fr/tel-01206111/document.

[50] Julien Favier et al. « Passive separation control using a self-adaptive hairy coating ». In : *Journal of Fluid Mechanics* 627 (mai 2009), p. 451–483. ISSN : 1469-7645, 0022-1120. DOI : 10.1017/S0022112009006119. URL : https://www.cambridge.org/core/journals/journal-of-fluid-mechanics/article/passive-separation-control-using-a-self-adaptive-hairy-coating/D57BDEAB405629B48AB60FCD40A1D2B9.

[51] W. Favoreel, B. De Moor et P. Van Overschee. « Subspace identification of bilinear systems subject to white inputs ». In : *IEEE Transactions on Automatic Control* 44.6 (juin 1999), p. 1157–1165. ISSN : 0018-9286. DOI : 10.1109/9.769370.

[52] Maxime Feingesicht et al. « A bilinear input-output model with state-dependent delay for separated flow control ». en. In : juin 2016. URL : https://hal.inria.fr/hal-01298166/document.

[53] Maxime Feingesicht et al. « Model-Based Feedforward Optimal Control applied to a Turbulent Separated Flow ». en. In : juil. 2017, p. 6. URL : https://hal.inria.fr/hal-01546424/document.

[54] M. Fiebig, A. Valencia et N. K. Mitra. « Wing-type vortex generators for fin-and-tube heat exchangers ». In : *Experimental Thermal and Fluid Science* 7.4 (nov. 1993), p. 287–295. ISSN : 0894-1777. DOI : 10.1016/0894-1777(93)90052-K. URL : http://www.sciencedirect.com/science/article/pii/089417779390052K.

[55] F. E. Fish et G. V. Lauder. « Passive and Active Flow Control by Swimming Fishes and Mammals ». In : *Annual Review of Fluid Mechanics* 38.1 (2006), p. 193–224. DOI : 10.1146/annurev.fluid.38.050304.092201. URL : http://dx.doi.org/10.1146/annurev.fluid.38.050304.092201.

[56] P. J Fleming et R. C Purshouse. « Evolutionary algorithms in control systems engineering : a survey ». In : *Control Engineering Practice* 10.11 (nov. 2002), p. 1223–1241. ISSN : 0967-0661. DOI : 10.1016/S0967-0661(02)00081-3. URL : http://www.sciencedirect.com/science/article/pii/S0967066102000813.

[57] Michel Fliess et Cédric Join. « Model-free control ». en. In : *International Journal of Control* 86.12 (déc. 2013), p. 2228–2252. doi : 10.1080/00207179.2013.810345. url : https://hal-polytechnique.archives-ouvertes.fr/hal-00828135/document.

[58] Emilia Fridman. *Introduction to Time-Delay Systems : Analysis and Control*. en. Basel, Switzerland : Birkhäuser, sept. 2014. isbn : 978-3-319-09393-2.

[59] L. Fridman, P. Acosta et A. Polyakov. « Robust eigenvalue assignment for uncertain delay control systems ». In : *Proc. 3rd IFAC Workshop on Time Delay Systems*. Santa Fe, New Mexico, USA, 2001, p. 239–244.

[60] François Gallaire, Matthieu Marquillie et Uwe Ehrenstein. « Three-dimensional transverse instabilities in detached boundary layers ». In : *Journal of Fluid Mechanics* 571 (jan. 2007), p. 221–233. issn : 1469-7645, 0022-1120. doi : 10.1017/S0022112006002898.

[61] William K George. « Is there a universal log law for turbulent wall-bounded flows ? » In : *Philosophical Transactions of the Royal Society of London A : Mathematical, Physical and Engineering Sciences* 365.1852 (2007), p. 789–806. issn : 1364-503X.

[62] William K George. « Lectures in Turbulence for the 21st Century ». In : *Chalmers University of Technology* (2013).

[63] William K George. « Recent advancements toward the understanding of turbulent boundary layers ». In : *AIAA journal* 44.11 (2006), p. 2435. issn : 0001-1452.

[64] Cécile Ghouila-Houri et al. « High temperature gradient calorimetric wall shear stress micro-sensor for flow separation detection ». In : *Sensors and Actuators A : Physical* 266.Supplement C (oct. 2017), p. 232–241. issn : 0924-4247.

[65] Cécile Ghouila-Houri et al. « Wall Shear Stress Calorimetric Micro-Sensor Designed for Flow Separation Detection and Active Flow Control ». en. In : *Proceedings* 1.4 (août 2017), p. 376.

[66] Ari Glezer et Michael Amitay. « Synthetic Jets ». In : *Annual Review of Fluid Mechanics* 34.1 (2002), p. 503–529. doi : 10.1146/annurev.fluid.34.090501.094913. url : http://dx.doi.org/10.1146/annurev.fluid.34.090501.094913.

[67] G. Godard et M. Stanislas. « Control of a decelerating boundary layer. » In : *Aerospace Science and Technology* 10 (avr. 2006). issn : 1270-9638. doi : 10.1016/j.ast.2005.11.007. url : http://www.sciencedirect.com/science/article/pii/S127096380500163X.

[68] Mark Goldhammer. « The next decade in commercial aircraft aerodynamics : a Boeing perspective ». In : 2009.

[69] G. H. Golub et C. Reinsch. « Singular value decomposition and least squares solutions ». en. In : *Numerische Mathematik* 14.5 (avr. 1970), p. 403–420. issn : 0029-599X, 0945-3245. doi : 10.1007/BF02163027. url : https://link.springer.com/article/10.1007/BF02163027.

[70] Graham Clifford Goodwin, Stefan F. Graebe et Mario E. Salgado. *Control System Design*. en. Google-Books-ID : 7dNSAAAAMAAJ. Prentice Hall, 2001. isbn : 978-0-13-958653-8.

[71] Laurent Graftieaux, Marc Michard et Nathalie Grosjean. « Combining PIV, POD and vortex identification algorithms for the study of unsteady turbulent swirling flows ». en. In : *Measurement Science and Technology* 12.9 (2001), p. 1422. issn : 0957-0233. doi : 10.1088/0957-0233/12/9/307. url : http://stacks.iop.org/0957-0233/12/i=9/a=307.

[72] Max D. Gunzburger. *Perspectives in Flow Control and Optimization*. Philadelphia, PA, USA : Society for Industrial et Applied Mathematics, 2002. isbn : 978-0-89871-527-9.

[73] Mohamed Gad-el Hak. *Flow Control : Passive, Active, and Reactive Flow Management*. en. Google-Books-ID : 1IiFetRXG3kC. Cambridge CB2 2RU, UK : Cambridge University Press, 2006. isbn : 978-0-521-03671-9.

[74] Jack K. Hale. « Caratheodory Conditions ». en. In : *Functional Differential Equations*. Applied Mathematical Sciences 3. Springer US, 1971, p. 30–31. isbn : 978-0-387-90023-0 978-1-4615-9968-5. doi : 10.1007/978-1-4615-9968-5_7.

[75] Aurelien Hervé et al. « A physics-based approach to flow control using system identification ». In : *Journal of Fluid Mechanics* 702 (juil. 2012), p. 26–58. issn : 1469-7645, 0022-1120. doi : 10.1017/jfm.2012.112.

[76] Raymond M. Hicks et Preston A. Henne. « Wing Design by Numerical Optimization ». In : *Journal of Aircraft* 15.7 (1978), p. 407–412. issn : 0021-8669. doi : 10.2514/3.58379. url : https://doi.org/10.2514/3.58379.

[77] Alberto Isidori. *Nonlinear Control Systems*. en. Springer Science & Business Media, avr. 2013. isbn : 978-1-84628-615-5.

[78] Z.-P. Jiang, A. R. Teel et L. Praly. « Small-gain theorem for ISS systems and applications ». en. In : *Mathematics of Control, Signals and Systems* 7.2 (juin 1994), p. 95–120. issn : 0932-4194, 1435-568X. doi : 10.1007/BF01211469. url : https://link.springer.com/article/10.1007/BF01211469.

[79] LV Kantorovich et GP Akilov. *Functional Analysis. 1982*. Pergamon Press, Oxford, 1982.

[80] J. Kautsky, N. K. Nichols et P. VAN Dooren. « Robust pole assignment in linear state feedback ». In : *International Journal of Control* 41.5 (mai 1985), p. 1129–1155. issn : 0020-7179. doi : 10.1080/0020718508961188.

[81] Hassan K. Khalil. *Nonlinear Systems*. en. Google-Books-ID : v_BjPQAACAAJ. Prentice Hall, 2000. isbn : 978-0-13-122740-8.

[82] Hassan K. Khalil. *Nonlinear Systems*. en. Google-Books-ID : t_d1QgAACAAJ. Prentice Hall, 2002. isbn : 978-0-13-067389-3.

[83] Rehan Salahuddin Khan et Sudhakar Umale. « CFD aerodynamic analysis of Ahmed body ». In : *International Journal of Engineering Trends and Technology (IJETT)* 18.7 (2014), p. 301–308.

[84] Tatiana Kharkovskaia et al. « On design of interval observers for parabolic PDEs ». en. In : juil. 2017. url : https://hal.inria.fr/hal-01508773/document.

[85] S. J. Kline et al. « The structure of turbulent boundary layers ». In : *Journal of Fluid Mechanics* 30.4 (déc. 1967), p. 741–773. issn : 1469-7645, 0022-1120. doi : 10.1017/S0022112067001740.

[86] Dr D. J. Korteweg et Dr G. de Vries. « On the change of form of long waves advancing in a rectangular canal, and on a new type of long stationary waves ». In : *Philosophical Magazine* 39.240 (mai 1895), p. 422–443. issn : 1941-5982. doi : 10.1080/14786449508620739. url : http://dx.doi.org/10.1080/14786449508620739.

[87] Miroslav Krstic, Ioannis Kanellakopoulos et Peter V. Kokotovic. *Nonlinear and adaptive control design*. 1995. url : http://cds.cern.ch/record/289254.

[88] Sébastien Le Digabel. « Algorithm 909 : NOMAD : Nonlinear optimization with the MADS algorithm ». In : *ACM Transactions on Mathematical Software (TOMS)* 37.4 (2011), p. 1–15.

[89] Chester Lee et al. « A piezoelectrically actuated micro synthetic jet for active flow control ». In : *Sensors and Actuators A : Physical*. Selected Papers from the Pacific Rim Workshop on Transducers and Micro/Nano Technologies 108.1–3 (nov. 2003), p. 168–174. issn : 0924-4247. doi : 10.1016/S0924-4247(03)00267-X. url : http://www.sciencedirect.com/science/article/pii/S092442470300267X.

[90] John C Lin. « Review of research on low-profile vortex generators to control boundary-layer separation ». In : *Progress in Aerospace Sciences* 38.4 (mai 2002), p. 389–420. issn : 0376-0421. doi : 10.1016/S0376-0421(02)00010-6. url : http://www.sciencedirect.com/science/article/pii/S0376042102000106.

[91] F.J. Lisy et R.N. Schmidt. « Deployable flow control device ». In : (août 2000). url : https://www.google.com/patents/US6105904.

[92] Lennart Ljung. *System identification - Theory for the User*. Prentice-Hall, 1999.

[93] Francisco Lopez-Ramirez et al. « Fixed-time output stabilization of a chain of integrators ». In : *Decision and Control (CDC), 2016 IEEE 55th Conference on*. IEEE, 2016, p. 3886–3891. url : http://ieeexplore.ieee.org/abstract/document/7798856/.

[94] R. Lozano et B. Brogliato. « Adaptive control of robot manipulators with flexible joints ». In : *IEEE Transactions on Automatic Control* 37.2 (fév. 1992), p. 174–181. issn : 0018-9286. doi : 10.1109/9.121619.

[95] J. L. Lumley. « The structure of inhomogeneous turbulent flows ». In : *Atmospheric Turbulence and Radio Wave Propagation* (1967). url : http://ci.nii.ac.jp/naid/10012381873/.

[96] A. R. Mitchell et D. F. Griffiths. *The finite difference method in partial differential equations*. John Wiley, 1980. isbn : 978-0-471-27641-8. url : https://infoscience.epfl.ch/record/60388.

[97] Rajat Mittal, Rupesh Kotapati et Louis Cattafesta. « Numerical Study of Resonant Interactions and Flow Control in a Canonical Separated Flow ». en. In : American Institute of Aeronautics et Astronautics, jan. 2005. isbn : 978-1-62410-064-2. doi : 10.2514/6.2005-1261. url : http://arc.aiaa.org/doi/10.2514/6.2005-1261.

[98] Bijan Mohammadi et and Olivier Pironneau. « Shape Optimization in Fluid Mechanics ». In : *Annual Review of Fluid Mechanics* 36.1 (2004), p. 255–279. doi : 10.1146/annurev.fluid.36.050802.121926. url : https://doi.org/10.1146/annurev.fluid.36.050802.121926.

[99] Bijan Mohammadi et Olivier Pironneau. *Applied Shape Optimization for Fluids*. en. Google-Books-ID : _wwUDAAAQBAJ. Oxford University Press, 2010. isbn : 978-0-19-954690-9.

[100] R. R. Mohler. « Natural Bilinear Control Processes ». In : *IEEE Transactions on Systems Science and Cybernetics* 6.3 (juil. 1970), p. 192–197. issn : 0536-1567. doi : 10.1109/TSSC.1970.300341.

[101] Kevin P Murphy. *Machine learning : a probabilistic perspective*. MIT press, 2012. isbn : 0-262-30432-5.

[102] James R Nagel. « Solving the generalized poisson equation using the finite-difference method (FDM) ». In : *Lecture Notes, Dept. of Electrical and Computer Engineering, University of Utah* (2011).

[103] Nam-Trung Nguyen. *Micromachined flow sensors—A review*. T. 8. Mar. 1997. doi : 10.1016/S0955-5986(97)00019-8.

[104] Juan J. Nieto. « Variational formulation of a damped Dirichlet impulsive problem ». In : *Applied Mathematics Letters* 23.8 (août 2010), p. 940–942. issn : 0893-9659. doi : 10.1016/j.aml.2010.04.015. url : http://www.sciencedirect.com/science/article/pii/S0893965910001217.

[105] Bernd R. Noack, Marek Morzynski et Gilead Tadmor. *Reduced-Order Modelling for Flow Control*. en. Google-Books-ID : NqTmEIjKeDIC. Springer Science & Business Media, mai 2011. isbn : 978-3-7091-0758-4.

[106] A Olbrot. « Control of retarded systems with function space constraints : Necessary optimality conditions ». In : *Control Cybernet* 5 (1976), p. 5–31.

[107] A. Polyakov. « Minimization of disturbances effects in time delay predictor-based sliding mode control systems ». In : *Journal of the Franklin Institute*. Special Issue on Optimal Sliding Mode Algorithms for Dynamic Systems 349.4 (mai 2012), p. 1380–1396. issn : 0016-0032. doi : 10.1016/j.jfranklin.2011.06.028.

[108] A. Polyakov, J. M. Coron et L. Rosier. « On finite-time stabilization of evolution equations : A homogeneous approach ». In : *2016 IEEE 55th Conference on Decision and Control (CDC)*. Déc. 2016, p. 3143–3148. doi : 10.1109/CDC.2016.7798740.

[109] A. Polyakov et al. « On homogeneous evolution equation in a Banach space ». In : *2015 European Control Conference (ECC)*. Juil. 2015, p. 2464–2469. doi : 10.1109/ECC.2015.7330908.

[110] L Polyakova. *Generalized fixed-point theorems and periodic solutions of non-linear equations*. 2006.

[111] Stephen B. Pope. « Turbulent Flows ». en. In : *Measurement Science and Technology* 12.11 (2001), p. 2020. issn : 0957-0233. doi : 10.1088/0957-0233/12/11/705. url : http://stacks.iop.org/0957-0233/12/i=11/a=705.

[112] L Prandtl. « On fluid motions with very small friction ». In : *Verhldg* 3 (1904), p. 484–91.

[113] Raghu S Raghunathan, H. D Kim et T Setoguchi. « Aerodynamics of high-speed railway train ». In : *Progress in Aerospace Sciences* 38.6 (août 2002), p. 469–514. issn : 0376-0421. doi : 10.1016/S0376-0421(02)00029-5. url : http://www.sciencedirect.com/science/article/pii/S0376042102000295.

[114] Cédric Raibaudo. « Characterization of the transient of a separated turbulent boundary layer under control and applications to advanced closed-loop controllers ». Thèse de doct. Ecole Centrale de Lille, 2015.

[115] Cédric Raibaudo, Franck Kerherve et Michel Stanislas. « Characterisation of the transient dynamics of a controlled separated flow using phase averaged PIV ». In : *International Conference on Instability and Control of Massively Separated Flows – ICOMASEF*. Prato, Italy, sept. 2013, p. 183–188.

[116] Ganesh Raman et David Cornelius. « Jet mixing control using excitation from miniature oscillating jets ». In : *AIAA Journal* 33.2 (1995), p. 365–368. issn : 0001-1452. doi : 10.2514/3.12444. url : https://doi.org/10.2514/3.12444.

[117] Ganesh Raman et al. « Development of powered resonance tube actuators for active flow control ». English (US). In : 2003. url : https://nebraska.pure.elsevier.com/en/publications/development-of-powered-resonance-tube-actuators-for-active-flow-c.

[118] James Reuther. « Aerodynamic shape optimization using control theory ». Thèse de doct. Mai 1996. url : https://ntrs.nasa.gov/search.jsp?R=19960029105.

[119] James J. Reuther et al. « Constrained Multipoint Aerodynamic Shape Optimization Using an Adjoint Formulation and Parallel Computers, Part 1 ». In : *Journal of Aircraft* 36.1 (1999), p. 51–60. issn : 0021-8669. doi : 10.2514/2.2413. url : https://doi.org/10.2514/2.2413.

[120] Hector Ríos et al. « Robust output-control for uncertain linear systems : Homogeneous differentiator-based observer approach ». In : *International Journal of Robust and Nonlinear Control* 27.11 (2017), p. 1895–1914. url : http://onlinelibrary.wiley.com/doi/10.1002/rnc.3643/full.

[121] Clarence W. Rowley, Tim Colonius et Richard M. Murray. « Model reduction for compressible flows using POD and Galerkin projection ». In : *Physica D : Nonlinear Phenomena* 189.1 (fév. 2004), p. 115–129. issn : 0167-2789. doi : 10.1016/j.physd.2003.03.001. url : http://www.sciencedirect.com/science/article/pii/S0167278903003841.

[122] A. Saberi, Zongli Lin et A. R. Teel. « Control of linear systems with saturating actuators ». In : *IEEE Transactions on Automatic Control* 41.3 (mar. 1996), p. 368–378. issn : 0018-9286. doi : 10.1109/9.486638.

[123] P. Lopes dos Santos, J. A. Ramos et J. L. Martins de Carvalho. « Identification of Bilinear Systems With White Noise Inputs : An Iterative Deterministic-Stochastic Subspace Approach ». In : *IEEE Transactions on Control Systems Technology* 17.5 (sept. 2009), p. 1145–1153. issn : 1063-6536. doi : 10.1109/TCST.2008.2002041.

[124] G. Schitter et A. Stemmer. « Identification and open-loop tracking control of a piezoelectric tube scanner for high-speed scanning-probe microscopy ». In : *IEEE Transactions on Control Systems Technology* 12.3 (mai 2004), p. 449–454. issn : 1063-6536. doi : 10.1109/TCST.2004.824290.

[125] Hermann Schlichting. « Boundary-layer theory ». In : (1968). url : https://infoscience.epfl.ch/record/1738.

[126] S Scott Collis et al. « Issues in active flow control : theory, control, simulation, and experiment ». In : *Progress in Aerospace Sciences* 40.4 (2004), p. 237–289.

[127] A. Seifert. « Closed-Loop Active Flow Control Systems : Actuators ». en. In : *Active Flow Control*. Notes on Numerical Fluid Mechanics and Multidisciplinary Design (NNFM). Springer, Berlin, Heidelberg, 2007, p. 85–102. isbn : 978-3-540-71438-5 978-3-540-71439-2. doi : 10.1007/978-3-540-71439-2_6. url : https://link.springer.com/chapter/10.1007/978-3-540-71439-2_6.

[128] T. Shaqarin et al. « Open and closed-loop experiments to identify the separated flow dynamics of a thick turbulent boundary layer ». en. In : *Experiments in Fluids* 54.2 (jan. 2013), p. 1–22. issn : 0723-4864, 1432-1114. doi : 10.1007/s00348-012-1448-4.

[129] Yuri Shtessel et al. *Sliding mode control and observation*. New York, NY 10013, USA : Springer, 2014.

[130] B. L. Smith et G. W. Swift. « A comparison between synthetic jets and continuous jets ». en. In : *Experiments in Fluids* 34.4 (avr. 2003), p. 467–472. issn : 0723-4864, 1432-1114. doi : 10.1007/s00348-002-0577-6. url : https://link.springer.com/article/10.1007/s00348-002-0577-6.

[131] Barton L. Smith et Ari Glezer. « The formation and evolution of synthetic jets ». en. In : *Physics of Fluids* 10.9 (sept. 1998), p. 2281–2297. issn : 1070-6631, 1089-7666. doi : 10.1063/1.869828. url : http://aip.scitation.org/doi/10.1063/1.869828.

[132] Barton L. Smith et Gregory W. Swift. « Synthetic jets at large Reynolds number and comparison to continuous jets ». In : *AIAA paper* 3030 (2001), p. 2001. URL : http://www.efdl.usu.edu/publications/AIAA01-3030.pdf.

[133] Eduardo D. Sontag. *Mathematical Control Theory : Deterministic Finite Dimensional Systems*. en. Google-Books-ID : f9XiBwAAQBAJ. Springer Science & Business Media, nov. 2013. ISBN : 978-1-4612-0577-7.

[134] E.A. Stalker. « Boundary layer control for drag reduction ». In : (nov. 1949). URL : https://www.google.com/patents/US2488991.

[135] E.A. Stalker. « Means of reducing the fluid resistance of propelled vehicles ». In : (avr. 1936). URL : https://www.google.com/patents/US2037942.

[136] Susumu Sugiyama, Mitsuharu Takigawa et Isemi Igarashi. « Integrated piezoresistive pressure sensor with both voltage and frequency output ». In : *Sensors and Actuators* 4.Supplement C (jan. 1983), p. 113–120. ISSN : 0250-6874. DOI : 10.1016/0250-6874(83)85015-X. URL : http://www.sciencedirect.com/science/article/pii/025068748385015X.

[137] Roger Temam. *Navier-stokes equations*. T. 2. North-Holland Amsterdam, 1984.

[138] Hendrik Tennekes et John Leask Lumley. *A First Course in Turbulence*. en. MIT Press, 1972. ISBN : 978-0-262-20019-6.

[139] F. O. Thomas, A. Kozlov et T. C. Corke. « Plasma Actuators for Cylinder Flow Control and Noise Reduction ». In : *AIAA Journal* 46.8 (2008), p. 1921–1931. ISSN : 0001-1452. DOI : 10.2514/1.27821. URL : https://doi.org/10.2514/1.27821.

[140] Vidar Thomée. *Galerkin finite element methods for parabolic problems*. T. 1054. Springer, 1984.

[141] K. Torii, K. M. Kwak et K. Nishino. « Heat transfer enhancement accompanying pressure-loss reduction with winglet-type vortex generators for fin-tube heat exchangers ». In : *International Journal of Heat and Mass Transfer* 45.18 (août 2002), p. 3795–3801. ISSN : 0017-9310. DOI : 10.1016/S0017-9310(02)00080-7. URL : http://www.sciencedirect.com/science/article/pii/S0017931002000807.

[142] Vadim I. Utkin. « Sliding Mode Control : Mathematical Tools, Design and Applications ». en. In : *Nonlinear and Optimal Control Theory*. Sous la dir. de Paolo Nistri et Gianna Stefani. Lecture Notes in Mathematics 1932. Springer Berlin Heidelberg, 2008, p. 289–347. ISBN : 978-3-540-77644-4 978-3-540-77653-6. DOI : 10.1007/978-3-540-77653-6_5.

[143] VI Utkin. *Sliding modes in optimization and control problems*. Springer Verlag, New York, 1992.

[144] P. S. Virk. « Drag reduction fundamentals ». en. In : *AIChE Journal* 21.4 (juil. 1975), p. 625–656. issn : 1547-5905. doi : 10.1002/aic.690210402. url : http://onlinelibrary.wiley.com/doi/10.1002/aic.690210402/abstract.

[145] Ralph J. Volino. « Separation Control on Low-Pressure Turbine Airfoils Using Synthetic Vortex Generator Jets ». In : *ASME Turbo Expo 2003, collocated with the 2003 International Joint Power Generation Conference*. Atlanta, Georgia, USA, 2003, p. 845–859. doi : 10.1115/GT2003-38729. url : http://dx.doi.org/10.1115/GT2003-38729.

[146] Edward A. Whalen et al. « Performance Enhancement of a Full-Scale Vertical Tail Model Equipped with Active Flow Control ». In : *53rd AIAA Aerospace Sciences Meeting*. American Institute of Aeronautics et Astronautics. doi : 10.2514/6.2015-0784. url : https://arc.aiaa.org/doi/abs/10.2514/6.2015-0784.

[147] Frank M White et Isla Corfield. *Viscous fluid flow*. T. 3. McGraw-Hill Higher Education Boston, 2006.

[148] Darrell Williamson. « Observation of bilinear systems with application to biological control ». In : *Automatica* 13.3 (mai 1977), p. 243–254. issn : 0005-1098. doi : 10.1016/0005-1098(77)90051-6. url : http://www.sciencedirect.com/science/article/pii/0005109877900516.

[149] Svante Wold, Kim Esbensen et Paul Geladi. « Principal component analysis ». In : *Chemometrics and Intelligent Laboratory Systems*. Proceedings of the Multivariate Statistical Workshop for Geologists and Geochemists 2.1 (août 1987), p. 37–52. issn : 0169-7439. doi : 10.1016/0169-7439(87)80084-9. url : http://www.sciencedirect.com/science/article/pii/0169743987800849.

[150] A Wortmann. *Alleviation of Fuselage from Drag Using Vortex Flows*. Rapp. tech. Department of Energy Report No. DOE/CE/15277-T1, Washington, DC, 1987.

[151] Y. Ying, M. Rao et S. X. Shen. « Bilinear Decoupling Control and Its Industrial Application ». In : *1992 American Control Conference*. Juin 1992, p. 1163–1167.

[152] K. B. M. Q. Zaman, M. F. Reeder et M. Samimy. « Control of an axisymmetric jet using vortex generators ». In : *Physics of Fluids* 6.2 (fév. 1994), p. 778–793. issn : 1070-6631. doi : 10.1063/1.868316. url : http://aip.scitation.org/doi/abs/10.1063/1.868316.

[153] Kemin Zhou et John Comstock Doyle. *Essentials of robust control*. T. 104. Prentice hall Upper Saddle River, NJ, 1998.

Appendix A

Sketch of the proof of Theorem 1

The proof is based on Fixed-Point Theorem for a generalized Banach spaces $\mathbf{B} = \mathbf{L}^2_{[0,\omega]} \times ... \times \mathbf{L}^2_{[0,\omega]}$, which have vector-valued norms :

$$[]\boldsymbol{x}[] = (\|\boldsymbol{x}_0\|_{\mathbf{L}^2_{[0,\omega]}}, ..., \|\boldsymbol{x}_{n-1}\|_{\mathbf{L}^2_{[0,\omega]}})^\top \in \mathbb{R}^n_+ \text{ for any } \boldsymbol{x} \in \mathbf{B}$$

The space $\mathbb{R}^n_+$ is semi-ordered using the conventional component-wise order relation, i.e. $\boldsymbol{x} \leq \boldsymbol{y}$ if $x_i \leq y_i$, $i = 1, ..., n$, where $\boldsymbol{x}, \boldsymbol{y} \in \mathbb{R}^n_+$. In this case the contraction condition of the operator $\mathcal{F} : \mathbf{B} \to \mathbf{B}$ is

$$[]\mathcal{F}\boldsymbol{x} - \mathcal{F}\boldsymbol{y}[] \leq Q[]\boldsymbol{x} - \boldsymbol{y}[], \quad \text{for all } \mathbf{x}, \mathbf{y} \in \mathbf{B},$$

where $Q \in \mathbb{R}^{n\times n}_+$ is a Schur stable matrix. Under this condition the operator $\mathcal{F}$ has the unique fixed point $\boldsymbol{x}^*$ on $\mathbf{B}$, i.e. $\mathcal{F}(\boldsymbol{x}^*) = \boldsymbol{x}^*$. To complete the proof of Theorem 1 let us consider the operator $\mathcal{F} = (\mathcal{F}_0, ..., \mathcal{F}_{n-1})^\top \in \mathbf{B}$ with

$$\mathcal{F}_j(\boldsymbol{x}) = \int_0^\omega G^{(j)}(t,s) f(s, x_0(s), ..., x_0(s - h_m), x_1(s), ...) ds,$$

where G is the Green function of the system $\mathcal{A}x_{h_m}(t) = 0$. Finally, it can be shown [110] that $\mathcal{F}$ satisfies the contraction condition with the matrix $Q = (l_0, ..., l_{n-1})^\top (\sigma_0, ..., \sigma_{n-1})$ that is Schur stable due to the condition :

$$(l_0, ..., l_{n-1})(\sigma_0, ..., \sigma_{n-1})^\top < 1$$

Appendix B

NOMAD

We will present here a short explanation of how NOMAD works. For more details, see the paper of S. Le Digabel [88].

NOMAD [88] is a software package implementing the Mesh Adaptive Direct Search (MADS) algorithm. NOMAD aims at solving constrained blackbox optimization problems of the forms :

$$\min_{x \in \Omega} f(x) \tag{B.1}$$

or

$$\min_{x \in \Omega} (f_1(x), f_2(x)) \tag{B.2}$$

where $\Omega = \{x \in X : c_j(x) \leq 0, j \in J\} \subset \mathbb{R}^n$ with $f, f_1, f_2, c_j : X \to \mathbb{R} \cup \{\infty\}$ for all $j \in J = \{1, 2, \ldots, m\}$ and $X \subset \mathbb{R}$.

This algorithm is capable of handling several types of constraints such as nonlinear inequalities or yes/no constraints. The variables x can be, amongst other, reals, integers or binaries.

NOMAD implements the MADS algorithm in C++ and has a Matlab version, developed by Mark Abramson.

Direct search methods use only function evaluations for optimization and do not need derivatives (see [30] for a overview about derivative-free optimization methods).

MADS is in iterative method that evaluates the blackbox functions on a mesh which is updated at each iteration. At an iteration k, the mesh is defined by :

$$M_k = \bigcup_{x \in V_k} \{x + \Delta_k^m D z : z \in \mathbb{N}^{n_D}\} \tag{B.3}$$

where Δ_k^m is the mesh size parameter, D a $n \times n_D$ matrix representing a finite set of directions in $\mathbb{R}^n$ and V_k is the set of points at which the objective functions were evaluated at iteration k (V_0 contains the starting points).

Each iteration has 3 steps :

1. *The search* : Choose trial points on the mesh
2. *The poll* : Explore the mesh around the current iterate x_k using the set of poll trial points $P_k = \{x_k + \Delta_k^m d : d\ inD_k\} \subset M_k$. D_k is the set of poll directions and its column are taken as an integer combination of the columns of the matrix D such that they form a positive spanning set. Δ_k^m is chosen such that $\Delta_k^m < \Delta_k^p$ where Δ_k^p is the poll size parameter that bounds the distance of the poll points from the poll center x_k and Δ_k^m is reduced faster than Δ_k^p. This is decribed in Figure B.1.
3. *The update* : After choosing the poll trial points, the blackbox function is evaluated at these points and the most promising point is chosen to be x_{k+1}. It is possible that $x_{k+1} = x_k$. The mesh size parameter is updated by

$$\Delta_{k+1}^m = \tau^{w_k} \Delta_k^m \tag{B.4}$$

   where $\tau > 1$ is a fixed rational number and w_k is a finite integer. w_k is positive or null if iteration k is a success, and negative otherwise. Therefore, the mesh size parameter is increased in case of success and decreased in case of failure. As an example, the LT-MADS method uses $\Delta_k^m < \Delta_k^p < 1$ and $\Delta_k^p = \sqrt{\Delta_k^m}$.

A flowchart of the NOMAD algorithm is presented in Figure B.2.

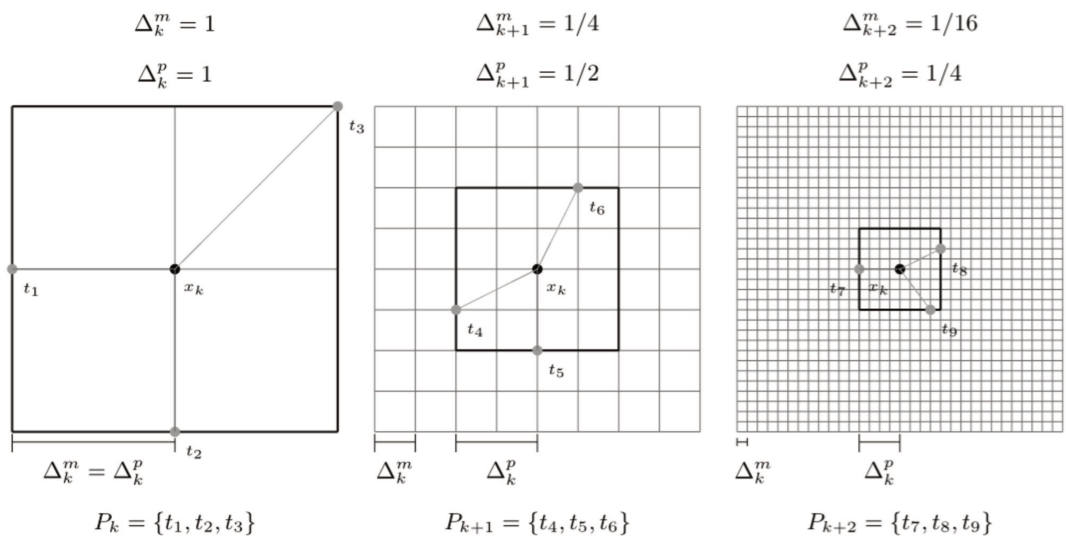

Figure B.1 – Example of different mesh configurations with $n = 2$. Thin lines represent the mesh of size Δ_k^m, and thick lines the points at distance Δ_k^p from x_k in norm L_∞. Poll trial points are illustrated with random LT-MADS $n+1$ directions. The mesh is reduced between the situations to show that mk is reduced faster than Δ_k^p. As the poll trial points lie at the intersection of the thick and thin lines, the number of possible locations grows larger and larger. Taken from [88]

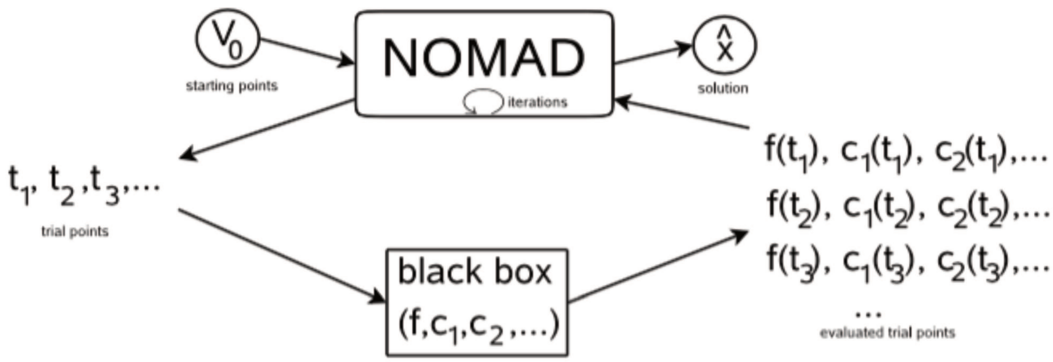

Figure B.2 – Flowchart of the NOMAD algorithm. Taken from [88]

Appendix C

Identification results

This chapter presents the identification results for the test case II and III.

C.1 Models for the test case II

Here we show 2 models (Equations D.1 and D.2) that were identified for control of the test case II.

C.1.1 $N_1 = 10$, $N_2 = 10$, $N_3 = 3$

This model is the one used for the feedfoward optimal control. It is the most accurate of the models and has therefore the most coefficients. Its delays and coefficients in discrete time are given in Table C.1 for $N_1 = 10$, $N_2 = 10$ and $N_3 = 3$. The three criteria from Section 3.4 are given in Table C.2. Other more accurate can be derived using more coefficients but this one was deemed accurate enough for the feedfoward control. The comparison between the identified model and the data is pictured in Figures C.1 for data set N°2 and C.2 for data set N°9.

C.1.2 $N_1 = 2$, $N_2 = 2$, $N_3 = 1$

This model is the one used for the feedback robust setpoint tracking control. Its delays and coefficients in discrete time is given in Table C.3 for $N_1 = 2$, $N_2 = 2$ and $N_3 = 1$. The three criteria from Section 3.4 are given in Table C.4. As it can be seen, it contains much less coefficients that the previous models but still provides good fit to the data.

τ_i	$\begin{bmatrix} 0.01 & 0.02 & 0.04 & 0.06 & 0.08 & 0.12 & 0.19 & 1.27 & 2.30 & 4.95 \end{bmatrix}$
h_j	$\begin{bmatrix} 0.01 & 0.02 & 0.17 \end{bmatrix}$
$\bar{\tau}_l$	$\begin{bmatrix} 0.01 & 0.03 & 0.04 & 0.05 & 0.09 & 1.08 & 3.97 & 4.13 & 4.67 & 493 \end{bmatrix}$
a_i	$\begin{bmatrix} 13.93 & -16.11 & 1.59 & 1.23 & -16.63 & \dots \\ \dots & 12.71 & -2.48 & 0.86 & -0.01 & 0.51 \end{bmatrix}$
b_l	$\begin{bmatrix} 2.18 & 0.50 & 1.52 \end{bmatrix}$
c_{jl}	$\begin{bmatrix} 0.70 & 6.40 & 0.11 & -11.11 & 1.64 & 0.13 & 0.07 & \dots \\ \dots & -0.08 & 0.26 & -0.13 & -11.08 & 16.20 & 0.03 & \dots \\ \dots & -2.36 & -2.84 & 0.13 & 0.03 & -0.89 & 0.43 & \dots \\ \dots & -0.30 & 0.95 & -1.58 & 8.40 & -3.58 & -7.58 & \dots \\ \dots & -0.42 & 0.41 & -0.27 & 1.34 & -1.02 & & \end{bmatrix}$

Table C.1 – Delays and coefficients of the model of the test case II with $N_1 = 10$, $N_2 = 10$ and $N_3 = 3$

FIT	ε	ρ
81.33	6.58	0.9936

Table C.2 – Values of the criteria of the model of the test case II with $N_1 = 10$, $N_2 = 10$ and $N_3 = 3$

τ_i	$\begin{bmatrix} 0.01 & 0.05 \end{bmatrix}$
h_j	$\begin{bmatrix} 0.05 \end{bmatrix}$
$\bar{\tau}_l$	$\begin{bmatrix} 0.05 & 0.06 \end{bmatrix}$
a_i	$\begin{bmatrix} 3.33 & -6.37 \end{bmatrix}$
b_l	$\begin{bmatrix} 1.31 \end{bmatrix}$
c_{jl}	$\begin{bmatrix} -8.91 & 8.91 \end{bmatrix}$

Table C.3 – Delays and coefficients of the model of the test case II with $N_1 = 2$, $N_2 = 2$ and $N_3 = 1$

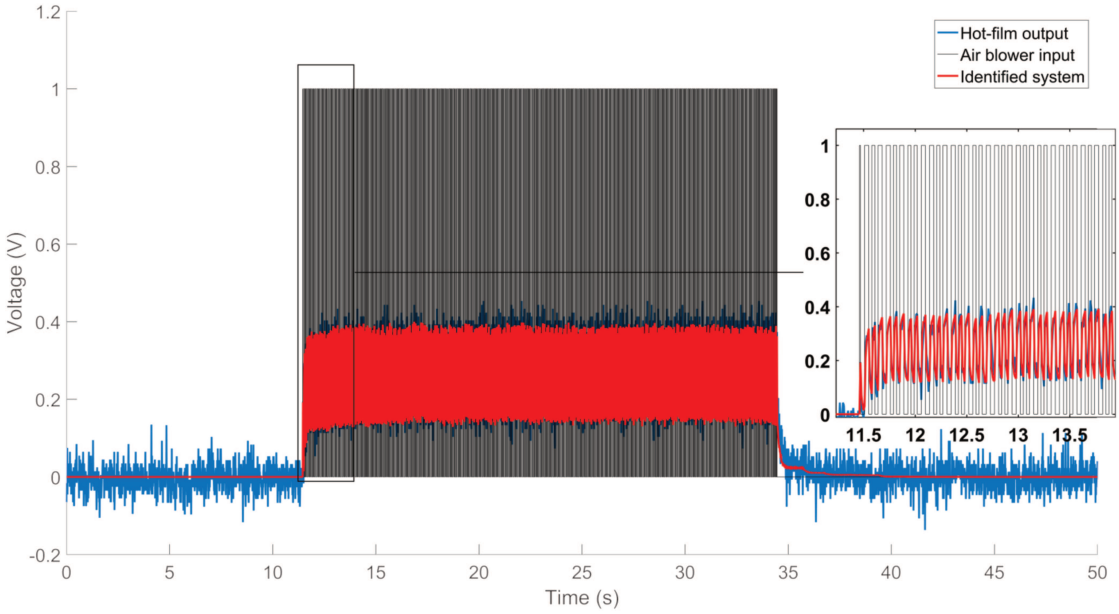

Figure C.1 – Identified model for test case II, zoom on data set N°2

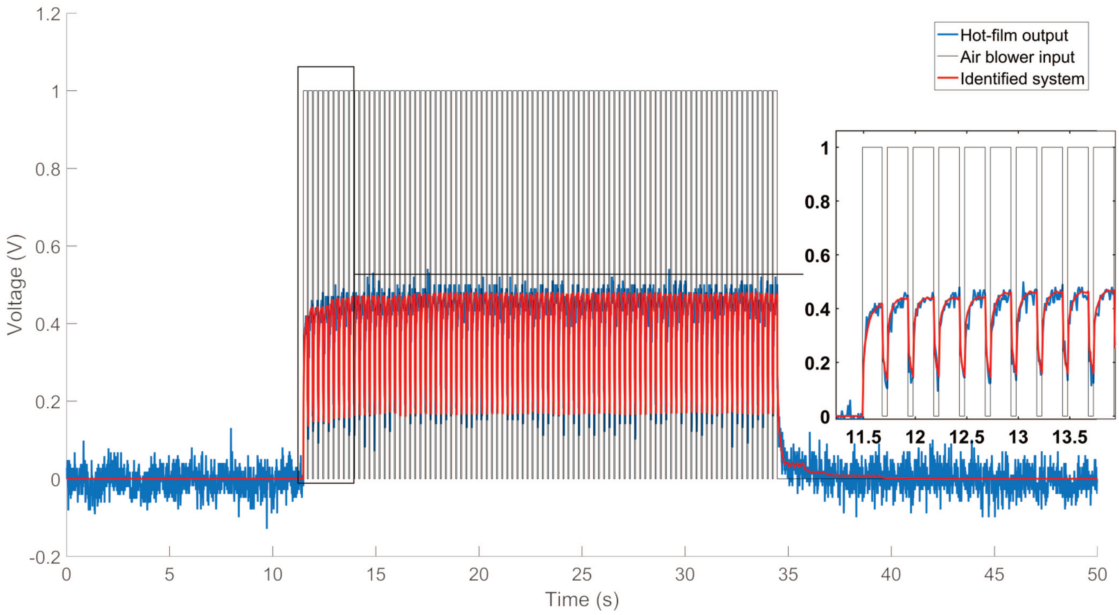

Figure C.2 – Identified model for test case II, zoom on data set N°9

FIT	ε	ρ
70.52	67.95	0.9603

Table C.4 – Values of the criteria of the model of the test case II with $N_1 = 2$, $N_2 = 2$ and $N_3 = 1$

τ_i	$\begin{bmatrix} 0.015 & 0.025 \end{bmatrix}$
h_j	$\begin{bmatrix} 0.025 \end{bmatrix}$
$\bar{\tau}_l$	$\begin{bmatrix} 0.025 & 0.975 \end{bmatrix}$
a_i	$\begin{bmatrix} -11.00 & 6.9367 \end{bmatrix}$
b_l	$\begin{bmatrix} 1.4633 \end{bmatrix}$
c_{jl}	$\begin{bmatrix} 0.0067 & -0.0067 \end{bmatrix}$

Table C.5 – Delays and coefficients of the model of the test case III with $N_1 = 2$, $N_2 = 2$ and $N_3 = 1$

C.2 Models for the test case III

C.2.1 $N_1 = 2$, $N_2 = 2$, $N_3 = 1$

Only the model for the feedback robust setpoint tracking control was identified on the data from the test case III. Is delays and coefficients in discrete time are given in Table C.5 for $N_1 = 2$, $N_2 = 2$ and $N_3 = 1$. The three criteria from Section 3.4 are given in Table C.6.

FIT	ε	ρ
33.77	46.25	0.8795

Table C.6 – Values of the criteria of the model of the test case III with $N_1 = 2$, $N_2 = 2$ and $N_3 = 1$

Appendix D

Publications

D.1 Paper presented in the European Control Conference ECC16 - Aalborg, Denmark - June 2016

2016 European Control Conference (ECC)
June 29 - July 1, 2016. Aalborg, Denmark

A bilinear input-output model with state-dependent delay for separated flow control

Maxime FEINGESICHT[1,2,4], Cédric RAIBAUDO[1,3], Andrey POLYAKOV[2,4], Franck KERHERVE[1,3] and Jean-Pierre RICHARD[1,2,4]

Abstract— **It is proposed a first step to the model-based closed-loop control of a separated flow. In such situations, fluid mechanics phenomena are highly nonlinear and can be represented by means of the Navier-Stokes equations. However, such a model still rises difficult issues for control practice. This paper proposes an alternative, bilinear and delayed model, the accuracy of which is studied. The identification technique combines least-square technique with a Mesh Adaptive Direct Search (MADS) algorithm. The main feature of the model is state dependent structure of input delay.**

I. INTRODUCTION

In transportation systems, aerodynamic loss are the most important source of energy wastage at speeds higher than 50km/h. The need of improvement cannot be met solely through the use of the vehicle shape, as it requires numerous tries for very few improvement, thus being very time consuming. In such a context, active control strategies are now expected.

Among the various strategies developed, those using pneumatic actuators, such as air blowers, are the most encountered. In the meantime, the preferred examined system concerns flow separating over a two-dimensional flap (see [1], [2], [3], [4] and [5]). These works generally study the system from the Fluid Mechanics point of view but the application of control theory should be fruitfull to control the opening and closing of the air blowers in an optimal and robust way. This is only possible once the model representing the system has been identified. Examples of separated flow control can be found in [6], [7] and [8], however these examples suffer from the lack of an adequate model. Modeling using Navier-Stokes equations can be found in [9], [10] and [11].

The main issue is that the physical system studied in this paper is known to be highly nonlinear, which is always the case in aerodynamic studies, and also contains time delays both on state and input due to the natural phenomenons that rule turbulent flow and the limited speed of the flow. The first approach would be to use partial differential equations, namely the equations of Navier-Stockes, but this implies complicated calculations and controller/observer design. The alternative we propose is to use "grey-box" identification techniques so to derive a simpler model that can be usefull for control purpose. The model we suggest is a bilinear, delayed difference equation which is able to catch both the nonlinear effects and diffusion delays. Such a model will be shown to be quite realistic in an identification perspective. From the control point of view, predictor-based ([12]), model predictive control (MPC, [13], [14]) and optimal control techniques ([15]) are possible future solutions.

This paper focuses on the identification of the model based on several experimental data sets. It presents the time delayed input/output model. The simplest scheme for input delay estimation is developed. The state delays identification is provided using the well-known derivative-free minimization algorithm MADS [16]. Some results on the identification of the delays for a related system can also be found in [17].

II. THE PHYSICAL SYSTEM

The physical system considered is a turbulent boundary layer developing along a ramp and subjected to separation due to the presence of a inclined flap with a sharp edge whose photography is shown in Fig. 2 with schematics in Fig. 1. The experiments were conducted in the LML boundary layer wind tunnel. The wind tunnel includes a 20 m long section with constant area of 2m x 1m along which the boundary layer can develop. The maximum free stream mean velocity and turbulence level are 10 m/s and 0.03% respectively. Under operation, the temperature is regulated to 0.2C . Full details of the wind tunnel and its characterisation can be found in [18]. The main flow direction is from left to right, except in a region close to the flap where the flow is reversed indicating the presence of a recirculation region due to a separation of the flow away from the wall. The mean streamwise velocity component is measured using Particle Image Velocimetry (PIV). This is illustrated in Fig. 4. This recirculation region is mainly responsible for aerodynamic loss. Control applications are hence designed with the objective to reduce (or annihilate) this reversed flow. In the present case, air blowing actuators were used. These are located upstream of the sharp edge and consist of 22 round jets regularly spaced in the spanwise z-direction as illustrated in Fig. 1. Details of the set-up can be found in [1] and [18]

Real-time survey of the flow is effected thanks to wall-sensors measuring the friction gain mounted along the inclined flap. These are known as hot-film sensors. Again, full details of the arrangements can be found in [1]. The actuators are controlled using a pulsed voltage as command law such as illustrated in Fig. 6. In practice, such sequences are repeated continuously over a long time: the flow is therefore repeatidly submitted to control during which it experiences successive reattachments (actuation on) and separation (actuation off) sequences. The friction gain is continuously recorded during all these sequences and an averaged response can be obtained. The latter is reported in Fig. 3. Since the flow dynamics in the separation region is strongly dependent on several inflow conditions, the instantaneous response of the wall-sensor may significantly vary from this averaged response. A first indication of how much the wall-sensor response varies may be obtained by repeating the operation described previously. Different sets of long measurements were effected. For each, an averaged

[1]Ecole Centrale de Lille, Cité Scientifique, 59651 Villeneuve-d'Ascq, France
maxime.feingesicht@ec-lille.fr ; cedric.raibaudo@ec-lille.fr
franck.kerherve@ec-lille.fr ; jean-pierre.richard@ec-lille.fr
[2]INRIA Team Non-A, Parc scientifique de la Haute-Borne, 40 Avenue Halley, Bt A - Park Plaza, Villeneuve-d'Ascq, France
andrey.polyakov@inria.fr
[3]LML, Laboratoire de Mécanique de Lille, CNRS UMR 8107, Boulevard Paul Langevin, 59655 Villeneuve d'Ascq Cédex, France
[4]CRIStAL, CNRS UMR 9189, Btiment M3, Université Lille 1, 59655 Villeneuve d'Ascq Cedex FRANCE

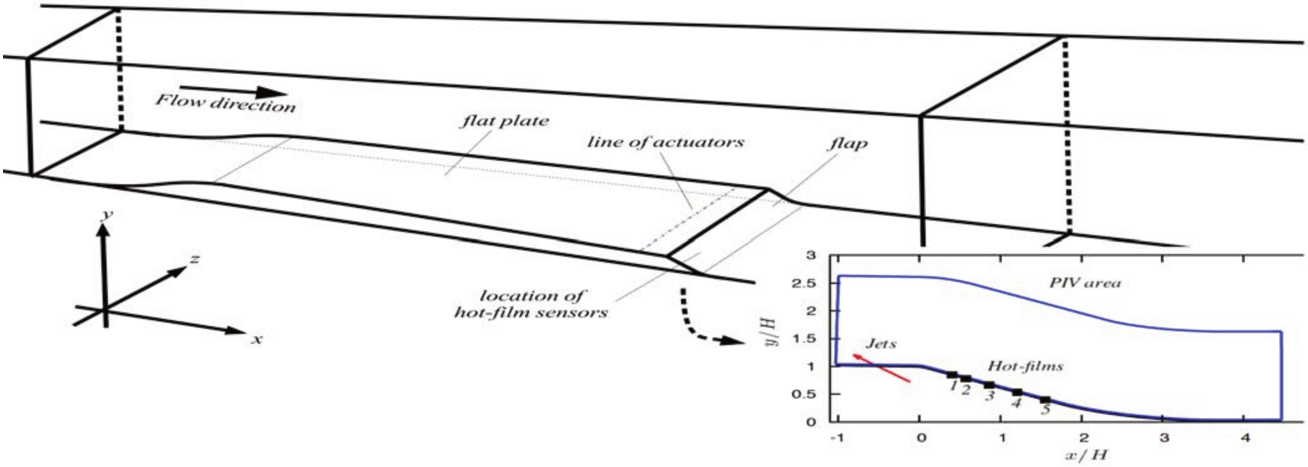

Fig. 1: Schematics of the experimental set-up. Enlarged picture: ramp model. Zoom: region of the flap with locations of the hot-film sensors and active air blowers

Fig. 2: Photography of the ramp model. The flow is coming from the left

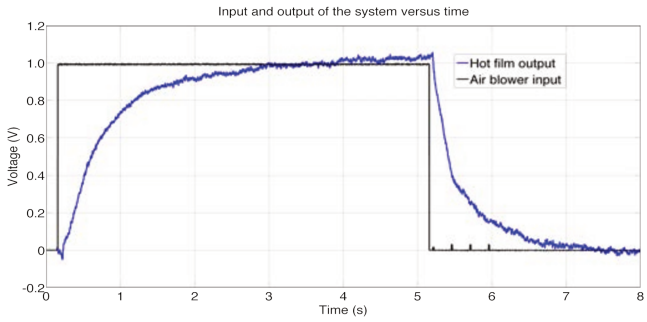

Fig. 3: Set of data N°1 used for identification

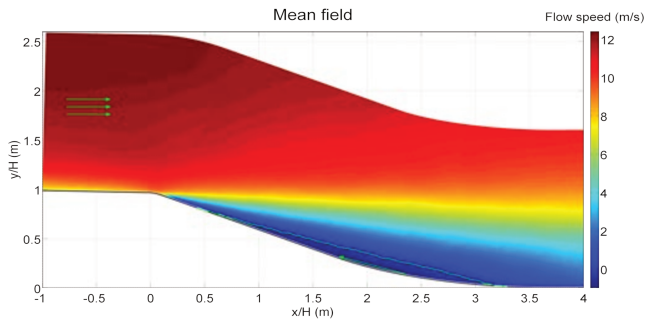

Fig. 4: Mean flow velocity field (streamwise component) in m/s. The green line delimits the recirculation region where the flow is reversed compared to the main direction. The main flow is from left to right.

response of the wall-sensor is calculated and the overall data set obtained can be used to bound the averaged response as shown in Fig. 5.

When the actuators are activated (t=0s) contra-rotating vortices are generated (see [1]). Due to the distance between the actuators and the wall-sensors, a time-delay is necessary before the hot-film can sense changes in the flow dynamics. The main effect of the actuators is to force the flow to reattach to the flow, leading to an increase in the friction gain. This increase is manifest when examining the averaged hot-film response of Fig. 6. Once the flow attained a stationary state under control effect, the friction gain remains almost constant. When the control is turned off, again a short time-delay is necessary before the hot-film signal can sense flow changes towards the natural separated state.

Using the available data, it is necessary to develop an input-output model describing the behavior of the hot-film, where the input will be the voltage input to the air blowers and the output will be the voltage output of the hot-film. Considering what was said before, the model need to be time-delayed and will be bilinear in order to catch the nonlinearities of the physical system while remaining simple enough for observation and control.

For our identification process, we will use the four data sets presented in Fig. 3, 6, 7 and 9. The maximum and minimum data can therefore be used for testing purpose in order to verify if the identified system remains within acceptable bounds (see [1] and [2]). These data sets use, respectively, a square wave at a frequency of 8Hz and 50% duty cycle, 4Hz and 80% duty cycle, 4Hz and duty cycle of 50% and a step input.

III. System identification

A. Estimation of the input delay

The motivation behind using a state-dependent input delay are based on physical considerations : if the air blower is placed before the flap and the hot-films on the flap, the air flow will take some time to travel the distance between them, thus implying a delay which depends on the speed of the flow. As the hot-film output is a measure of the friction in the flow which is related to the speed of the flow and the delay depends on the speed of the flow, the delay can hence be directly estimated from the output of the hot-film.

We then need to obtain the function giving the state-dependent input delay, which will be noted $\tilde{h}(y_k)$. **The delays between a**

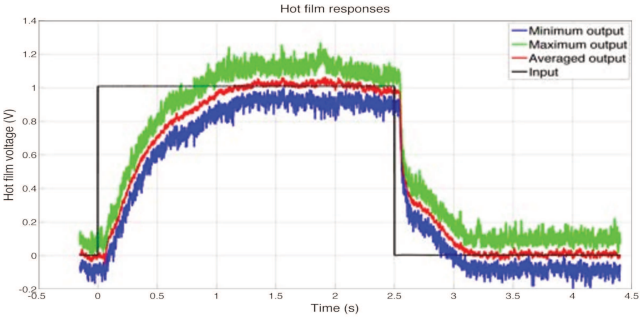

Fig. 5: Voltage output of one hot-film

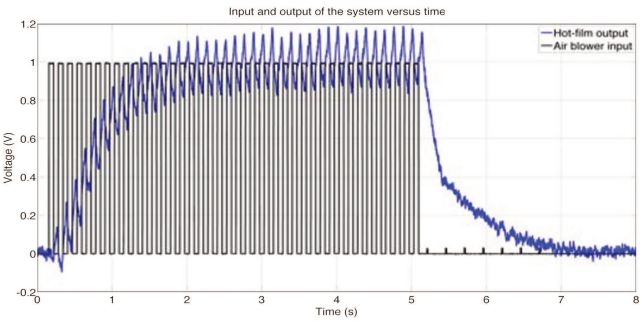

Fig. 6: Hot-film output voltage versus the air blower input voltage for data set n°4

variation in the input (on/off, rising or falling edge) and the corresponding variation in the hot-film signal can be measured directly from the data using Matlab functions. For the set of data N°2, this is represented on Fig. 7. In order to take in account the prehistory of the state-function of the time-delayed system in a simple way, the function giving the delay will be evaluated using the mean value (averaged value) of this function, which corresponds to measure the value on an averaged, smoother model, as described in (1).

$$\widetilde{y_k} = \frac{1}{W}\sum_{s=1}^{W-1} y_{k-s} \tag{1}$$

where W is the averaging window, chosen equal to 250 in our simulations and y_k is the output of the system at sample k

As the system has short time constants, once the time delay has expired, reaction to the input is very fast, thus our method will not be influenced by the phase of the system and will give sufficiently good estimation of the input delays.

Applying this to the 4 data sets and plotting the measured delays versus the hot-film output value, we obtain Fig. 8. The fitting is done using Matlab's "fit" function. It is to be noted that applying the fitting to only one of the data sets gives very similar results but using all 4 sets is more reliable.

The fitted function is given by (2).

$$\widetilde{h}(\widetilde{y_k}) = 47.35 + 12.69\,\mathrm{e}^{-20.18\widetilde{y_k}} \tag{2}$$

where $\widetilde{y_k}$ is the averaged system output as defined in Eq. 1 and $\widetilde{h}(\widetilde{y_k})$ is the state dependent input delay that will be used in the identified model in the next section.

A linear statistical analysis on the values of the state-dependent input delay for the fitting presented in Fig. 8 gives the following values :

- Mean = 47.83
- Standard deviation = 2.70
- Correlation coefficient with the model input = -0.07
- Correlation coefficient with the model output = -0.30

B. Bilinear delayed difference model

We will use two similar system forms to identify the physical process. Both of the forms are bilinear, the first one, given by (3), uses a fixed input delays while the second one, given by (4), uses state dependent input delays. The model is chosen bilinear in order to be simple enough for easy control design while still capturing nonlinear dynamics of the Navier-Stokes equation, which also contains bilinear terms. The model is chosen to be including time delays in order to have an infinite dimension to be closer to a partial differential equation. Example of modeling with linear first order models can be found in [1], where it can be seen that this type of model capture the mean tendency but not the oscillations around this tendency. It is to be noted that we do not intend to represent exactly the model, as we focus more on simple design control and that a robust control well designed can overcome the inaccuracies of our identified model.

$$y_{k+1} = \sum_{i=1}^{N_1}\left(a_i y_{k-\tau_i}\right) + \sum_{l=1}^{N_3}\left(b_l + \sum_{j=1}^{N_2}\left(c_{jl} y_{k-\bar{\tau}_j}\right)\right) u_{k-h_l} \tag{3}$$

$$y_{k+1} = \sum_{i=1}^{N_1}\left(a_i y_{k-\tau_i}\right) + \sum_{l=1}^{N_3}\left(b_l + \sum_{j=1}^{N_2}\left(c_{jl} y_{k-\bar{\tau}_j}\right)\right) u_{k-\widetilde{h}_l(\widetilde{y_k})} \tag{4}$$

where $0 \le k \le N-1$ is the number of the measure y, considering that $y_j = 0$ for $j < 0$; τ, $\bar{\tau}$ and h are prescribed delays ; N, N_1, N_2 and N_3 are respectively the number of measures y, delays τ, $\bar{\tau}$ and input delays (h or $\widetilde{h}$) ; $\widetilde{h}_l(\widetilde{y_k}) = \mathrm{round}(f_l \widetilde{h}(\widetilde{y_k}))$ are the state dependent input delays of the second model with f_l a multiplicative factor used to derive several state dependent input delays from the delay identification ; a_i, b_l and c_{jl} are the coefficients to identify.

The variables N_1, N_2 and N_3 are to be chosen by the user in a compromise between complexity of the model and precision. It

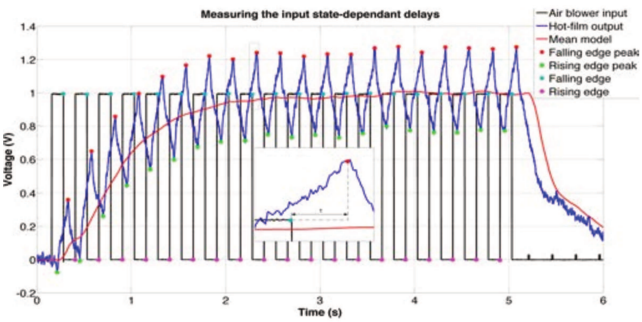

Fig. 7: Identification of the input state-dependent delay for data set N°2

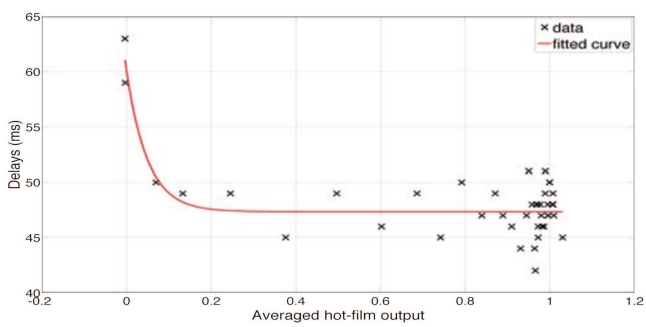

Fig. 8: Fitting of the input state-dependent delays

will also impact the time required for the optimization used in the identification process. Furthermore, augmenting the size of the model makes control design more complicated. The coefficients used in this paper were found to give good results for our purposes with short enough for efficient computations.

In the continuous time domain, these systems are described by (5) and (6), where T is the sampling period, fixed at 1ms for our systems and the function $\widetilde{y}(t)$ is defined by (7).

$$\begin{aligned}\dot{y}(t) = \frac{1}{T}\Bigg(&-y(t) + \sum_{i=1}^{N_1}(a_i y(t-\tau_i T)) + \sum_{l=1}^{N_3}(b_l u(t-h_l T)) \\ &+ \sum_{l=1}^{N_3}\sum_{j=1}^{N_2}\left(c_{jl} u(t-h_l T)\, y(t-\widetilde{\tau}_j T)\right)\Bigg)\end{aligned} \tag{5}$$

$$\begin{aligned}\dot{y}(t) = \frac{1}{T}\Bigg(&-y(t) + \sum_{i=1}^{N_1}(a_i y(t-\tau_i T)) + \sum_{l=1}^{N_3} b_l u\left(t-\widetilde{h}_l(\widetilde{y}(t))T\right) \\ &+ \sum_{l=1}^{N_3}\sum_{j=1}^{N_2}\left(c_{jl} u\left(t-\widetilde{h}_l(\widetilde{y}(t))T\right) y(t-\widetilde{\tau}_j T)\right)\Bigg)\end{aligned} \tag{6}$$

$$\widetilde{y}(t) = \frac{1}{WT}\int_0^{WT} y(t-s)ds \tag{7}$$

The identification has been done using a least-square method. We refer the reader to [19] for more details.

To obtain the values of the coefficients contained in the matrix A_1, we use the Moore-Penrose pseudo-inverse on the matrix W. Noting W^+ the Moore-Penrose pseudo-inverse of W, we obtain (8).

$$A(\tau,\bar{\tau},h,x) = W^+ x \tag{8}$$

The quality of the identification will be estimated using the three following indicators : the L_2 error norm $\varepsilon(\tau,\bar{\tau},h,A)$ given by (9), the fit coefficient as defined in [20] $\mathrm{FIT}(\tau,\bar{\tau},h,A)$ given by (10) for the first system and the correlation coefficient between the data and the identified model $\rho(\tau,\bar{\tau},h,A)$ given by (11) for the first system.

$$\varepsilon(\tau,\bar{\tau},h,A) = \|x - x^{simu}(\tau,\bar{\tau},h,A)\| \tag{9}$$

$$\mathrm{FIT}(\tau,\bar{\tau},h,A) = 1 - \sqrt{\frac{\sum_{k=1}^{N}(y_k - y_k^{\mathrm{simu}})^2}{\sum_{k=1}^{N}(y_k - \bar{y}_k)^2}} \tag{10}$$

$$\rho(\tau,\bar{\tau},h,A) = \frac{\mathrm{cov}(x,x^{simu})}{\sigma_x \sigma_{x^{simu}}} \tag{11}$$

where $x = [y_0, y_1, \ldots, y_N]^T$ is the vector of data and $x_1^{sim}(\tau,\bar{\tau},h,A_1)$ is the vector obtained by simulating the system using the identified coefficients, y_k is the measured system output (data) at sample k, y_k^{simu} is the simulated system output at sample k using the identified coefficients and $\bar{y}_k$ is the average of the measured system output (therefore constant signal). cov(X,Y) is the covariance matrix between the vectors X and Y and σ_X is the standard deviation of the vector X.

Please note that, for the system with fixed input delays, we will note these indicators ε_1, FIT_1 and ρ_1 and for the system with state-dependent input delays we will note them ε_2, FIT_2 and ρ_2.

As the fixed delays τ, $\bar{\tau}$ and h and the multiplicative factor f, are still to be determined, we can run an optimization algorithm that minimizes ε in order to find these delays. The chosen algorithm is NOMAD (Nonlinear Optimization with the MADS Algorithm), which is based on the Mesh Adaptative Direct Search (MADS) algorithm. It is capable of blackbox optimization for nonlinear objective functions, with linear and nonlinear equalities and inequalities constraints on continuous, integer or binary variables. NOMAD and the MADS algorithm are very well documented as it can be seen in [21], [16], [22], [23]. NOMAD is implementend in the Opti Toolbox for Matlab, see [24]. For comparison, using Matlab's Genetic Algorithm (ga function) and NOMAD for a maximum of 4000 iterations on a delay optimization problem on the 4 concatened sets gives the following cost functions values : between 1.26 and 1.267 for GA (over 10 tests, it may vary at each test) and 1.2576 for NOMAD. With default settings, NOMAD stops after 4545 functions counts with an objective function value of 1.2571 whereas GA stops after 5200 to 5500 functions counts (over 10 tests) with objective function value of 1.2593 to 1.2643. **Therefore, NOMAD has better performance (lower objective function value), is faster (1000 less function evaluations in the previous test) and is more reliable (every test gives the same results).**

The overall algorithm that is used is described as follows:

1) Start
2) Use NOMAD to find the optimal set of delays
3) Calculate the coefficients with the determined set of delays
4) Test the coefficients by simulating the model
5) end

To obtain identified coefficient that best fit the 4 sets of data, and by extension the sets generated for different pulsed inputs, we will apply the identification process to the concatenation of the 4 sets. Notice that each set is ended by a series of 0 for both input and output and for a duration of 1.5s over a total of 10s, the concatenation is possible and the system will have enough time to go back to 0 between each set.

The identification process can finally be applied, leading to Fig. 9 for the simulation results of data set N°3 using identified coefficients. For the 4 concatenated data sets, the least-square errors are $\varepsilon_1 = 10.1529$ for the model with constant input delay and $\varepsilon_2 = 9.7349$ for the model with state-dependent input delay.

The values of the delays values and the identified coefficients can be found in the TABLE II for $N_1 = 5$, $N_2 = 10$ and $N_3 = 1$. Is is noticeable that the L_2 norm of the state-dependent input delay model is smaller that the one with fixed delay as it can be seen in the TABLE I, where the f stands for the frequency of the pulses and DC for the duty cycle in case of pulsed input signals.

Comparing to [20], we can see that our fit coefficients are close to the higher coefficients found in the paper. It is noticeable, even if the data are different from the ones used here, that they obtain the best fit coefficients for quasi constant data and for other type of data it rapidly falls under 70% while here the fit coefficients remain around 90% for constant of varying inputs with various frequencies and duty cycles. To the author knowledge, there is no other paper presenting model identification with data similar to the ones presented here.

In TABLE I it is noticeable that the correlation coefficient between data and model output is very high, typically around 99.7%, meaning that our model capture well enough the dynamics of the data.

C. Averaged model

Based on the idea used to develop $\widetilde{y}$ for the state dependent delay identification, we can develop an averaged model using equations (12) and (13). This model will ease the development of control on the system by separating the part with slow dynamics (averaged part) from the one with fast dynamics (difference between non-averaged and averaged part).

$$y_k^{avg} = \frac{1}{W}\sum_{i=0}^{W-1} y_{k-i} \tag{12}$$

$$u_k^{avg} = \frac{1}{W}\sum_{i=0}^{W-1} u_{k-i} \tag{13}$$

The averaged models are given by (14) and (15).

TABLE I: Comparison of L_2 norm values, FIT coefficients and correlation for state-dependent and fixed input delay models for the complete model

Set of data	Fixed delay			State-dependent delay		
	ε_1	FIT_1	ρ_1	ε_2	FIT_2	ρ_2
Data set N°1 (constant)	4.78	90.43%	0.9981	4.69	90.61%	0.9984
Data set N°2 ($f = 4Hz$, $DC = 50\%$)	6.24	87.62%	0.9964	5.70	88.70%	0.9958
Data set N°3 ($f = 4Hz$, $DC = 80\%$)	3.00	94.03%	0.9984	3.07	93.90%	0.9985
Data set N°4 ($f = 8Hz$, $DC = 50\%$)	5.63	88.76%	0.9961	5.10	89.82%	0.9965
Data set not used in identification N°1 (constant)	5.33	89.58%	0.9958	5.30	89.65%	0.9959
Data set not used in identification N°2 ($f = 8Hz$, $DC = 80\%$)	3.77	92.53%	0.9972	4.01	92.04%	0.9969
Concatenated data sets	10.13	89.91%	0.9950	9.48	90.55%	0.9955

TABLE II: Values of the delays and identified coefficients (all values have No Unit) for the complete model

	Fixed delay	State-dependent delay
τ_i	$\begin{bmatrix} 1 & 48 & 352 & 371 & 496 \end{bmatrix}$	$\begin{bmatrix} 1 & 44 & 123 & 479 & 496 \end{bmatrix}$
$\bar{\tau}_i$	$\begin{bmatrix} 1 & 66 & 242 & 249 & 260 & \dots \\ \dots & 276 & 300 & 409 & 475 & 491 \end{bmatrix}$	$\begin{bmatrix} 1 & 73 & 242 & 264 & 299 & \dots \\ \dots & 335 & 414 & 477 & 494 & 500 \end{bmatrix}$
h_l	49	$f = 1$
a_i	$\begin{bmatrix} 0.9744 & 0.0171 & -0.0028 \\ \dots & 0.0040 & 0.0009 \end{bmatrix}$	$\begin{bmatrix} 0.9759 & 0.0141 & 0.0025 \\ \dots & -0.0042 & 0.0055 \end{bmatrix}$
b_l	0.0063	0.0080
c_{jl}	$\begin{bmatrix} -0.0116 & 0.0070 & 0.0483 & 0.0253 \\ \dots & -0.0455 & -0.0243 & -0.0038 \\ \dots & -0.0014 & -0.0074 & 0.0138 \end{bmatrix}$	$\begin{bmatrix} -0.0228 & 0.0138 & 0.0621 & -0.0286 \\ \dots & -0.0186 & -0.0121 & -0.0035 \\ \dots & -0.0056 & 0.0189 & -0.0049 \end{bmatrix}$

$$y_{k+1}^{avg} = \sum_{i=1}^{N_1} \left(a_i^{avg} y_{k-\tau_i^{avg}}^{avg} \right) + \sum_{l=1}^{N_3} \left(b_l^{avg} + \sum_{j=1}^{N_2} \left(c_{jl}^{avg} y_{k-\bar{\tau}_j^{avg}}^{avg} \right) \right) u_{k-h_l^{avg}}^{avg} \tag{14}$$

$$y_{k+1}^{avg} = \sum_{i=1}^{N_1} \left(a_i^{avg} y_{k-\tau_i^{avg}}^{avg} \right) + \sum_{l=1}^{N_3} \left(b_l^{avg} + \sum_{j=1}^{N_2} \left(c_{jl}^{avg} y_{k-\bar{\tau}_j^{avg}}^{avg} \right) \right) u_{k-\tilde{h}_l^{avg}(y_k^{avg})}^{avg} \tag{15}$$

For $N_1 = 2$, $N_2 = 2$ and $N_3 = 2$, the delays and identified coefficients for the averaged model are presented in the TABLE IV. As it can be seen in the TABLE III, applying the same analysis as before for the compelete model, it is noticeable that the L_2 norm of the state-dependent input delay model is smaller that the one with fixed delay as for the complete model. In the same way, the fit coefficients remain around 92% for constant of varying inputs with various frequencies and duty cycles which is typically higher than the values obtained in [20] and that the correlation coefficient between data and model output is very high, typically around 99.9%, meaning that our model capture well enough the dynamics of the averaged data.

As for the non-averaged model, Fig. 10 presents the simulation results of the averaged data set N°2 using identified coefficients for the averaged model. For the 4 concatenated data sets, the least-square errors are $\varepsilon_1 = 5.5275$ for the averaged model with constant input delay and $\varepsilon_2 = 4.8734$ for the averaged model with state-dependent input delay. Again, the model using state dependent input delays gives better performances in term of the L_2 norm. It is to be noted that a longer series of 0 have been added at the end of each data set than in the non averaged case, in order to ensure that the averaged system has enough time to go back to 0 between each set.

TABLE III: Comparison of L_2 norm values, FIT coefficients and correlation for state-dependent and fixed input delay models for the averaged model

Set of data	Fixed delay			State-dependent delay		
	ε_1	FIT_1	ρ_1	ε_2	FIT_2	ρ_2
Data set N°1 (constant)	2.57	94.84%	0.9991	2.32	95.34%	0.9992
Data set N°2 ($f = 4Hz$, $DC = 50\%$)	6.82	86.21%	0.9979	2.72	94.49%	0.9987
Data set N°3 ($f = 4Hz$, $DC = 80\%$)	3.19	93.63%	0.9994	1.62	96.77%	0.9995
Data set N°4 ($f = 8Hz$, $DC = 50\%$)	5.76	88.38%	0.9976	2.90	94.14%	0.9987
Data set not used in identification N°1 (constant)	4.05	92.07%	0.9978	2.83	94.45%	0.9985
Data set not used in identification N°2 ($f = 8Hz$, $DC = 80\%$)	3.40	93.25%	0.9990	2.45	95.12%	0.9991
Concatenated data sets	10.23	89.72%	0.9969	4.87	95.10%	0.9988

TABLE IV: Values of the delays and identified coefficients for the averaged model (all values have No Unit) for the averaged model

	Fixed delay	State-dependent delay
τ_i^{avg}	$\begin{bmatrix} 1 \\ 269 \end{bmatrix}$	$\begin{bmatrix} 6 \\ 384 \end{bmatrix}$
$\bar{\tau}_i^{avg}$	$\begin{bmatrix} 1 \\ 307 \end{bmatrix}$	$\begin{bmatrix} 6 \\ 454 \end{bmatrix}$
h_l^{avg}	$\begin{bmatrix} 49 \\ 417 \end{bmatrix}$	$f^{avg} = \begin{bmatrix} 1.5513 \\ 106.7560 \end{bmatrix}$
a_i^{avg}	$\begin{bmatrix} 1.0027 \\ -0.0027 \end{bmatrix}$	$\begin{bmatrix} 1.0117 \\ -0.0121 \end{bmatrix}$
b_l^{avg}	$\begin{bmatrix} 0.0009 \\ 0.0030 \end{bmatrix}$	$\begin{bmatrix} 0.0096 \\ 0.0000 \end{bmatrix}$
c_{jl}^{avg}	$\begin{bmatrix} -0.0008 \\ 0.0045 \\ -0.0085 \\ 0.0010 \end{bmatrix}$	$\begin{bmatrix} -0.0179 \\ 0.0088 \\ -0.0490 \\ 0.0208 \end{bmatrix}$

D. Identification results

Now that the identification is completed, we can apply the identified models to each data set separately. Fig. 9 depicts the outputs of the model and real plant for the data set N°2. In the same way, Fig. 10 depicts the outputs of the averaged identified model for data set N°2.

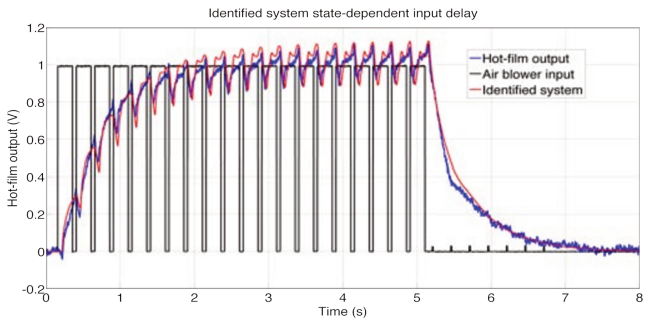

Fig. 9: Identified model with state-dependent input delay, zoom on data set N°3

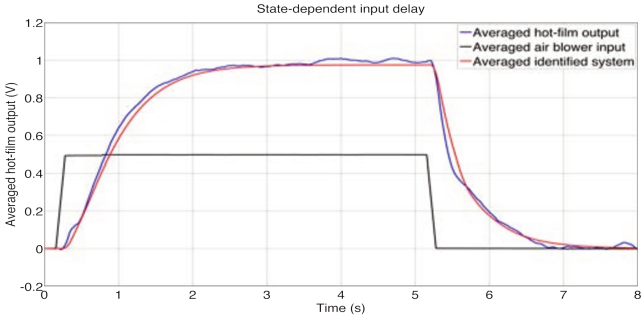

Fig. 10: Averaged identified model with state-dependent input delay, zoom on data set N°3

It can be seen that both models follow closely enough the data but, again, **the model using state-dependent input delay is better.** There are some inaccuracies mainly around peaks but these are caused partly by noise in the data signal, the fact that we wish to fit several type of input-output and the simplicity of our model as we do need seek exact fitting but good tendency estimation, which is what we get here.

IV. CONCLUSIONS AND FUTURE WORKS

The identification of a highly nonlinear model using a discrete bilinear state and input delayed system has been proposed. Two cases have been presented : one where the input delay is constant and one where it is state-dependent. The results showed that the state-dependent case is more reliable in the L_2 sense for simulation.

The next step concerns the application to close-loop control : our ongoing work, presently limited to simulation, shows these model can have a valuable contribution to flow control. However, due to length constrain and preliminary nature of this extension, we do not consider it here. We will only show a plot in Fig. 11 obtained in simulation of the effect of a control designed in order to maximize the friction gain of the averaged model. It can be observed that the friction gain takes values higher than 1, with an average around 1.2, resulting in a approximately 20% increase compared to the control signals used previously. Then, the design of an appropriate nonlinear control can lead to improvement in the friction gain and then in the reattachment of the separation.

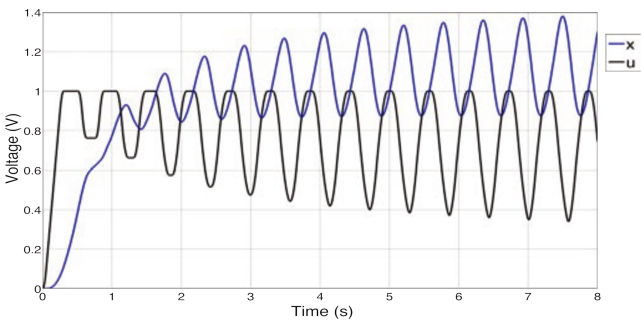

Fig. 11: Testing of a nonlinear control input

V. ACKNOWLEDGMENTS

This work was supported by the Région Nord Pas-de-Calais in the framework of the ELSAT-CISIT program.

REFERENCES

[1] C. Raibaudo, F. Kerherve, and M. Stanislas, "Characterisation of the transient dynamics of a controlled separated flow using phase averaged PIV," in *International Conference on Instability and Control of Massively Separated Flows – ICOMASEF*, 2013.

[2] C. Raibaudo, A. Polyakov, D. Efimov, F. Kerherve, J.-P. Richard, and M. Stanislas, "Experimental closed-loop control of a detached boundary layer at high Reynolds number," in *10th EUROMECH Fluid Mechanics Conference*, 2014.

[3] T. Chabert, J. Dandois, É. Garnier, and L. Jacquin, "Experimental detection of flow separation over a plain flap by wall shear stress analysis with and without steady blowing," *Comptes Rendus Mécanique*, vol. 342, no. 6, pp. 389–402, 2014.

[4] T. Chabert, J. Dandois, and É. Garnier, "Experimental closed-loop control of flow separation over a plain flap using slope seeking," *Experiments in Fluids*, vol. 55, no. 8, pp. 1–19, 2014.

[5] T. Shaqarin, C. Braud, S. Coudert, and M. Stanislas, "Open and closed-loop experiments to identify the separated flow dynamics of a thick turbulent boundary layer," *Experiments in Fluids*, vol. 54, pp. 1–22, Jan. 2013.

[6] G. V. Selby, J. C. Lin, and F. G. Howard, "Control of low-speed turbulent separated flow using jet vortex generators," *Experiments in Fluids*, vol. 12, pp. 394–400, Apr. 1992.

[7] K. B. Chun and H. J. Sung, "Control of turbulent separated flow over a backward-facing step by local forcing," *Experiments in Fluids*, vol. 21, pp. 417–426, Nov. 1996.

[8] E. Åkervik, J. Hoepffner, U. Ehrenstein, and D. S. Henningson, "Model reduction and control of a cavity-driven separated boundary layer," in *IUTAM Symposium on Flow Control and MEMS*, pp. 147–155, Springer, 2008. bibtex: akervik_model_2008.

[9] D. Wachsmuth, *Optimal control of the unsteady Navier-Stokes equations*. PhD thesis, PhD thesis, Technische Universität Berlin, 2006.

[10] O. Ghattas and J.-H. Bark, "Optimal Control of Two- and Three-Dimensional Incompressible Navier–Stokes Flows," *Journal of Computational Physics*, vol. 136, pp. 231–244, Sept. 1997.

[11] E. Fernández-Cara, S. Guerrero, O. Y. Imanuvilov, and J. P. Puel, "Local exact controllability of the Navier–Stokes system," *Journal de Mathématiques Pures et Appliquées*, vol. 83, pp. 1501–1542, Dec. 2004.

[12] H. Jin-quan and F. Lewis, "Neural-network predictive control for nonlinear dynamic systems with time-delay," *IEEE Transactions on Neural Networks*, vol. 14, pp. 377–389, Mar. 2003.

[13] S. C. Jeong and P. Park, "Constrained MPC algorithm for uncertain time-varying systems with state-delay," *IEEE Transactions on Automatic Control*, vol. 50, pp. 257–263, Feb. 2005.

[14] M. V. Kothare, V. Balakrishnan, and M. Morari, "Robust constrained model predictive control using linear matrix inequalities," *Automatica*, vol. 32, pp. 1361–1379, Oct. 1996.

[15] G. M. Schoen, *Stability and stabilization of time-delay systems*. PhD thesis, Swiss Federal Institute of Technology Zurich, 1995.

[16] S. Le Digabel, "Algorithm 909: NOMAD: Nonlinear optimization with the MADS algorithm," *ACM Transactions on Mathematical Software (TOMS)*, vol. 37, no. 4, p. 44, 2011.

[17] F. Veysset, L. Belkoura, P. Coton, and J.-P. Richard, "Delay system identification applied to the longitudinal flight of an aircraft through a vertical gust," in *14th Mediterranean Conference on Control and Automation, 2006. MED '06*, pp. 1–6, June 2006.

[18] J. Carlier and M. Stanislas, "Experimental study of eddy structures in a turbulent boundary layer using particle image velocimetry," *Journal of Fluid Mechanics*, vol. 535, pp. 143–188, July 2005.

[19] L. Ljung, *System identification - Theory for the User*. Prentice-Hall, 1999.

[20] J. Dandois, E. Garnier, and P.-Y. Pamart, "NARX modelling of unsteady separation control," *Experiments in fluids*, vol. 54, no. 2, pp. 1–17, 2013.

[21] C. Audet, J. E. D. Jr, and S. L. Digabel, "Globalization strategies for Mesh Adaptive Direct Search," *Computational Optimization and Applications*, vol. 46, pp. 193–215, June 2009.

[22] C. Audet, V. Béchard, and S. L. Digabel, "Nonsmooth optimization through Mesh Adaptive Direct Search and Variable Neighborhood Search," *Journal of Global Optimization*, vol. 41, pp. 299–318, Oct. 2007.

[23] C. Audet and J. Dennis, "Mesh Adaptive Direct Search Algorithms for Constrained Optimization," *SIAM Journal on Optimization*, vol. 17, pp. 188–217, Jan. 2006.

[24] J. Currie and D. I. Wilson, "OPTI: Lowering the Barrier Between Open Source Optimizers and the Industrial MATLAB User," in *Foundations of Computer-Aided Process Operations* (N. Sahinidis and J. Pinto, eds.), (Savannah, Georgia, USA), Jan. 2012.

D.2 Paper published in the International Journal of Robust and Nonlinear Control

INTERNATIONAL JOURNAL OF ROBUST AND NONLINEAR CONTROL
Int. J. Robust Nonlinear Control (2017)
Published online in Wiley Online Library (wileyonlinelibrary.com). DOI: 10.1002/rnc.3843

SISO model-based control of separated flows: Sliding mode and optimal control approaches

Maxime Feingesicht[1,2,3,*,†], Andrey Polyakov[1,2], Franck Kerhervé[4] and Jean-Pierre Richard[1,2,3]

[1]*Inria Lille Nord Europe, Parc Scientifique de la Haute Borne, Villeneuve-d'Ascq 59650, France*
[2]*CRIStAL UMR CNRS 9189, Centrale Lille, Villeneuve d'Ascq 59651, France*
[3]*Centrale Lille, Villeneuve-d'Ascq 59651, France*
[4]*Institut P', CNRS UPR 3346, Universit de Poitiers, Futuroscope Chasseneuil Cedex F86962, France*

SUMMARY

The challenging problem of active control of separated flows is tackled in the present paper using model-based design principles and applied to data issued from a two-dimensional separated flow experiment. First, a bilinear state and input delay model of the system has been obtained from experimental data by means of a modified identification procedure. Adequacy and precision of the obtained model are demonstrated and compared with existing results. Next, two control problems (setpoint tracking and optimal control) have been formulated and studied using sliding mode control methodology and averaging analysis. The theoretical control results are supported with numerical simulations. Copyright © 2017 John Wiley & Sons, Ltd.

Received 7 October 2016; Revised 3 February 2017; Accepted 12 April 2017

KEY WORDS: sliding mode control; bilinear time-delay systems; flow control

1. INTRODUCTION

Control problems for separated turbulent flow are of great interest in the view of many modern challenges [1]. For example, aerodynamic losses are believed to be one of the main source of energy wastage for a vehicle at speeds higher than 50 km/h. According to the existing ecological estimates, the reduction of these losses at 25% will decrease pollution for more than 10^7 tonnes of CO_2 per year. Optimization of the vehicles' shapes remains the preferred solution for reducing aerodynamic losses (or drag) because of turbulence-related mechanisms such as flow separation. Such optimization constitutes a passive control approach that cannot lead to an optimal solution, in particular when the incoming flow faces dramatic changes because of large unsteady events. Other passive control solutions include fixed objects such as small delta wings or so-called vortex generators located on the vehicle surface in order to manipulate the boundary layer (see [2] and [3] for extensive reviews). Such strategy requires generally extensive parametric studies to find the geometrical parameters (dimensions and locations) of the actuators leading to a solution that can only be optimal for a limited range of flow conditions. In such a context, active control strategies [1, 4–8] implying actuators interacting with the flow and whose control parameters can be varied online to maintain an optimal solution leading to minimization of the aerodynamic losses constitute an attractive solution.

Fluidic actuators are the most encountered solutions in turbulent flow control applications, at least at the academic level (e.g. [9–11]). Flow separation occurring because of a large adverse pressure gradient such as observed for two-dimensional flap ([12–16]) constitutes one of the standard

*Correspondence to: Maxime Feingesicht, Inria Lille Nord Europe, Parc Scientifique de la Haute Borne, 40 Avenue du Halley Bat. A, Park Plaza, 59650 Villeneuve-d'Ascq, France.
†E-mail: maxime.feingesicht@inria.fr

Copyright © 2017 John Wiley & Sons, Ltd.

benchmark for development of new actuators or advanced control strategies [4, 5, 17, 18] and [19]. This configuration will be considered in the present paper as a test case to apply recently developed methods of the Control Theory.

The main difficulty of turbulence control is that the behavior of the physics underlying the plant (here designing the flow system) is highly nonlinear. The flow dynamics are effectively driven by the Navier–Stokes equation which is a distributed parameter model. Implementation of controllers or observers for such infinite dimensional systems needs huge computational resources, which cannot be provided in real-time [20–22].

Various strategies for separated flow control can be found in the literature. The most of them use very local (linear) models [6–8] (i.e., basically skip nonlinear turbulent dynamics) and deal mainly with feedforward control [4, 5, 17, 18] and [19]. In this context, the recent control design approach based on machine learning (model-free) techniques [23] looks rather promising among others. However, long series of repeated experiments are required for its proper tuning. In addition, the machine learning approach leaves open a question of robustness of the designed control, and the convergence is not totally proven. A recent survey about various approaches to flow control design is given by Brunton and Noack [1]. Model-based robust control of separated flows remains of particular interest and can be implemented in real system without too much complexity. One of the objectives of the present paper is to study new perspectives in this topic.

To design a practically realizable control law, a sufficiently simple model of the plant should be constructed. For this purpose, the paper uses a modified gray-box identification technique and constructs a model that adequately describes an input/output behavior of the flow control system. The obtained model is bilinear and presented by difference-differential equation with state/input delays. One more feature of the control system under consideration is relay ('ON'/'OFF') actuation provided by pulsed jets (air blowers). The preliminary results on modeling of the control system of separated flows can be found in [24].

The present paper is focused on development of control strategies by means of applying appropriate mathematical methods to the obtained bilinear time-delay model, so its main contribution is theoretical. In particular, an optimal control problem is formulated, and a scheme for a sub-optimal feedforward periodic control design is developed based on averaging analysis. Next, a setpoint tracking algorithm is designed using a sliding mode control methodology [25–29] jointly with a prediction technique (e.g., [30, 31]). The choice of sliding mode control technique is motivated by the nature of the actuators used in the experiments, which can only be turned on or off, such as relays. It is well known [25] that the sliding mode is the usual operation mode of relay control systems. Relay control and/or sliding mode control systems with delays are studied, for example, in [32, 33]. Despite of the fact that bilinear systems were considered in literature (e.g., [34]), to the best of our knowledge, the considered control problems for bilinear models with state and input delays have never been studied before.

Notation:

- $\mathbb{R}$ is the set of real numbers, $\mathbb{R}_+ = \{x \in \mathbb{R} \mid x \geqslant 0\}$;
- $\mathbf{C}_\Omega$ is the space of continuous functions;
- $\mathbb{1} \in \mathbf{C}_\Omega$ is the unit constant function: $\mathbb{1}(s) = 1, \forall s \in \Omega$;
- $\mathbf{L}^2_\Omega$ is the space of quadratically integrable functions, $\|z\|_{\mathbf{L}^2_\Omega} = \sqrt{\int_\Omega z^2(s)ds}$;
- $\mathbf{L}^\infty_\Omega$ is the space of locally measurable essentially bounded functions, $\|z\|_{L^\infty} = \operatorname*{ess\,sup}_{s\in\Omega} |z(s)|$;
- if $\tau > 0$, $y \in \mathbf{L}^\infty_\mathbb{R}$, and $t \in \mathbb{R}$, then $\xi_\tau(t) \in \mathbf{L}^\infty_{[-\tau,0]} : (y_\tau(t))(\sigma) = y(t+\sigma)$ for $\sigma \in [-\tau, 0]$. The notation $y_\tau(t)$ and $y_{-\tau}(t)$ is commonly used for time-delay models [35].

2. FLOW CONTROL SYSTEM

2.1. Flow control problem

The problem of flow control is basically the meeting point of three research areas [1]:

1. Fluid mechanics (for analysis of flow dynamics and formulation of control goals),

Copyright © 2017 John Wiley & Sons, Ltd.

DOI: 10.1002/rnc

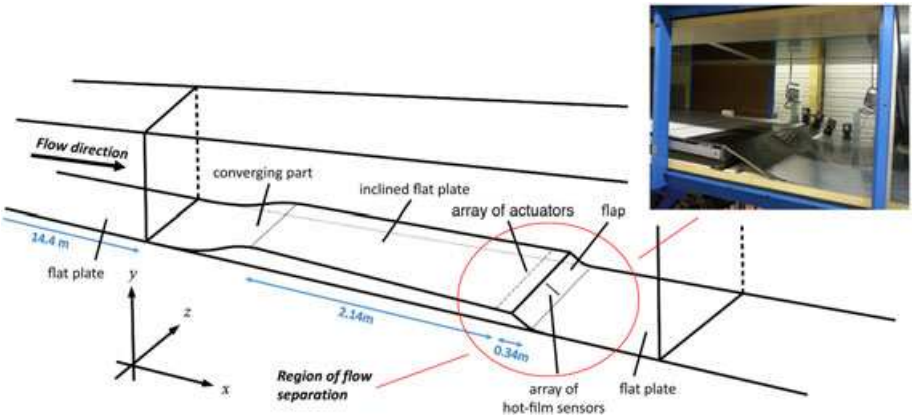

Figure 1. Diagram and photo of the experimental setup courtesy of Laboratoire de Mécanique de Lille. [Colour figure can be viewed at wileyonlinelibrary.com]

2. Electronics (for sensing and actuation developments),
3. Control theory and optimization (for designing of control laws).

Flow control experimental setup is generally designed and assembled based on current technological achievements in the field of fluid dynamics and electrical engineering. In such a context, the operator cannot have any impact on the setup, except on the control parameters that drive the actuators. The problem resulting is therefore to optimize efficiency and robustness of the controller by designing appropriate control algorithms.

To the best of our knowledge, the paper presents the first attempt in the context of nonlinear (in particular, bilinear) single input single output (SISO) model-based control design for separated flows. It deals with two classical control paradigms: open-loop (feedforward) and closed-loop (feedback). While an optimal control problem is studied in the open-loop context, sliding mode methodology is applied in order to design robust feedback that tracks a given setpoint.

2.2. *Experimental test case*

The experimental test case considered is that of a turbulent boundary layer flow occurring separation along a two-dimensional ramp whose geometry and dimensions are illustrated in Figure 1. Full details of the experiments, which were conducted in the large boundary layer wind tunnel at Laboratoire de Mécanique de Lille (France) can be found in [36, 37]. The boundary layer flow first develops along a flat horizontal plate (floor of the wind tunnel) before reaching a smooth convergent where it occurs acceleration. The flow continues to develop along a slightly inclined flat plate to recover a zero pressure streamwise gradient. This is followed by a flap along which the boundary layer occurs separation and reattaches further downstream to the floor of the wind tunnel. This is illustrated in Figure 2(b) where streamlines for the averaged natural flow are reported. Note that the flow comes from the left of the figure. The ramp geometry is shown as the thick black line. In the present configuration, the location where the flow separates from the wall is fixed and located at the edge between the inclined flat plate and the flap (chosen as origin of the coordinate system in Figure 2). Just downstream of the edge, a shear layer forms, and a recirculation region (reversed flow) appears along the flap because of flow separation. The border between positive and negative streamwise mean velocity is represented as the blue line. Below this blue line, the flow is, in average, reversed compared with the flow above the line. The flow in this separation region constitutes the physical system of interest and to control, the main objective of the control being to reduce the recirculation region.

An array of 22 co-rotating round jets acting as air blowers, aligned parallel to the flap edge is used as actuators. The control input $u(t)$ is a relay ('on'/'off') signal sent to the actuators with a given frequency and duty cycle. An example of the averaged flow obtained when using continuous actuation (relay remains 'ON') is illustrated in Figure 2(a). Compared with the natural flow discussed

Copyright © 2017 John Wiley & Sons, Ltd.

DOI: 10.1002/rnc

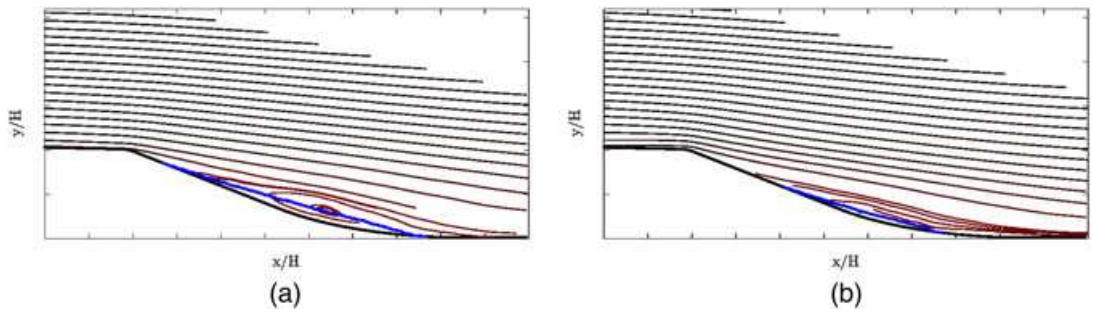

Figure 2. Streamlines for (a) the natural flow without control and (b) the flow under continuous actuation. The blue line represents the border between the reversed flow (negative streamwise velocity, region of the flow below the line) and the freestream (positive streamwise velocity, region of the flow above the line). In the controlled case (b), the recirculation region is shown to be drastically reduced and the flow almost fully reattached to the wall. [Colour figure can be viewed at wileyonlinelibrary.com]

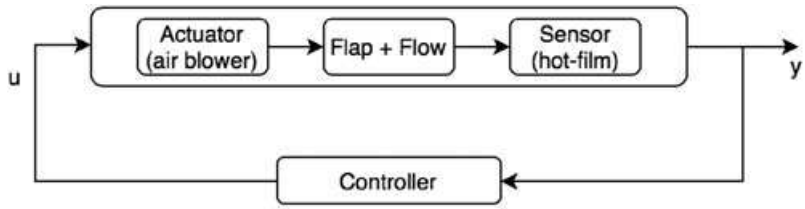

Figure 3. Feedback scheme.

previously and shown in Figure 2(b), the region of reversed flow is drastically reduced, and the flow is found to be almost fully attached to the bottom wall.

For real-time survey, hot-film sensors located along the flap are used to measure the gain in skin friction: an increase in friction gain being representative of flow reattachment. In the present configuration, output voltages of hot-film sensors are the only signals that can be measured in on-line and utilized for control proposes. The output voltages of the sensors are constants in the steady state. From the point of view of Control Theory, the control problem examined here admits conventional interpretation given in Figure 3.

2.3. *Control aims*

2.3.1. Setpoint tracking control. Based on flow velocity surveys (not detailed in the present paper), the capability of the actuators to reattach the flow to the wall has been shown by Raibaudo [36, 37] to be well characterized by skin friction gain measured by the hot-film sensors. Therefore, the first control problem to be studied here is stabilization of the output y at the desired setpoint y^*. The relay nature of actuators motivates us to apply sliding mode principles in order to design a robust feedback law, which guarantees $y(t) \to y^*$ as $t \to \infty$.

2.3.2. Optimal control. Let us consider the cost functional

$$J(y,u) = \lim_{T\to+\infty} \frac{1}{T}\int_0^T \alpha y(s) - (1-\alpha)u(s)ds \tag{1}$$

with $0 \leqslant \alpha \leqslant 1$, which characterizes the averaged value of y in the steady state and the averaged control value required to obtain it. Because increasing of the output y implies better reduction of turbulence [12] and our objective is to reattach the flow as much as possible, we also study the problem: to design a control law u such that

$$J(y,u) \to \max . \tag{2}$$

The trade-off between the turbulence reduction and the energy consumed by the actuation is provided by the choice of the parameter α.

Copyright © 2017 John Wiley & Sons, Ltd.

DOI: 10.1002/rnc

3. INPUT-OUTPUT MODELING OF FLOW SEPARATION

3.1. Experimental data and pre-processing

The only data we can use for modeling are the input signals to the actuators and the output voltages of the hot-film sensors measured with a frequency of 1 kHz. Therefore, we cannot design a model separately for actuator, sensor, and plant, but our model will implicitly include them all.

Several experiments have been performed in order to collect an experimental database appropriate for model design. Each experiment consists of two phases: actuation and relaxation. Actuation is performed by means of a periodic on/off input signal u with a fixed frequency and duty cycle (DC). Actuation time is 5 s. Seven different input signals have been tested: (1) constant input; (2) Freq = 4 Hz with DC = 50%; (3) Freq = 4 Hz with DC = 80%; (4) Freq = 8 Hz with DC = 50%; (5) Freq = 8 Hz with DC = 80%; (6) Freq = 80 Hz with DC = 50%; (6) Freq = 80 Hz with DC = 80%.

During the relaxation phase, the control is switched off for 5 s in order to let the flow to return to a natural steady separated state. Each experiment is repeated for more than 50 times, and the results are phase averaged in order to obtain an output signal less effected by measurement noises and exogenous perturbations. This phase-averaged data (Figure 4) is utilized for modeling.

3.2. Bilinear model

The dynamics of the flow considered here are highly nonlinear and governed by partial differential equations (e.g., Navier–Stokes equations). The only SISO model can be designed using the experimental dataset. However, this model should take into account nonlinearity and an infinite dimensional nature of the control system. That is why we identify an appropriate model from the class of bilinear control systems governed by differential equations with time delays (i.e., differential-difference equations):

$$\dot{y}(t) = \sum_{i=1}^{N_1} a_i y(t-\tau_i) + \sum_{k=1}^{N_2} \left(b_k + \sum_{j=1}^{N_3} c_{jk} y(t-\tilde{\tau}_j) \right) u_i(t-h_k), \tag{3}$$

where N_1, N_2, and N_3 are nonnegative integers, $a_i, b_i, c_{ij} \in \mathbb{R}$ are constant parameters, and both state $\tau_i, \tilde{\tau}_j$ and input delays h_i are considered in order to capture as much as possible the infinite dimensional dynamics of the system. However, this model is sufficiently simple and of small order to design some practically implementable control laws.

The identification has been performed using a least-square method supported with global optimization algorithm NOMAD (nonlinear optimization by mesh adaptive direct search) [38–41] required for optimal assignment of delays. The reader can refer to [24] for more details about identification of the considered bilinear model.

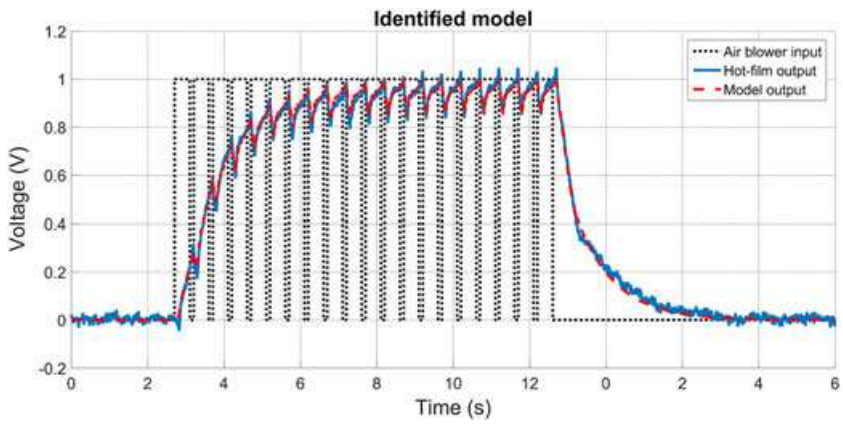

Figure 4. Phase-averaged data for Freq = 4 Hz, DC = 80%. [Colour figure can be viewed at wileyonlinelibrary.com]

Copyright © 2017 John Wiley & Sons, Ltd.

DOI: 10.1002/rnc

Table I. Precision of the identified models.

	ε	FIT(%)	ρ
$N_3 = 1$	0.0495	87.56	0.9926
$N_3 = 2$	0.0341	91.44	0.9965

Table II. Identified parameters of the models.

	$N_3 = 1$	$N_3 = 2$
τ_i	[0.054; 0.006]	[0; 0.116]
$\bar{\tau}_j$	[0.054; 0.360]	[0.036; 0.001]
h_k	0.054	[0.045; 0.315]
a_i	[9.6468; −12.6195]	[−11.7146; 7.9658]
b_k	3.5632	[4.4759; 0.3652]
c_{jk}	[−2.6470; 2.6470]	[29.1680; −28.7925; −24.1864; 23.4018]

3.3. *Results of identification*

The bilinear models have been identified for $N_1 = N_2 = 2$ and $N_3 = 1$ or 2. The precision of the models has been analyzed using the three indicators: ϵ is L_2-norm of the error, FIT index[‡] introduced in [42], and ρ the correlation between the experimental data and the identified model.

$$\epsilon = \|y_{\text{exp}} - y_{\text{sim}}\|_{\mathbf{L}^2}, \quad \rho = \frac{\text{cov}(y_{\text{exp}}, y_{\text{sim}})}{\sigma_{y_{\text{exp}}}\sigma_{y_{\text{sim}}}}, \quad \text{FIT} = \left(1 - \frac{\|y_{\text{exp}} - y_{\text{sim}}\|_{\mathbf{L}^2}}{\|y_{\text{exp}} - \bar{y}_{\text{exp}}\|_{\mathbf{L}^2}}\right) \times 100\%,$$

where y_{exp} is the output of the system obtained from the experiment, y_{sim} is the output generated by the identified bilinear model (3), $\bar{y}_{\text{exp}}$ is the mean value of y^{exp}, cov $\left(y_{\text{exp}}, y_{\text{sim}}\right)$ is the covariance of y_{exp} and y_{sim}, but $\sigma_{y_{\text{exp}}}$ and $\sigma_{y_{\text{sim}}}$ are standard deviations of y_{exp} and y_{sim}, respectively. The results are summarized in Tables I and II.

It is worth stressing that the obtained models have very high precision comparing with the existing results [42]. The FIT index is improved for almost 30% using the model with only eight parameters (Table I). The NARX (Nonlinear Autoregressive Exogenous Model) model obtained in [42] has hundreds of coefficients and FIT = 59%.

4. SETPOINT TRACKING CONTROL PROBLEM

4.1. *Plant model and basic assumptions*

For the design of a tracking control, we use the simplest model obtained during the identification procedure, namely,

$$\dot{y}(t) = a_1 y(t-h) - a_2 y(t-\tau) + (b - cy(t-h) + cy(t-\bar{\tau}))u(t-h), \tag{4}$$

$$y(s) = 0, \quad u(s) = 0 \quad \text{for} \quad s \leqslant 0, \tag{5}$$

where $a_1 > 0, a_2 > 0, b > 0, c > 0, \bar{\tau} > 0, h > 0$, and $\tau > 0$ are constant parameters, $y(t) \in \mathbb{R}$ is the output and $u \in \mathbf{L}^\infty_{\mathbb{R}} : u(t) \in \{0, 1\}, t \geqslant 0$ is the input. Note that for any $u \in L^\infty_{\mathbb{R}_+}$, the considered system has a unique Caratheodory solution [43] at least locally.

We deal with a model of physical system. To exclude non-feasible dynamics, we assume that the system (4), (5) has bounded positive solution for any input signal $u \in \mathbf{L}^\infty_{\mathbb{R}_+} : u(t) \in \{0, 1\}$. The sufficient condition of positivity and boundedness of solutions to the system (4) is given by the next proposition proven in Appendix.

[‡]FIT is the word 'fit' in capital letters

Copyright © 2017 John Wiley & Sons, Ltd.

DOI: 10.1002/rnc

Proposition 1
If $c < a_1$, $(a_1 + c)\tau < a_2\tau < \frac{1}{e}$ and $\tau \leqslant h \leqslant \bar{\tau}$, then the system (4), (5) is positive, and its solution is globally bounded for any input signal $u \in \mathbf{L}^\infty : u(t) \in \{0, 1\}$ as follows:

$$0 \leqslant y(t) < y_{\max} := \frac{b}{a_2 - a_1} \text{ for all } t \geqslant 0.$$

4.2. *Sliding mode control for time-delay bilinear system*

The conventional sliding mode control methodology [25–27] is developed for delay-free systems. We emphasize again that, in our case, the choice of sliding mode control was motivated by the fact that the actuator is relayed. In order to design the sliding mode control, we need to compensate input delay using, for example, the prediction technique (e.g., [30, 31, 44, 45]). Developed originally for linear plants, this idea can also be applied for bilinear systems under consideration.

A simple example of a predictor is given here:

Suppose that we study the positive system $\dot{x}(t) = ax(t) + bu(t - h)$ *with* $a < 0$, $b > 0$, *and* $u(t) \in \{0, 1\}$. *The maximum value of* $x(t)$ *is* $x_{\max} = -\frac{b}{a}$, *with* $0 < x(t) < x_{\max}$.

Consider the following prediction variable: $\sigma(t) = ax(t) + b\int_{t-h}^{t} u(s)ds$. *Its derivative is* $\dot{\sigma}(t) = ax(t) + bu(t)$. *Note that the control input u is not delayed with respect to the sliding variable* σ, *so the conventional sliding mode design scheme can be utilized* [25]. *Take* $u(t) = sign\,(\sigma(t) - \sigma^*) = \begin{cases} 1 \text{ if } \sigma(t) - \sigma^* < 0 \\ 0 \text{ if } \sigma(t) - \sigma^* > 0 \end{cases}$, *where* $\sigma^* = ax^* + b$ *and* $x^* \in (0, x_{\max})$ *is the desired value to track. If* $\sigma(t) > \sigma^*$, *then* $\dot{\sigma}(t) = ax(t) < 0$, *and if* $\sigma(t) < \sigma^*$, *then* $\dot{\sigma}(t) = ax(t) + b > ax_{\max} + b > 0$.

Therefore, $\frac{d}{dt}(\sigma(t) - \sigma^*)(\sigma(t) - \sigma^*) < 0$, *and according to* [25], *sliding mode arises on the surface* $\sigma(t) - \sigma^* = 0$ *in a finite time, that is,* $\sigma(t) = \sigma^*$ *for* $t > t^*$.

Assuming $\bar{\tau} > h$, we introduce the following sliding variable for our model, according to [31]

$$\sigma(t) = y(t) - a_2 \int_{t-\tau}^{t} y(s)ds + c \int_{t-\bar{\tau}+h}^{t} y(s)ds + \int_{t-h}^{t} a_1 y(s) + (b - cy(s) + cy(s - \bar{\tau} + h))u(s)ds. \quad (6)$$

Obviously, the variable σ satisfies the equation

$$\dot{\sigma}(t) = (a_1 - a_2 + c(1 - u(t)))y(t) + c(u(t) - 1)y(t - \bar{\tau} + h) + bu(t).$$

Proposition 2
If conditions of Proposition 1 hold and

$$Q(j\omega) \neq 0 \quad \text{for} \quad \omega \neq 0, \quad (7)$$

where $Q(s) = s + a_2 e^{-s\tau} - (a_2 - c)e^{-sh} - ce^{-s\bar{\tau}}$, $s \in \mathbb{C}$ and $j = \sqrt{-1}$, then the control law

$$u(t) = \begin{cases} 1 \text{ if } \sigma(t) < \sigma^*, \\ 0 \text{ if } \sigma(t) > \sigma^*, \end{cases} \quad (8)$$

with $\sigma^* = y^*(1 + a_2(h - \tau) + c(\bar{\tau} - h))$ and $y^* \in \left(0, \frac{b}{a_2 - a_1}\right)$ guarantees $y(t) \to y^*$ as $t \to +\infty$.

The proof of this proposition is given in Appendix, where it is shown that the control (8) guarantees finite-time convergence of the sliding variable $\sigma(t)$ to σ^*, so $\sigma(t) = \sigma^*$ for all $t \geqslant T$. It is worth stressing that when sliding mode arises, the system motion is governed by the infinite dimensional dynamic system

$$\sigma^* = y(t) + a_2 \int_{t-h}^{t-\tau} y(s)ds + c \int_{t-\bar{\tau}}^{t-h} y(s)ds.$$

This means that our sliding surface $\sigma = \sigma^*$ is 'infinite dimensional'. Using condition (7), it is proven that the output $y(t)$ tends to y^* asymptotically as $t \to \infty$.

Copyright © 2017 John Wiley & Sons, Ltd.

DOI: 10.1002/rnc

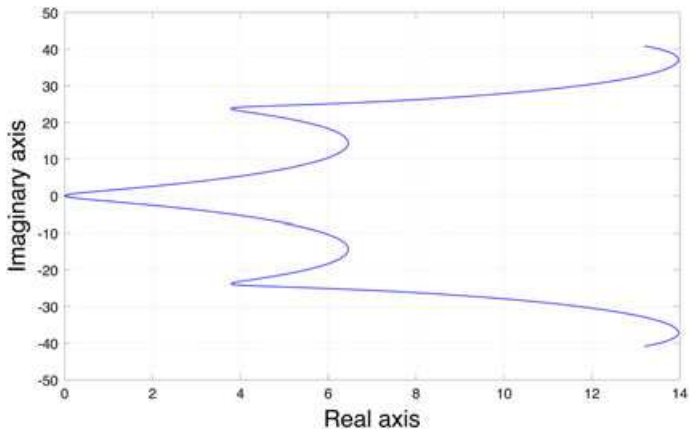

Figure 5. Parametric plot for $Q(j\omega)$ for $-2(a_2 + c) < \omega < +2(a_2 + c)$. [Colour figure can be viewed at wileyonlinelibrary.com]

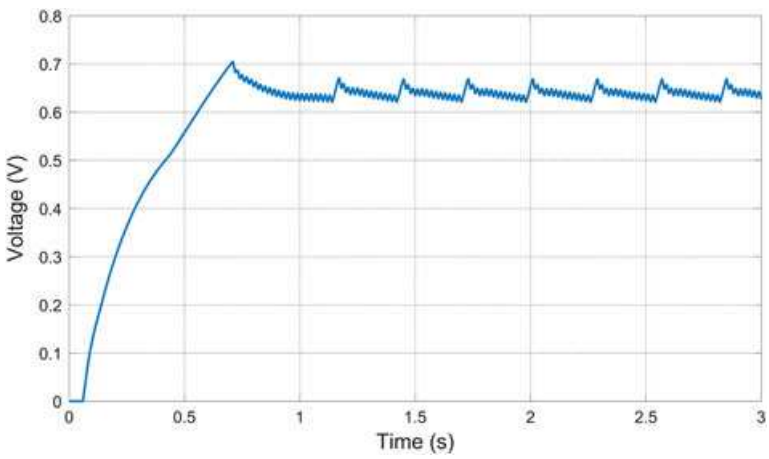

Figure 6. Application of the setpoint tracking control: output of the system. [Colour figure can be viewed at wileyonlinelibrary.com]

Remark 1
Because

$$Re(Q(j\omega)) = a_2 \cos(\tau\omega) - (a_2 - c)\cos(h\omega) - c\cos(\bar{\tau}\omega)$$
$$Im(Q(j\omega)) = \omega - a_2 \sin(\tau\omega) + (a_2 - c)\sin(h\omega) + c\sin(\bar{\tau}\omega),$$

then to check the condition (7), it is sufficient to consider $\omega \in (0, 2(a_2 + c)]$.

4.3. Numerical simulation of setpoint tracking control

Obviously, the plant model obtained by the identification (Table I, $N_3 = 1$) satisfies the proposition 1 with $a_1 = 9.6468$, $a_2 = 12.6195$, $c = 2.6470$, $b = 3.5632$, $\tau = 0.006$, $h = 0.054$, $\bar{\tau} = 0.360$, and with the admissible setpoint value $y^* \in (0, y_{\max})$, $y_{\max} = \frac{b}{a_2 - a_1} = 1.20$. According to Remark 1, the condition (7) has been validated graphically using the parametric plot of the function Q in the complex plane (Figure 5).

Results from a numerical simulation are depicted in Figures 6 and 7 for $y^* = 0.65$ ($\sigma^* = 1.5702$, respectively). The simulation has been performed using explicit Euler method and a rather large step size 10^{-2} (corresponding to the technological limitations of most of the actuators). Such discretization step is selected in order to evaluate on simulations a possible amplitude of chattering [25], which always accompanies the sliding mode control. In addition, such step size corresponds to physical restrictions on the maximum frequency of many pneumatic actuators.

Copyright © 2017 John Wiley & Sons, Ltd.

DOI: 10.1002/rnc

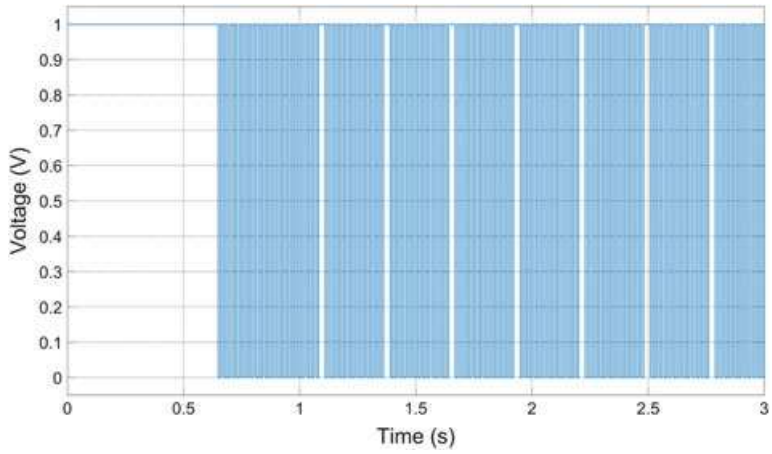

Figure 7. Application of the setpoint tracking control: control signal. [Colour figure can be viewed at wileyonlinelibrary.com]

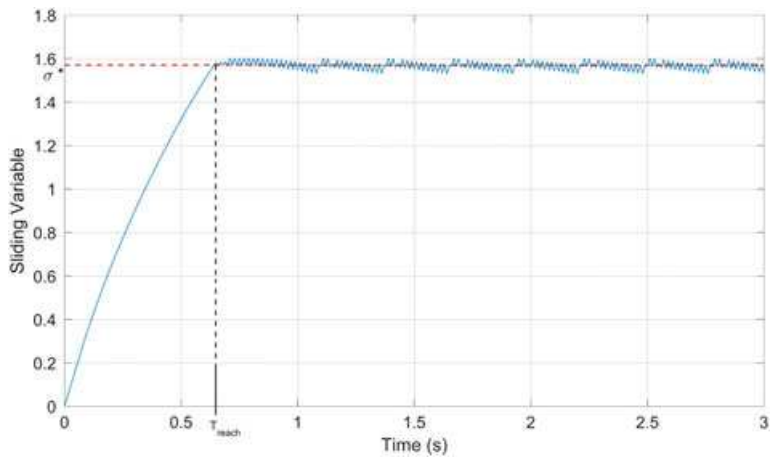

Figure 8. Application of the setpoint tracking control: sliding variable. [Colour figure can be viewed at wileyonlinelibrary.com]

Figure 7 shows that after approximately 0.65 s, the sliding mode appears making the input oscillate between 0 and 1 at high frequency. Next, the output $y(t)$ converges to the desired setpoint y^* with an error of the order 10^{-2}. The numerical simulations have been also made for the smaller step size 10^{-4}. They confirmed convergence of $y(t)$ to y^* with an error of the order 10^{-4}, which corresponds to numerical precision of the Euler method.

Figure 8 plots the value of the sliding variable with respect to time and, except for the chattering phenomenon, it shows finite-time convergence to the sliding surface $\sigma(t) = \sigma^*$. For small time steps, σ reaches σ^* in finite-time, and the reaching time is approximately $T_{\text{reach}} = 0.65$ s.

Please note that all simulations are performed using a zero initial condition for y.

5. OPTIMAL CONTROL PROBLEM

5.1. Model description and basic assumptions

Let us consider the functional differential equation

$$\dot{y}(t) = A(y_\tau(t)) + \sum_{i=1}^{N_3} (b_i + B_i(y_\tau(t-h_i)))u(t-h_i), \tag{9}$$

where $y_\tau(t) \in \mathbf{C}^1_{[-\tau,0]}$ is the state of the system, $(y_\tau(t))(s) = y(t+s)$ for $s \in [-\tau, 0]$, $A : \mathbf{C}^1_{[-\tau,0]} \subset \mathbf{L}^2_{[-\tau,0]} \to \mathbb{R}$ and $B_i : \mathbf{C}^1_{[-\tau,0]} \subset \mathbf{L}^2_{[-\tau,0]} \to \mathbb{R}$ are linear continuous functionals, $b_i \in \mathbb{R}_+$ are positive

Copyright © 2017 John Wiley & Sons, Ltd.

DOI: 10.1002/rnc

constants, $u(t) \in \{0, 1\}$ is the relay control input, and $h_i \in \mathbb{R}_+$ are input delays. For any $u \in \mathbf{L}^{\infty}_{\mathbb{R}_+}$, the considered system has a unique Caratheodory solution [43]. Similarly to the previous section, we assume that the system (9) with $y(s) = 0$ for all $s \leqslant 0$ has bounded positive solution for any input signal $u \in \mathbf{L}^{\infty}_{\mathbb{R}_+} : u(t) \in \{0, 1\}$. We also assume that the class of admissible control inputs is restricted to ω-periodic functions $u(t) = u(t + \omega)$, $\forall t > 0$.

5.2. *Periodic feedforward control*

In the periodic case, the optimization problem $J(y, u) \to \max$ subject to (9) considered over infinite interval of time can be reduced to the optimal control over finite time interval. Indeed, if for any ω-periodic input $u \in \mathbf{L}^{\infty}_{\mathbb{R}_+}$, the system (9) has a unique stable ω-periodic solution y^{ω}, then

$$J(y^{\omega}, u) = \frac{1}{\omega} \int_0^{\omega} \alpha y^{\omega}(s) - (1 - \alpha) u(s) ds. \tag{10}$$

To solve this optimization problem, we need a proper algorithm of finding of periodic solutions to the system (9) with a given periodic control input u. Existence of periodic solution to a particular system (9) as well as algorithm for its finding is provided by the next theorem.

Theorem 1 ([46]*)*
If $0 = h_0 < h_1 < \ldots < h_m$ and

- a function $f : \mathbb{R}_+ \times \mathbb{R}^{n(m+1)} \to \mathbb{R}$ is measurable and ω-periodic: $f(t, \mathbf{x}) = f(t + \omega, \mathbf{x})$, $t \in \mathbb{R}_+$, $\mathbf{x} \in \mathbb{R}^{n(m+1)}$, and satisfies Lipschitz condition:
$$|f(t, \mathbf{x}) - f(t, \mathbf{y})| \leqslant \sum_{i=0}^{n-1} \sum_{j=0}^{m} l_{ij} |x_{ij} - y_{ij}|, \ \mathbf{x}, \mathbf{y} \in \mathbb{R}^{n(m+1)},$$
where $l_{ij} \geqslant 0$ are constants, $\mathbf{x} = (x_{00}, x_{01}, \ldots, x_{ij}, \ldots) \in \mathbb{R}^{n(m+1)}$ and $\mathbf{y} = (y_{00}, y_{01}, \ldots, y_{ij}, \ldots) \in \mathbb{R}^{n(m+1)}$;
- a liner functional $\mathcal{A} : \mathbf{C}^n_{[-h_m, 0]} \to \mathbb{R}$ is defined as
$$\mathcal{A} x_{h_m}(t) = \sum_{i=0}^{m} \sum_{j=0}^{n} a_{ij} x^{(j)}(t - h_i), \quad a_{ij} \in \mathbb{R},$$
$$x_{h_m}(t) = x(t + s) \text{ for } s \in [-h_m, 0];$$
- the frequency $\theta = \frac{2\pi}{\omega}$ satisfies the non-resonance conditions: $L(\mathrm{i}k\theta) \neq 0$ for $k = 0, \pm 1, \pm 2, \ldots$ where $p = 0, 1, \ldots, n - 1$ and $L(\lambda) = \sum_{i=0}^{m} \sum_{j=0}^{n} a_{ij} \lambda^j e^{-h_i \lambda}$ is the characteristic quasi-polynomial of the operator $\mathcal{A}$;
- the inequality $q = \sum_{p=0}^{n-1} l_p \sigma_p < 1$ holds for $l_p = l_{p0} + l_{p1} + \ldots + l_{pm}$ and $\sigma_p = \max_{r \in \mathbb{R}} \left| \frac{(ir\theta)^p}{L(ir\theta)} \right|$,

then the equation $\mathcal{A} x_{h_m}(t) = f(t, x(t), x(t - h_1), \ldots, x^{(n-1)}(t - h_m))$ has a unique ω-periodic solution $x_{\omega} \in \mathbf{C}_{[0,\omega]}$,

which satisfies the estimate $\|x^{(i)}_{\omega}\|_{\mathbf{L}^2_{[0,\omega]}} \leqslant \frac{\sigma_i}{1-q} \|f(t, \mathbf{0})\|_{\mathbf{L}^2_{[0,\omega]}}$, $i = 0, 1, \ldots, n - 1$ and can be found by means of iterations

$$\mathcal{A} x^{[k+1]}_{h_m}(t) = f(t, \mathbf{x}^{[k]}(t)), k = 0, 1, 2, \ldots, \tag{11}$$

where $x^{[0]}$ is an arbitrary ω-periodic function and $\mathbf{x}^{[k]}(t) = (x^{[k]}(t), x^{[k]}(t - h_1), \ldots, x^{[k]}(t - h_m), \ldots) \in \mathbb{R}^{n(m+1)}$ and the following estimate:

$$\left\| \frac{d^i x^{[k]}}{dt^i} - \frac{d^i x_{\omega}}{dt^i} \right\|_{\mathbf{L}^2_{[0,\omega]}} \leqslant \frac{q^k}{1 - q} \sigma_i \sum_{p=0}^{n-1} l_p \left\| \frac{d^p x^{[0]}}{dt^p} - \frac{d^p x_{\omega}}{dt^p} \right\|_{\mathbf{L}^2_{[0,\omega]}} \tag{12}$$

holds for $i = 0, 1, 2, \ldots, n - 1$.

Copyright © 2017 John Wiley & Sons, Ltd.

DOI: 10.1002/rnc

To the best of our knowledge, the proof of Theorem 1 for $\mathbf{L}^2$ spaces has never been presented in English literature. Its proof given originally in [46] is sketched in the Appendix.

The formula (11) provides simple recursive procedure for numerical finding of periodic solution with precision controlled by the formula (12). Combination of this algorithm with some infinite dimensional optimization procedure [47] allows us to find numerically an optimal input signal u for a fixed period ω. The corresponding algorithms are usually computationally hard. That is why, for practice, it is also important to provide a simple sub-optimal algorithm. One has the following proposition, which is proved in the Appendix.

Proposition 3
If for any ω-periodic input signal $u \in \mathbf{L}^{\infty}_{\mathbb{R}}$, the positive system (9) has a unique globally asymptotically stable periodic solution and $A(\mathbb{1}) + \omega^{-1}\int_0^{\omega}\sum_{i=1}^{N_2} B_i(\bar{u}_\tau(s))ds < 0$, then

$$J(y,u) \geqslant \tilde{J}(u) = \frac{1}{\omega}\left(\alpha - 1 - \frac{\alpha\sum_{i=1}^{N_2} b_i}{A(\mathbb{1}) + \omega^{-1}\int_0^{\omega}\sum_{i=1}^{N_2} B_i(\bar{u}_\tau(s))ds}\right)\int_0^{\omega} u(s)ds.$$

Therefore, if conditions of Proposition 3 holds, then the sub-optimal control can be found by means of maximization of the functional $\tilde{J}(u)$.

If periodic control inputs are restricted to

$$u_{\omega,t'}(t) = \begin{cases} 1 & \text{for } t \in [k\omega, k\omega + t'), \\ 0 & \text{for } t \in [k\omega + t', (k+1)\omega), \end{cases} \tag{13}$$

then, in the view of Proposition 3, a quasi optimal solution to (2) can be found from the finite dimensional optimization problem: $\tilde{J}(u_{\omega,t'}) \to \max$. Such class of input signals is motivated by natural practical demands to minimize the number of switchings.

In this case, the condition $A(\mathbb{1}) + \omega^{-1}\int_0^{\omega}\sum_{i=1}^{N_2} B_i(\bar{u}_\tau(s))ds < 0$ of 3 simplifies to $A(\mathbb{1}) + \frac{t'}{\omega}\sum_{i=1}^{N_2} B_i(\mathbb{1}) < 0$, and $\tilde{J}(u)$ to

$$\tilde{J}(u) = \left(\alpha - 1 - \frac{\alpha\sum_{i=1}^{N_2} b_i}{A(\mathbb{1}) + \frac{t'}{\omega}\sum_{i=1}^{N_2} B_i(\mathbb{1})}\right)\frac{t'}{\omega}. \tag{14}$$

This optimization problem can be solved analytically for $\tilde{J}$. For any fixed value ω_0 of ω, the value of t' noted by t'_0 is given by

$$t'_0 = \begin{cases} 0 & \text{if } \alpha = 0 \\ \omega & \text{if } \alpha = 1 \\ \omega\,\mathrm{sat}_{[0,1]}\left(\dfrac{-A(\mathbb{1})}{\sum_{i=1}^{N_2} B_i(\mathbb{1})} - \dfrac{\sqrt{\frac{\alpha}{(\alpha-1)}A(\mathbb{1})\left(\sum_{i=1}^{N_2} b_i\right)}}{\sum_{i=1}^{N_2} B_i(\mathbb{1})}\right) & \text{if } 0 < \alpha < 1, \end{cases} \tag{15}$$

where $\mathrm{sat}_{[0,1]}$ is the saturation function on the interval [0, 1] such that $\mathrm{sat}_{[0,1]}(x) = x$ for $0 \leqslant x \leqslant 1$, $\mathrm{sat}_{[0,1]}(x) = 1$ for $x > 1$, and $\mathrm{sat}_{[0,1]}(x) = 0$ for $x < 0$.

It is worth stressing that the identified model of the flow control system (Table I) satisfies Proposition 3.

Copyright © 2017 John Wiley & Sons, Ltd.

DOI: 10.1002/rnc

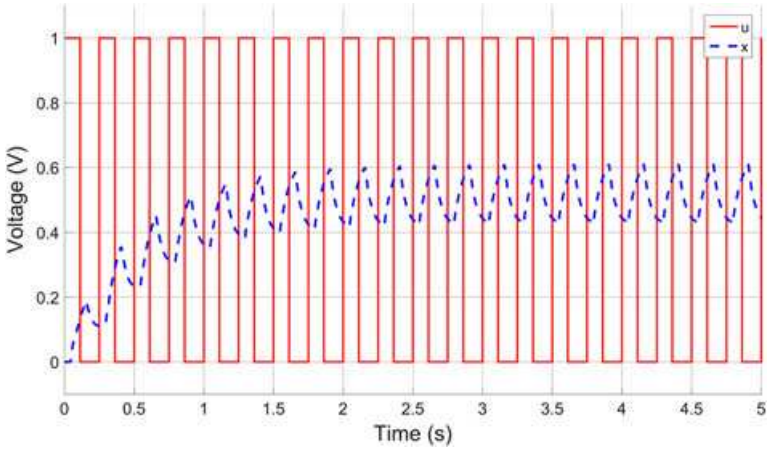

Figure 9. Application of the feedforward control with $\alpha = 0.46$. [Colour figure can be viewed at wileyonlinelibrary.com]

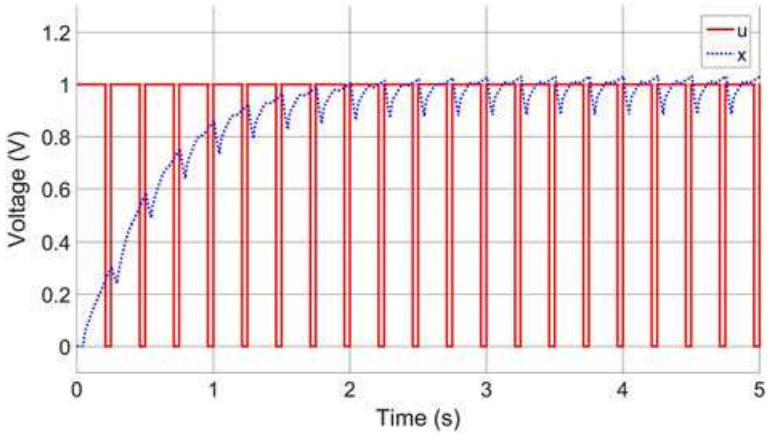

Figure 10. Application of the feedforward control with $\alpha = 0.48$. [Colour figure can be viewed at wileyonlinelibrary.com]

5.3. Numerical simulation results

Let us find the sub-optimal feedforward control of the form (13) for our system with two input delays as presented in Section 5.2. It is easy to compute that $A(\mathbb{1}) = -3.7488 < 0$ and $A(\mathbb{1}) + B(\mathbb{1}) = -4.1578 < 0$, then the conditions of Proposition 3 are fulfilled for every couple (ω, t').

A numerical simulation of the model (9) with the coefficients chosen in the column $N_3 = 2$ of Table I can be found in Figure 9. This simulation was performed for $\alpha = 0.46$ and $\omega = 0.25$, leading to $t' = 0.1119$ and the duty cycle $\frac{t'}{\omega} \times 100\% = 44.76\%$. The value of the cost function for this simulation is $J = -0.0339$. For comparison, and for identical values of α and ω, taking a constant control equal to one give $J = -0.0711$ and a control with a duty cycle of 50% gives $J = -0.0389$. Another simulation with $\alpha = 0.48$ can be found in Figure 10. It is to be noted that, in the case of our model, the choice of alpha requires great precision as the saturation of t_{sw} occurs for $\alpha < 0.436$ and $\alpha > 0.488$. Therefore, the choice of the parameter α greatly depends on the system studied, and its range and effect may vary from one experiment to another.

Please note that all simulations are performed using a zero initial condition for y.

6. DISCUSSION AND CONCLUSIONS

In the paper, the problem of model-based control of separated flows is studied.

The bilinear time-delay model of turbulent flow introduced in [24] is considered and identified. It is shown that both sub-optimal (feedforward) and robust (feedback) control laws can be designed

Copyright © 2017 John Wiley & Sons, Ltd.

DOI: 10.1002/rnc

based on the identified model. Classical control approaches like sliding mode design can be utilized for this purpose. The proposed control was tested in the ONERA Lille wind tunnel. A video if the open-loop optimal control can be found at : https://youtu.be/BLG5e9obQK0. The robustness of the closed-loop control has been experimentally validated through repeated testing with several changes in the setup (flow speed, actuators mass flow and flap angle of attack). A video of the experiment can be found at : youtu.be/b5NnAV2qeno. Their extensions to more exact models of separated flows are planned for the future work.

Chattering reduction of sliding mode control was not studied in this paper. Today, the way for chattering reduction is to use higher order sliding mode. However, till now, there is no efficient scheme for its application to time-delay bilinear systems. We consider this problem as important direction for future research. Another possible direction is related to disturbance reduction and noise sensitivity analysis using, for example, the results of the papers [31, 33, 48]. This would also allow us to cover a wider range of flow types and experiments.

APPENDIX

A.1 Positive systems with time-delay

Lemma 1
If $a > 0, \tau > 0$, and $a\tau < \frac{1}{e}$, then the system $\dot{z}(t) = -az(t-\tau) + f(t),\ z(s) = 0$ for $s \leqslant 0$ is positive for any nonnegative $f \in \mathbf{L}^{\infty}_{\mathbb{R}}$, i.e. $z(t) \geqslant 0$ if $f(t) \geqslant 0$ for all $t \geqslant 0$.

Proof
See Lemma 4 of [49] *or Corollary 15.9 from* [50]. □

Lemma 2
Let the system $\dot{z}(t) = -az(t-\tau) + b$ with $z(s) = 0$ for $s \leqslant 0$ be positive and $a > 0, b > 0$, $0 \leqslant a\tau < \ln(2)$. Then, it has a unique solution defined on $\mathbb{R}_+$ such that $0 < z(t) < \frac{b}{a}$ and $\dot{z}(t) > 0$ for all $t > 0$.

Proof
For existence and uniqueness of solution of time-delay systems, see [35]. *Let us suppose a contrary, that is, there exists $t^* > 0$ such that $z(t^*) = \frac{b}{a}$, but $z(t) < \frac{b}{a}$ for all $t > t^*$. This immediately implies that $\dot{z}(t) > 0$ and $z(t) > 0$ for all $t \in (0, t^*]$.*
Let us denote $p(t) = z(t) - a\int_{t-\tau}^{t} z(s)ds$. Hence, we have

$$\dot{p}(t) = -az(t) + b = -ap(t) + b - a^2 \int_{t-\tau}^{t} z(s)ds$$

and

$$\begin{aligned}
z(t) &= \frac{b(1-e^{-at})}{a} + a\int_{t-\tau}^{t} z(s)ds - a^2\int_{0}^{t} e^{-a(t-\sigma)}\int_{\sigma-\tau}^{\sigma} z(s)dsd\sigma \\
&= \frac{b(1-e^{-at})}{a} + a\int_{t-\tau}^{t} z(s)ds - a\int_{0}^{t} e^{-a(t-\sigma)}\int_{t-\tau}^{t} z(\sigma-t+s)dsd\sigma \\
&= \frac{b(1-e^{-at})}{a} + a\int_{t-\tau}^{t}\left(z(s) - a\int_{0}^{t} e^{-a(t-\sigma)} z(\sigma-t+s)d\sigma\right)ds \\
&= \frac{b(1-e^{-at})}{a} + a\int_{t-\tau}^{t}\left(z(s) - a\int_{-t}^{0} e^{a\sigma} z(s+\sigma)d\sigma\right)ds \\
&= \frac{b(1-e^{-at})}{a} + a\int_{t-\tau}^{t}\left(z(s) - ae^{-as}\int_{s-t}^{s} e^{a\sigma} z(\sigma)d\sigma\right)ds \\
&= \frac{b}{a}(1-e^{-at}) + a\int_{t-\tau}^{t} e^{-as} f(s,t)ds,
\end{aligned}$$

Copyright © 2017 John Wiley & Sons, Ltd.

DOI: 10.1002/rnc

where $f(s,t) = e^{as}z(s) - a\int_{s-t}^{s} e^{a\sigma}z(\sigma)d\sigma$. *Because for* $s \in [t-\tau, t]$ *and* $0 < t \leqslant t^*$, *we have*

$$\frac{\partial f}{\partial s} = e^{as}\dot{z}(s) + ae^{as}z(s) - ae^{as}z(s) + ae^{a(s-t)}z(s-t) \geqslant 0,$$

then $z(t) \leqslant \frac{b(1-e^{-at})}{a} + af(t,t)\int\limits_{t-\tau}^{t}\frac{ds}{e^{as}} = \frac{b(1-e^{-at})}{a} + f(t,t)\frac{e^{a\tau}-1}{e^{at}}$ *or, equivalently,* $z(t) \leqslant \frac{b(1-e^{-at})}{a(2-e^{a\tau})} - \frac{a(e^{a\tau}-1)}{2-e^{a\tau}}\int_0^t e^{-a(t-\sigma)}z(\sigma)d\sigma$. *Hence,* $z(t) \leqslant w(t)$, *where* $w(t)$ *satisfies the integral equation* $w(t) = \frac{b(1-e^{-at})}{a(2-e^{a\tau})} - \frac{a(e^{a\tau}-1)}{2-e^{a\tau}}\int_0^t e^{-a(t-\sigma)}w(\sigma)d\sigma, w(0) = 0$ *or, equivalently,*

$$\dot{w}(t) = -a\left(1 + \frac{e^{a\tau}-1}{2-e^{a\tau}}\right)w(t) + \frac{b}{2-e^{a\tau}} = \frac{-aw(t)+b}{2-e^{a\tau}}.$$

Therefore, we derive that $z(t) \leqslant \frac{b}{a}\left(1 - e^{-\frac{a}{2-e^{a\tau}}t}\right) < \frac{b}{a}$ *for all* $t > 0$. *This contradicts our supposition.* □

A.2 Proof of Proposition 1

I. Let us consider the system $\dot{y}(t) = -a_2 y(t-\tau) + f(t),\ y(s) = 0, s \leqslant 0$, *where* f *is a locally integrable function. If* $f(t) \geqslant 0$ *and* $a_2\tau \leqslant e^{-1}$, *then the delay-dependent positivity conditions hold (Lemma 1) and* $y(t) \geqslant 0$, *for all* $t \geqslant 0$. *On the one hand, if* $a_1 \geqslant c$ *and* $y(s) \geqslant 0$ *for* $s \leqslant t$, *then* $f(t) = a_1 y(t-h) + (b - cy(t-h) + cy(t-\bar{\tau}))u(t-h) \geqslant 0$. *Therefore, using the method of steps (i.e., considering sequentially the intervals* $[0,h], [h,2h]\ldots$*), we prove positivity of the system* (4), (5).
II. Now let us prove boundedness of solutions. Suppose the contrary: there exists an input signal $u(t)$ *and an instant of time* $t^* > 0$: $y(t^*) = y_{\max}$ *and* $y(s) < y_{\max}$ *for* $s < t^*$.
In this case, because $b - cy(t-h) + cy(t-\bar{\tau}) \geqslant b - cy(t-h) = (a_2 - a_1)y_{\max} - cy(t-h) > 0$ *for all* $t \in [0, t^*]$, *then* $y(s) \leqslant y_{\mathbb{1}}(s)$ *for all* $s \leqslant t^*$, *where* $y_{\mathbb{1}}$ *is the solution to the positive system* $\dot{y}_{\mathbb{1}}(t) = (a_1 - c)y_{\mathbb{1}}(t-h) - a_2 y_{\mathbb{1}}(t-\tau) + cy_{\mathbb{1}}(t-\bar{\tau}) + b$. *Let us prove boundedness of solutions of the latter system; for this purpose, let us study the auxiliary system:*

$$\dot{z}(t) = -(a_2 - a_1)z(t-\tau) + b, \quad z(s) = 0 \textit{ for } s \leqslant 0.$$

For $\Delta(t) = z(t) - y_{\mathbb{1}}(t)$, *we derive*
$\dot{\Delta}(t) = -a_2\Delta(t-\tau) + a_1 z(t-\tau) - (a_1 - c)y_{\mathbb{1}}(t-h) - cy_{\mathbb{1}}(t-\bar{\tau})$. *According to Lemma 2, the function* z *satisfies the inequalities* $0 < z(t) < b/(a_2 - a_1) = y_{\max}$ *and* $\dot{z}(t) > 0$ *for all* $t > 0$. *Hence,* $z(t-\tau) \geqslant z(t-h) \geqslant z(t-\bar{\tau})$ *and*

$$\dot{\Delta}(t) = -a_2\Delta(t-\tau) + (a_1 - c)\Delta(t-h) + c\Delta(t-\bar{\tau}) + \eta(t),$$

where $\eta(t) = a_1 z(t-\tau) - (a_1 - c)z(t-h) - cz(t-\bar{\tau}) \geqslant 0$ *and* $\Delta(s) = 0$ *for* $s \leqslant 0$. *Because the latter system is positive (see the first part of this proof), then* $\Delta(t) \geqslant 0$ *and* $y_{\mathbb{1}}(t) \leqslant z(t) < y_{\max}$ *for all* $t \geqslant 0$. *This contradicts our supposition.*

A.3 Proof of Proposition 2

Firs of all, let us note that $0 < y(t) < \frac{b}{a_2 - a_1}$ *for all* $t > 0$ *due to Proposition 1.*
I. Because the system (4) *is positive, then* $y(t) \geqslant 0$ *for all* $t \geqslant 0$. *Moreover, if* $u(t) = 0$ *and* $y(t) > 0$, *then* $\dot{\sigma}(t) < 0$, *but if* $u(t) = 1$ *and* $y(t) < \frac{b}{a_2 - a_1}$, *then* $\dot{\sigma}(t) > 0$. *Therefore, while* $0 < y(t) < \frac{b}{a_2 - a_2}$, *we have* $(\sigma(t) - \sigma^*)\frac{d}{dt}(\sigma(t) - \sigma^*) < 0$. *Obviously,* $\sigma(0) = 0$. *To guarantee*

Copyright © 2017 John Wiley & Sons, Ltd.

DOI: 10.1002/rnc

existence of sliding mode, we just need to show that the state $\sigma(t) = \sigma^* > 0$ is reachable in a finite time $t = t^* > 0$. Let us suppose contrary: $\sigma(t) < \sigma^*$ for all $t > 0$. This means that $u(t) = 1$ for all $t > 0$ and

$$\dot{y}(t) = (a_1 - c)y(t-h) - a_2 y(t-\tau) + cy(t-\bar{\tau}) + b.$$

Using the last identity, let us rewrite the formula (6) *as*

$$\begin{aligned}\sigma(t) &= y(t) - a_2\int_{t-\tau}^{t} y(s)ds + c\int_{t-\bar{\tau}+h}^{t} y(s)ds + \int_{t-h}^{t}\dot{y}(s+h) + a_2 y(s+h-\tau)ds\\ &= 2y(t) - y(t-h) + a_2\int_{t}^{t+h-\tau} y(s)ds + c\int_{t-\bar{\tau}+h}^{t} y(s)ds.\end{aligned}$$

Hence, $\sigma(t) \geqslant \sigma^*$ if $y(t) \geqslant y^*$. Let us show that there exists $t^* > 0$ such that $y(t) > y^*$ for all $t > t^*$. Because $\dot{y}(t) > -a_2 y(t-\tau) + b$ for all $t > 0$, then, obviously, there exists $t_1 > 0$ such that $y(t) > \frac{b}{a_2}$ for all $t > t_1$. In this case, we derive $\dot{y}(t) > -a_2 y(t-\tau) + b\left(1 + \frac{a_1}{a_2}\right)$ for all $t > t_1 + \bar{\tau}$, and there exists $t_2 > t_1 + \bar{\tau}$ such that $y(t) > \frac{b}{a_2}\left(1 + \frac{a_1}{a_2}\right)$ for all $t > t_2$ and so on. Therefore, for $t > t_i$, we derive

$$y(t) > \frac{b}{a_2}\left(1 + \frac{a_1}{a_2} + \ldots + \left(\frac{a_1}{a_2}\right)^{i-1}\right) = \frac{b\left(1 - \left(\frac{a_1}{a_2}\right)^{i}\right)}{a_2 - a_1}$$

and for some i^* we have $y(t_{i^*}) > y^* \in \left(0, \frac{b}{a_2 - a_1}\right)$. Therefore, the sliding mode existence condition [25] *holds and $\sigma(t) = \sigma^*$, $\forall t > t^*$.*
II. Using the equivalent control method [25], *we derive $u_{eq}(t) = \frac{(a_2-a_1-c)y(t)+cy(t-\bar{\tau}+h)}{b-cy(t)+cy(t-\bar{\tau}+h)}$ and*

$$\begin{aligned}\sigma^* &= y(t) - a_2\int_{t-\tau}^{t} y(s)ds + c\int_{t-\bar{\tau}+h}^{t} y(s)ds + \int_{t-h}^{t} a_2 y(s) - cy(s) + cy(s-\bar{\tau}+h)ds\\ &= y(t) + a_2\int_{t-h}^{t-\tau} y(s)ds + c\int_{t-\bar{\tau}}^{t-h} y(s)ds\end{aligned}$$

for all $t > t^*$. Introducing the variable $\Delta(t) = y(t) - y^*$, we obtain the equation

$$\Delta(t) + a_2\int_{t-h}^{t-\tau}\Delta(s)ds + c\int_{t-\bar{\tau}}^{t-h}\Delta(s)ds = 0. \tag{16}$$

It has the characteristic equation $\frac{1}{s}Q(s) = 0$, $s \in \mathbb{C}$. We have already proven that all solutions of the closed-loop system are bounded (Proposition 1), and the sliding mode exists for all $t > t^*$, so the equation (16) *does not have unbounded dynamics. The condition $Q(j\omega) \neq 0$ for all $\omega \neq 0$ implies that this equation does not have non-constant periodic solutions. So the only stable solution is $\Delta(t) \equiv C$, where $C \in \mathbb{R}$ is some constant. Because $1 + a_2(h-\tau) + c(\bar{\tau} - h) > 0$, then from the equation for $\Delta(t)$, we immediately derive $C = 0$ and $y(t) \to y^*$ as $t \to \infty$.*
A.4 Elements of averaging analysis
Let us introduce some additional notations.

- $\mathbf{L}^2_\Omega$ *is the Hilbert space of quadratically integrable functions $\Omega \subseteq \mathbb{R} \to \mathbb{R}$ with the norm $\|\cdot\|_{\mathbf{L}^2}$ induced by the inner product $\xi \cdot \eta = \int_\Omega \xi(s)\eta(s)ds$.*

Copyright © 2017 John Wiley & Sons, Ltd.

DOI: 10.1002/rnc

- *If* $\tau > 0$, $\xi \in \mathbf{L}^{\infty}_{\mathbb{R}}$ *and* $t \in \mathbb{R}$, *then*

$$\bar{\xi}_{\tau}(t) \in \mathbf{L}^{\infty}_{[-\tau,0]} : (\bar{\xi}_{\tau}(t))(\sigma) = \xi(t-\sigma) \text{ for } \sigma \in [-\tau, 0].$$

- *For* $\xi, \nu \in \mathbf{L}^{\infty}_{\Omega}$ *with* $\mathbb{R}_+ \subset \Omega$, *let us define the operation*

$$\langle \xi, \nu \rangle := \lim_{T \to +\infty} \frac{1}{T} \int_0^T \xi(\tau)\nu(\tau) d\tau,$$

  which, in particular, defines the scalar product in the space $\mathbf{L}^{\infty}_{\mathbb{R}_+}$.
- *For* $\xi, \nu \in \mathbf{L}^{\infty}_{\mathbb{R}}$, *let us define* $\langle \xi_{\tau}, \nu \rangle \in \mathbf{L}^{\infty}_{[-\tau,0]}$ *as*

$$\langle \xi_{\tau}, \nu \rangle(\sigma) := \lim_{T \to +\infty} \frac{1}{T} \int_0^T \xi(s+\sigma)\nu(s) ds \text{ for } \sigma \in [-\tau, 0].$$

Lemma 3
If $\xi, \nu \in \mathbf{L}^{\infty}_{\mathbb{R}}$ and $\tau \in \mathbb{R}_+$, then $\langle \xi_{\tau}, \nu \rangle = \langle \xi, \bar{\nu}_{\tau} \rangle$.

Proof
The change of integration variable $\theta = s + \sigma$ *gives*

$$\langle \xi_{\tau}, \nu \rangle(\sigma) = \lim_{T \to +\infty} \int_0^T \frac{\xi(s+\sigma)\nu(s)}{T} ds = \lim_{T \to +\infty} \int_0^{T+\sigma} \frac{\xi(\theta)\nu(\theta-\sigma)}{T} d\theta = \langle \xi, \bar{\nu}_{\tau} \rangle(\sigma)$$

for $\sigma \in [-\tau, 0]$. □
This proposition immediately implies the following.

Corollary 1
If $\xi \in \mathbf{L}^{\infty}_{\mathbb{R}}$ and $\tau \in \mathbb{R}_+$, then $\langle \xi_{\tau}, \mathbb{1} \rangle \in \mathbf{C}_{[-\tau,0]}$ is the constant function: $\langle \xi_{\tau}, \mathbb{1} \rangle(\sigma) = \langle \xi, \mathbb{1} \rangle$ for all $\sigma \in [-\tau, 0]$, where $\mathbb{1} \in \mathbf{C}_{\mathbb{R}}$ is the unit constant function (i.e., $\mathbb{1}(s) = 1$ for all $s \in \mathbb{R}$).

Lemma 4
If $\Phi : \mathbf{L}^2_{[-\tau,0]} \to \mathbb{R}_+$ is a linear continuous functional, then $\langle \Phi(\xi_{\tau}), \nu \rangle = \Phi(\langle \xi_{\tau}, \nu \rangle)$ for any $\xi, \nu \in \mathbf{L}^{\infty}_{\mathbb{R}}$.

Proof
Because Φ *is the linear continuous functional* $\mathbf{L}^2_{[-\tau,0]} \to \mathbb{R}_+$, *then by Riesz Theorem* [51], *it can be presented as*

$$\Phi(\eta) = \mu \cdot \eta = \int_{-\tau}^0 \mu(s)\eta(s) ds, \quad \eta \in \mathbf{L}^2_{[-\tau,0]}$$

with some $\mu \in \mathbf{L}^2_{[-\tau,0]}$. *Hence,*

$$\frac{1}{T} \int_0^T \Phi(\xi_{\tau}(s))\nu(s) ds = \frac{1}{T} \int_0^T \int_{-\tau}^0 \mu(\sigma)\xi(s+\sigma) d\sigma \nu(s) ds = \int_{-\tau}^0 \mu(\sigma) \frac{1}{T} \int_0^T \xi(s+\sigma)\nu(s) ds d\sigma.$$

Taking the limit for both sides, we complete the proof. □

Corollary 2
If $\Phi : \mathbf{L}^2_{[-\tau,0]} \to \mathbb{R}_+$ is a linear continuous functional, then $\lim_{T \to +\infty} \frac{1}{T} \int_0^T \Phi(\xi_{\tau}(s)) ds = \langle \xi, \mathbb{1} \rangle \Phi(\mathbb{1})$, for any $\xi \in \mathbf{L}^{\infty}_{\mathbb{R}}$, where $\mathbb{1} \in \mathbf{C}_{\mathbb{R}_+}$ is the unit constant function.

Copyright © 2017 John Wiley & Sons, Ltd.

DOI: 10.1002/rnc

Lemma 5
If $A : \mathbf{C}^1_{[-\tau,0]} \subset \mathbf{L}^2_{[-\tau,0]} \to \mathbb{R}$ and $B : \mathbf{C}^1_{[-\tau,0]} \subset \mathbf{L}^2_{[-\tau,0]} \to \mathbb{R}$ are linear continuous functionals and the system (9) has bounded solution for any $u \in \mathbf{L}^\infty_{\mathbb{R}}$, then

$$\sum_{i=1}^{N_2} b_i \langle u, \mathbb{1}\rangle + \langle y, B_i(\bar{u}_\tau)\rangle + \langle y, \mathbb{1}\rangle A(\mathbb{1}) = 0,$$

where $\mathbb{1}$ is the unit constant function, y is a solution to (9) with $u \in \mathbf{L}^\infty_{\mathbb{R}}$ and $\bar{u}_\tau(t) \in \mathbf{L}^\infty_{[-\tau,0]} : (\bar{u}_\tau(t))(\sigma) = u(t-\sigma)$ for $\sigma \in [-\tau, 0]$.

Proof
From the equation (9)*, we have*

$$\begin{aligned}\int_0^T \frac{\dot{y}(s)}{T} ds &= \int_0^T \frac{A(y_\tau(s))}{T} + \sum_{i=1}^{N_2} \frac{b_i + B_i(y_\tau(s-h_i))u(s-h_i)}{T} ds \\ &= A\left(\int_0^T \frac{y_\tau(s)}{T} ds\right) + \sum_{i=1}^{N_2} \frac{1}{T} \int_{-h_i}^{T-h_i} b_i u(s) + B_i\left(y_\tau(s)\right) u(s) ds.\end{aligned}$$

Because the function y is bounded, then $\lim_{T\to+\infty} \frac{1}{T}\int_0^T \dot{y}(s)ds = \lim_{T\to+\infty} \frac{1}{T}(y(T) - y(0)) = 0$*, and using Corollary 1 and Lemma 4, we derive* $\lim_{T\to+\infty} \frac{1}{T}\int_0^T A\left(y_\tau(s)\right) ds = \langle y, \mathbb{1}\rangle A(\mathbb{1})$*. Because*

$$\lim_{T\to+\infty} \frac{1}{T} \int_{-h_i}^{T-h_i} B_i\left(y_\tau(s)\right) u(s) ds = \langle B_i(y_\tau), u\rangle,$$

then

$$0 = \langle y, \mathbb{1}\rangle A(\mathbb{1}) + \langle u, \mathbb{1}\rangle \sum_{i=1}^{N_2} b_i + \langle B_i(y_\tau), u\rangle.$$

Finally, Lemmas 3 and 4 imply $\langle B_i(y_\tau), u\rangle = B_i(\langle y_\tau, u\rangle) = B_i(\langle y, \bar{u}_\tau\rangle) = \langle y, B_i(\bar{u}_\tau)\rangle$. □

A.5 Proof of Proposition 3
In the periodic case, we derive $\langle u, \mathbb{1}\rangle = \frac{1}{\omega}\int_0^\omega u(s)ds$*,* $\langle y, \mathbb{1}\rangle = \frac{1}{\omega}\int_0^\omega y^\omega(s)ds$*, and* $\langle y, B_i(\bar{u}_\tau)\rangle = \frac{1}{\omega}\int_0^\omega B_i(\bar{u}_\tau(s))y^\omega(s)ds$*, where y^ω is ω-periodic solution that corresponds to ω-periodic control input u. On the one hand, the functional B_i is linear and continuous, so it is bounded, and there exists a constant M such that $M - B_i(\bar{u}_\tau(s)) \geqslant 0$ for all $s \in [0, \omega]$. On the other hand, for any $\xi, \eta \in \mathbf{L}^\infty_{[0,\omega]}$ we have $\xi \cdot \eta \leqslant \|\xi\|_{\mathbf{L}^2_{[0,\omega]}} \|\eta\|_{\mathbf{L}^2_{[0,\omega]}}$ and $\|\xi\|_{\mathbf{L}^2_{[0,\omega]}} \leqslant \frac{1}{\sqrt{\omega}} \|\xi\|_{\mathbf{L}^1_{[0,\omega]}}$. Hence, taking into account positivity of the system* (9)*, we derive*

$$\begin{aligned}\frac{1}{\omega}\int_0^\omega -B_i(\bar{u}_\tau(s))y^\omega(s)ds &= -\frac{M}{\omega}\int_0^\omega y^\omega(s)ds + \frac{1}{\omega}\int_0^\omega (M - B_i(\bar{u}_\tau(s)))y^\omega(s)ds \\ &\leqslant -\frac{M}{\omega}\int_0^\omega y^\omega(s)ds + \left(\frac{1}{\omega}\int_0^\omega M - B_i(\bar{u}_\tau(s))ds\right)\left(\frac{1}{\omega}\int_0^\omega y^\omega(s)ds\right) \\ &= \left(-\frac{1}{\omega}\int_0^\omega B_i(\bar{u}_\tau(s))ds\right)\left(\frac{1}{\omega}\int_0^\omega y^\omega(s)ds\right).\end{aligned}$$

Copyright © 2017 John Wiley & Sons, Ltd.

DOI: 10.1002/rnc

Taking into account Lemma 5, we derive

$$\langle u, \mathbb{1}\rangle \sum_{i=1}^{N_2} b_i = -A(\mathbb{1})\langle y, \mathbb{1}\rangle - \sum_{i=1}^{N_2} \langle y, B_i(\bar{u}_\tau)\rangle \leqslant -\left(A(\mathbb{1}) + \frac{1}{\omega}\int_0^\omega \sum_{i=1}^{N_2} B_i(\bar{u}_\tau(s))ds\right)\langle y, \mathbb{1}\rangle.$$

Using the fact that $\bar{u}$ is ω-periodic such that $\frac{1}{\omega}\int_0^\omega \bar{u}(s)ds = \frac{t'}{\omega}$ and Riesz Theorem [51]*, we can write for some $\mu_i \in \mathbf{L}^2_{[-\tau,0]}$:*

$$\frac{1}{\omega}\int_0^\omega \sum_{i=1}^{N_2} B_i(\bar{u}_\tau(s))ds = \frac{1}{\omega}\int_0^\omega \sum_{i=1}^{N_2}\int_{-\tau}^0 \mu_i(\sigma)\bar{u}_\tau(s+\sigma)d\sigma ds = \sum_{i=1}^{N_2}\int_{-\tau}^0 \mu_i(\sigma)\left(\frac{1}{\omega}\int_0^\omega \bar{u}_\tau(s+\sigma)ds\right)d\sigma$$
$$= \sum_{i=1}^{N_2}\int_{-\tau}^0 \mu_i(\sigma)\left(\frac{t'}{\omega}\right)d\sigma = \frac{t'}{\omega}\sum_{i=1}^{N_2} B_i(\mathbb{1}),$$

which completes the proof.

A.6 Sketch of the proof of Theorem 1

The proof is based on Fixed-Point Theorem for a generalized Banach spaces $\boldsymbol{B} = \mathbf{L}^2_{[0,\omega]} \times \ldots \times \mathbf{L}^2_{[0,\omega]}$, which have vector-valued norms: $[\![\boldsymbol{x}]\!] = (\|\boldsymbol{x}_0\|_{\mathbf{L}^2_{[0,\omega]}}, \ldots, \|\boldsymbol{x}_{n-1}\|_{\mathbf{L}^2_{[0,\omega]}})^\top \in \mathbb{R}^n_+$ for any $\boldsymbol{x} \in \boldsymbol{B}$. The space $\mathbb{R}^n_+$ is semi-ordered using the conventional component-wise order relation, that is, $\boldsymbol{x} \leqslant \boldsymbol{y}$ if $x_i \leqslant y_i$, $i = 1, \ldots, n$, where $\boldsymbol{x}, \boldsymbol{y} \in \mathbb{R}^n_+$. In this case, the contraction condition of the operator $\mathcal{F} : \boldsymbol{B} \to \boldsymbol{B}$ is

$$[\![\mathcal{F}\boldsymbol{x} - \mathcal{F}\boldsymbol{y}]\!] \leqslant Q[\![\boldsymbol{x} - \boldsymbol{y}]\!], \quad \textit{for all } \mathbf{x}, \mathbf{y} \in \boldsymbol{B},$$

where $Q \in \mathbb{R}^{n\times n}_+$ is a Schur stable matrix. Under this condition, the operator $\mathcal{F}$ has the unique fixed point $\boldsymbol{x}^*$ on $\boldsymbol{B}$, that is, $\mathcal{F}(\boldsymbol{x}^*) = \boldsymbol{x}^*$. To complete the proof of Theorem 1, let us consider the operator $\mathcal{F} = (\mathcal{F}_0, \ldots, \mathcal{F}_{n-1})^\top \in \boldsymbol{B}$ with

$$\mathcal{F}_j(\boldsymbol{x}) = \int_0^\omega G^{(j)}(t,s) f(s, x_0(s), \ldots, x_0(s-h_m), x_1(s), \ldots)ds,$$

where G is the Green function of the system $\mathcal{A}x_{h_m}(t) = 0$. Finally, it can be shown [46] *that $\mathcal{F}$ satisfies the contraction condition with the matrix $Q = (l_0, \ldots, l_{n-1})^\top(\sigma_0, \ldots, \sigma_{n-1})$ that is Schur stable due to condition $(l_0, \ldots, l_{n-1})(\sigma_0, \ldots, \sigma_{n-1})^\top < 1$.*

ACKNOWLEDGEMENTS

This work was carried out within the framework of the CNRS Research Federation on Ground Transports and Mobility, in articulation with the ELSAT2020 project sup- ported by the European Community, the French Ministry of Higher Education and Research, the Hauts de France Regional Council. The authors gratefully acknowledge the support of these institutions. The authors are indebted to C. Raibaudo for the courtesy of the experimental data and to the LML for the experimental campaign conducted.

REFERENCES

1. Brunton SL, Noack BR. Closed-loop turbulence control: progress and challenges. *Applied Mechanics Reviews* 2015; **67**(5):050801–050801. Available: https://doi.org/10.1115/1.4031175. Accessed August 26, 2015.
2. Gad-el Hak M. *Flow Control: Passive, Active, and Reactive Flow Management*. Cambridge University Press: Cambridge, UK, 2006. Google-Books-ID: 1IiFetRXG3kC.
3. Palaviccini M, Cattafesta L, George B. Passive flow control over a three-dimensional turret with a flat aperture, 2011. American Institute of Aeronautics and Astronautics, Available: http://arc.aiaa.org/doi/10.2514/6.2011-3265. Accessed June 27, 2011.

Copyright © 2017 John Wiley & Sons, Ltd.

4. Chun KB, Sung HJ. Control of turbulent separated flow over a backward-facing step by local forcing. *Experiments in Fluids* 1996; **21**(6):417–426.
5. Selby GV, Lin JC, Howard FG. Control of low-speed turbulent separated flow using jet vortex generators. *Experiments in Fluids* 1992; **12**(6):394–400.
6. Tian Y, Song Q, Cattafesta L. Adaptive feedback control of flow separation, 2006. American Institute of Aeronautics and Astronautics, Available: http://arc.aiaa.org/doi/10.2514/6.2006-3016. Accessed June 5, 2006.
7. Tian Y, Cattafesta L, Mittal R. Adaptive control of separated flow, 2006. American Institute of Aeronautics and Astronautics, Available: http://arc.aiaa.org/doi/10.2514/6.2006-1401. Accessed January 9, 2006.
8. Cattafesta III LN, Song Q, Williams DR, Rowley CW, Alvi FS. Active control of flow-induced cavity oscillations. *Progress in Aerospace Sciences* 2008; **44**(7–8):479–502. Available: //www.sciencedirect.com/science/article/pii/S0376042108000584. Accessed October, 2008.
9. Volino RJ. Separation Control on Low-Pressure Turbine Airfoils Using Synthetic Vortex Generator Jets, In *ASME Turbo Expo 2003, collocated with the 2003 International Joint Power Generation Conference*., Atlanta, Georgia, USA, 2003:845–859. Available: https://doi.org/10.1115/GT2003-38729.
10. McManus K, Legner H, Davis S. Pulsed vortex generator jets for active control of flow separation, 1994. American Institute of Aeronautics and Astronautics, Available: https://arc.aiaa.org/doi/10.2514/6.1994-2218. Accessed June 20, 1994.
11. Eldredge R, Bons J. Active Control of a Separating Boundary Layer with Steady Vortex Generating Jets - Detailed Flow Measurements, In *42nd AIAA Aerospace Sciences Meeting and Exhibit, ser. Aerospace Sciences Meetings*. American Institute of Aeronautics and Astronautics, Reno, Nevada, USA, Jan. 2004, DOI: 10.2514/6.2004-751. Available: http://dx.doi.org/10.2514/6.2004-751.
12. Raibaudo C, Kerherve F, Stanislas M. Characterisation of the transient dynamics of a controlled separated flow using phase averaged PIV. *International Conference on Instability and Control of Massively Separated Flows – ICOMASEF*, Prato, Italy, 2013:183–188.
13. Raibaudo C, Polyakov A, Efimov D, Kerherve F, Richard J-P, Stanislas M. Experimental closed-loop control of a detached boundary layer at high Reynolds number. *10th EUROMECH Fluid Mechanics Conference*, Cambridge UK, 2015.
14. Chabert T, Dandois J, Garnier É, Jacquin L. Experimental detection of flow separation over a plain flap by wall shear stress analysis with and without steady blowing. *Comptes Rendus Mécanique* 2014; **342**(6):389–402.
15. Chabert T, Dandois J, Garnier É. Experimental closed-loop control of flow separation over a plain flap using slope seeking. *Experiments in Fluids* 2014; **55**(8):1–19.
16. Shaqarin T, Braud C, Coudert S, Stanislas M. Open and closed-loop experiments to identify the separated flow dynamics of a thick turbulent boundary layer. *Experiments in Fluids* January 2013; **54**(2):1–22.
17. Cierpka C, Weier T, Gerbeth G. Electromagnetic control of separated flows using periodic excitation with different wave forms. In *Active Flow Control*, King PDR (ed.)., Notes on Numerical Fluid Mechanics and Multidisciplinary Design (NNFM). Springer Berlin Heidelberg, 2007; no 95. 27–41.
18. Ciobaca V, Wild J. An Overview of Recent DLR Contributions on Active Flow-Separation Control Studies for High-Lift Configurations. *Aerospace Lab,* 2013; **2013**(6):1–12.
19. Åkervik E, Hoepffner J, Ehrenstein U, Henningson DS. Model reduction and control of a cavity-driven separated boundary layer. In *IUTAM Symposium on Flow Control and MEMS*. Springer:London, England, 2008:147–155.
20. Wachsmuth Daniel. Optimal control of the unsteady Navier–Stokes equations. *Ph.D. dissertation, PhD thesis*, Technische Universität Berlin, 2006.
21. Ghattas O, Bark J-H. Optimal control of two- and three-dimensional incompressible Navier–Stokes flows. *Journal of Computational Physics* September 1997; **136**(2):231–244.
22. Fernández-Cara E, Guerrero S, Imanuvilov OY, Puel JP. Local exact controllability of the Navier–Stokes system. *Journal de Mathématiques Pures et Appliquées* 2004; **83**(12):1501–1542.
23. Duriez T, Parezanovic V, Laurentie J-C, Fourment C, Delville J, Bonnet J-P, Cordier L, Noack BR, Segond M, Abel MW, Gautier N, Aider J-L, Raibaudo C, Cuvier C, Stanislas M, Brunton SL. Closed-loop control of experimental shear flows using machine learning. *7th AIAA Flow Control Conference.* American Institute of Aeronautics and Astronautics, Atlanta, GA, USA, 2014:2219–2234.
24. Feingesicht M, Raibaudo C, Polyakov A, Kerherve F, Richard J-P. A bilinear input-output model with state-dependent delay for separated flow control, 2016. Available: https://hal.inria.fr/hal-01298166/document. Accessed June 29, 2016.
25. Utkin VI. *Sliding Modes in Optimization and Control Problems*. Springer Verlag: New York, 1992.
26. Edwards C, Spurgeon S. *Sliding Mode Control: Theory and Applications*. CRC Press: London, UK, 1998. Google-Books-ID: uH2RJhIPsiYC.
27. Shtessel Y, Edwards C, Fridman L, Levant A. *Sliding Mode Control and Observation*. Springer: New York, NY, USA, 2014.
28. Liu J, Luo W, Yang X, Wu L. Robust model-based fault diagnosis for PEM fuel cell air-feed system. *IEEE Transactions on Industrial Electronics* 2016; **63**(5):3261–3270.
29. Liu J, Vazquez S, Wu L, Marquez A, Gao H, Franquelo LG. Extended state observer-based sliding-mode control for three-phase power converters. *IEEE Transactions on Industrial Electronics* 2017; **64**(1):22–31.
30. Fridman L, Acosta P, Polyakov A. Robust eigenvalue assignment for uncertain delay control systems. *Proc. 3rd IFAC Workshop on Time Delay Systems*, Santa Fe, New Mexico, USA, 2001; 239–244.

Copyright © 2017 John Wiley & Sons, Ltd.

DOI: 10.1002/rnc

31. Polyakov A. Minimization of disturbances effects in time delay predictor-based sliding mode control systems. *Journal of the Franklin Institute* May 2012; **349**(4):1380–1396.
32. Fridman L, Strygin V, Polyakov A. Nonlocal stabilization via delayed relay control rejecting uncertainty in a time delay. *International Journal of Robust and Nonlinear Control* 2004; **14**(1):15–37.
33. Yan X-G, Spurgeon SK, Edwards C. Static output feedback sliding mode control for time-varying delay systems with time-delayed nonlinear disturbances. *International Journal of Robust and Nonlinear Control* 2010; **20**(7):777–788.
34. Gauthier JP, Kupka I. A separation principle for bilinear systems with dissipative drift. *IEEE transactions on automatic control* 1992; **37**(12):1970–1974.
35. Fridman E. *Introduction to Time-Delay Systems: Analysis and Control*. Birkhäuser: Basel, Switzerland, 2014.
36. Raibaudo C, Polyakov A, Kerherve F, Richard J-P, Stanislas M. Experimental open-loop and closed-loop control of a massive separated boundary layer at high Reynolds number, 2015.
37. Raibaudo Cédric. Characterization of the transient of a separated turbulent boundary layer under control and applications to advanced closed-loop controllers. *Ph.D. dissertation*, Ecole Centrale de Lille, 2015.
38. Audet C, Jr J. ED, Digabel SL. Globalization strategies for Mesh Adaptive Direct Search. *Computational Optimization and Applications* 2009; **46**(2):193–215.
39. Le Digabel S. Algorithm 909: NOMAD: Nonlinear optimization with the MADS algorithm. *ACM Transactions on Mathematical Software (TOMS)* 2011; **37**(4):1–15.
40. Audet C, Béchard V, Digabel SL. Nonsmooth optimization through Mesh Adaptive Direct Search and Variable Neighborhood Search. *Journal of Global Optimization* 2007; **41**(2):299–318.
41. Audet C, Dennis J. Mesh adaptive direct search algorithms for constrained optimization. *SIAM Journal on Optimization* January 2006; **17**(1):188–217.
42. Dandois J, Garnier E, Pamart P-Y. NARX modelling of unsteady separation control. *Experiments in Fluids* 2013; **54**(2):1–17.
43. Hale JK. Caratheodory Conditions. In *Functional Differential Equations*, Applied Mathematical Sciences. Springer: US, 1971; no 3, 30–31.
44. Olbrot A. Control of retarded systems with function space constraints: necessary optimality conditions. *Control Cybernet* 1976; **5**:5–31.
45. Artstein Z. Linear systems with delayed controls: a reduction. *IEEE Transactions on Automatic Control* 1982; **27**(4):869–879.
46. Polyakova L. Generalized fixed-point theorems and periodic solutions of non-linear equations, 2006.
47. Kantorovich L, Akilov G. *Functional Analysis. 1982*. Pergamon Press: Oxford, 1982.
48. Wu L, Zheng WX, Gao H. Dissipativity-based sliding mode control of switched stochastic systems. *IEEE Transactions on Automatic Control* 2013; **58**(3):785–791.
49. Efimov D, Polyakov A, Fridman E, Perruquetti W, Richard J-P. Delay-dependent positivity: application to interval observers, 2015. Available: https://hal.inria.fr/hal-01140336/document. Accessed July 17, 2015.
50. Agarwal RP, Berezansky L, Braverman E, Domoshnitsky A. *Nonoscillation Theory of Functional Differential Equations with Applications*. Springer New York: New York, NY, 2012.
51. Davies EB. *Linear Operators and their Spectra*. Cambridge University Press: Cambridge, UK, 2007. Google-Books-ID: 6AjuCoaL34AC.

Copyright © 2017 John Wiley & Sons, Ltd.

DOI: 10.1002/rnc

Résumé étendu

La croissance actuelle de l'industrie du transport est impactée par le désir d'atteindre de plus grandes vitesses pour des temps de trajet plus courts ainsi que par le besoin de réduire les coûts énergétiques dans une optique de développement durable. Les communautés scientifique et industrielle cherchent à obtenir de plus faibles coûts de transport et une réduction drastique des émissions annuelles de CO_2.

Une des causes de ces pertes d'énergie est liée à des effets aérodynamiques tels que la trainée ou le décollement de l'écoulement sur le véhicule. Historiquement, le décollement était contré par du contrôle passif. Le contrôle passif consiste en une modification de la géométrie du véhicule en changeant sa forme ou en ajoutant de petits éléments ("actionneurs passifs") fixés sur la surface à des positions appropriées. Ces éléments peuvent être statiques ou rétractables. Bien qu'ils n'ont pas de coût énergétique, ils peuvent amener à une augmentation significative de la trainée totale et souffrent d'un manque d'adaptabilité à un changement dans l'écoulement et manquent donc de robustesse. Une modification des actionneurs en réponse à un changement dans l'écoulement, connu sous le nom de contrôle actif d'écoulement, requiert de la flexibilité de ces actionneurs ainsi que des mesures en temps-réel sur l'écoulement. Ces deux conditions (flexibilité et mesures en temps-réel) sont nécessaires pour maintenir l'écoulement dans un état satisfaisant les objectifs désirés (par exemple trainée, bruit, réduction de vibration) malgré des perturbations dans l'écoulement.

Ce travail s'appuie sur des tests expérimentaux réalisées dans les souffleries du Laboratoire de Mécanique de Lille (LML), de l'Office National d'Études et de Recherches Aérospatiales (ONERA) de Lille et du Laboratoire d'Automatique, de Mécanique et d'Informatique industrielles et Humaines (LAMIH) à Valenciennes :

- LML : soufflerie de couche limite dans laquelle est placé une maquette constituée d'une plaque plaque terminée par un volet. Un schéma est présenté Figure D.1a et une photo Figure D.1b. Le volet est équipé de capteurs films chauds et d'actionneurs jets d'air.

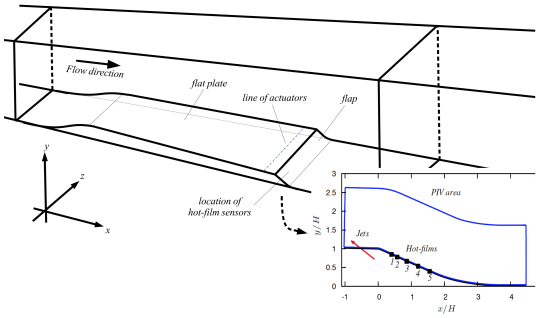

(a) Schéma de l'expérience du LML avec un zoom sur le volet et le positionnement des films chauds et des jets d'air

(b) Photo de l'expérience du LML. L'écoulement vient de la gauche.

Figure D.1 – Présentation de l'expérience du LML

- ONERA : soufflerie L1 de l'ONERA Lille dans laquelle est placée entre deux plaques verticales, à mi-hauteur de la veine, une plaque plane terminée par un volet basé sur le profil NACA4412. Un schéma du placement de l'aile dans la soufflerie est présenté Figure D.2a et un schéma de l'aile Figure D.2b. Le volet est équipé de capteurs films chauds et d'actionneurs jets d'air.
- LAMIH : soufflerie dans laquelle est placé un corps d'Ahmed, représentant une simplification géométrique d'une voiture, surélevé 3.5cm au dessus du sol. Un schéma du corps d'Ahmed est présenté Figure D.3. La face arrière du corps est équipée de 3 jets d'air (sur le côté supérieur et les deux côtés latéraux) et le corps est placé sur une balance aérodynamique afin de mesurer la trainée, la portance et la dérive.

Dans un premier temps, des modèles de ces expériences sont identifiés. Les formes de modèles choisies sont décrites dans les Equations (D.1) et (D.2). Ces équations sont dérivées (par approximation et simplification) de l'équation de Burgers qui est une simplification de l'équation de Navier-Stokes. Dans ces modèles, nous noterons y la mesure effectuée sur le système et nous l'appellerons la sortie du système ou du modèle et nous noterons u le signal de commande envoyé aux actionneurs et nous l'appellerons l'entrée du système ou du modèle. Le premier modèle contient des retards constants sur l'entrée et est directement dérivé de l'équation de Burgers. Le second modèle contient des retards dépendant de l'état sur l'entrée et est une modification du modèle précédent basé sur une analyse des données expérimentales. Le premier modèle est utilisé

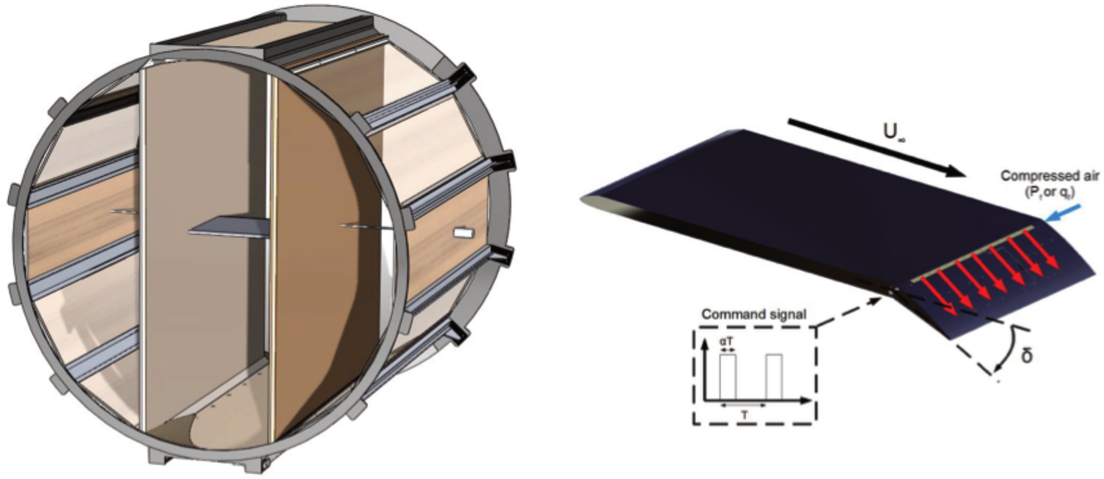

(a) Schéma du placement de l'aile dans la soufflerie de l'ONERA.

(b) Schéma de l'aile de l'ONERA.

Figure D.2 – Présentation de l'expérience de l'ONERA

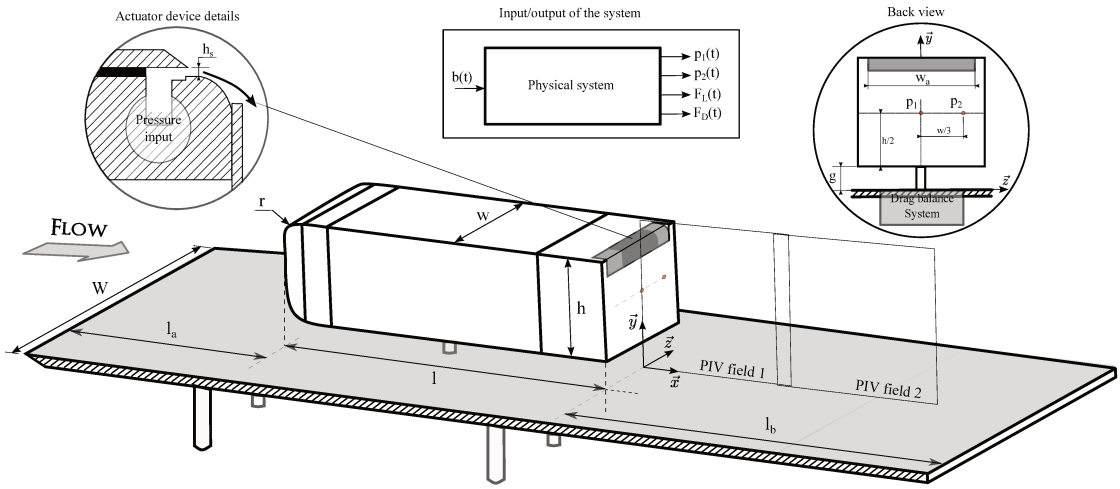

Figure D.3 – Schéma du corps d'Ahmed du LAMIH.

pour l'élaboration de contrôleurs alors que le second sert uniquement pour l'identification.

$$y_{k+1} = \sum_{i=1}^{N_1}\left(a_i y_{k-\tau_i}\right) + \sum_{l=1}^{N_3}\left(b_l + \sum_{j=1}^{N_2}\left(c_{jl} y_{k-\bar{\tau}_j}\right)\right) u_{k-h_l} \quad , \quad 0 \leq k \leq N-1 \tag{D.1}$$

$$y_{k+1} = \sum_{i=1}^{N_1}\left(a_i y_{k-\tau_i}\right) + \sum_{l=1}^{N_3}\left(b_l + \sum_{j=1}^{N_2}\left(c_{jl} y_{k-\bar{\tau}_j}\right)\right) u_{k-\widetilde{h}_l(\widetilde{y}_k)} \quad , \quad 0 \leq k \leq N-1 \tag{D.2}$$

$$y_m = 0, m < 0 \tag{D.3}$$

Les retards et bilinéarités dans ces équations permettent d'approximer les non-linéarités de l'équation de Burgers ou de Navier-Stokes ainsi que les temps de transport de l'information à travers l'écoulement. L'identification des coefficients des modèles est réalisée à l'aide de la méthode des Moindres Carrés. Afin d'obtenir les valeurs de retards un algorithme d'optimisation est utilisé. Étant donné que le modèle et les données sont en temps discret, les retards sont des entiers à déterminer. Le problème d'optimisation est non-convexe de par le fait que plusieurs jeux de coefficients peuvent donner une correspondance identique ou presque entre le modèle et les données et non-linéaire de par les bilinéarités du modèle. Il est donc nécessaire d'employer un algorithme capable de résoudre des problèmes dits Non-Convex Mixed-Integer Nonlinear. Le choix a été fait d'utiliser deux algorithmes : NOMAD et l'Algorithme Génétique (GA). Ces deux algorithmes sont testés et comparés, montrant que NOMAD est plus rapide et précis (temps de calcul plus faible, meilleure valeur de la fonction coût) mais que GA est plus simple à mettre en oeuvre pour les problèmes de grandes dimensions de par son implémentation en calcul parallèle dans le logiciel Matlab®. Les modèles sont également comparés au modèle ARMAX (Auto-Regressive Moving Averaged with eXogeneous inputs) qui est classique dans la littérature d'identification des écoulements. Cette comparaison montre que les modèles bilinéaires développés ici ont une meilleure correspondance aux données en utilisant le même nombre de coefficients.

A l'aide des modèles obtenus, deux contrôleurs sont développés. Le premier est un contrôle optimal en boucle ouverte qui permet, à partir des coefficients du modèle, d'obtenir le signal créneau permettant de maximiser une fonction coût qui représente le compromis entre le recollement de l'écoulement et le coût énergétique du contrôle. La fonction coût est donnée par l'Equation (D.4).

$$J(y,u) = \lim_{T\to+\infty} \frac{1}{T}\int_0^T \alpha y(s) - (1-\alpha)u^2(s)ds \tag{D.4}$$

Le problème d'optimisation est alors le suivant :

$$\text{Élaborer une loi de contrôle } u \text{ telle que } J(y,u) \to \max. \tag{D.5}$$

Maximiser la valeur de y revient à maximiser le recollement de l'écoulement, alors que minimiser u (ou maximiser $-u$) permet de réduire le coût énergétique du contrôle. Le paramètre α permet de faire le compromis entre ces deux objectifs.

Le signal créneau est donné par l'Équation D.6 :

$$u_{\omega,t'}(t) = \begin{cases} 1 & \text{pour} \quad t \in [k\omega, k\omega + t'), \\ 0 & \text{pour} \quad t \in [k\omega + t', (k+1)\omega), \end{cases} \tag{D.6}$$

pour tout $k > 0$.

Le problème d'optimisation (D.5) peut être résolu de façon suboptimale menant à, pour une valeur fixée de ω, le calcul de t' selon l'Équation (D.6) :

$$t' = \begin{cases} 0 & \text{if } \alpha = 0 \\ \omega & \text{if } \alpha = 1 \\ \omega \, \mathrm{sat}_{[0,1]}\left(\dfrac{-A(\mathbb{1})}{\sum_{i=1}^{N_2} B_i(\mathbb{1})} - \dfrac{\sqrt{\frac{\alpha}{(\alpha-1)} A(\mathbb{1}) \left(\sum_{i=1}^{N_2} b_i \right)}}{\sum_{i=1}^{N_2} B_i(\mathbb{1})} \right) & \text{if } 0 < \alpha < 1 \end{cases} \tag{D.7}$$

où $\mathrm{sat}_{[0,1]}$ est la fonction saturation sur l'intervalle $[0,1]$ telle que $\mathrm{sat}_{[0,1]}(x) = x$ for $0 \le x \le 1$, $\mathrm{sat}_{[0,1]}(x) = 1$ pour $x > 1$ et $\mathrm{sat}_{[0,1]}(x) = 0$ for $x < 0$.

Le second contrôleur est un contrôle robuste en boucle fermée permettant la poursuite d'une consigne. Le modèle utilisé pour ce contrôleur est le modèle le plus simple obtenu lors des tests d'identification en temps continu, donné par les Équations (D.8) et (D.9)

$$\dot{y}(t) = a_1 y(t-h) - a_2 y(t-\tau) + (b - cy(t-h) + cy(t-\bar{\tau}))u(t-h), \tag{D.8}$$

$$y(s) = 0, \quad u(s) = 0 \quad \text{pour} \quad s \le 0. \tag{D.9}$$

A l'aide de la méthode des Modes Glissants (Sliding Modes), nous définissons la surface de glissement $\sigma(t)$ dans l'Équation (D.10) :

$$\sigma(t) = y(t) - a_2 \int_{t-\tau}^{t} y(s)ds + c \int_{t-\bar{\tau}+h}^{t} y(s)ds + \int_{t-h}^{t} a_1 y(s) + (b - cy(s) + cy(s-\bar{\tau}+h))u(s)ds \tag{D.10}$$

La loi contrôle est alors donnée par l'Équation (D.11) :

$$u(t) = \begin{cases} 1 & \text{if} \quad \sigma(t) < \sigma^*, \\ 0 & \text{if} \quad \sigma(t) > \sigma^*, \end{cases} \tag{D.11}$$

où $\sigma^* = y^*(1 + a_2(h - \tau) + c(\bar{\tau} - h))$ et $y^* \in \left(0, \frac{b}{a_2 - a_1}\right)$. Sous les bonnes conditions sur les paramètres du modèle, cette loi garantit $y(t) \to y^*$ lorsque $t \to +\infty$. De plus, cette loi de contrôle permet de rejeter les perturbations bornées si la borne n'est pas trop grande par rapport à la force du contrôle (donnée dans le modèle par le coefficient b).

Cette loi de contrôle a été testée sur les expériences de l'ONERA et du LAMIH offrant des résultats convaincants. En effet, à l'ONERA, le contrôleur n'a pu être mis en défaut que lorsque la puissance des actionneurs n'était plus suffisante pour atteindre la consigne souhaitée. De plus, l'algorithme de contrôle a été implémenté sur un Arduino®, montrant sa simplicité, son faible coût algorithmiques et sa rapidité de calcul.

Liste des publications :

Brevet :

1. M. Feingesicht, A. Polyakov, F. Kerherve and J. P. Richard, **Contrôle par modes glissants du décollement d'un écoulement**

Article de vulgarisation scientifique :

1. **Améliorer l'aérodynamisme des avions en contrôlant l'écoulement de l'air**,
   `https://www.inria.fr/centre/lille/actualites/ameliorer-l-aerodynamisme-des-avions`

Article de journal :

1. M. Feingesicht, A. Polyakov, F. Kerherve and J. P. Richard, **SISO model-based control of separated flows**, *International Journal of Robust and Nonlinear Control*

Articles de conférences :

1. M. Feingesicht, A. Polyakov, F. Kerherve and J. P. Richard, **Nonlinear Control for Turbulent Flows**, *IFAC 2017 World Congress, Toulouse, 2017*
2. M. Feingesicht, A. Polyakov, F. Kerherve and J. P. Richard, **Model-Based Feedforward Optimal Control Applied to a Turbulent Separated Flow**, *IFAC 2017 World Congress, Toulouse, 2017*

3. M. Feingesicht, A. Polyakov, F. Kerherve and J. P. Richard, **A bi-linear input-output model with state-dependent delay for separated flow control**, *2016 European Control Conference (ECC), Aalborg, 2016*

Contrôle non linéaire actif d'écoulements turbulents décollés : Théorie et expérimentations.

Résumé

Le contrôle des écoulements est un domaine en forte croissance visant à modifier un écoulement à l'aide d'actionneurs et d'algorithmes de contrôle. Un axe important du contrôle des écoulements est le contrôle des décollements car le décollement de la couche limite provoque des augmentations de traînée et donc des pertes énergétiques et des coûts en carburant. Cette thèse vise à développer des algorithmes de contrôle pour le recollement des écoulements à l'aide de jets pulsés. La première partie de cette thèse expose une technique d'identification de modèle basée sur des données expérimentales. Les modèles sont déduits de considérations physiques et de l'Automatique. Ils offrent une bonne correspondance aux données tout en restant simples et en contenant peu de coefficients. La seconde partie de cette thèse utilise ces modèles pour élaborer deux algorithmes de contrôle : le premier est un contrôle optimal en boucle ouverte et le second un contrôle robuste en boucle fermée. Ces algorithmes ont été implémentés sur diverses plateformes expérimentales (LML, ONERA, LAMIH) et leurs propriétés ont été testées avec succès. Les tests ont été réalisés en utilisant un Arduino Uno pour les mesures et le calcul du contrôle, ce qui montre que la méthode développée est simple à appliquer et requiert peu de puissance de calcul.

Mots clés : contrôle des écoulements, contrôle par modes glissants, contrôle non linéaire, systèmes bilinéaires, systèmes à retard

---

Nonlinear active control of turbulent separated flows: Theory and experiments.

Abstract

Flow control is a strongly growing field aiming at modifying fluid flows using actuators and control algorithms. An important part of flow control is the control of flow separation as boundary layer separation increases drag and therefore energy losses and fuel consumption. This thesis focuses on developing control algorithms for flow reattachment using pulsed jets actuators. The first part of this work develops a model identification technique based on experimental data. The models are derived from physical and control theory considerations. They provide a good fit to the data while remaining simple and using few coefficients. The second part of this work uses this models in order to design two different control algorithms : the first one is an optimal open-loop control while the second one is a robust feedback control. The control algorithms have been applied on several experimental setups (LML, ONERA, LAMIH) and their properties have been successfully tested. The tests were conducted using a simple Arduino Uno for the measurements and computation of the control, showing that the developed method is easy to apply and requires very few computational resources.

Keywords: flow control, sliding mode control, nonlinear control, bilinear systems, time-delay systems